DOE/ET/33001--T41

DE83 001134

Dynamic Isotope Power System

Final Report

Technology Verification Phase

DISTRIBUTION OF THIS DOCUMENT IS UNLIMITED

Sundstrand Energy Systems
ROCKFORD ILLINOIS 61101
unit of Sundstrand Corporation

DISCLAIMER

This report was prepared as an account of work sponsored by an agency of the United States Government. Neither the United States Government nor any agency Thereof, nor any of their employees, makes any warranty, express or implied, or assumes any legal liability or responsibility for the accuracy, completeness, or usefulness of any information, apparatus, product, or process disclosed, or represents that its use would not infringe privately owned rights. Reference herein to any specific commercial product, process, or service by trade name, trademark, manufacturer, or otherwise does not necessarily constitute or imply its endorsement, recommendation, or favoring by the United States Government or any agency thereof. The views and opinions of authors expressed herein do not necessarily state or reflect those of the United States Government or any agency thereof.

DISCLAIMER

Portions of this document may be illegible in electronic image products. Images are produced from the best available original document.

DISCLAIMER

This report was prepared as an account of work sponsored by an agency of the United States Government. Neither the United States Government nor any agency thereof nor any of their employees makes any warranty, express or implied, or assumes any legal liability or responsibility for the accuracy, completeness, or usefulness of any information, apparatus, product or process disclosed, or represents that its use would not infringe privately owned rights. Reference herein to any specific commercial product, process, or service by trade name, trademark, manufacturer, or otherwise, does not necessarily constitute or imply its endorsement, recommendation, or favoring by the United States Government or any agency thereof. The views and opinions of authors expressed herein do not necessarily state or reflect those of the United States Government or any agency thereof.

REPORT NO 2032
DATE 3/10/82
REVISION DATE
FILE REF.
DOE/ET/33001--T41

SUNDSTRAND CORPORATION
ADVANCED TECHNOLOGY GROUP
4747 HARRISON AVE ROCKFORD IL 61101
AVIATION ELECTRIC POWER • AVIATION MECHANICAL • ENERGY SYSTEMS • OPERATIONS

MASTER

ENGINEERING REPORT

FINAL REPORT

TECHNOLOGY VERIFICATION PHASE

DYNAMIC ISOTOPE POWER SYSTEM

CONTROLLED DISTRIBUTION COPY
FOR
APPROVED
CONTRACT DATA MANAGER DATE

NOTICE

PORTIONS OF THIS REPORT ARE ILLEGIBLE. It has been reproduced from the best available copy to permit the broadest possible availability.

PREPARED FOR THE

U.S. DEPARTMENT OF ENERGY
UNDER CONTRACT DE-AC02-77ET-33001

APPROVAL AND CLASSIFICATION				
Internal Distribution Only	VICE PRES OF ENGRG	DATE	D.A. Halsey	3-10-82
Controlled Distribution (See EN 10.07)	VICE PRES OF ENGRG	04.13-82 DATE	PREPARED BY	DATE
Distribution Prohibited	VICE PRES OF ENGRG	DATE	R.J. Sorensen	3-11-82
			GROUP ENGINEER	DATE
			R.E. Thogmartin	3-10-82
			SECTION MANAGER	DATE
Military Contract No.			George W. Kemp	4-7-82
			ENGINEERING MANAGER	DATE
			Don A. Thayer	14 Apr 82
Witnessed by me or by under my Supervision			DIRECTOR OF ENGINEERING	DATE
	QAR DCASO ROCKFORD	DATE	Max Reich	3-15-82
			PROGRAM MANAGER	DATE

Form 5160L

NOTICE

"This report was prepared as an account of work sponsored by the United States Government. Neither the United States nor the United States Department of Energy, nor any of their employees, nor any of their contractors, subcontractors, or their employees, make any warranty, express or implied, or assumes any legal liability or responsibility for the accuracy, completeness or usefulness of any information, apparatus, product or process disclosed, or represents that its use would not infringe privately-owned rights".

TABLE OF CONTENTS

TITLE	SECTION NO.
Introduction	1
Summary	2.
Technology Verification Phase Achievements	2.1
Technology Status	2.2
Final Assessment	2.3
GDS Phase II Development	3.
GDS Performance	3.1
CRU	3.2
Regenerator	3.3
Electrical System Performance	3.4
System Insulation	3.5
Condensing Heat Exchanger	3.6
Fluid Degradation Products Removal System	3.7
Control System	3.8
Potential Performance Improvements	3.9
GDS Testing	4.0
Operating Hours Summary	4.1
Operational Problems and Solutions	4.2
Measurement System Improvements	4.3

Appendix

A. Battelle NaK Loading Report

B. Temperature Measurement

C. Low Pressure Measurement

D. GDS Teardown Report

LIST OF FIGURES

TITLE	FIGURE NO.
DIPS System Assembly	2.2.1
Dowtherm Degradation	2.2.2
Turbine Exhaust Pressure	2.2.3
Final DIPS Assembly	3.0.1
DIPS Design Point Operating Conditions	3.0.2
DIPS System Schematic	3.0.3
GDS Primary Data	3.1.1
GDS Secondary Data	3.1.2
System Schematic	3.1.3
Dowtherm Properties	3.1.4
CRU/Regenerator Heat Balance	3.1.5
J/C Bypass Valve Heat Balance	3.1.6
System Heat Balance	3.1.7
Analysis Program Results-Simulation of Measured Operation	3.1.8
Analysis Program Results-Increased Turbine Outlet Heat Loss	3.1.9
Phase I Thermal Analysis of CRU	3.1.10
Phase II Thermal Analysis of CRU	3.1.11
CRU Modifications To Reduce Thermal Losses	3.1.12
Required CRU Instrumentation	3.1.13
Alternator Condensing Potential	3.1.14
Effect Of Alternator Heating On Output Power	3.1.15
Combined Rotating Unit	3.2.1
Nozzle Discharge Coefficient	3.2.2
Turbine Nozzle Section-Photo	3.2.3
Turbine Blade Contours	3.2.4
Turbine Nozzle Contours	3.2.5
System Centrifugal Pump	3.2.6
Pump Pressure Rise Characteristics	3.2.7
Pump Head Flow Characteristics	3.2.8
Measured Pump Performance	3.2.9
GDS Pressure Levels	3.2.10
Homopolar Alternator	3.2.11
DIPS Alternator Efficiency Vs. Air Gap	3.2.12
Bearing Geometries	3.2.13
Seal Configurations Tested	3.2.14
Hybrid Visco Seal	3.2.15
Hybrid Visco Seal - Photo	3.2.16
GDS Pump End Seal Leakage	3.2.17
GDS Pump End Seal Power Loss	3.2.18
GDS Seal Power Loss	3.2.19
Split Regenerator Design	3.3.1
CRU/Regenerator Package	3.3.2
Regenerator - Photo	3.3.3
Regenerator - Photo	3.3.4
Electrical System Schematic	3.4.1
Feeder Losses	3.4.2
GDS Insulation Installation - Photo	3.5.1

LIST OF FIGURES CONTINUED

TITLE	FIGURE NO.
Measured Conductivity For Fibrefax And TG15000	3.5.2
GDS Jet Condenser	3.6.1
GDS System Configuration	3.6.2
Focused Stream Of Jet Condenser Liquid Jets	3.6.3
Single Nozzle Test Rig	3.6.4
Jewel Orifice Configuration	3.6.5
Ninety Nozzle Jet Condenser Shower Head	3.6.6
Jet Condenser Jewel Nozzles	3.6.7
Schematic For Jet Condenser Gas Sensitivity Tests	3.6.8
Jet Condenser Sensitivity Bottle Test System	3.6.9
Jet Condenser Vibration Test Rig	3.6.10
Jet Condenser Vibration Data	3.6.11
Effects Of Non-Condensible Air On Jet Condenser Performance	3.7.1
Non-Condensible Gas Separator	3.7.2
Theoretical And Measured Performance Of NCGS (Vertical)	3.7.4
NCGS Performance Instability	3.7.5
Simplified Test Rig Schematic	3.7.6
NCGS Serial No. 001 - Photo	3.7.7
NCGS Serial No. Ex	3.7.8
Demister/Evaporator	3.7.9
Modified Serial No. Ex As Installed On GDS	3.7.10
Serial No. Ex Test Result Summary	3.7.11
Analytical And Experimental Comparison	3.7.12
Modified Serial No. Ex NCGS Prior To Installation On GDS	3.7.13
Turbine Back Pressure Variation	3.7.14
Centrifugal Separator	3.7.15
KIPS Block Diagram	3.8.1
GDS Fluid Loop Controls	3.8.2
KIPS Turbine Loop Flow Control Valve	3.8.3
Phase I Control System Block Diagram	3.8.4
Alternator Controller Schematic - Phase I	3.8.5
GDS Controller - Phase I	3.8.6
Phase II Controller Block Diagram	3.8.7
Controller Schematic Phase II	3.8.8

1. INTRODUCTION

The Technology Verification Phase of the Dynamic Isotope Power System was carried out by Sundstrand Energy Systems, a unit of Sundstrand Corporation, under Department of Energy Contract DE-AC02-77ET-33001. The objectives of this phase of the program were:

- To increase system efficiency by component development, with a goal of 18.1%.
- To further demonstrate system reliability by performing an endurance test.
- To update the flight system design.

This final report presents the results of the work performed under the Technology Verification Phase of the program.

2. SUMMARY

2.1 Technology Verification Phase (Phase II) Achievements

At the initiation of Phase II a program plan (document Coo-4299-038) which outlined in detail the planned approach for the development phase, including a comprehensive schedule was prepared. The basic intention of the plan was to increase system efficiency to 18.1% by component development, to demonstrate system reliability by a 5000 hour endurance test and to update the flight system design.

In summary, during Phase II, system performance was improved from 15.1% to 16.6%, an endurance test of 2000 hours was performed while the Flight design analysis was limited to a study of the General Purpose Heat Source, a study of the regenerator manufacturing technique and analysis of the hardness of the system to a laser threat.

The following paragraphs compare the Phase II achievements with the program plan for the major system development tasks.

2.1.1 Flight System Design and Analysis

The scope of this task was greatly reduced early in Phase II due to the lack of a specific mission. It was realized that an integrated spacecraft-power system would be the optimum design approach and therefore a mission was

essential to a satisfactory flight design. However, some of the Flight Design tasks were performed and are summarized below.

A detailed study of the use of the General Purpose Heat Source (GPHS) was performed by Teledyne Energy Systems. A trade-off analysis of weight, heat loss and number of heat sources led to the selection of two Heat Sources Assemblies each containing 15 GPHS modules. These results are reported in Topical Report No. 80-DIPS-2.

The preferred regenerator configuration employed 14 fins per inch but this fin density could only be obtained as a brazed fin assembly. The maximum fin density finned tubing available was 11 fins per inch. The use of an 11 fin per inch tubing required a larger and heavier heat exchanger and subsequently higher pressure drop. During Phase II, a technique for manufacturing integrally finned tubing with 14 fins per inch was developed and demonstrated. A butt weld technique for the reverse tube bends in the regenerator was also developed at Oak Ridge using an automatic welding machine. These would replace the socket welds currently used, which are another potential source of contamination.

A study was made of the effects of a high energy laser beam incident on the system radiator to determine the hardness of the system to such a threat. The results were very promising and showed the system capable of absorbing significant amounts of energy without delerious effects.

2.1.2 Ground Demonstration System

Table 2.1 presents the Phase II goals and the final Phase II projections for component and system performance compared to the measured or inferred values at the termination of the contract.

It can be seen from the table that most components met or exceeded their planned performance. However, system performance of 18% anticipated at the beginning of Phase II was not obtained. This is partly due to lower than expected turbine efficiency higher bearing losses and lower jet-condenser performance but also to an internal heat loss resulting in a depressed turbine outlet temperature. These facts are discussed in detail in Section 3.

Emphasis in Phase II was placed on those components which either impacted reliability or yielded the highest potential efficiency improvement.

The following components were investigated per the program plan and ultimately incorporated into the GDS.

2.1.2.1 Turbine

Further component testing of a full admission wheel and reduced chord resulted in additional improvement in component efficiency. The testing was enhanced by the development of low pressure transducers capable of accurately and repeatedly measuring pressures in the range of 0.1 psia with a condensible vapor. The optimum configuration nozzle block was incorporated in the GDS with a resultant improvement in performance. This is discussed in detail in Section 3.2.

2.1.2.2 Rotating Seals

A test facility was developed to allow leakage and power loss to be determined for candidate shaft seal configurations. System operating conditions were simulated using Dowtherm as the test fluid. Various seal configurations were tested and a seal developed which has zero leakage and low power consumption. The seal type was incorporated into the GDS early in Phase II eliminating all leakage and in the final build a smaller seal of the same type was introduced with significantly lower power loss. The seals are discussed in Section 3.2.

2.1.2.3 System Pump

A system pump was successively trimmed in diameter and performance maps generated for each impeller size. When the system hydraulic characteristics were finalized and jet condenser characteristics determined, a pump size was selected. After manufacture the final pump characteristics were determined and it was incorporated in the final build. The pump is discussed in Section 3.2.

2.1.2.4 Alternator

Analysis showed that the alternator "air" gap could have a significant effect on efficiency. The test rig was upgraded to incorporate an electric motor in place of the air turbine prime mover. This provided improved accuracy by ensuring constant speed operation during tests. An accurate assessment of the effect of air

gap and rotor machining techniques on efficiency was made. From these tests a configuration with a 1% point improvement in efficiency was incorporated into the GDS.

Tests were also performed at Battelle Memorial Institute to investigate the outgassing characteristics of the alternator stator. The results showed that the electrical insulation selection was capable of withstanding the required operational temperatures without effecting system pressure levels. The alternator is discussed in Sections 3.2 and 3.4.

2.1.2.5 Electronic Controller

The controller specification was revised to satisfy reduced ripple requirements and improved efficiency. The simulated flight design was converted to a breadboard design located outside the vacuum chamber to allow changes to be readily made with the GDS operational. Controller development included improvement of rectifier performance, reduced ripple content and optimizing control characteristics. Rectifier performance was improved to design levels but these gains were offset by losses in the additional filtering, resulting in an overall controller efficiency seomwhat lower than in Phase I. These results are discussed in detail in Section 3.4.

2.1.2.6 Working Fluid

Further study of the thermal degradation characteristics of the working fluid was performed by Battelle Memorial Institute. These included tests in which the main non-condensible degradation product, hydrogen, was continuously removed from the loop, thereby precluding an equilibrium type reaction. The results, though not totally conclusive, indicated that the upper temperature limit of the system could be safely raised to 700°F as long as a non-condensible gas separator was incorporated in the system. These results are discussed in Section 3.7 and are presented in report 80-DIPS-19.

2.1.2.7 Jet Condenser

The Phase I single nozzle test rig was converted from steam to Dowtherm operation and used to test the jewel nozzles for the 90 nozzle configuration jet condenser. A focus rig was built and allowed the 90 nozzle condenser to be successfully focussed. A test facility was also designed and built for vibration testing and the 90

nozzle condenser and accumulator assembly demonstrated the ability to sustain vibrations perpendicular to the injection plane exceeding space shuttle launch loads by a significant margin while actively condensing Dowtherm. These results are presented in Section 3.6. The 90 nozzle condenser was incorporated in the GDS. Newly developed pressure instrumentation allowed an accurate assessment of the condenser vapor pressure to be determined for the first time.

2.1.2.8 Non-Condensible Gas Separator

The non-condensible gas separator (NCGS) was the subject of intense investigation during Phase I. The NCGS was developed considerably from the Phase I configuration and finally demonstrated adequate separation capability. A mathematical model capable of predicting temperatures and gas concentrations was generated to aid in the development process. The NCGS was incorporated in the final build of the GDS and demonstrated the ability to maintain a constant system pressure. This component is discussed in detail in Section 3.7.

2.1.2.9 Flow Control Valve

After contamination problems were discovered early in the program a concerted effort was made to develop a Nak filling procedure for the thermal sensor which precluded the potential for contamination. A successful filling procedure was developed at Battelle and a sensor incorporated into the GDS to demonstrate reliability. The flow control valve with Nak filled sensors operated for over 2000 hours with no performance change. This is reported in detail in Section 3.8.

2.1.2.10 Insulation

An insulation test program was added to the program plan during Phase II after elimination of the seal leakage did not eliminate the turbine exit temperature depression and system heat losses became suspect. Two types of insulation material were tested as well as the effectiveness of radiation shields. These results are reported in Section 3.5 and were used to determine the best way of insulating the final GDS configuration.

2.1.2.11 Ground Demonstration System

The modified and developed components were incorporated into the final build of the GDS. Delays in component test schedules (the non-condensible gas separator in

particular) and in the manufacture of the turbine nozzle housing precluded a 5000 hour endurance test. However, 2000 hours of testing on the final configuration of the GDS were accomplished and 10606 hours of GDS operating time were accumulated during both phases of the program. Unfortunately, system performance was not as high as had been hoped although most components met their design goals. Turbine outlet temperature remained depressed despite efforts to minimize external and internal heat losses. However, it was noted that a negative heat loss occurred in the heat sources and that the magnitude of this loss was approximately the same as the apparent loss in the CRU. Instrumentation was greatly improved for the final build lending credence to the indicated results. Wet vapor (i.e. superheated vapor with entrained mist) leaving the heat sources would satisfy both these anomalies and would need to be investigated further in another design.

2.2 TECHNOLOGY STATUS

2.2.1 Introduction

The Phase I requirements of the Kilowatt Isotope Power System (KIPS) program were to make a detailed Flight System Conceptual Design (FSCD) for an isotope fueled organic Rankine cycle and to build and test a Ground Demonstration System (GDS) which simulated as closely as possible the operational characteristics of the FSCD. Deviation of the GDS from the FSCD was necessary in several aspects to allow satisfactory testing of a GDS. The heat sources were electrically heated instead of using isotope fuel; instrumentation was necessary to determine operating characteristics; the radiator was tested as a component while GDS heat was rejected via an auxiliary heat exchanger; the GDS used 'O' rings and demountable fittings in place of the all-welded configuration of a flight design. GDS testing was performed in a vacuum chamber to simulate space vacuum and to eliminate the potential air leakage into low pressure regions of the system.

Figure 2.2.1 shows the Phase I GDS prior to application of the insulation blanket and installation in the vacuum chamber. At the end of Phase I the GDS had been operated for greater than 1000 hours and had achieved greater than 15% system efficiency. However, certain component deficiencies existed and certain operational characteristics were deemed inadequate to proceed into a Flight Design.

The Phase II, Technology Verification Phase, contract for the newly named Dynamic Isotope Power System (DIPS) was intended for performance improvement of both components and system and satisfactory resolution of certain component operating characteristics.

Early in Phase II a Department of Energy "Ad-Hoc" Committee was organized to investigate the status of the technology. The Committee conclusions were summarized in a report, reference 1. Sundstrand responded to that report in reference 2, explaining the causes and solutions to some of the committee's concerns.

In the following sections those items which were considered to be of high or moderate risk in the Committee report are discussed. Items of low risk have not been addressed.

Most items of concern were eliminated by the end of Phase II and it is felt that the Technology Development Phase has adequately demonstrated the viability of the system. Some improvement in system efficiency is still needed to meet the design efficiency goal and some further refinement of the non-condensable gas separator is required, but the Dynamic Isotope Power System has shown, both by its relatively high efficiency and reliable, repeatable operation, that an isotope fueled organic Rankine System is an excellent approach to the increasing power needs for satellites in the 1985 - 1985 time frame.

2.2.2 Working Fluid Stability - Battelle Tests

An item of significant concern to the Committee was the fact that the apparent gas generation rates from the Phase II capsule tests were a factor of 5 to 10 times higher than the gas generation rates from the Phase I capsule testing. The Phase I capsules were designed by Battelle to percolate liquid working fluid into the vapor-gas space of the capsule to provide a means of dissolving some of the non-condensable gas in the liquid working fluid. This was done in an attempt to simulate the conditions of the working fluid in a power system utilizing a jet condenser, which does recirculate non-condensable gas along with the liquid feed to the boiler.

Reference 2 Sundstrand internal memo ESD-79-M-315 'Response to Report of the DIPS Technology Status Committee'
Reference 1 Dynamic Isotope Power System Technology Status Committee Report. DOE Report FSEC-ESD-217-79/160

The Phase II capsules were designed by Battelle with a reflux condenser gas trap in order to minimize the amount of non-condensable gas being dissolved in the working fluid. This was done in order to determine if any deleterious effects on working fluid stability would occur if all of the non-condensable gas was removed from the system. The necessity for removal of non-condensable gases from the system was apparent during Phase I jet condenser testing where it was found that the jet condenser backpressure capability was perceptibly affected by air concentrations greater than 10 PPM, and that the jet condenser would cease functioning due to jet brooming-floodout at air contents of approximately 100 PPM.

Figure 2.2.2 shows an Arrhenius plot of the disappearance rate of Dowtherm A for the various capsules which were run for 1000 hours. 1000 hours is a 10 year equivalent time at temperature in the DIPS. From this it is apparent that the actual decomposition rate is slightly lower for the Phase II tests than for the Phase I tests which is most encouraging. However, as indicated above, the gas evolution rates from these Phase II capsules was approximately 5 to 10 times higher than for the Phase I capsules.

This higher rate of gas (hydrogen)* generation is apparently to be expected since removal of the hydrogen by the gas trap decreases the potential for either physical or chemical back reaction with the fluid, and thus reduces the inhibition of the overall process of hydrogen formation.

Since the gas evolution rates scattered by as much as a factor or 5 for a given temperature level in the Phase II tests it is not clear that all the gas traps were functioning to the same efficiency level. Thus no firm data were developed relating the hydrogen gas generation rate to the concentration of dissolved gas. All of the results of capsule testing done to date indicate that this is the question that needs to be answered in order to be able to properly size a non-condensable gas separator for the DIPS.

*In the Battelle tests where no air in-leakage was experienced, hydrogen was the principal component of the non-condensable gas with methane and CO_2 present on minor quantities.

Battelle personnel attempted an experiment to measure the hydrogen pressure in a capsule continuously with a mass spectrometer. This measurement combined with hydrogen solubility measurements, would have allowed estimation of the gas generation rate as a function of dissolved gas concentration, which is the information needed. Unfortunately test loop equipment performance limitations prevented meaningful data via this approach. Thus the DIPS GDS was deemed to be the best source of information on gas generation rates.

The DIPS GDS was run for many thousands of hours before the non-condensable gas separator was installed. During this time the system would operate for periods of as much as 500 hrs. before the non-condensable gas had to be removed from the system via the deaerator.

On one occasion (8-31-80) with a non-functioning gas separator installed in the system, the accumulation of non-condensable gas caused a jet condenser floodout. The measured turbine exhaust pressure had increased from a value of .145 psia shortly after deaerating the system to a value just over .170 psia when the floodout occured.

A typical history of turbine exhaust pressure with a non-functioning gas separator is shown in Figure 2.2.3 for the 9-11-80 to 9-18-80 time period. Also shown in Figure 2.2.3 is a history of turbine exhaust pressure after the non-condensable gas separator was made functional. It is seen that the pressure rose gradually from the "just deaerated" value of .145 psia to a steady state value of .149 psia where it remained throughout the subsequent system operation. (300 hrs.)

This behavior indicates that the non-condensable gas concentration builds up to some level at which the gas separator has sufficient capacity to eject non-condensable gases at the rate they are being generated. The fact that this steady state gas concentration results in a turbine exhaust pressure very near the value of a just deaerated system indicates that the non-condensable gas evolution in the DIPS GDS operating with a 700°F turbine inlet temperature is easily handled by the gas separator and results in no perceptable system performance degradation due to non-condensable gas generation or removal.

2.2.3 Non-Condensable Gas Separator

The Ad-Hoc Committee expressed serious concerns about the operational capability of the gas separator, mainly because of the increasing realization of the necessity for the device and because of testing difficulties at the time of review.

The first unit, designed and built to simulate a Flight Design, suffered from design flaws which could not easily be corrected because of its all-welded construction. Additional units, including an experimental, disassemblable unit were built to enable the various operational difficulties to be investigated and eliminated. The different separator designs had mostly shown adequate separation capability when operated in the vertical orientation, i.e. with gravity assisting operation, but exhibited periodic fluctuations when operated horizontally i.e. without gravity assist.

A mathematical model was generated to simulate operation and provided good correlation with test data. This model could be used to investigate different design changes without manufacturing test hardware.

The final configuration, which employed a .010 inch capillary, demonstrated satisfactory operation in the vertical mode. Performance was also adequate in the horizontal mode. At low injection rates in the horizontal orientation some instability and lower throughputs were noted, but at the higher injection rates the flow recovered to its previous (i.e. vertical) value and stable operation was obtained. The higher injection rates were those expected to be experienced in the DIPS.

2.2.4 Jet Condenser

At the time of the committee review, Sapphire nozzle inserts for the jet condenser had been successfully tested and thereby confirmed the viability of a 90 nozzle shower head. There was, hoever, serious concern about the capability of the condenser assembly to meet launch vibration and shock requirements. At that time confidence in the capability of successful operation was based on calculation of relative motion between the liquid streams and the diffuser throat

combined with experimental data from static, misaligned jet tests.

Vibration tests were made on an operating jet condenser and demonstrated the capability of withstanding at least 10g's throughout the frequency range of 5-500Hz.

These tests were performed with the vibration input perpendicular to the liquid injection direction which is the most critical mode. The tests were performed with non-condensable air concentrations in the range of 5-20 ppm which is consistent with the 1 ppm concentration of hydrogen expected for system operation with a gas separator. A video tape was made of one test run and is available for viewing at Sundstrand.

2.2.5 Bearings and Seals

2.2.5.1 Seals

The seals which separate the liquid cavities of the bearings from the vapor space of the turbine and alternator had leaked during Phase I with subsequent performance penalties. The committee showed concern with the problems of developing a zero leakage seal and inconsistent test results on the seal test rig.

A zero leakage seal was subsequently developed which showed repeatable results with very low power consumption. The seal was a hybrid design which employed a visco pumping section to provide zero leakage with a smooth bore section to allow free floating operation and therefore relatively tight operational clearance compared to standard visco seals. Endurance and start-stop testing was performed on the seal test rig prior to installation into the GDS with very satisfactory results.

2.2.5.2 Bearings

There were several areas of concern about the bearings; scratches, discoloration, preload determination and assembly techniques. The scratching after 1000 hours of testing was suspected to be due to contamination at assembly and process changes were instituted to eliminate the cause. The process changes included demagnetization of the bearing module and a shrink fit assembly process rather than a press fit assembly. The scratches of concern were measured to be less than .0001 inches deep and confirmed the ability of the surface coating to absorb debris without damage.

The presence of discoloration of the hotter bearings has not been explained. Sandia laboratories performed tests on the material but the source could not be determined. The discoloration certainly would not affect bearing operation. The concern about bearing preload resulted from the operation of initial GDS builds with tighter than design bearing clearances due to a drawing error. The actual design preloads, which were employed in the final build, were selected to provide stable bearing operation over the entire operating range while minimizing losses. The use of tighter preloads than design would, in fact, improve the stability range but with an increase in losses.

Manufacturing techniques were suspected by the committee as being the cause of the scratching of the radial bearings and also could cause problems in alignment of the thrust bearings.

Experimental investigations of the thrust bearing showed that a misalignment of up to .004 inches could be tracked by the thrust bearing, but beyond this interference could occur on the locating pins. Although this misalignment is much greater than would occur with the manufacturing tolerances employed, the hardware was modified to eliminate the interference. The manufacturing technique used for the radial bearings employed an oversized mandrel rather than actual GDS hardware. This manufacturing technique was developed so that scratching on assembly would not occur.

2.2.6 Flow Control Valve

The committee raised several questions with respect to the flow control valve:

2.2.6.1 Bubble Analysis

At the time of the committee report a gas bubble was known to be present in the only existing thermal sensor assembly. The source of the bubble was not known with certainty. Battelle personnel were successful in their attempt to determine the composition of the bubble. The bubble was argon. Argon was used as a cover gas over the Nak to prevent oxygen contamination during the filling procedure. It is likely that some of the argon was introduced into the sensor during filling. During Phase II an intensive development effort with Battelle resulted in a successful filling

procedure. Five temperature sensor assemblies were ultimately filled.

2.2.6.2 Pressure Regulator Gain

The measured pressure regulator gain of the flow control valve was found to be slightly smaller than the computer model had predicted. The question of whether this might cause stability problems when the temperature loop was closed around the pressure regulator loop was raised. The flow control valve with functioning temperature sensor was installed prior to the last rebuild of the GDS and was present for the 2002 hours of operation of the last build. The system was shown to be stable.

2.2.6.3 Controlling Sensor

The question of which of the two temperature sensors was controlling the GDS operating temperature was raised. As a corollary to this question, the point that a temperature shift would occur if one sensor were to fail was raised.

2.2.6.3.1 Controlling Sensor

At the acceptance test of the temperature sensor, the temperature gradient or the change in length per degree temperature change for both temperature sensors on the thermal sensor assembly is measured. The gradient for both sensors of any assembly must be within acceptable limits. The limits were selected to ensure that either temperature sensor would yield acceptable operating points if controlling. The length of each sensor is also measured at the minimum system operating temperature. The valve is then assembled so that both sensors are in contact with the flapper arm at the minimum operating temperature. This assures that the sensor with the larger relative gradient will always be in control. (Relative gradient is the absolute gradient, as measured, corrected for sensor lever arm ratios with respect to the flex pivot location).

2.2.6.3.2 Temperature Shift

Obviously a temperature shift will occur if the controlling sensor fails. The range of acceptable gradients was selected to assure that all sensors would yield acceptable operating points if controlling. Thus if the controlling sensor were to fail, the operating temperature would rise slightly to another

acceptable operating point. The maximum temperature shift would be less than 2°F.

2.2.6.4 Fail Extended

A question was raised on the possibility of the thermal sensor failing in the extended position. It was observed that if either sensor were to fail extended, temperature compensation would be lost. Accordingly the system could be less reliable with two sensors than with one. The fail extended failure mode and its consequences were previously acknowledged by Sundstrand in the Phase II Program Plan, Vol. 5, Section 8.

The mechanism by which the sensor could fail in an extended position is by the development of a clog in the capillary tube between the helical temperature bulb and the bellows actuator assembly. The mechanism by which a clog could form is by accumulation of sodium and potassium oxides. Sodium and potassium oxides are crystalline materials with solubility in NaK dependent on temperature. The solubilities increase with increasing temperature. Thus sodium and potassium oxides will precipitate from saturated contaminated Nak as the temperature of the contaminated NaK is decreased. In flowing NaK systems clogs have been known to form at locations of sharp temperature gradients. The oxides are transported by the flowing NaK to precipitate from the NaK as the temperature changes and accumulate forming the clog.

In the DIPS thermal sensor the NaK is essentially static. The maximum travel of a volume of NaK in the transition capillary in an operating system would be less than .2 inches. The filling procedure used for DIPS insured that the oxygen was removed from the assembly prior to filling and that the oxygen content of the NaK was very low. The inside diameter of the transition capillary was increased to further decrease the probability of clogging.

In order to determine the impact of having two sensors on the overall probability of flow control valve failure, it is not possible to simply multiply the probability of failure of a single sensor by two. The probability of either or both temperature sensors within a given assembly failing is reduced from twice the probability of a single sensor failing by the amount of stochastic dependency which exists between the probabilities of failure of the individual sensors within an assembly. Since the mechanism of failure is oxide

accumulation, and since oxide accumulation is known to result from either oxygen contaminated NaK and/or filling procedure errors and since both sensors on an assembly will be filled simultaneously; there is reason to expect a high degree of dependency. Consequently the probability of either or both sensors failing should be significantly less than twice the probability of failure of either sensor.

2.3 Final Assessment

The assessment made by Sundstrand at the conclusion of the DIPS program is one of success tempered by the lack of a customer with a specific mission for the power generating system. The major items of note are summarized below:

- The GDS was basically prototypic of a flight design except for instrumentation (with associated penetrations) demountable flanges, electric heating of the HSA and a water cooled heat rejection system.

- All the components necessary for satisfactory operation were demonstrated successfully at the system level including the non-condensible gas separator and vapor flow control valve.

- Significant endurance operation was demonstrated. Although a 5000 hour endurance test was not performed on the final build, it was operated successfully for over 2000 hours and demonstrated the capability of operation without any umbilical. In addition, over 11,000 total hours of operation without any component failure attested to the inherent reliability of this type of system.

- It is recognized that some further development is required, specifically in the area of performance. The main shortfall here may well be due to the presence of wet turbine vapor and therefore be relatively easy to correct.

- Additional effort is required for a final flight design since that effort was not performed in Phase II.

- It is recognized that probable applications for isotope powered systems are for hardened missions at higher power levels. If so, the system efficiency will inherently improve.

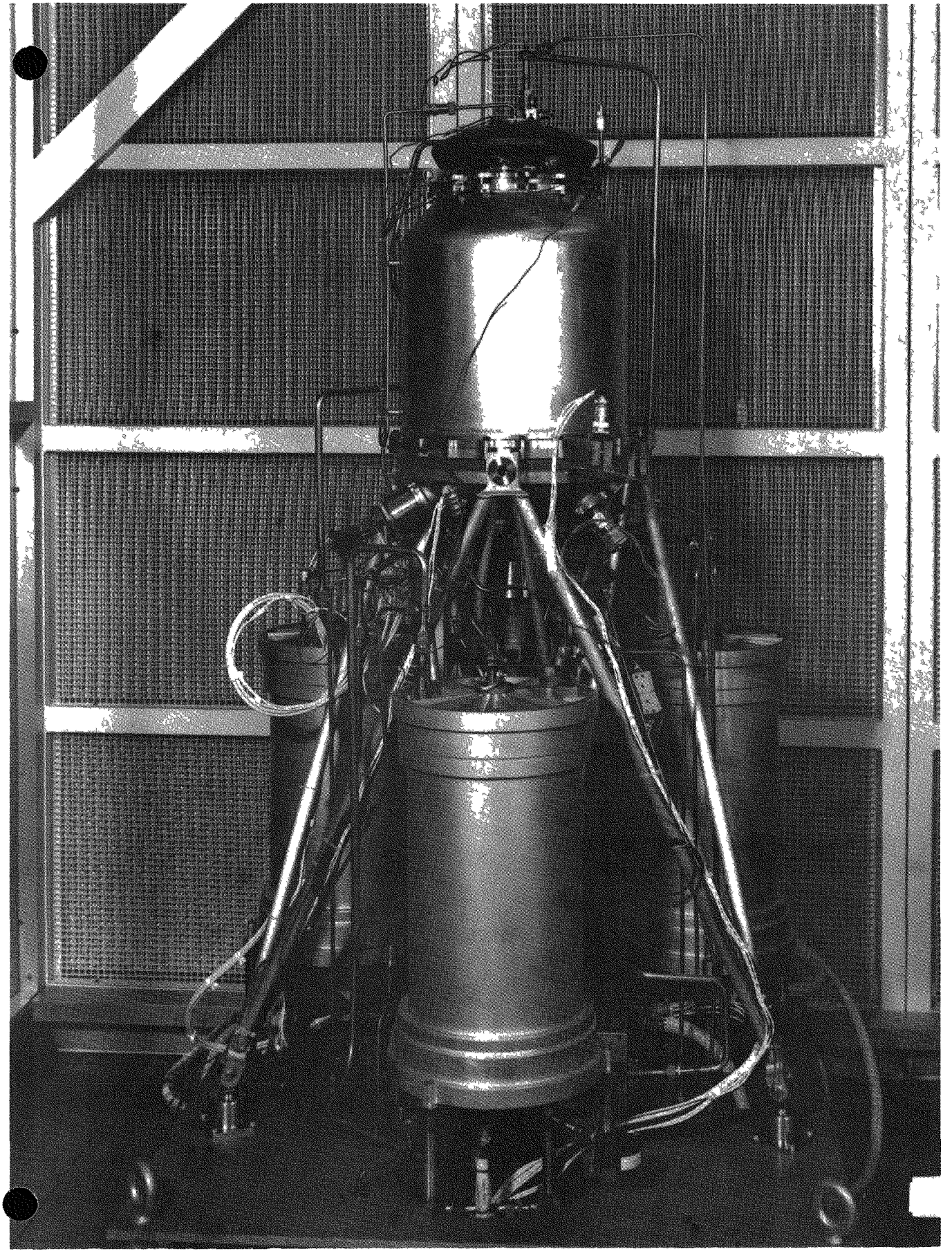

Fig. 2.2-1

Dowtherm Degradation

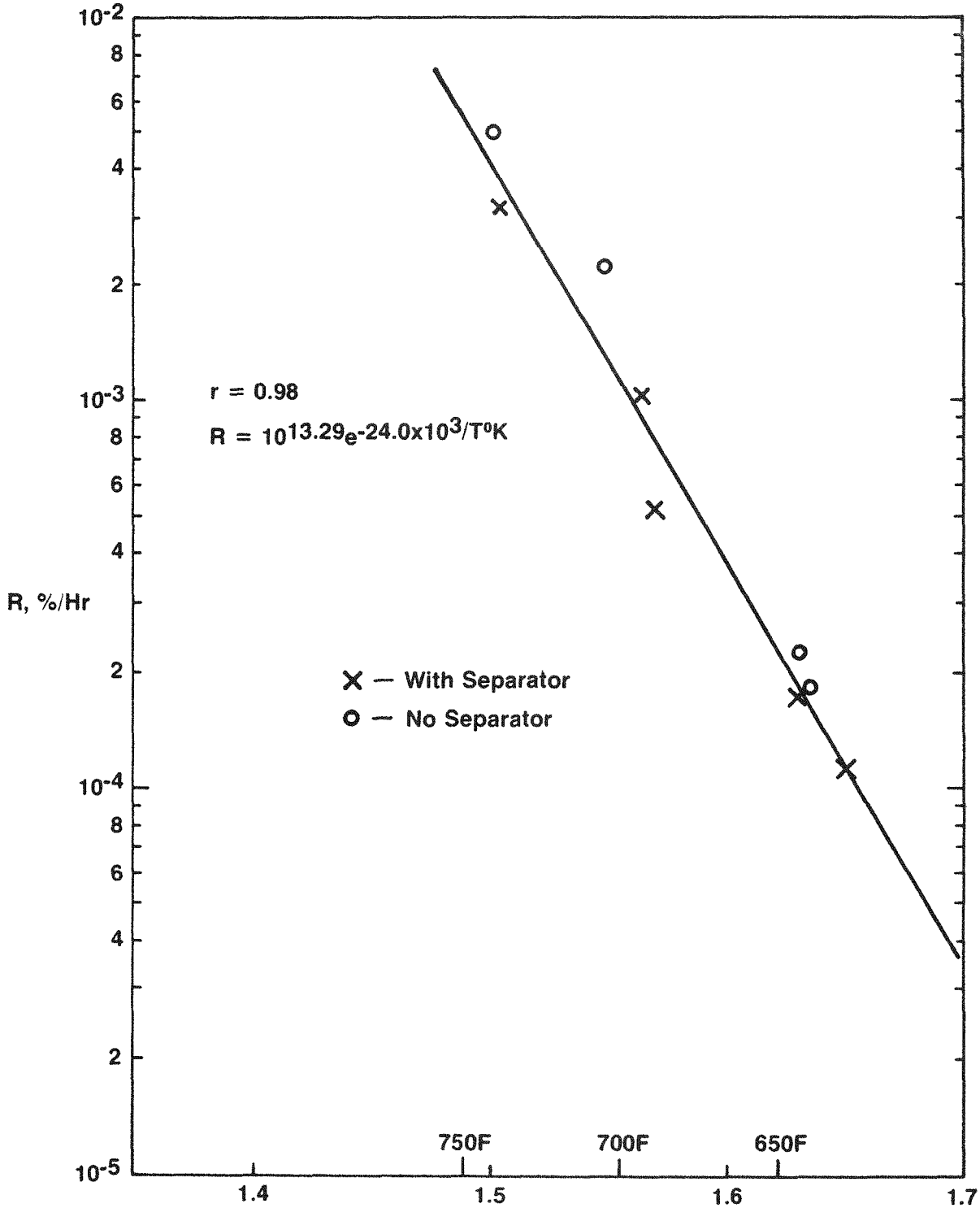

Figure 2.2.2

Turbine Exhaust Pressure

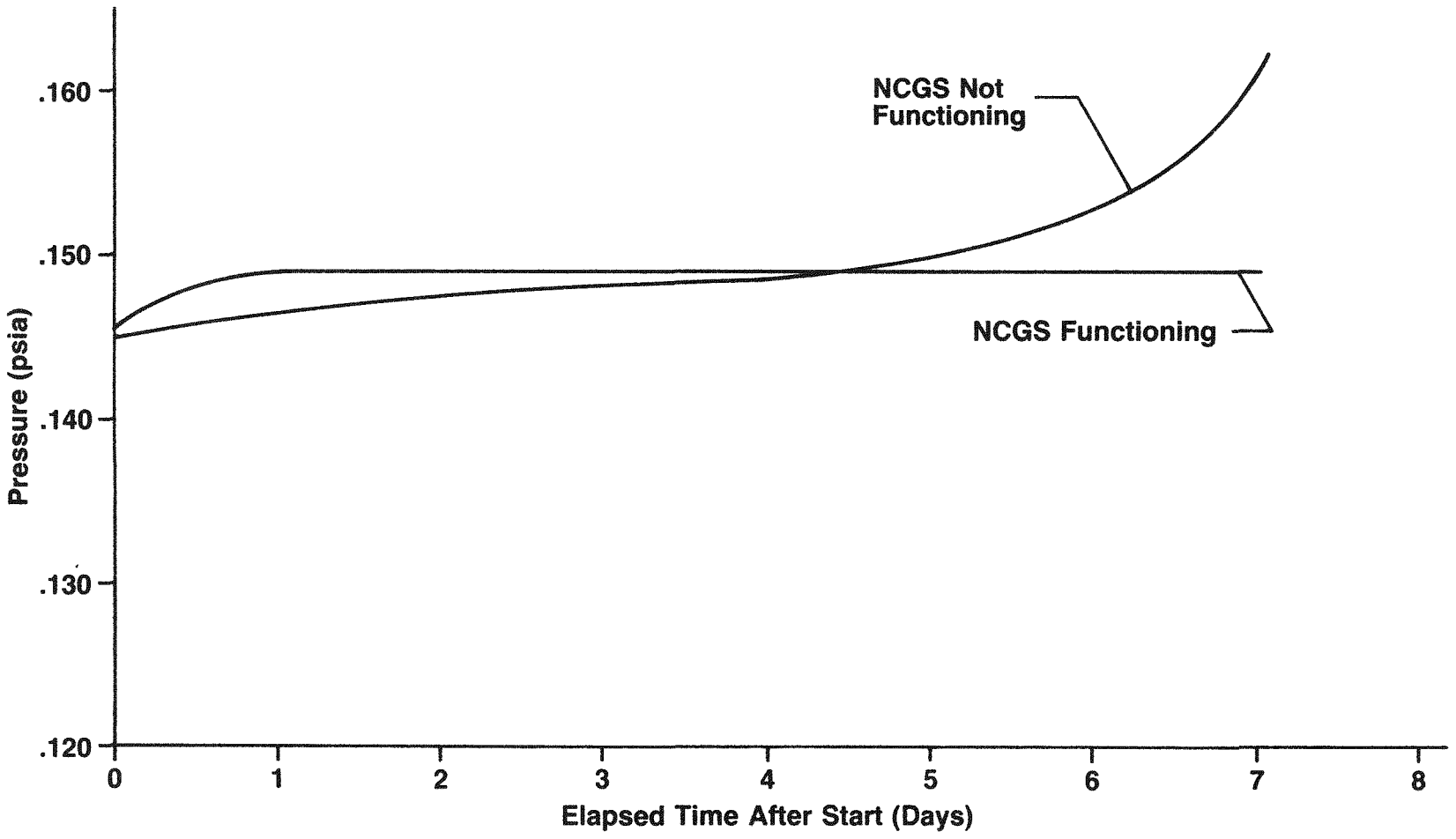

Fig. 2.2.3

3. GDS PHASE II DEVELOPMENT

3.0 SYSTEM DESCRIPTION

The Ground Demonstration System is shown in Figure 3.0.1 prior to its final installation in the vacuum chamber during Phase II, the Technology Verification Phase. Clearly visible in the photograph are two of the three heat source assemblies, the insulation blanket applied to the PCS, the mounting structure and thermocouple instrumentation.

Figure 3.0.2 shows a simplified block diagram of the system with design state points superimposed. The block diagram shows the major system components tested during Phase II. These include the combined rotating unit, comprised of turbine, alternator and pump; the heat source assemblies; the regenerator and the jet condenser accumulator. The heat rejection heat exchanger was used in place of the space radiator for heat rejection. Not shown is the system electronic controller used for control of speed and voltage and to rectify AC power to DC.

The system uses an organic working fluid, Dowtherm A (a high purity eutectic mixture of biphenyl and biphenyl ether) in a Rankine thermodynamic cycle. There are two major operating loops in the system, the power loop where power is extracted and the heat rejection loop for waste heat rejection.

In the power loop, high pressure liquid from the pump first cools the alternator before passing to the regenerator where it absorbs turbine exhaust superheat and then to the heat source assemblies. Here additional heat is transferred to the working fluid which boils and enters the turbine as high pressure, superheated vapor. The vapor is expanded across the turbine and power is extracted to drive the alternator and pump. The fluid leaves the turbine as low pressure superheated vapor and passes through the regenerator where most of the superheat is removed before entering the jet condenser. In the condenser the vapor condenses on subcooled jets before returning to the pump to complete the loop.

In the heat rejection loop the majority of the pump discharge flows to the heat rejection heat exchanger where waste heat is absorbed. The cold liquid from the heat exchanger outlet is injected through multiple nozzles in the jet condenser where the vapor condenses on the liquid jets. Some of the injected dynamic pressure is recovered and the mixed power loop flow and heat rejection loop flow returns to the pump inlet.

The system schematic is shown in Figure 3.0.3. The schematic describes in detail the system plumbing, shows all the system and shows the location of all the system instrumentation used for the final build. As can be seen from the accompanying instrumentation table, redundancy was added in the areas necessary to provide an understanding of the system thermal operation.

The Ground Demonstration system underwent considerable development during Phase I and Phase II. A summary of the major changes made at each rebuild is presented in Table 3.0.1. The system will be described component by component in the following sections.

Final DIPS Assembly Prior To Installation In Vacuum Chamber

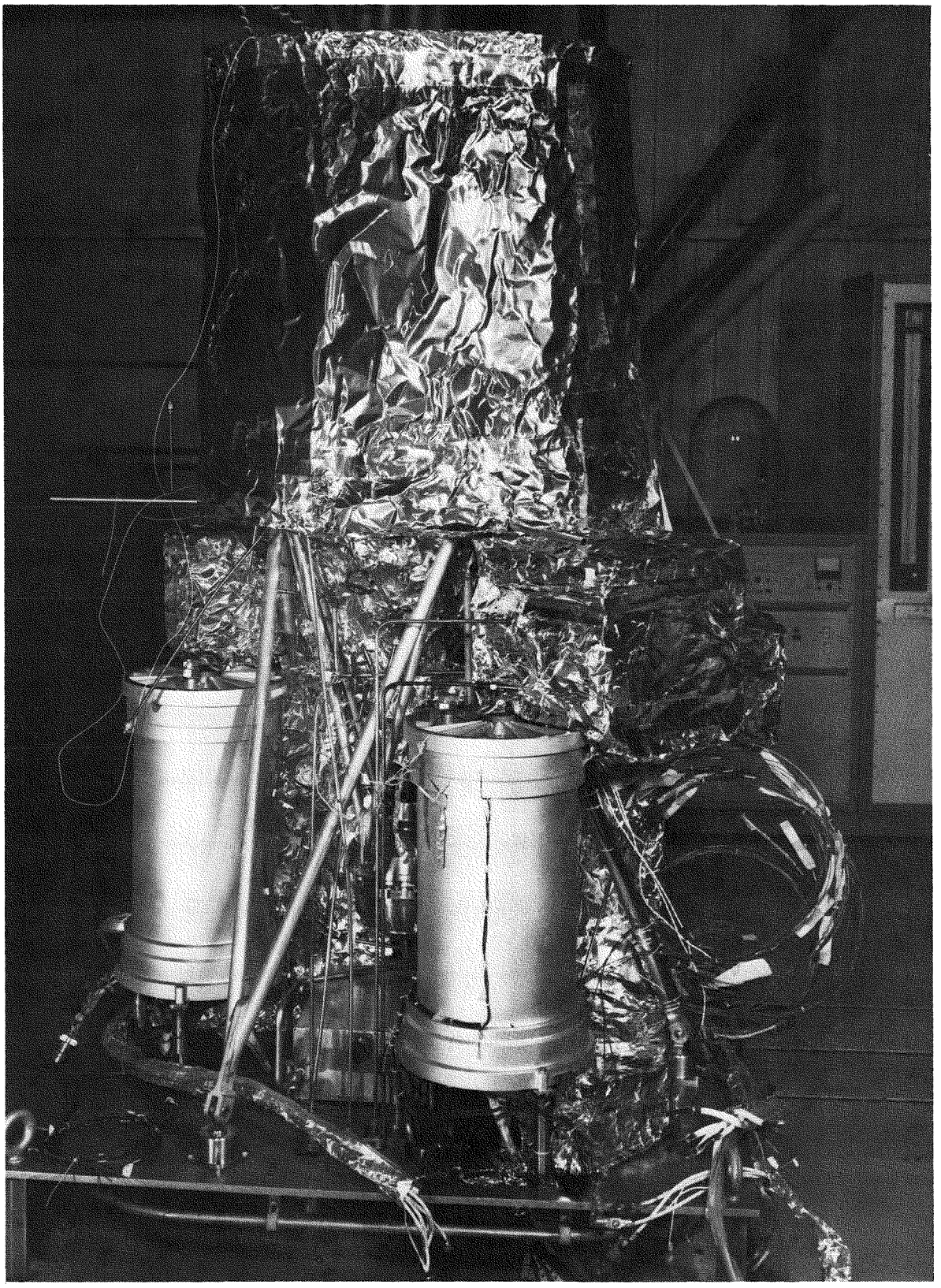

Figure 3.0.1

DIPS Design Point Operating Conditions

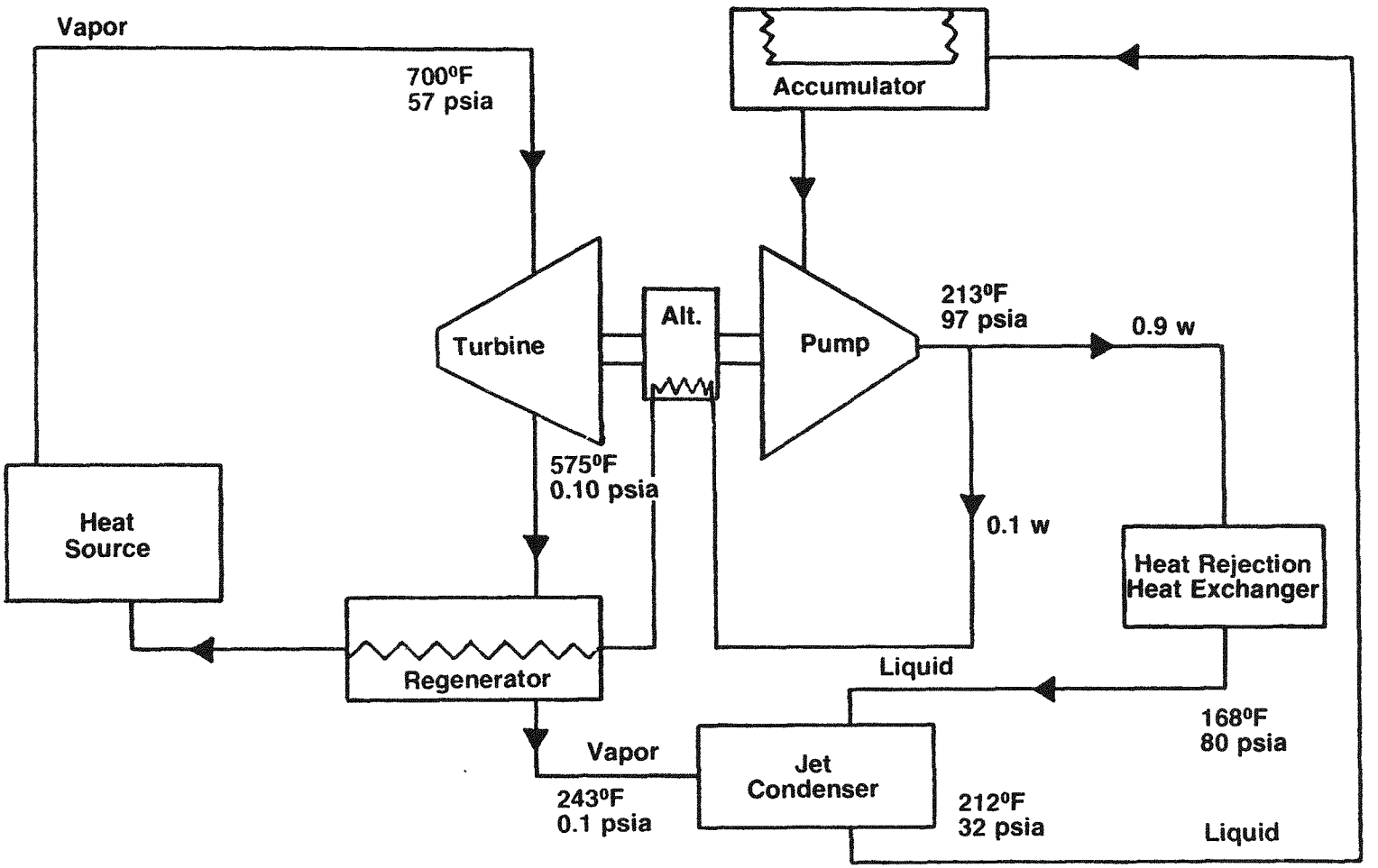

Figure 3.0.2

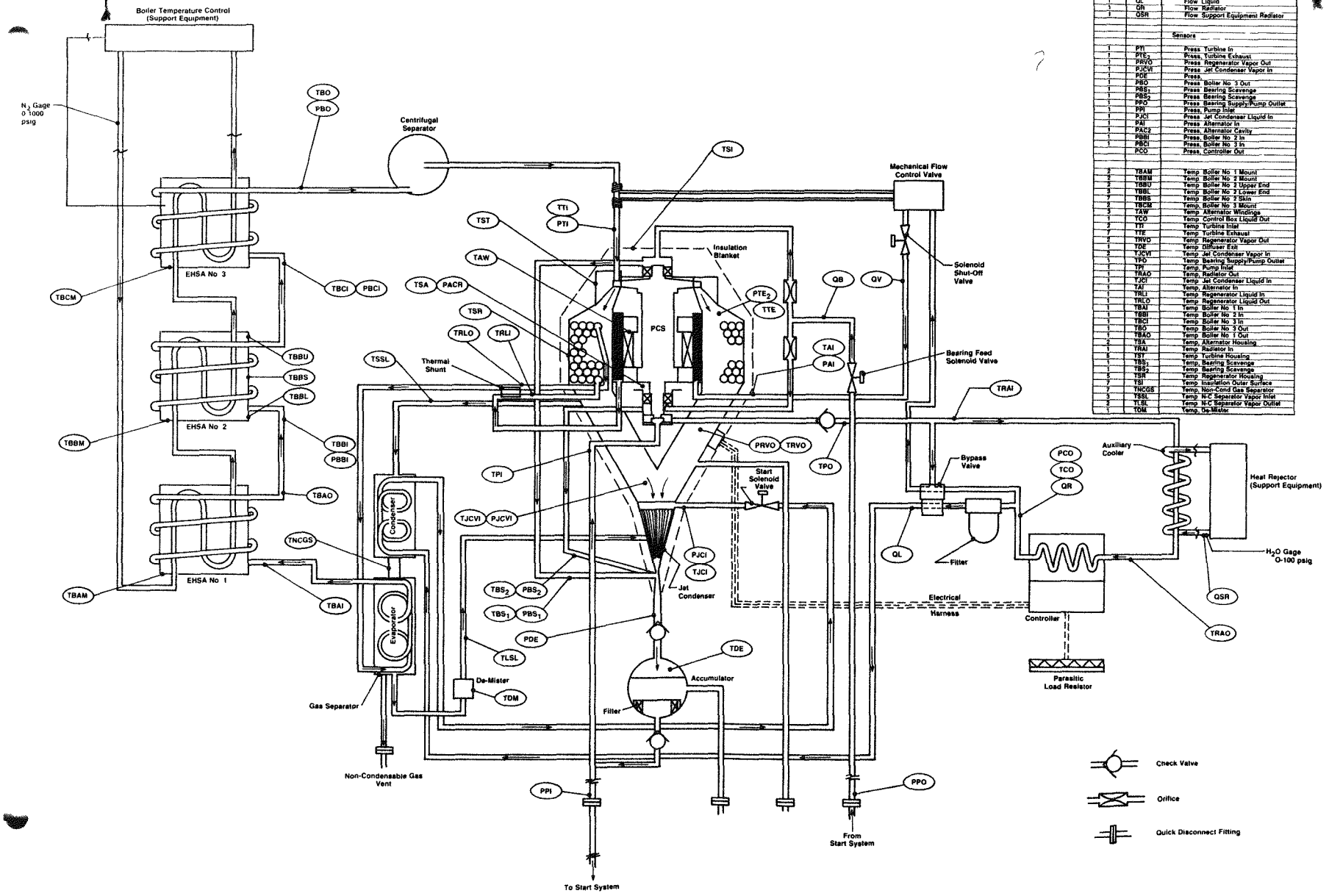

Quantity	Ident	Table Of Instrumentation Description
		Meters
1	QB	Flow Bearing
1	QV	Flow Vapor
1	QL	Flow Liquid
1	QR	Flow Radiator
1	QSR	Flow Support Equipment Radiator
		Sensors
1	PTI	Press Turbine In
1	PTE_2	Press, Turbine Exhaust
1	PRVO	Press Regenerator Vapor Out
1	PJCVI	Press Jet Condenser Vapor In
1	PDE	Press,
1	PBO	Press Boiler No 3 Out
1	PBS_1	Press Bearing Scavenge
1	PBS_2	Press Bearing Scavenge
1	PPO	Press Bearing Supply/Pump Outlet
1	PPI	Press, Pump Inlet
1	PJCI	Press Jet Condenser Liquid In
1	PAI	Press Alternator In
1	PACP	Press, Alternator Cavity
1	PBBI	Press, Boiler No 2 In
1	PBCI	Press, Boiler No 3 In
1	PCO	Press, Controller Out
2	TBAM	Temp Boiler No 1 Mount
2	TBBM	Temp Boiler No 2 Mount
2	TBBU	Temp Boiler No 2 Upper End
3	TBBL	Temp Boiler No 2 Lower End
7	TBBS	Temp Boiler No 2 Skin
2	TBCM	Temp, Boiler No 3 Mount
3	TAW	Temp Alternator Windings
1	TCO	Temp Control Box Liquid Out
2	TTI	Temp Turbine Inlet
7	TTE	Temp Turbine Exhaust
2	TRVO	Temp Regenerator Vapor Out
1	TDE	Temp Diffuser Exit
2	TJCVI	Temp Jet Condenser Vapor In
3	TPO	Temp Bearing Supply/Pump Outlet
1	TPI	Temp, Pump Inlet
1	TRAO	Temp, Radiator Out
1	TJCI	Temp Jet Condenser Liquid In
1	TAI	Temp, Alternator In
1	TRLI	Temp Regenerator Liquid In
1	TRLO	Temp Regenerator Liquid Out
1	TBAI	Temp Boiler No 1 In
1	TBBI	Temp Boiler No 2 In
1	TBCI	Temp Boiler No 3 In
1	TBO	Temp Boiler No 3 Out
1	TBAO	Temp Boiler No 1 Out
2	TSA	Temp, Alternator Housing
1	TRAI	Temp Radiator In
5	TST	Temp Turbine Housing
1	TBS_1	Temp, Bearing Scavenge
1	TBS_2	Temp Bearing Scavenge
5	TSR	Temp Regenerator Housing
7	TSI	Temp Insulation Outer Surface
7	TNCGS	Temp, Non-Cond Gas Separator
3	TSSL	Temp N-C Separator Vapor Inlet
2	TLSL	Temp N-C Separator Vapor Outlet
1	TDM	Temp, De-Mister

Fig. 3.0.3

3.1 System Performance

During Phase I testing the KIPS system performance was improved from an initial value of 10.5% for the development system to a final value of 15.1% after significant modifications to the design. Phase II was both a component verification phase, in which the operational characteristics of certain components were investigated, and a performance improvement phase.

As a result of component improvements and system maximum temperature increase the system performance was raised to 16.56% at the end of Phase II.

3.1.1 System Efficiency

3.1.1.1 Efficiency Measurement

System efficiency in this report refers to D.C. efficiency and is defined as

$$n_{sys} = \frac{\text{28V DC output power}}{\text{HSA electrical input power}}$$

In order to avoid difficulties in measurement of controller losses the system A.C. efficiency is also used. This is defined as follows:

$$n_{AC} = \frac{\text{Alternator AC output power}}{\text{HSA electrical power input}}$$

The value of n_{AC} is higher than n_{sys} because it does not include controller losses. However, changes in thermodynamic performance are more easily recognized by using n_{AC} since many changes were made to the controller, frequently changing its operational characteristics and losses.

Accurate determination of system efficiency required accurate measurement of electrical input and output power. The electrical input power was read directly from the Teledyne HSA control consoles. These measured the AC current fed to each heater block while the voltage was measured at the heater terminal inside the HSA. The conductors from the connector to the voltage tap dissipated a small amount of heat, some of which was lost through the insulation and outer surface and the rest absorbed in the heater block. Calculations were made of these losses and the indicated readings modified accordingly. The voltage drop was measured from the console to the voltage tap for calibration purposes. Towards the end of Phase II the HSA voltage tap lead wires of heat sources number 1 and number 2 failed and the voltage at the console had to be used for power input measurements. These were then corrected for previously measured voltage drop.

System output power measurements were made in two locations. The system AC output was measured at the PCS connector inside the vacuum chamber before any losses occurred in the electrical feeder wires. The D.C. output power was measured at the output terminals of the controller. During all of Phase I testing and some of Phase II testing the controller was located inside the vacuum chamber. This necessitated routing the A.C. power leads outside the chamber to current transformers and back in again to the controller. During controller development during Phase II the controller was mounted outside the chamber to simplify required modifications.

Although the 28V DC efficiency is the officially recognized performance criterion for the system, it is felt by Sundstrand that the A.C. efficiency was more representative of the system operation. This efficiency eliminated any doubts about power lead and controller losses and represented the

Table 3.1.1.1 Comparison Of Component Performance In Phase I And Phase II

	PHASE I	PHASE II
Turbine Efficiency (%)	66*	68*
Regenerator Effectiveness (%)	92	97
Radiator Pressure Drop (psid)	20	10
Pump Efficiency (%)	65	71+
Pump Work (%)	137	108+
Alternator Efficiency (%)	92	93.5
Controller Efficiency (%)	93.1	90.6
Bearing & Seal Loss (watts)	92*	95*
Jet Condenser Vapor Pressure (psia)	.11*	.126
Jet Condenser Inlet Temperature (^{0}F)	158	157
Rotational Speed rpm	28650	34610

* Inferred Data
+Extrapolated Data

capability of an Organic Rankine Cycle to generate power efficiently. The controller losses of the final configuration were considerably higher than anticipated, partly due to tighter filtering requirements. Potential improvements in performance of the controller still exist.

The electrical power leads from the alternator connector to the controller were long enough that resistive dissipation was a significant factor. The losses were calibrated as a function of A.C. power and were used to compensate the measured D.C. output power with the assumption that a flight system configuration would have power feeder losses of seven watts.

3.1.1.2 Component Performance

Table 3.1.1.1 summarizes major component performances at the end of Phase II compared to their indicated values at the end of Phase I. The performances of some components were inferred and these have been noted by an asterisk. Individual component performances will be discussed in the component description sections but there are a few additional comments to be made in this section.

Because of the reduction in pump size during Phase II, the optimal rotational speed increased. The increase in speed resulted in turbine performance and in bearing losses somewhat higher than had been predicted at the end of Phase II.

The regenerator effectiveness was measured using improved instrumentation and the higher value is consistent with the excess area (i.e. the number of tube rows) employed.

The jet condenser vapor pressure is higher than anticipated and higher than Phase I even though the 90 nozzle jet condenser should provide lower pressures. This is probably due both to inadequate knowledge of the old value of vapor pressure and to a slightly lower than intended flow ratio. The lower than intended flow ratio resulted from higher than expected non-condensable gas separator pressure drop and lower than expected nozzle discharge coefficients. The final build of the system provided the first successful operation of the low pressure transducers.

Controller efficiency shows reduced performance. This results from much tighter ripple requirements in Phase II. The 0.1% ripple requirement resulted in a filter which consumed over 40 watts. The filter loss compensated for the gains made in rectifier performance, i.e., the use of ion-implant rectifiers. In addition, the gain in alternator efficiency resulting from air gap optimization was counterbalanced by the removal of the tuning capacitors. The capacitors were removed to stabilize the system under overspeed conditions where the system was found to self-excite if the capacitors were present.

3.1.1.3 System Performance Summary

Figures 3.1.1 and 3.1.2 summarize system performance parameters for a data point at the end of Phase II. In Figure 3.1.1 primary data used for the on-line data reduction system is reproduced in channels A1 through A48. Some of the pressures in this list are gauge pressures and have been corrected in Figure 3.1.2. Channels BO through B98 represent thermocouples which were connected to the Fluke data logger. All the thermocouple data have been corrected per individual calibration curves generated for each thermocouple in a calibration bath.

As a result of the thermal degradation studies performed at Battelle Memorial Laboratories (see Appendix E) it was decided that a turbine inlet temperature of 700°F is compatible with a 10 year mission. This was based on the presumption that the non-condensible gas separator worked as designed. Based upon thermodynamic analyses this should result in a significant improvement in performance compared to the Phase I operation. Similar thermodynamic analyses were used to determine the sensitivity of the system performance to various component performances in order to determine the most effective components for improvement. These sensitivity results are summarized in Table 3.1.1.2.

Table 3.1.1.3 summarizes the measured system performance characteristics at the end of Phase II compared to those at the end of Phase I.

Table 3.1.1.2 System Performance Sensitivity Analysis

PARAMETER	SYSTEM PERFORMANCE SENSITIVITY
Turbine Inlet Temperature	0.0144% pts Per ^{0}F
Turbine Efficiency	0.23% pts Per % pt Efficiency
Regenerator Effectiveness	0.088% pts Per % pt Effectiveness
Radiator Pressure Drop	0.007% pts Per psid Pressure Drop
Pump Efficiency	0.018% pts Per % pt Efficiency
Alternator Efficiency	0.18% pts Per % pt Efficiency
Controller Efficiency	0.20% pts Per % pt Efficiency
J/C Vapor Pressure	15.3% pts Per psia Pressure
Bearing/Seal Losses	0.012% pts Per Watt Loss
Pump Work	0.012% pts Per Watt Loss
Heat Source Heat Loss	0.003% pts Per Watt Loss

Table 3.1.1.3 System Performance Comparison

PARAMETER	PHASE I	PHASE II
Turbine Inlet Temperature (^{0}F)	675	700
Electrical Input Power (watts)	7834	7515
DC Output Power (watts)	1187	1239
System DC Efficiency (%)	15.1	16.56
AC Output Power (watts)	1285	1387
System AC Efficiency (%)	16.4	18.5
Turbine Flow Rate (lb/hr)	112.3	111.6
Rotational Speed (rpm)	28650	34610

It should be noted that a significant improvement in system performance was achieved during Phase II, especially in terms of A.C. efficiency which is the best indicator of system performance. The indicated D.C. efficiency was corrected to a 700°F turbine inlet temperature, since further adjustments of the flow control valve would have allowed this temperature to be attained.

3.1.2 System Thermal Performance Analysis

3.1.2.1 Thermodynamic Analysis

Predicted system performance is based on individual component performance and thermodynamic analysis of the state points for the system shown in Figure 3.1.3 using thermodynamic data for the working fluid such as that presented in Figure 3.1.4.

System analysis proceeds stepwise from location to location for a given turbine inlet temperature, using known operating characteristics of the jet condenser and other components. Heat losses from the system, both internal (for instance into the bearing lubricant) and external (to the vacuum chamber) are subtracted at the appropriate locations. System mass flow is iterated until required output power is obtained, at which point the thermodynamic conditions may be fixed.

There are several anomalies between anticipated performance and measured performance. These are discussed in the following paragraphs.

3.1.2.1.1 Turbine Outlet Temperature

In Phase I, the turbine outlet temperature was depressed as much as 55°F. The prime cause of this was thought to be liquid leakage from the bearing seals. Component testing confirmed the leakage from the seals but when zero leakage seals were installed in the unit in Phase II, considerable turbine exit temperature depression still existed.

The amount of insulation on the boiler feed tubes was also increased. The insulation blanket around the turbine and regenerator was increased in thickness from 3 layers of Hitco TG15000 to 3 layers TG15000 and 8 layers of Carborundum Fibrefrax. It was found that the increased insulation reduced the turbine temperature drop by 29°F to 148°F.

These values of temperature drop can be compared to expected values of 122°F-128°F for turbine efficiencies of 63-66%.

It was also found that there was approximately 10°F difference in measured temperature between a thermocouple located in the flowing stream and one in the stagnant zone outside the turbine diffuser.

During Phase II the system thermal model was revised and for the final build of the CRU some modifications were made to the CRU to reduce internal heat losses. An improved insulation blanket was installed and the turbine and alternator efficiencies were somewhat higher. In addition, improved instrumentation was used to allow a more accurate assessment of turbine temperature drop to be made. The combination of reduced heat losses and increased efficiencies leads to about the same expected turbine temperature drop. From Figure 3.1.1 it can be seen that the temperature drop based on stagnant flow (channels A30, B59, 61, 63) measured 148-153°F and for the flowing stream (channels B60, 62, 64) 148-152°F, which is much the same as before the final build. The thermocouple at location A30 is a plain sheathed type and reads about the same temperature as the special finned and shielded thermocouple in the other locations, indicating that the values reported in the previous build were probably fairly accurate.

The seven turbine exit thermocouples show a circumferential gradient. Approximately 50% of the arc reads about 642°F while the remainder reads about 646°F. This is not a large variation but may indicate flow or heat loss maldistribution.

The difference between expected turbine temperature drop and the measured value represents about 950 Btu/hr heat loss. If the cause of the quenching could be determined and eliminated, significant gains (0.5-1.% points plus) in system performance would accrue depending on where the heat loss is occurring.

3.1.2.1.2 <u>CRU/Regenerator Heat Balance</u>

A heat balance was made on the combination of CRU and regenerator. This is important because it provides a somewhat independent check of the apparent turbine heat loss by making measurements downstream of the regenerator and compensating for internal heat losses. The results are shown in Figure 3.1.5. About 800 BTU/hr more heat enters than leaves. This is consistent with

the apparent temperature drop previously reported.

3.1.2.1.3 Jet Condenser Heat Balance

The jet condenser heat balance comprises the following elements:

inlet: Hot vapor from regenerator

Cold liquid from nozzles

Hot liquid from bearings

outlet: Mixed outflow at diffuser temperatures

Heat losses from skin

Reference to Figure 3.1.6 shows an apparent heat gain in the jet condenser, but comparison of the value of heat gain with the total heat transfer in the heat exchanger results in an error of only 0.49% from a true heat balance.

3.1.2.1.4 HSA Heat Loss

The indicated negative loss of Figure 3.1.7 implies that the fluid absorbs more heat than is input electrically. Calculated heat losses for the boilers and interconnecting plumbing are approximately 750 BTU/hr indicating an error of about 975 BTU/hr. It should also be noted that the indicated temperature drop from the boiler outlet to turbine inlet is more than 6°F compared to previous measurements of about 2°F. The difference of 4°F represents a discrepancy of about 223 BTU/hr.

A potential explanation for this discrepancy is an error in turbine flow measurement. This was checked by using turbine inlet pressure and temperature, combined with the flow calibration of the nozzle block previously made with nitrogen during the manufacturing process. On this basis, using a pressure of 56.4 psia and a temperature of 694.3°F, a mass flow of .0306 lb/sec was calculated, representing an apparent error of 1.3% too high. If the flow were reduced by 1.3% the HSA heat losses would still be negative at -37.5 BTU/hr.

It is noteworthy that the apparent value of turbine heat loss corresponds in magnitude with the negative heat loss in the HSA's. A very likely cause of this correspondence is the presence of a small amount of liquid mist in the superheated vapor at the boiler outlet. This would explain the temperature drop both in the turbine inlet line and in the turbine where saturated liquid would evaporate and cool the bulk superheated vapor. The indicated heat loss would require a flow rate of about 5 lb/hr of liquid. The fact that the nozzle inlet pressure indicates lower flow than the flow meter is additional evidence for the possible presence of liquid.

It should be noted that wet vapor results in reduced system performance but has no deleterious impact on inventory control, since the mist apparently vaporizes in the turbine. It would be possible to redesign the boiler superheat region to eliminate the problem and if redesign were not possible a demister could be added to eliminate the droplets. An experimental demister was tried during Phase I when wet vapor was first suspected. At that time no change in temperature could be obtained but it is likely that the device was too small.

3.1.2.1.5 PCS Insulation Loss

Heat losses from the PCS are calculated from thermocouples located on the PCS metal skin and on the aluminum foil applied to the outer layer of insulation. Two methods are used. Conductive losses are based upon measured conductivity from the insulation test program while the radiation losses are based upon the measured foil temperatures and the value of emissivity measured by TRW of samples of the same foil. In the new, flat condition the measured emissivity was 0.01, while higher values were obtained for wrinkled material. There was doubt on the validity of the latter data so a value of 0.01 was used. Very good correlation exists for the two methods, but the measured value is significantly lower than the expected value of about 35 BTU/hr.

3.1.2.1.6 Heat Balance

System heat balance is presented in Figure 3.1.7. The overall system heat balance is good.

Figure 3.1.8 is a computer printout from the system analysis program, using measured operating conditions and calculated internal heat losses. A 700°F turbine inlet temperature and housings modified to reduce turbine inlet losses were assumed. As can be seen, the regenerator inlet temperature is considerably higher than measured in Figure 3.1.1 and system efficiency is 0.53% points higher.

Figure 3.1.9 uses the same input data but the internal heat losses from turbine exhaust have been adjusted to try to match the measured regenerator inlet temperature. In this case the calculated efficiency matches the observed value, leading to the conclusion that a 950 BTU/hr. heat loss from the turbine exit is required to match the observed value.

3.1.2.2 Thermal Model

During the investigation of the depressed turbine outlet temperature in Phase I it was found that increasing the number of layers of insulation from 7 to 11 made only a slight difference in the turbine outlet temperature. Even with eleven layers of insulation the temperature was depressed by more than 20°F. The CRU configuration had been changed considerably from the original GDS design to enable the alternator housing to be located in a vacuum rather than being exposed to vapor, thus precluding condensation. The original thermal model was checked at that time but no major revision was made for the new configuration.

A completely new thermal model was therefore generated to simulate the new CRU configuration and to include all modifications of the revised turbine and bearing/seal housings. The SINDA (Systems Improved Numerical Differencing Analyzer) computer program was used. SINDA is more versatile than the original program. Figures 3.1.10 and 3.1.11 compare the predicted temperatures for selected locations of the original thermal model and the updated model. The new thermal model was based on a turbine inlet temperature of 675°F which was the operating temperature of the system when the investigation was made. There were two conclusions from the analysis; firstly the calculated internal losses were higher than expected and secondly alternator/bearing support housing temperatures were close to saturation conditions.

Predicted and measured heat losses for the build at that time are summarized in Table 3.1.2.1. As a result of this analysis, the model was used to investigate potential hardware modifications to reduce the losses. These modifications are shown in Figure 3.1.12. The actual modifications incorporated in the final build were numbers 2, 3 and 5, with potential savings of approximately 85 BTU/hr. from the turbine inlet losses.

In addition, it was recommended that additional instrumentation be added to the CRU to help calibrate the thermal model by establishing boundary conditions. The recommended standard thermocouple and platinum resistance temperature sensor installation locations are shown in Figure 3.1.13. Unfortunately, budgetary constraints precluded the incorporation of most of these. Thermocouples were installed on the alternator housing, however, to allow a check to be made of condensation. This will be discussed in the following section.

3.1.2.3 Heated Alternator Test

The thermal model calculations indicated the possibility of condensation occuring inside the alternator cavity on the housing surfaces cooled by pump flow and alternator coolant flow. Figure 3.1.14 summarizes the calculated values of the critical housing temperatures for different alternator coolant inlet temperatures and a fixed pump flow temperature of 202°F. It can be seen that the bearing housing has a saturation pressure of only 0.11 psia compared with a calculated jet condenser pressure of 0.10, leaving little margin. Heating the alternator coolant raises the saturation pressure and hence margin quite dramatically.

It was realized that if condensation did occur several major effects would result. There would be a noticeable discrepancy in the CRU heat balance, drag losses associated with liquid in the air gap could be significant and, for a flight system, severe liquid inventory management problems would occur. For this reason, it was decided to perform a test to heat the alternator coolant and determine whether significant changes in performance were noted.

Table 3.1.2.1 Heat Loss Summary (November 1979)

TURBINE	
New Thermal Model Prediction Of Turbine Delta T	= 128°F
Measured Turbine Delta T	= 144-149°F
Turbine Heat Loss Unaccounted	= 960 btu/hr
ALTERNATOR	
New Thermal Model Prediction Of Heat Absorbed	= 703 btu/hr
Measured Heat Absorbed	= 887 btu/hr
Alternator Heat Gain Unaccounted	= 184 btu/hr
TURBINE BEARING	
New Thermal Model Prediction Of Heat Absorbed	= 627 btu/hr
Measured Heat Absorbed	= 584 btu/hr
Bearing Heat Gain Unaccounted	= 43 btu/hr
OVERALL	
New Model Prediction Of Thermal Loss To Liquid	= 818 btu/hr
Old Model Prediction Of Thermal Loss To Liquid	= 342 btu/hr
Measured Thermal Loss To Liquid	= 959 btu/hr

The liquid was heated by a regenerative heat exchanger applied across the alternator and controlled by solenoid valves. This allowed a test to be performed at a steady state condition and then to rapidly change the temperature. Tests were performed at different speeds and small increases in electrical output were noted with temperature increase. The difference increased with increasing speed and it was found to match fairly closely the difference in bearing losses associated with the viscosity decrease of the pump bearing lubricant which, because of the plumbing arrangement, was heated at the same time as the alternator. This is shown in Figure 3.1.15. The conclusions from the test was that if condensation were occuring, liquid was not entering the air gap and absorbing shaft power.

The final build incorporated thermocouples on the bearing housing in the coldest location and included a static pressure tap reaching into the alternator. Comparison between measured housing temperature (231°F-233°F) and saturation temperature based on measured pressure (229°F) showed that condensation probably does not occur.

The alternator cavity pressure was measured to be 0.118 psia, i.e. lower than the jet condenser pressure of 0.126 psia. The explanation for this apparent anomoly is that the turbine wheel acts as a pump, reducing the pressure in the alternator and inducing some flow through the wiring harness duct. The flow is relatively low because of significant blockage and inadequate to affect turbine outlet temperature.

GDS Primary Data

Stand 280 Time 9.0:3 Date 12 22 80
DIPS GSD Primary Data-Temp Corrections Applied

Channel	Symbol	Parameter	Value	Channel	Symbol	Parameter	Value
A 1	QB	Bearing Flow	0.06	A 2	QV	Vapor Flow	0.22
A 3	QL	Liquid Flow	1.80	A 4	QR	Radiator Flow	1.60
A 5	QSR	Auxilary HX Flow	0.00	A 6	RPM	Turbine Speed	34610.00
A 7	ACW	AC Power Out	1387.00	A 8	DCV	DC Volts Output	28.17
A 9	PTI	Turbine Inlet Press	41.96	A10	PBSI	Turb Brg Scav Press	0.99
A11	PBS2	Pump Brg Scav Press	0.64	A12	PDE	J/C Diff Exit Press	22.73
A13	PPI	Pump Inlet Press	4.23	A14	PPO	Pump Outlet Press	87.32
A15	PJCI	J C Liq Inlet Press	70.85	A16	PAI	Alter Inlet Press	62.27
A17	PCO	Controller Out Press	81.21	A18	PBBI	Boiler B Inlet Pres	57.81
A19	PBCI	Boiler C Inlet Press	56.89	A20	PBO	Boiler Out Press	46.71
A21	PCC	Press Check Channel	11.91	A22	PACR	Alter Cavity Press	0.12
A23	PTE2	Turb Exhaust Press	0.15	A24	PRVO	Regen Vap Out Press	0.13
A25	PJCVI	J C Vap Inlet Press	0.13	A26		Not Used	0.0
A27		Not Used	0.0	A28		Not Used	0.0
A29	TBO	Boiler Outlet Temp	700.54	A30	TTE	Turbine Exit Temp-7	542.43
A31	TRVO	Regen Vap Out Temp	244.60	A32	TDE	J/C Liq Out Temp	207.68
A33	TCC	Temp Check Channel	250.97	A34	TRAI	Radiator Inlet Temp	208.08
A35	TRAO	Radiator Out Temp	148.26	A36	TJCI	J/C Liq Inlet Temp	156.20
A37	TJCVI	J C Vap Inlet Temp	241.26	A38	TAI	Alter Inlet Temp	204.89
A39	TRLI	Regen Liq In Temp	237.01	A40	TRLO	Regin Liq Out Temp	477.35
A41		Not Used	0.62	A42	TPO	Pump Outlet Temp	207.28
A43	TPI	Pump Inlet Temp	207.68	A44	DCAP	PLR DC Current	24.15
A45	DCAL	Customer DC Current	16.95	A46	HSAWI	Power In HSA-I	2503.00
A47	HSAW2	Power In HSA-2	2511.00	A48	HSAW3	Power In HSA-3	2501.00
B 0	TBBUI	Boiler B Upper End1	211.10	B 1	TBBU2	Boiler B Upper End2	211.80
B 2	TBBMI	Boiler B Mount 1	193.47	B 3	TBBM2	Boiler B Mount 2	117.18
B 4	TBBLI	Boiler B Low End 1	210.80	B 5	TBBL2	Boiler B Low End 2	215.90
B 6	TBBL3	Boiler B Low End 3	210.10	B 7	TBBS1	Boiler B Skin 1	203.90
B 8	TBBS2	Boiler B Skin 2	203.40	B 9	TBBS3	Boiler B Skin 3	200.80
B10	TBBS4	Boiler B Skin 4	199.70	B11	TBBS5	Boiler B Skin 5	205.90
B12	TBBS6	Boiler B Skin 6	207.60	B13	TBBS7	Boiler B Skin 7	208.40
B14	TPT1	Press Transducer 1	0.0	B15	TPT2	Press Transducer 2	340.40
B16	TPT3	Press Transducer 3	322.60	B17	TPT4	Press Transducer 4	0.0
B18	TPTL1	Press XDR Line 1	291.20	B19	TPTL2	Press XDR Line 2	277.00
B20	TPTL3	Press XDR Line 3	286.60	B21	TPTL4	Press XDR Line 4	264.00
B22	TAW1	Alt End Turn (Pump)	257.50	B23	TAW2	Alt End Turn (Turb)	254.60
B24	TAW3	Alt Slot Pump End	269.70	B25	TSSL2	Short Sep. Line 2	338.46
B26	TBAM1	Boiler A Mount 1	169.26	B27	TBAM2	Boiler A Mount 2	113.44
B28	TBAL1	Boiler A Low End 1	0.0	B29	TBAL2	Boiler A Low End 2	0.0
B30	TRVO2	Regen Vap Out 2	246.76	B31	TBAS1	Boiler A Skin 1	0.0
B32	TBAS2	Boiler A Skin 2	0.0	B33	TBAS3	Boiler A Skin 3	0.0
B34	TBAS4	Boiler A Skin 4	0.0	B35	TBAS5	Boiler A Skin 5	0.0
B36	TBAS6	Boiler A Skin 6	0.0	B37	TLSL	Long Sep. Line	331.80
B38	TBCI	Boiler C Vap Inlet	651.94	B39	TBBI	Boiler B Vap InLet	614.54
B40	TBAI	Boiler A Liq Inlet	473.92	B41	TBAO	Boiler A Vap Out	615.54
B42	TBCU1	Boiler C Upper End1	0.0	B43	TBCU2	Boiler B Upper End2	0.0
B44	TBCM1	Boiler C Mount 1	205.40	B45	TBCM2	Boiler C Mount 2	125.99
B46	TJCVI2	J C Vap Inlet 2	242.34	B47	TBS1	Bearing Scavenge 1	285.36
B48	TBS2	Bearing Scavenge 2	226.13	B49	TBCL1	Boiler C Low End 1	0.0
B50	TBCL2	Boiler C Low End 2	0.0	B51	TBCL3	Boiler C Low End 3	0.0
B52	TBCS1	Boiler C Skin 1	0.0	B53	TBCS2	Boiler C Skin 2	0.0
B54	TBCS3	Boiler C Skin 3	0.0	B55	TBCS4	Boiler C Skin 4	0.0
B56	TBCS5	Boiler C Skin 5	0.0	B57	TBCS6	Boiler C Skin 6	0.0
B58	TBCA7	Boiler C Skin 7	0.0	B59	TTE1	Turbine EX 1 Fin	542.73
B60	TTE2	Turbine EX 2 Shield	542.09	B61	TTE3	Turbine EX 3 Fin	541.23
B62	TTE4	Turbine EX 4 Shield	546.20	B63	TTE5	Turbine Ex 5 Fin	545.84
B64	TTE6	Turbine EX 6 Shield	546.00	B65	TTI	Turbine Inlet	694.28
B66	TSSI	PCS Insul Top Cent	160.19	B67	TSS2	PCS Insul Top Edge	141.32
B68	TSS3	PCS Insul Side Turb	136.21	B69	TSS4	PCS Insul Side Reg1	139.11
B70	TSS5	PCS Insul Side Gap	148.03	B71	TSS6	PCS Insul Side Reg2	160.69
B72	TSSL3	Short Sep. Line 3	254.16	B73	TSS8	Alt Hsg Brg Lub Man	231.58
B74	TSS9	Alt Hsg 80 Deg CW	233.38	B75	TSS10	Turb Brg Hsg	292.23
B76	TSS11	Turb Brg Skin	605.53	B77	TSS12	Turb Hsg Skin	623.92
B78	TSS13	Turb Side of Flange	578.72	B79	TSS14	Turb Diffuser Skin	544.10
B80	TSS15	Reg Top Coils Skin	499.05	B81	TSS16	Reg Top Coils Skin	497.86
B82	TSS17	Reg Top Coils Skin	485.94	B83	TSS18	Reg Gap Skin	434.54
B84	TSS19	Reg Bot Coils Skin	337.07	B85	TSS20	J/C Funnel	231.46
B86	TSS21	Insul TBO-TTI Tube	249.89	B87	TNCGS5	N/C Separator	245.00
B88	TNCGS6	N/C Separator	248.00	B89	TNCGS8	N/C Separator	241.60
B90	TNCGS9	N/C Separator	226.90	B91	TNCGS10	N/C Separator	192.80
B92	TCO	Controller Out	150.44	B93	TNCGS12	N/C Separator	182.50
B94	TNCGS13	N C Separator	188.10	B95	TDM	Demister	344.60
B96	TGSL	Gas Sep Line	233 20	B97	TSSL1	Short Sep. Line	337.50
B98	TLSL2	Long Sep. Line	334.00				

Fig. 3.1.1

GDS Secondary Data

Stand 280 Time 9: 0: 3 Date 12/22/80
DIPS GDS Seconday Data Reduction

	Press (PSIA)	Temp (Def F)	Enthalpy (B/Lb)
Turbine In	56.4	694.3	418.055
Ex	0.130	544.8	350.520
Regen Vap In	0.149	544.8	350.518
Out	0.128	246.8	231.921
Jet Cond Vap In	0.126	242.3	230.059
Jet Cond Liq In	85.2	156.2	40.017
Out	22.7	207.7	61.603
Feed Pump In	18.6	207.7	61.603
Bypass Valve In	101.7	208.1	61.774
Radiator Out	95.6	148.3	36.776
Alt Cooling In	76.7	204.9	60.406
Regen Liq In	76.7	237.0	74.340
Out	72.2	477.3	190.703
Boiler A In	72.2	473.9	188.891
Boiler B In	72.2	614.5	
Boiler C In	71.3	651.9	
Boiler Out	61.1	700.5	420.899
Bear Scavenge 1	1.0	285.4	96.026
2	0.6	226.1	69.581
Alt Cavity Brg Man.	0.118	231.6	
Alt Cavity 80Deg CW	0.118	233.4	
Alt Sat. Temp.		229.4	

Flow Rates (Lb/Sec)

Vapor	Liquid	Radiator	Bearings	Pump
0.0310	0.2557	0.2286	0.0082	0.2948

Heat Rates (Btu/Hr)

Heat Rej	Heat Abs	Reg Vap	Reg Liq
20575.	25874.	13226.	12977.
Sys Heat Loss	HSA Heat Loss	Turb Ht Loss	JC Heat Loss
1348.	-225.	1800.	-327.
PCS Insul Cond	PCS Insul Rad		
18.	18.		
Cont Loss	Turb Bear	Pump Bear	
0.	671.	76.	

Component DT, DH

Boiler	Turbine	Alt	Reg Liq	Reg Vap	J/C Liq
226.6	149.5	32.1	240.3	300.2	51.5
232.008	67.536	12.178	116.363	118.599	21.586

Powers (Watts)

DC Plr	DC L Bank	AC Out	Alt Shaft	Field
680.	477.	1387.	1470.	12.
Pump	Brgs/Seals	Feeder Loss	Controller	
108.	95.	95.	122.	
DC Output Indicated	DC Output Customer	Heat In		
1158.	1239.	7515.		

Efficiencies

Turb (Shaft)	Turb (Enth)	Alt	Pump	Shaft
0.669	0.879	0.936	0.709	0.223
Regen	JC Recov	Speed		
0.968	0.267	34610.000		

** System-AC	System-DC	(Corr. For TTI) ***
0.1846	0.1656	

Figure 3.1.2

System Schematic

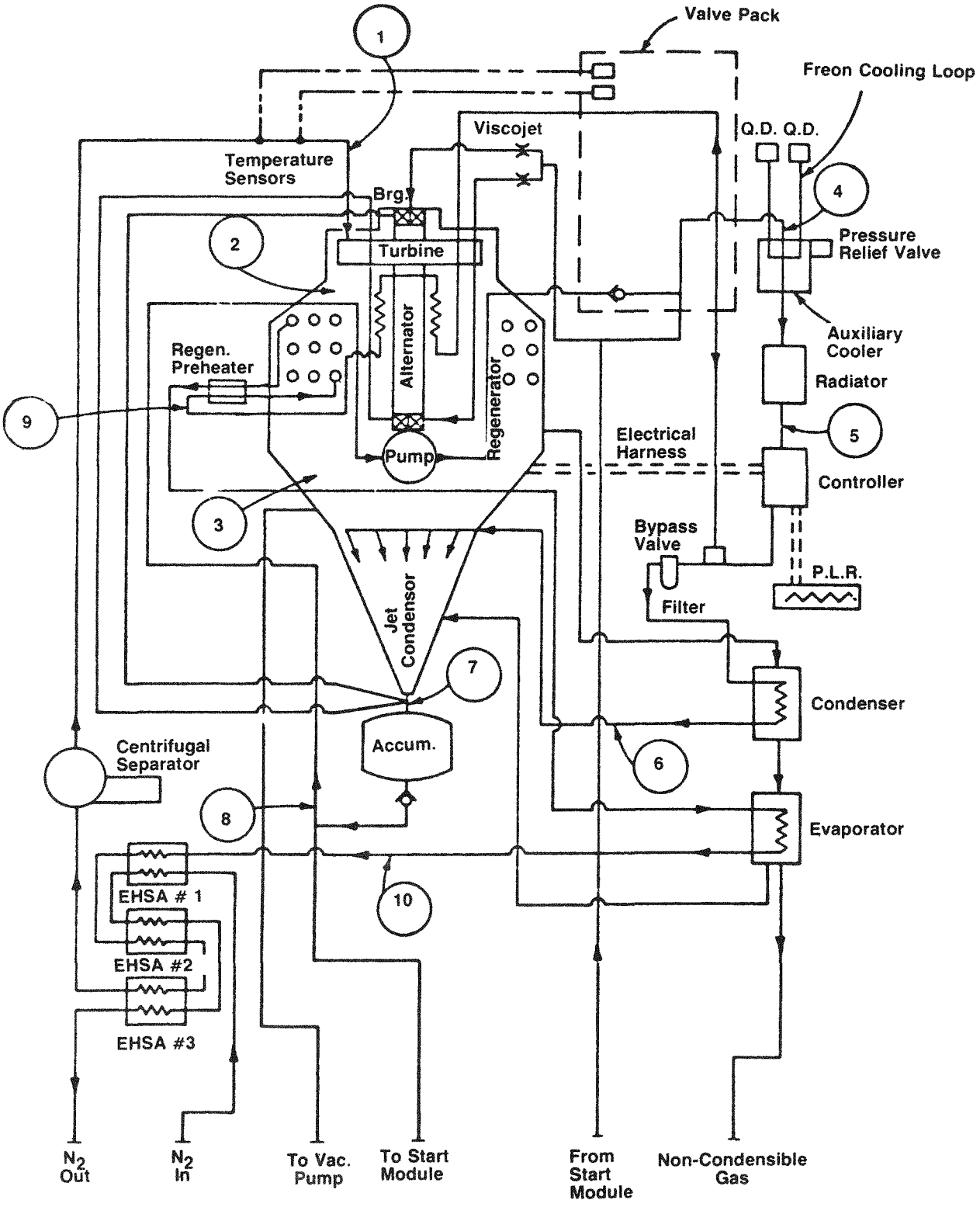

Figure 3.1.3

Dowtherm Properties

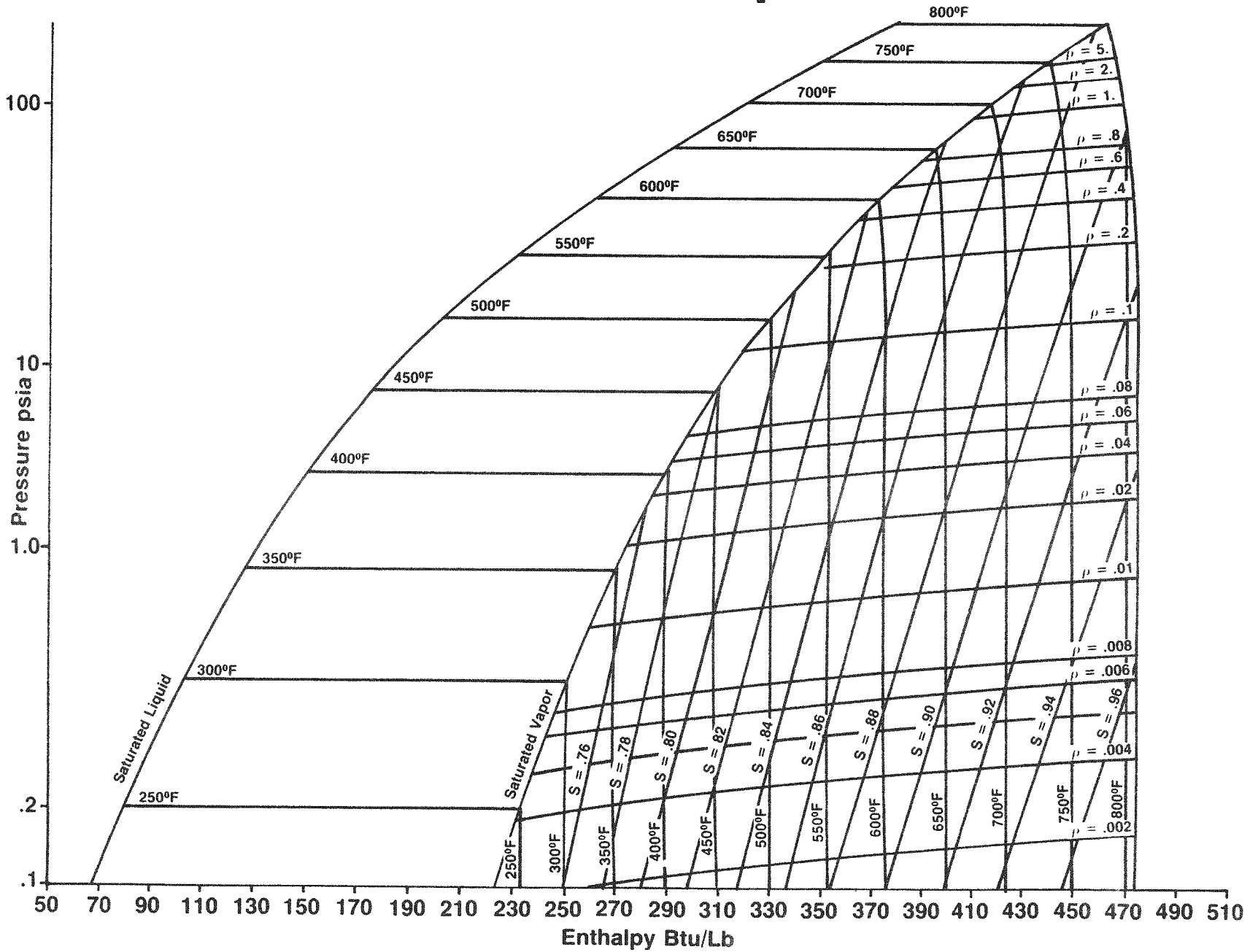

Figure 3.1.4

CRU/Regenerator Heat Balance

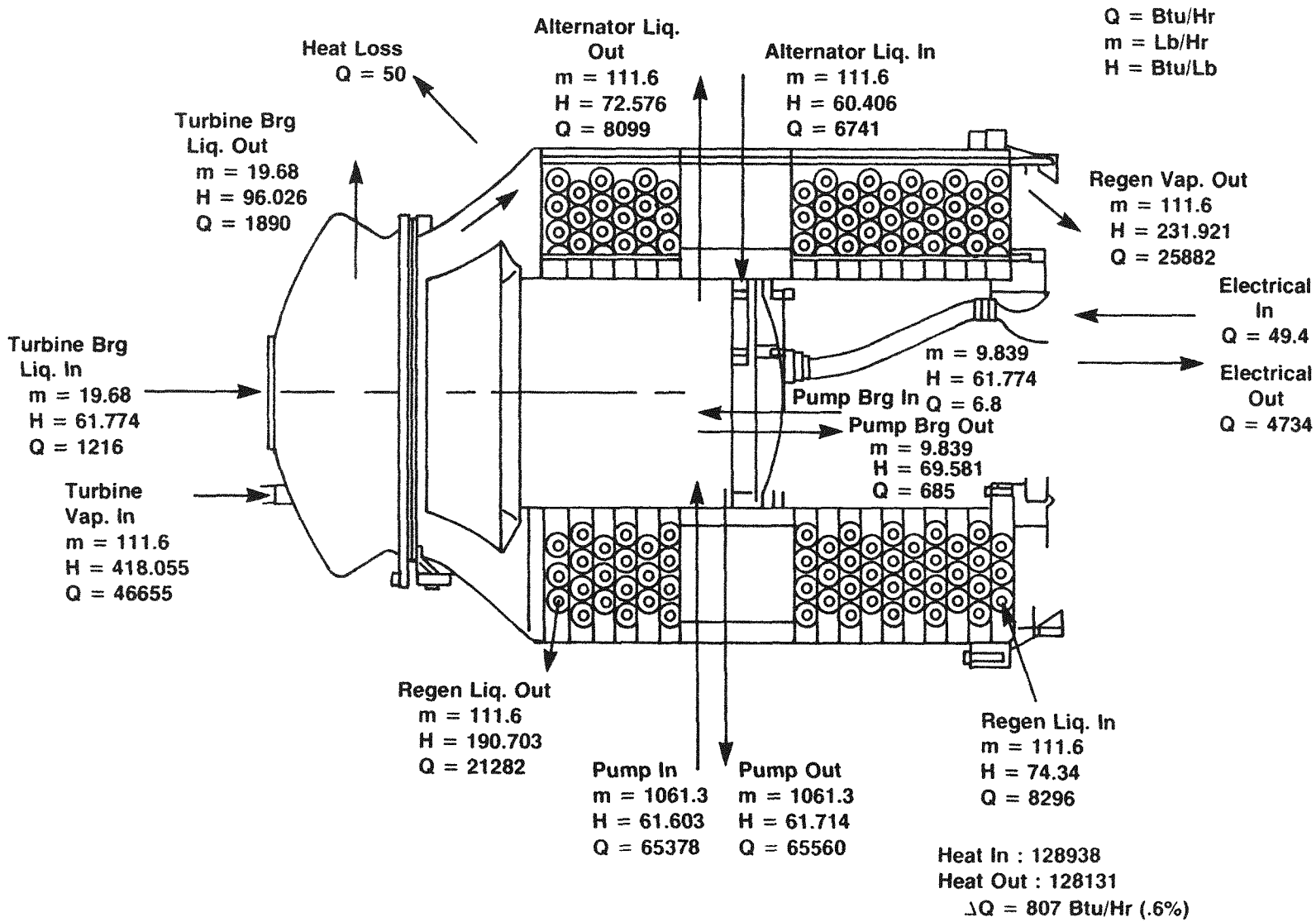

Figure 3.1.5

J/C Bypass Valve Heat Balance

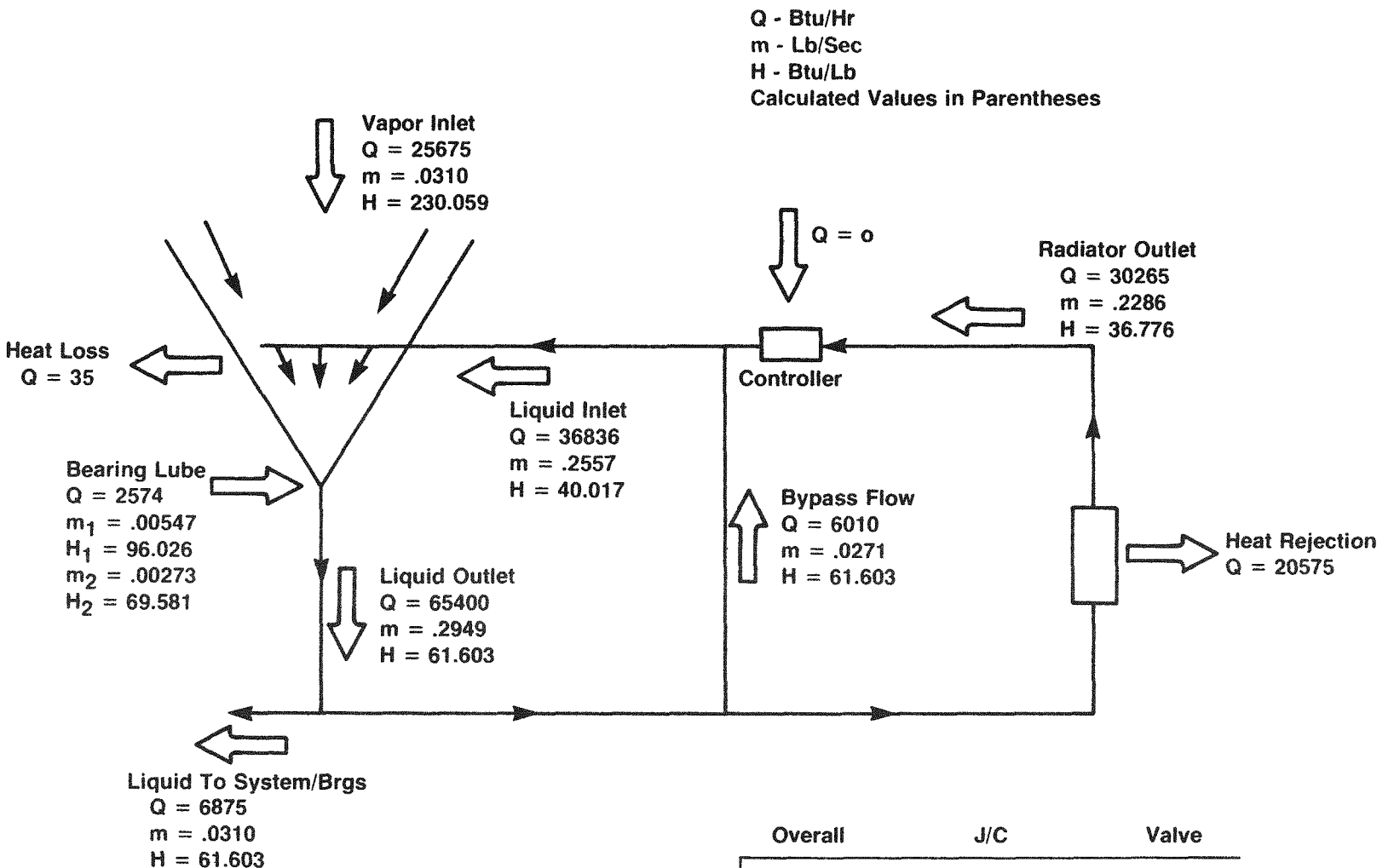

	Overall	J/C	Valve
Heat In	28249	65085	36275
Heat Out	27485	65435	36836
% Error	2.7	0.5	1.5

Figure 3.1.6

System Heat Balance

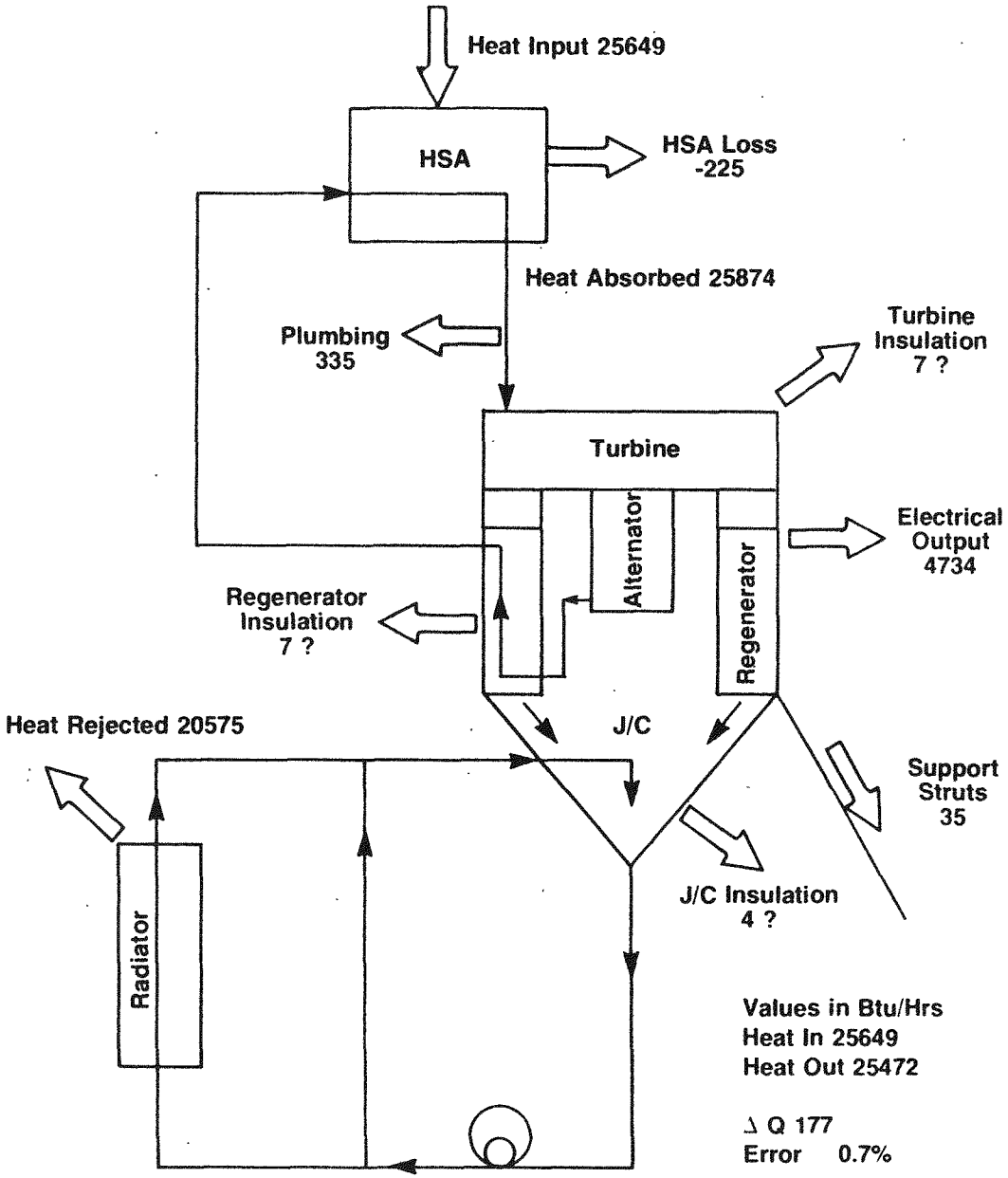

Figure 3.1.7

Analysis Program Results
Simulation Of Measured Operating

DIPS ORC - GDS Final Build Dec 1980

INPUT
*****

Turb Eff	=	0.680	Alternator Eff	=	0.935
Bear + Seal Loss	=	0.095	Conditioning Eff	=	0.906
Regen Effec (Des)	=	0.970	J Cond Recovery	=	0.267
CRU rpm	=	34610.	Pump Flow Ratio	=	9.248
Net O/P Power	=	1.239	Parasitic Power	=	0.030
Des Turb In Pres	=	56.400	Turb Inlet Temp	=	694.3
Cond Press	=	0.126	Boiler Heat Loss	=	-225.0
Regen Vap P Drop	=	0.023	Regen Liq P Drop	=	4.50
Boiler Pres Drop	=	11.10	Cent Sep P Drop	=	4.70
Radiator P Drop	=	6.10	Con Valve P Drop	=	25.00
Control P Drop	=	10.40	Accum P Drop	=	4.10
Diff Pres Rise	=	0.019	Alt Windage	=	0.013
Turb Heat Loss	=	332.0	Regen Heat Loss	=	440.0
Turb In Ht Loss	=	10.0	Reg Hsg Ht Loss	=	8.0
Plumbing Ht Loss	=	346.0			
Rad Des Flow	=	0.0	J-Cond Des Pin	=	85.2

Output
******

State Point	Press (psia)	Temp (F)	Enthalpy (B/Lb)
Turbine Plenum In	56.400	694.300	418.065
Turb Noz In	56.400	688.410	415.144
Turb Out	0.130	572.720	363.213
Regen Vap In	0.149	564.349	359.386
J Cond Vap In	0.126	232.607	227.158
J Cond Outlet	22.748	204.563	60.253
Pump Inlet	18.648	205.975	60.859
Rad+C Valve In	101.700	206.858	61.238
Rad Outlet	95.600	156.106	40.017
J Cond Liq In	85.200	156.106	40.017
Reg Liq In	76.700	222.331	67.939
Boiler Inlet	72.200	495.335	200.167
Boiler Out	61.100	700.776	421.020

Turbine CP	=	0.401	Turbine Gamma	=	1.037
Pump Spec Speed	=	988.	Pump Efficiency	=	0.650
Turbine Flow Lb/Sec	=	0.03252	Radiator Flow Lb/Sec	=	0.268
Turbine Flow gpm	=	0.234	Radiator Flow gpm	=	1.890
Heat Added In Boiler	=	25859.	Heat Rej By Radiator	=	21246.
Alt Heat Added	=	784.6	Controller Heat Added	=	0.0
Output kw	=	1.286	Alt Input kw	=	1.553
Bearing+Seal Loss kw	=	0.095	Pump Shaft kw	=	0.120
Seal Leak Lb/Hr	=	0.0	Leak Power Loss kw	=	0.0
Alternator Eff	=	0.935	Pump Flow Ratio	=	9.25
Rectifier Loss kw	=	0.137	Boiler Heat Loss	=	-225.0
Heat Source Watts	=	7510.8	Regen Effec (Act)	=	0.970
System Efficiency	=	17.11958	Cycle Efficiency	=	16.97063

Figure 3.1.8

Analysis Program Results
Increased Turbine Outlet Heat Loss

DIPS ORC - GDS Final Build Dec 1980

Input
*****

Turb Eff	=	0.680	Alternator Eff	=	0.935
Bear + Seal Loss	=	0.095	Conditioning Eff	=	0.906
Regen Effec (Des)	=	0.970	J Cond Recovery	=	0.267
CRU rpm	=	34610.	Pump Flow Ratio	=	9.248
Net O/P Power	=	1.239	Parasitic Power	=	0.030
Des Turb In Pres	=	56.400	Turb Inlet Temp	=	694.3
Cond Press	=	0.126	Boiler Heat Loss	=	-225.0
Regen Vap P Drop	=	0.023	Regen Liq P Drop	=	4.50
Boiler Pres Drop	=	11.10	Cent Sep P Drop	=	4.70
Radiator P Drop	=	6.10	Con Valve P Drop	=	25.00
Control P Drop	=	10.40	Accum P Drop	=	4.10
Diff Pres Rise	=	0.019	Alt Windage	=	0.013
Turb Heat Loss	=	332.0	Regen Heat Loss	=	1440.0
Turb In Ht Loss	=	10.0	Reg Hsg Ht Loss	=	8.0
Plumbing Ht Loss	=	346.0			
Rad Des Flow	=	0.0	J-Cond Des Pin	=	85.2

Output
******

State Point	Press (psia)	Temp (F)	Enthalpy (B/Lb)
Turbine Plenum In	56.400	694.300	418.065
Turb Noz In	56.400	688.236	415.058
Turb Out	0.130	572.551	363.135
Regen Vap In	0.149	544.509	350.404
J Cond Vap In	0.126	253.343	234.159
J Cond Outlet	22.748	206.326	61.010
Pump Inlet	18.648	207.777	61.633
Rad+C Valve In	101.700	208.659	62.013
Rad Outlet	95.600	156.106	40.017
J Cond Liq In	85.200	156.106	40.017
Reg Liq In	76.700	244.324	77.609
Boiler Inlet	72.200	483.498	193.855
Boiler Out	61.100	700.950	421.106

Turbine CP	=	0.401	Turbine Gamma	=	1.036
Pump Spec Speed	=	974.	Pump Efficiency	=	0.650
Turbine Flow Lb/Sec	=	0.03160	Radiator Flow Lb/Sec	=	0.261
Turbine Flow gpm	=	0.228	Radiator Flow gpm	=	1.836
Heat Added In Boiler	=	25848.	Heat Rej By Radiator	=	21373.
Alt Heat Added	=	1774.0	Controller Heat Added	=	0.0
Output kw	=	1.245	Alt Input kw	=	1.505
Bearing+Seal Loss kw	=	0.095	Pump Shaft kw	=	0.117
Seal Leak Lb/Hr	=	0.0	Leak Power Loss kw	=	0.0
Alternator Eff	=	0.935	Pump Flow Ratio	=	9.25
Rectifier Loss kw	=	0.132	Boiler Heat Loss	=	-225.0
Heat Source Watts	=	7507.5	Regen Effec (Act)	=	0.970
System Efficiency	=	16.58694	Cycle Efficiency	=	16.44257

Figure 3.1.9

Phase I
Thermal Analysis Of CRU
(TT1 = 650°F)

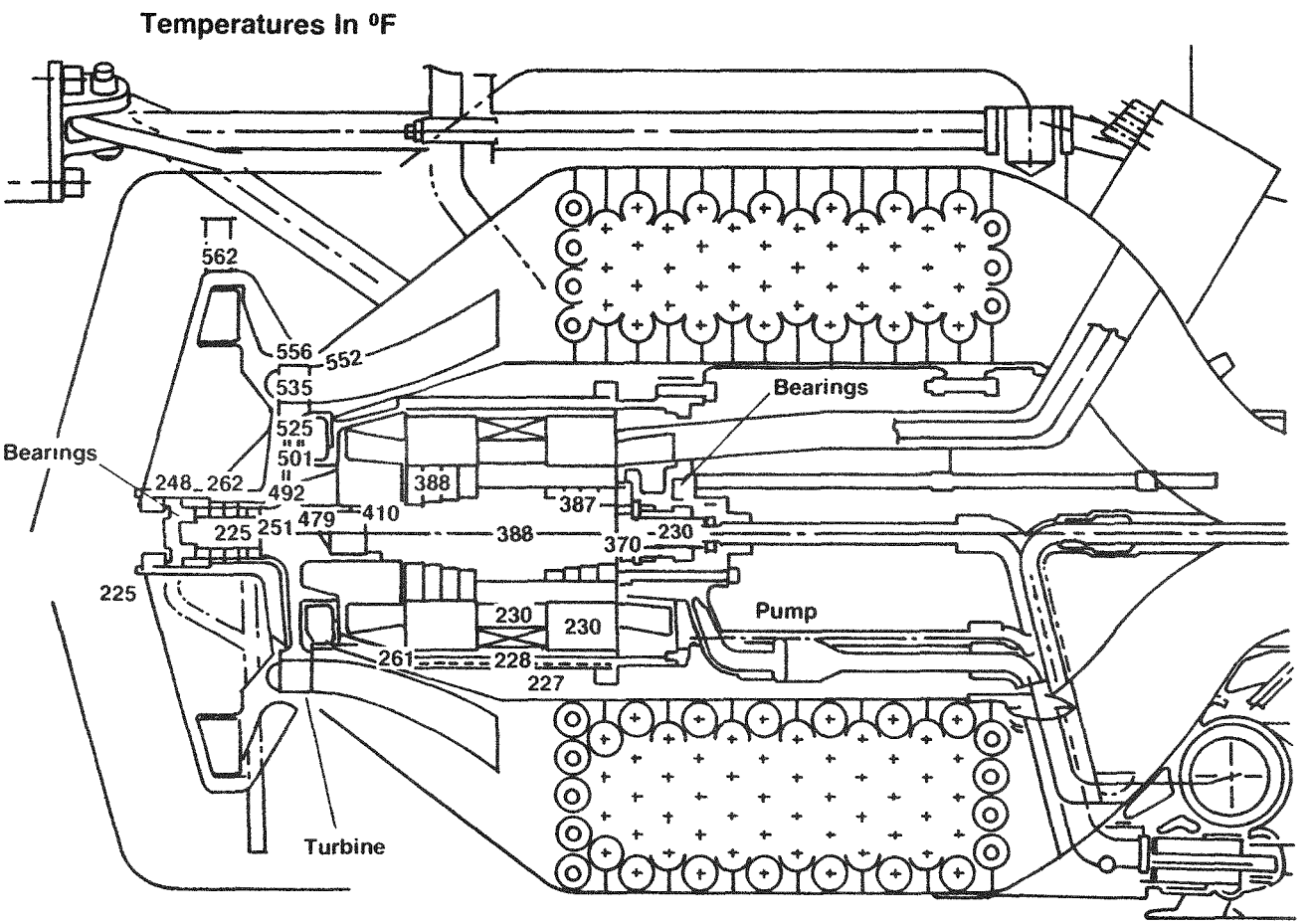

Figure 3.1.10

Phase II
Thermal Analysis Of CRU
(TTI = 675°F)

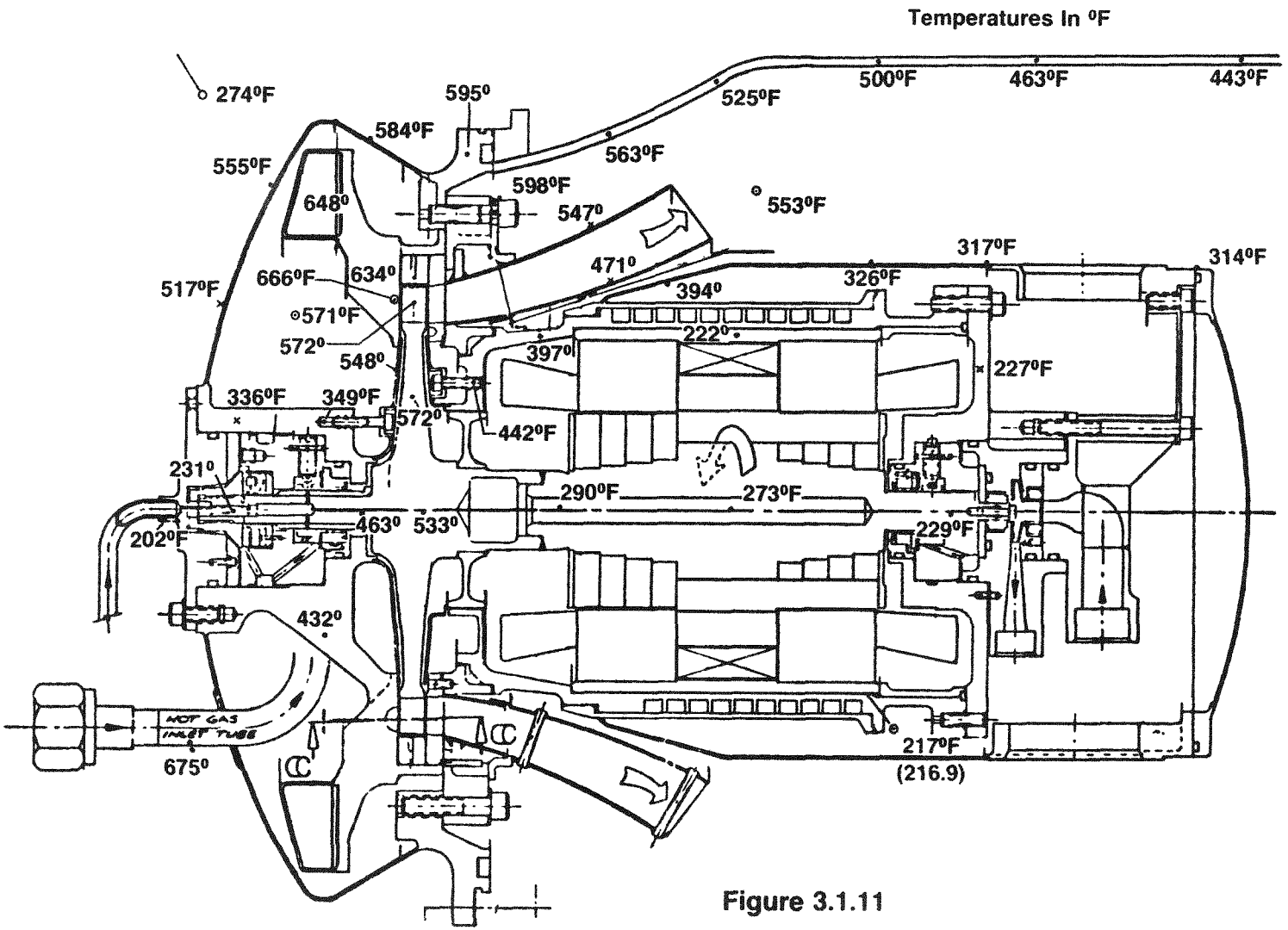

Figure 3.1.11

CRU Modifications To Reduce Thermal Losses

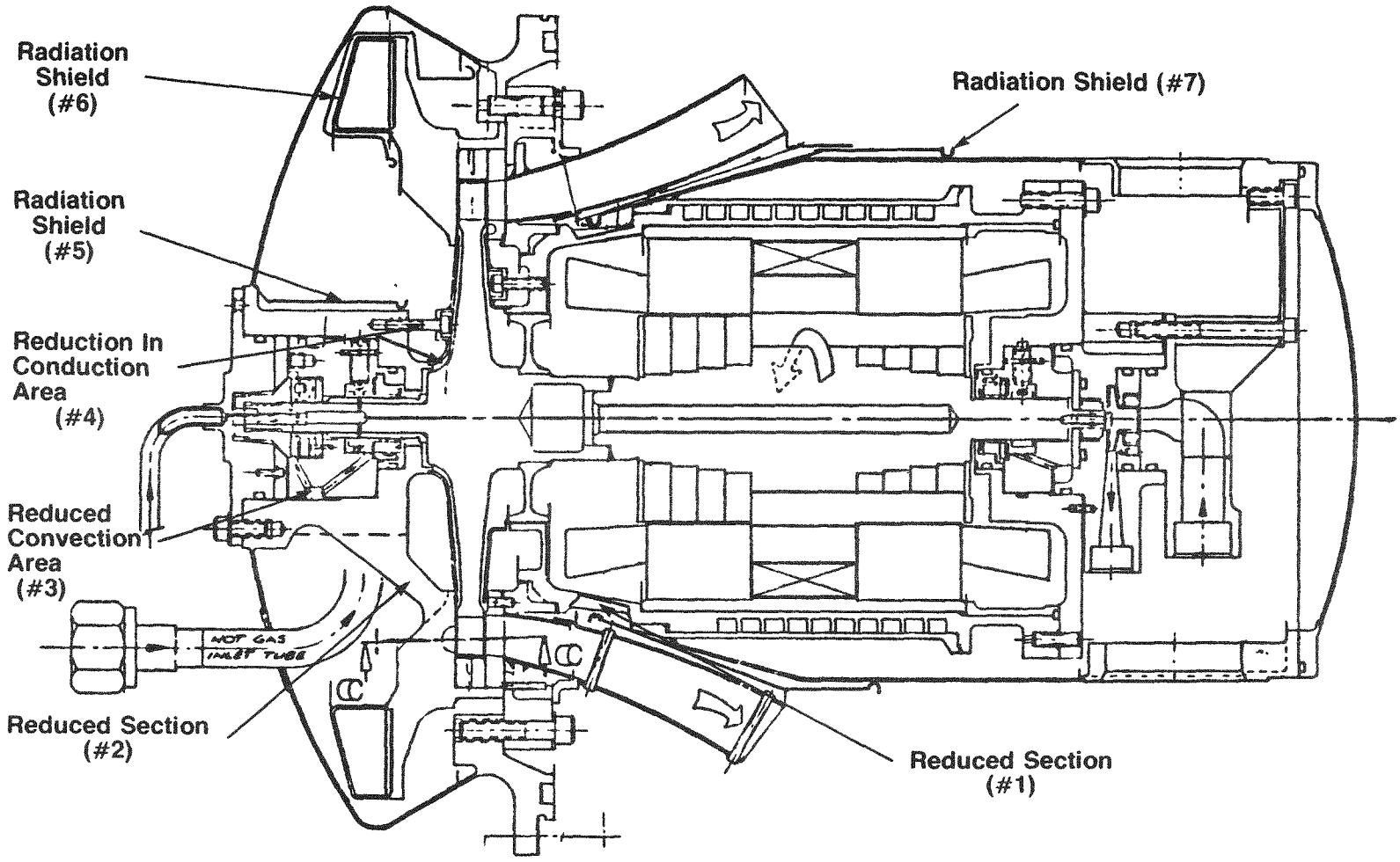

Figure 3.1.12

Required CRU Instrumentation

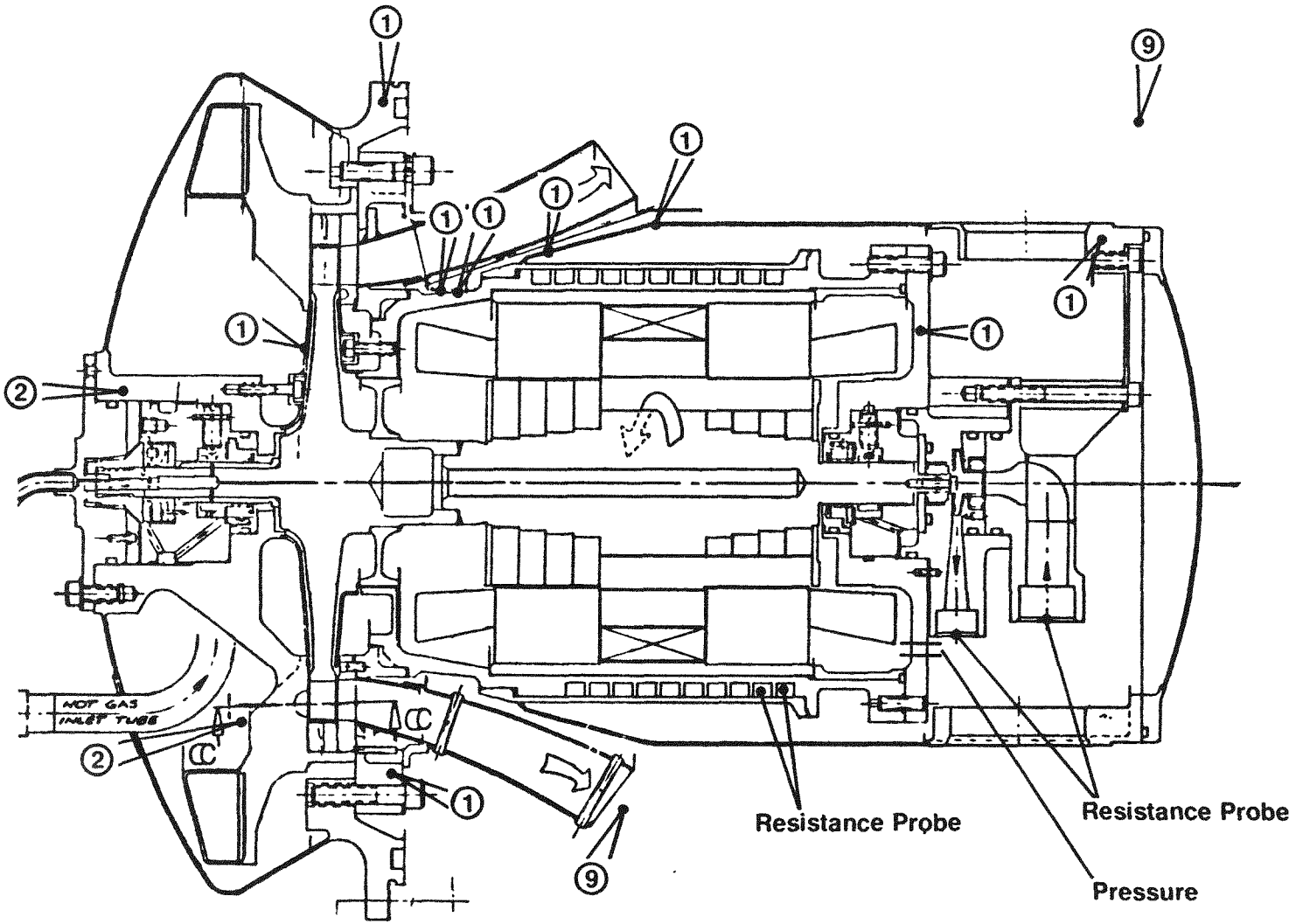

Figure 3.1.13

Alternator Condensing Potential

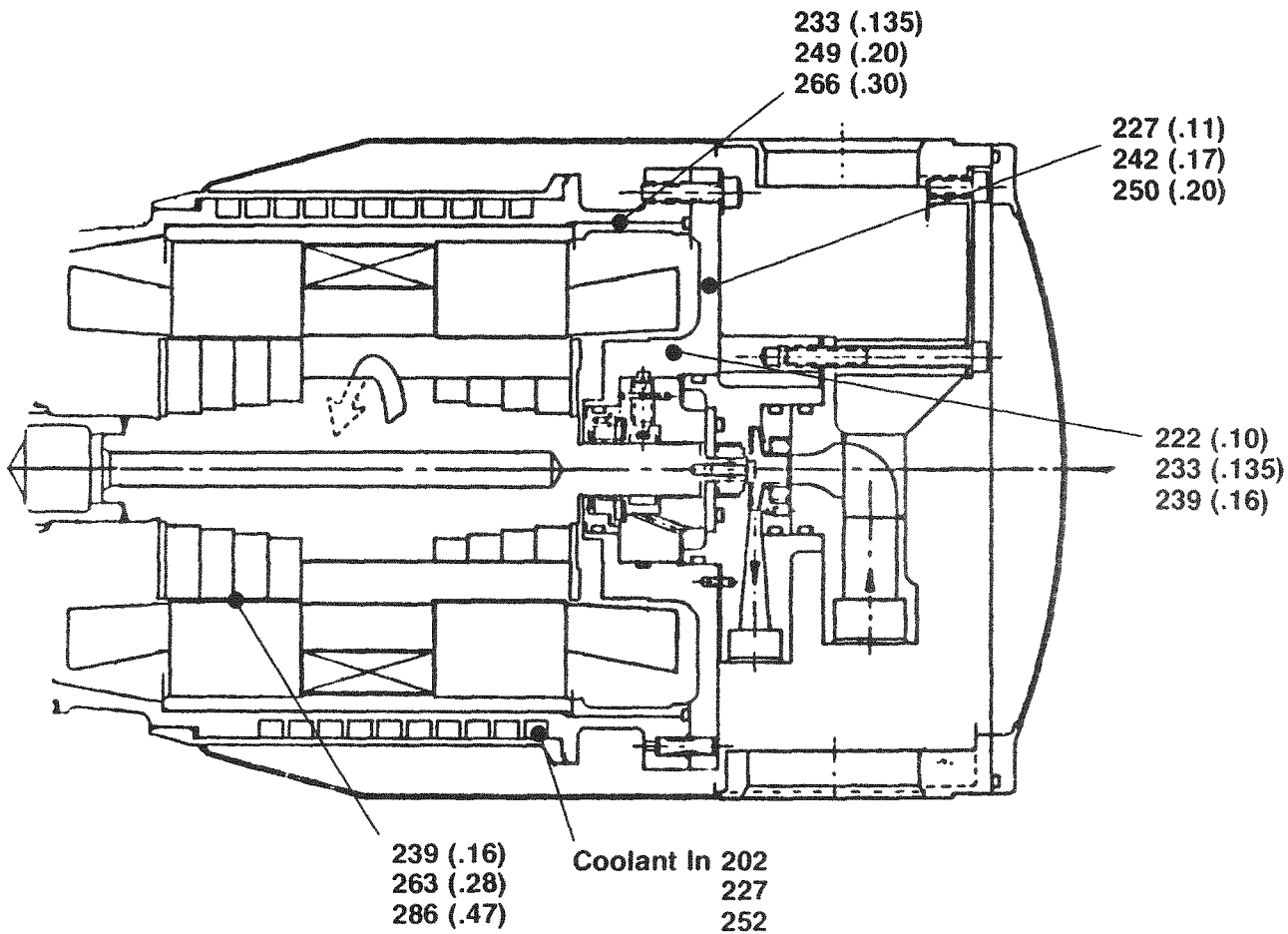

Temperatures In ^{0}F (Sat. Pressure psia)

Figure 3.1.14

Effect Of Alternator Heating On Output Power

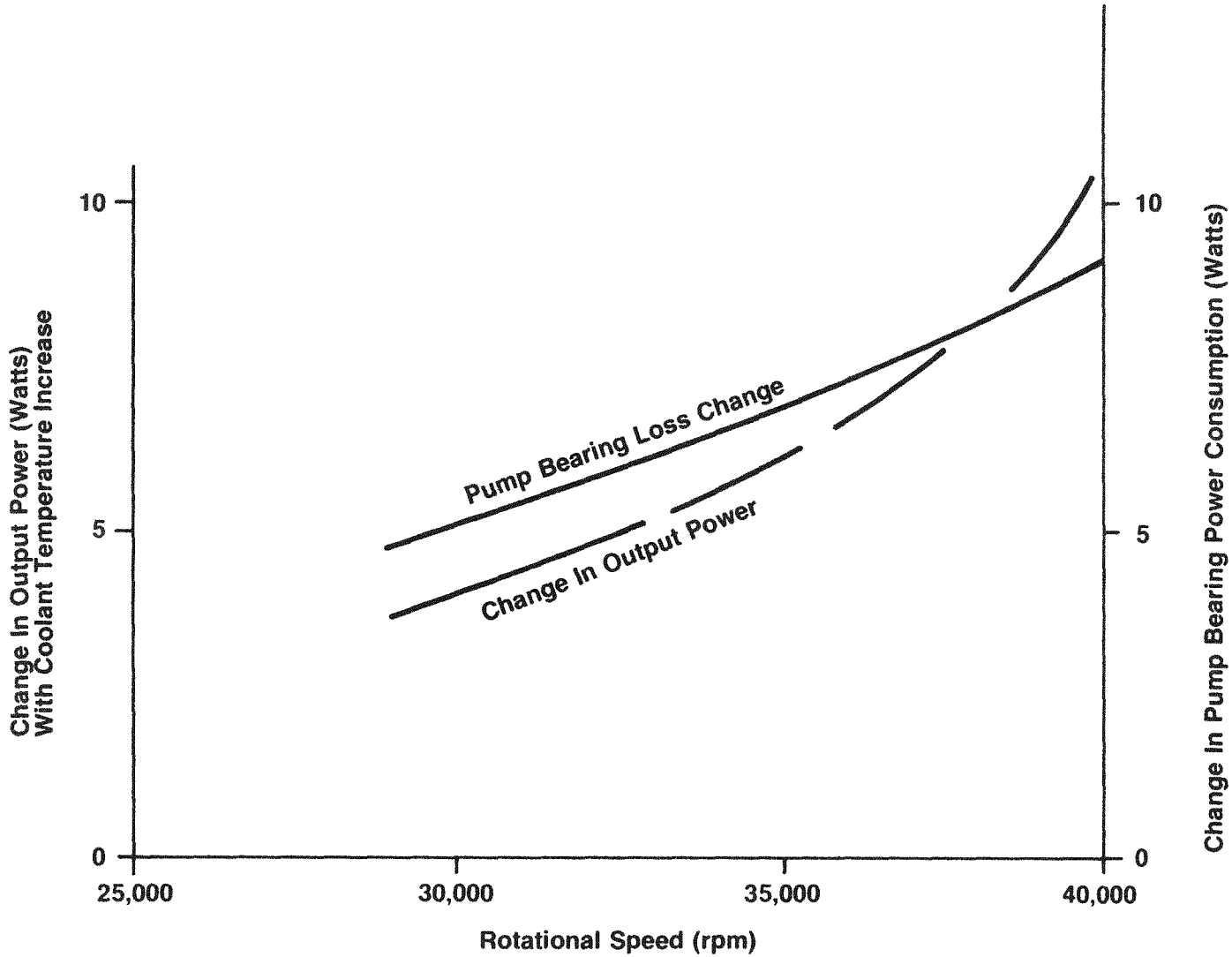

Figure 3.1.15

3.2 Combined Rotating Unit

The Combined Rotating Unit (CRU) extracts useful work from the Dowtherm fluid and converts it into electric power from the alternator and hydraulic power from the system pump.

The CRU comprises three major components, the turbine, the alternator, and the pump, ounted on a common shaft and supported on working fluid lubricated bearings.

The turbine extracts work from the high temperature, high pressure fluid leaving the boiler and converts it to useful shaft power. The KIPS turbine is a single stage, axial flow supersonic impulse type with a constant channel type shrouded blading. It uses multiple shock-cancellation type nozzles.

The turbine directly drives the alternator rotor. The alternator is a monopolar, induction type with four laminated poles on the shaft rotating within the stator windings. High efficiency is achieved by minimizing current density. The alternator waste heat is extracted by the working fluid flowing through a cooling coil. Thermal input from the turbine is minimized by thermal dams in the shaft and the turbine housings.

The system pump is at the end of the shaft away from the turbine. It is a six vaned, centrifugal type employing backward swept vanes and shrouds at both front and back. The flow exits from the impeller into a volute and is discharged through a diffuser for recovery of dynamic pressure. A floating close-clearance seal minimizes leakage into the bearing cavity. Sufficient inlet pressurization to prevent cavitation is provided by the jet condenser.

The rotating shaft is supported radially by two sets of tilting pad bearings, each comprised of four pads. Axial load, which is unidirectional, is supported by a set of tilting pad thrust bearings utilizing six pads with load equalizers. All bearings are lubricated by the liquid working fluid.

A cross sectional view of the combined rotating unit is shown in Figure 3.2.1.

Major developmental changes were incorporated into the CRU during Phase II operation. A rebuild early in Phase II incorporated zero-leakage bearing seals which allowed the bearing cavities to be operated at a pressure adequate to prevent lubricant vaporization. During the final rebuild of the unit, the same type of zero-leakage seals were incorporated but with a smaller diameter to reduce power consumption.

Also during the final rebuild a new turbine wheel and full admission improved performance nozzle block was incorporated; the alternator air-gap was reduced to maximize alternator efficiency and a smaller pump impeller was added. The latter change was made to allow the shaft to rotate at its optimum

speed for maximum CRU efficiency. The optimum speed was determined by analyzing the effects of speed on the efficiencies of turbine, pump and alternator and the hydrodynamic losses of the bearings and seals. The optimum speed occurs at maximum electrical output commensurate with the head-flow requirements of the pump. The calculated value was close to the original design speed of 33,700 rpm.

Experimental results from the final build are presented in detail in Section 3.1. Greatly improved performance did result, however, and the majority of this improvement came from changes in the CRU configuration. Potential improvements due to insulation installation and lower internal heat transfer did not appear to have been realized since the depression of the turbine outlet temperature was not alleviated.

3.2.1 Turbine

3.2.1.1 Turbine Description

The turbine prime mover is a single-stage, supersonic, axial impulse type whose design was based upon real gas properties for Dowtherm A. The turbine blades are shrouded for long fatigue life and an exit diffuser is incorporated to recover exit dynamic pressure. Thermally isolated, close fitting side shrouds are used to eliminate disc friction effects.

3.2.1.2 Turbine/Nozzle Development

Experimental testing of different turbine configurations on a test rig during Phase I led to a reduction in blade chord from 0.6 to 0.36 inches and a change of blade channel shape from a converging-diverging shape to a constant area configuration.

Further testing on the turbine test rig during Phase II of varying wheel chords, blade-nozzle overlap and arc of admission led to the conclusion that a further reduction in chord would be advantageous, despite the reduction in blade Reynolds number. The results of these turbine tests are summarized in Table 3.2.1.1.1.

Table 3.2.1.1.1 Turbine Evaluation Test Results

	Nozzles		Wheel Type		
Blade Tip Overlap	Admission Configuration	Discharge Coefficient	.36 Chord Impulse	.30 Chord Impulse	Stationary Tip Shroud
			Normalized Efficiency		
30%	Partial	.99	.984		Honeycomb
15%	Partial	.99	.977		Solid
52%	Full	.91	.953		Solid
52%	Full	.91		.992	Solid
37%	Full	.91		1.0	Solid
22%	Full	.91		.984	Solid

The high performance of the full admission nozzle block, even with very low nozzle discharge coefficients, indicated that the use of a full admission configuration with an improved nozzle construction would give higher performance than the partial admission. This is consistent with the elimination of partial admission losses.

It was decided that the performance improvement resulting from the use of a full-admission nozzle block, outweighed the disadvantage of having to change turbine wheels for different power level machines. In contrast, the Phase I design had depended upon using varying numbers of nozzles for different power levels with the same rotating assembly and hence the same turbine blade height.

The final selected number of nozzles was 14 with a throat diameter reduced from 0.0566 to 0.0375 inches. Table 3.2.1.1.2 summarizes the critical dimensions of the Phase I and final Phase II turbine configurations. The full-admission configuration was incorporated into the final build, but the turbine test rig results were unavailable in time to incorporate the most efficient blade-to-nozzle overlap and the 22% overlap configuration was used instead of the 37%. The results from Table 3.2.1.1.1 indicated that further turbine improvement is thus feasible.

A nozzle cant or 2 degrees, in which the nozzles are pointed slightly towards the wheel center-line, was also incorporated into the new design to compensate for the inlet axial clearance and to improve flow into the blading. Full admission, with all nozzles just touching was obtained by slightly reducing the nozzle angle from the Phase I configuration, thus effectively increasing the nozzle exit elipse major axis length.

Considerable developmental effort was necessary to manufacture the new full admission nozzle block with the small nozzle throat diameter. The first attempt at the nozzle manufacturing process resulted in an effective nozzle discharge coefficient of less than 0.8 because the throat center-line was offset from the exit center-line resulting in a much larger effective throat area than required.

Table 3.2.1.1.2 Turbine Configuration

	Phase 2 Configuration	Final Configuration
NOZZLE:		
Throat Diameter (In)	.0566	.0375
Number Of Nozzles	7	14
Total Throat Area (Sq. In.)	.01761	.01548
Exit Diameter (In)	.5419	.3373
Total Exit Area (Sq. In.)	1.6145	1.2513
Area Ratio	91.68	80.8
Nozzle Angle (Deg)	15.0	14.42
Arc Of Admission	.747	1.000
Pitch Diameter (In)	5.95	5.95
Design Mass Flow (Lb/Sec)	.030	.0305
Design Inlet Pressure (Lb/In^2)	49.0	57.0
Design Inlet Temperature (^{0}F)	650	675
Measured Discharge Coef't	.987	.99
TURBINE WHEEL:		
Mean Channel Width	.0699 (Constant)	.0629 (Constant)
Axial Chord (In)	.36	.30
Blade Height (In)	.732	.477
Channel Flow Area (In^2)	.0512	.030
Minimum Blade Thickness (In)	.008	.007
Blade Edge Blockage	.103	.104
Blade Mean Diameter (In)	6.607	5.95
No. Of Blades	111	129
Solidity	2.14	2.07
Blade Inlet/Outlet Angle (Deg)	27.35	28.60
Hub Blade/Nozzle Overlap (%)	5	22
Tip Blade/Nozzle Overlap (%)	30	22
Blade Reynold's No. At Exit	7269	5712
Hydraulic Reynold's No. At Inlet	2596	2658

The nozzle was manufactured using both standard milling and Electrical Discharge Machining (EDM) processes. The final nozzle contour was then polished to give the required surface finish. The second attempt at the nozzle block gave excellent nozzle contours with an average discharge coefficient of better than 0.99 at the design point Reynold's number. The measured discharge coefficient as a function of Reynold's number is shown in Figure 3.2.2 for the final nozzle ring.

Because of the manufacturing difficulties experienced by the turbine nozzle block vendor,attempts were made by both Thermo Electron Corporation (TECO) and Sundstrand to manufacture a sample nozzle in a test coupon. Both of these test pieces utimately gave excellent results. Figure 3.2.3 shows a section cut through the TECO nozzle. The smoothly blended inlet radius and good surface finish of the nozzle expansion section are clearly visible in this figure.

The blade and nozzle contours are shown in Figures 3.2.4 and 3.2.5. Experimental results from the final configuration showed an increase in turbine temperature drop over the Phase I turbine. This is consistent with an increase in turbine efficiency. However, the turbine outlet temperature remained depressed below the expected value. This was discussed in detail in the performance section. Based upon test rig data and results inferred from system testing, the turbine efficiency was increased from 66% in Phase I to 68% in Phase II. A further increase to the original design value of 69% is feasible through the use of longer blades.

3.2.2 System Pump

The system pump is located on the turbine shaft outboard of the radial bearings at the opposite end from the turbine wheel, thus minimizing heat losses. Its function is to provide high pressure working fluid for the power loop flow through the turbine and for the heat rejection loop flow through the radiator and jet condenser nozzles. The pump is shown in Figure 3.2.6. The pump impeller is manufactured from 17-4 PH steel with the front shroud and seal ring brazed to the blading. Carbon floating seals are used on both the backside and frontside of the impeller to

minimize leakage into the bearing cavity and recirculation losses. The pump is a centrifugal type with backward swept vanes for stability. A collection scroll is used for improved performance.

The pump impeller used during the Phase I testing was oversized to compensate for short-falls in component and system performance. This oversized pump consumed considerable power at the original design speed of 33,700 RPM and consequently the CRU was operated at reduced speed (approximately 28,000 RPM) to optimize performance.

The pump impeller was trimmed in diameter for the final build to enable the CRU to operate at its design optimum rotational speed.

In order to determine the required diameter a pump impeller was successively trimmed in diameter and tested on a pump test rig to determine operating head-flow characteristics and power loss at different diameters. This testing was performed with a fixed scroll size since it was felt that changing the scroll width would not impact performance greatly, while manufacturing a new pump housing would be very expensive.

The results of these tests are summarized in Figure 3.2.8 and 3.2.9 showing pressure rise as a function of pump diameter and head-flow curves for different diameters.

The test results for the pump which was installed in the unit are presented in Figure 3.2.7. The performance for this impeller at 33,700 RPM was measured to be significantly better than the larger impellers but about the same at other speeds. Repeat tests and recalibration of the test stand did not eliminate the apparent discrepancy. At 2 gpm the measured loss was 85 watts while extrapolation of data from other pump sizes indicated the loss should be 100 watts. For purposes of system performance analysis, the latter value was presumed to be correct and the only explanation of the discrepancy was that the torque meter scale was changed at this point.

The selection of the required pump diameter was based upon measured pressure drops for the various components, and a jet condenser pressure recovery capability of 35%. Tests performed on the GDS

prior to the final rebuild indicated that a separate regenerator preheater for start-up purposes was not required with the 90 nozzle jet condenser and this component was therefore removed for the final rebuild to give a 8 psi saving in pump pressure requirement. The 90 nozzle jet condenser had a lower discharge coefficient than anticipated so that the pump had to be capable of overcoming the higher pressure drop. The assumed system pressure levels and pressure drops are shown in Figure 3.2.10.

The final estimated pump requirements were a flow-rate of 2.3 GPM with a pressure rise of 75 PSID. The final pump configuration tested had a diameter of .696 inches and delivered 74 PSID at 2.3 GPM and 33,700 RPM on the test rig. This impeller was therefore installed in the final build knowing that slightly higher speeds might be required.

The jet condenser nozzle coefficients were slightly lower than had been previously measured and the non-condensable gas separator liquid side pressure drops were higher than anticipated. These effects combined with the undersized pump led to an optimum CRU speed of about 34,700 RPM.

3.2.3 Alternator

The KIPS alternator is a four-pole, homopolar, inductor device. Selection of this type of alternator was dictated by the high operating speed and long service life of this application. A homopolar inductor alternator contains no rotating electrical windings, slip rings, cages or magnets. All electrical windings are contained in the stator and are not subjected to rotational stresses and vibrations. This eliminates winding failures commonly associated with rotational loads.

The rotor of the flight system alternator is an integral part of the combined rotating unit (CRU), as shown in Figure 3.2.11. The rotor configuration is a typical four pole, homopolar, inductor design with two poles of like polarity at each end, the ends displaced 90° (180 electrical degrees) from each other and connected by means of a magnetic shaft. To control pole face losses, the rotor is designed with laminated pole structures. Rotor laminations are made from fully processed AISI grade M-19 electrical sheet steel, 0.014 in. thick.

They are electron beam welded to a shaft made from AISI 8620 steel.

The stator assembly consists of a magnetic yoke containing the field coil sandwiched between two cores, which contain the armature windings. The yoke is a cylindrical piece of low carbon steel (AISI 1008) fully annealed to obtain maximum permeability. Each stator core is a stack of laminations containing 24 slots on its inner periphery. The laminations are made from 3% silicon sheet steel (Magnesil-N) and are 0.005 in. thick. This material was chosen for its high permeability, its low core loss characteristics, and its ability to produce a high resistance oxide surface coating which is essential to control eddy current iron losses and maintain high efficiency.

The stator winding is a conventional three phase, WYE connected, 60° phase, belt winding. Because of the stringent efficiency requirements, the winding was designed for minimum I^2R losses and measures were taken to minimize eddy current losses. These latter can be considerable when the stator slot is relatively deep and the alternator output frequency is high. To reduce eddy current losses, the stator conductors are made up of 31 strands of AWG No. 20 insulated wire each, and the strands are transposed (twisted) in the end turn area such that those located at the bottom of one slot will be at the top of the next slot. In this fashion, all strands have nearly equal reactances and the eddy current producing voltages are minimized. Because specific output voltage waveform requirements were not defined, the stator winding was designed with a full pitch and minimum distribution to obtain maximum posswble output with minimum field excitation.

The field coil of the alternator is a simple toroid of 375 turns of DuPont HML Insulated AWG No. 19 wire wound on an aluminum bobbin. As the coil was wound, DuPont ML varnish per MIL-L-24092B was brushed on each layer of wire and then cured to hold the winding together during handling, prior to insertion into the magnetic yoke. The coil was insulated with double layers of 0.005" thick Kapton sheet. Once installed in the stator assembly, the coil is snugly held on both sides by the stator cores, the yoke on the OD, and the aluminum bobbin on the ID.

The materials for the alternator insulation system were selected on the basis of dielectric strength, long term compatibility with Dowtherm A, and best life versus temperature characteristics.

With the exception of teflon sleeving and fiber-glass tie cord, the entire KIPS alternator insulation system consists of polyimides in various forms (see Table 3.2.3.1). Polyimides possess the greatest dielectric strength and best life versus temperature rating of all known organic insulation materials.

The alternator is nominally rated at 1.56 KVA, 22.5 volts line-to-line, 40 amps, 0.93 to 1.0 power factor. It has a continuous thermal overload capability of 2.5 KVA; with added cooling, the electromagnetic capacity is well over 3 KVA.

In the alternator, both the armature and field windings contain sufficient copper to maintain low current densities and, therefore, low copper losses. At rated load, the current densities are 1620 amps per square inch in the armature and 1980 amps per square inch in the field windings.

The alternator rotor is assembled by welding and becomes an inseparable one piece assembly. The stator laminations are assembled into cores using Scotchcast 265 epoxy adhesive, and the cores are fitted into the yoke with a 0.001 in. diametral interference fit. The armature windings are held within the cores by the semiclosed slot design. The alternator stator is held in its housing by means of a shrink fit. No mechanical fasteners are used in the alternator assembly.

Additional testing of different generator configurations was performed in Phase II in an attempt to improve electromagnetic efficiency. Phase I testing had indicated that a potential improvement was obtainable from a change in rotor-stator air-gap.

The alternator test rig was upgraded to improve measurement accuracy by installing an electric motor in place of an air-turbine as the prime mover. The rotor-stator air-gap was varied from the Phase I design value of 0.025 inches to as much as 0.038 inches. The intention was to maximize efficiency at a 1500 watt electrical load so as

Table 3.2.3.1 KIPS GDS Alternator Insulation System

Component	Trade Name	Material
Magnet Wire	DuPont Heavy ML Film	Double Coat Polyimide Varnish
Slot Cells	DuPont Kapton Sheet .005" Thick	Polyimide Sheet (Flexible)
Field Coil Ins.	DuPont Kapton Sheet .005" Thick	Polyimide Sheet (Flexible)
Tie Cord	Varglas Non-Fray Sleeving	Braided Fiberglass Sleeving
Slot Wedges	Dixon Corp. Meldin Polyimide 0.025" Thick	Polyimide Sheet (Rigid)
Impregnating Varnish	DuPont Pyre ML Varnish	Polyimide Varnish
End Leads	Teflon	

to maximize the GDS performance. As part of the efficiency improvement investigation, it was found that a special machining technique helped performance. By using a diamond tool turning process rather than a grinding process for machining the rotor pole tips, smearing of the laminations was obviated, reducing eddy current losses.

Figure 3.2.12 shows a summary of this testing, indicating an optimum air gap of 0.0284 inches and an efficiency improvement of about 1% point over the original 0.025 air-gap. The final rebuild of this system incorporated the 0.0284 inch air-gap.

3.2.4 Bearings and Seals

3.2.4.1 Bearings

The bearings for the combined rotating unit (CRU) support both axial and radial loads under a variety of different operating conditions. The baseline operating point for which losses need to be minimized and, hence, performance maximized is the zero g condition when bearing loads are at a minimum and comprise only turbine, pump, alternator, and imbalance loads. The most stringent operating conditions will be during launch when either: (1) accelerations in the axial and radial directions reach nine and five g's respectively with superimposed vibration loads or, (2) the short term shock loads are applied independently of the acceleration load. In addition, ground operation in the vertical direction will have one g axial load while horizontal operation would have one g radial load. The bearing geometries are shown in Figure 3.2.13.

The radial bearings consist of working fluid lubricated tilting-pad bearings. Each set of bearings comprises four tilting pads of 80 degrees of arc pivoted at 44 degrees from the leading edge. The bearing pads are hardened M-50 tool steel with a thin electroplated silver coating. The coating enhances start-stop characteristics.

The tilting-pad radial bearing is inherently stable due to the fact that the shaft movement is essentially colinear with the applied loads. The tilting pad bearing comprises a series of equally spaced shoes arranged circumferentially around the shaft. A pivot in the backside of the shoe allows it to tilt in the pitch direction in order to form

Table 3.2.3.2 Radial Bearing Geometry

Number Of Pads:	4
Pad Length: (In)	0.275 ± 0.005
Shaft Diameter: (In)	0.5500 + .0000 − .0002
Pad I.D.: (In)	0.5525 + 0.0002 − .0000
Machined Clearance: (In)	0.0025 ± 0.0002
Assembled Clearance: (In)	0.00175
Preload Coefficient:	0.3
Pad Thickness At Pivot: (In) (Tapered Towards Leading And Trailing Edges)	0.150
Pad Arc: (Degree)	80
Pivot Point Location (Degrees From Leading Edge)	44
Leading Edge Radius: (In)	0.05
Pad Material:	M-50 With Silver Flash
Shaft Material:	M-50 At Turbine End AISI 8620 At Pump End
Pivot Spherical Diameter: (In)	0.666
Socket Spherical Diameter: (In)	1.00
Design Point Power Loss: (Watts/Hz)	7.5

a converging wedge for hydrodynamics pressure generation. Typically, instability only arises in tilting pad bearings when pad pitch inertia is high enough to prevent adequate shaft tracking. This potential instability can be precluded by "preloading" the bearing and minimizing pad inertia. Preloading sets the bearing pads closer to the shaft than would be dictated by the machined clearance and thus has the same effect as applying an external load. An additional advantage of the tilting pad bearing is the self-aligning characteristic which eliminates alignment problems common with rigid bearings.

The radial bearings operate in the laminar flow regime throughout the operating range with Reynold's number of 544 and 920 at design point and maximum speeds, respectively. The radial bearing geometry is summarized in Table 3.2.3.2.

The maintenance of bearing radial clearances is important to prevent excessive whirl orbit amplitudes and prevent the possibility of other components with close radial clearances from contacting. For this reason, special attention has been given to restraining the radial movement of the bearing pads. The bearings are preassembled into steel support modules. The bearing clearance is set using an oversized mandrel by tightening a threaded pivot pin which, in turn, is locked in place by drilling and inserting a roll pin.

The materials selected for the radial bearings comprise a hard-hard combination of M-50 pads versus either an M-50 sleeve at the turbine end or carburized AISI 8620 shaft at the pump end. A flash silver plate is added to the pad inner surface to give additional bearing protection in the event of a high speed rub, and to enhance start-stop capability. The pivot pin is silver plated M-2 hardened tool stell and is screwed into an AISI 8620 housing.

The thrust bearing is designed for unidirectional thrust loading. Short term reverse loads resulting, for instance, from rocket staging, can be accommodated.

The thrust bearing configuration employs six M-50 tool steel tilting pads with two rows of six leveling pads. A hemispherical pivot engages into a hemispherical socket in each pad. The pivot pin is mounted to the first leveler which, in turn,

Table 3.2.3.3 Thrust Bearing Geometry

Number Of Pads:	6
Active Pad Circumferential Length:	0.25 In
Active Pad Radial Width:	0.25 In
Pad Thickness:	0.10 In
Pivot Location From Leading Edge:	0.15 In
Pad Material:	M-50 With Silver Flash
Thrust Runner Material:	M-50
Pivot Spherical Diameter:	0.666 Inch
Socket Spherical Diameter:	1.00 Inch
Number Of Upper Load Levelers:	6
Cylindrical Pivot Diameter:	0.125 In
Cylindrical Pivot Length:	0.125 In
Number Of Lower Load Levelers:	6
Cylindrical Pivot Diameter:	1.00 In
Cylindrical Pivot Length:	0.175 In
Total Axial Clearance:	0.007 In
Design Point Power Loss:	25 Watts

pivots on two of the second levelers by contact along radial lines. The bottom leveler pivots on an M-50 insert which doubles as a shim to set the turbine wheel clearance. The pin through the bottom leveler prevents circumferential motion while relatively tight radial clearances act as restraints in that direction. Similarly, a tight clearance at the inner diameter of the thrust pads prevents windmilling of the pads about the pivots. The pad surfaces and the pivot surfaces have a flash of silver plate (0.0004 in.). The thrust runner is also made of M-50 tool steel. The geometry is summarized in Table 3.2.3.3.

Although the preferred orientation of the power system axis precludes reverse thrust during normal operation and through launch, it is feasible that momentary reverse thrust loading could occur during orbit transfer or within the Space Shuttle bay. This can be accommodated by a bronze snubber which can withstand the surface speeds at which this occurs without lubrication and damage. This snubber also serves as a protection for the turbine wheel during handling and accommodates the initial reverse thrust load at start resulting from pump inlet pressurization by the start pump.

In order to maintain the design point operating characteristics of the bearings throughout the operating life, it is necessary to preclude any possibility of pivot fretting type wear. The results of such wear are a decrease in the pad stability due to an increase in the pivot friction and an increase in the bearing clearance leading to a change in minimum film thickness. For this reason, maximum Hertz stresses were limited to 220,000 psi and a radius ratio of 1.5 was selected. A summary of the pivot geometry is given in Table 3.2.3.4.

3.2.4.2 Bearing Development

No significant development changes were made during Phase II. The major difference in operation resulted from zero leakage seals allowing the bearing cavities to operate at liquid pressures high enough to preclude local vaporization under the radial pad edges.

An additional change was made to the thrust bearing load leveling system to allow free motion of the pads under the worst case tolerance situation.

Table 3.2.3.4 Pivot Design

Pivot Location	Pivot Type	Pivot Diameter (Inch)	Socket Diameter (Inch)	Pivot Length (Inch)
Thrust Pad	1	0.666	1.00	— —
Upper Load Leveler	2	0.125	— —	0.25
Lower Load Leveler	2	1.00	— —	0.175
Radial Pad	1	0.666	1.00	— —

(1) Spherical Pivot In Spherical Socket.

(2) Cylinder On Flat.

3.2.4.3 Bearing Seals

Bearing cavity seals are necessary in the CRU to prevent bearing lubricant from leaking into the alternator and turbine cavities. Leakage into the alternator cavity would cause increased hydraulic losses and potential inventory management problems under zero 'g' conditions. Leakage into the turbine cavity results in increased shaft losses and also a depression of turbine outlet temperature.

All of these effects were noted in Phase I using centrifugal seals and bearing cavity pressures of 1-2 psia. Operation of the bearing cavities at very low pressures essentially eliminated the leakage but allowed lubricant vaporization under the radial pads which in turn led to some signs of surface distress at the pad outer edges, where hydrodynamic film pressures approach ambient pressures.

3.2.4.4 Seal Development

The pump test rig was modified to allow the testing of various configuration seals. The first configuration to be tested was the tapered centrifugal seal installed in the Phase I CRU. These experiments confirmed leakage at low pressures with higher power losses than anticipated. These test results led to the realization of the need to develop a low leakage, low power loss seal to solve the CRU operational problems. Figure 3.2.14 shows a summary of the different seal configurations tested during the developmental process, leading ultimately to the floating hybrid visco seal as the seal type which satisfied the requirements.

This seal type, the floating visco seal, is shown in greater detail in Figure 3.2.15 with a photograph in Figure 3.2.16. The operation of the seal depends upon the smooth journal bearing area of the floating carbon to stabilize and centralize the seal while the grooved section acts as a pump. Tests of plain floating visco seals without the smooth section were dynamically unstable.

The first installation of this seal configuration into the GDS employed seals with a diameter of 0.75 inches since they could directly replace the existing centrifugal seals. The final rebuild employed seals with a diameter of 0.55 inches which is the same diameter as the radial bearings.

The smaller diameter seals were chosen because of their lower power consumption. Figure 3.2.17 shows the leakage of the pump end seal installed in the final build and Figure 3.2.18 shows the power loss. Figure 3.2.19 shows the power loss for the larger diameter visco seal for comparison.

Combined Rotating Unit

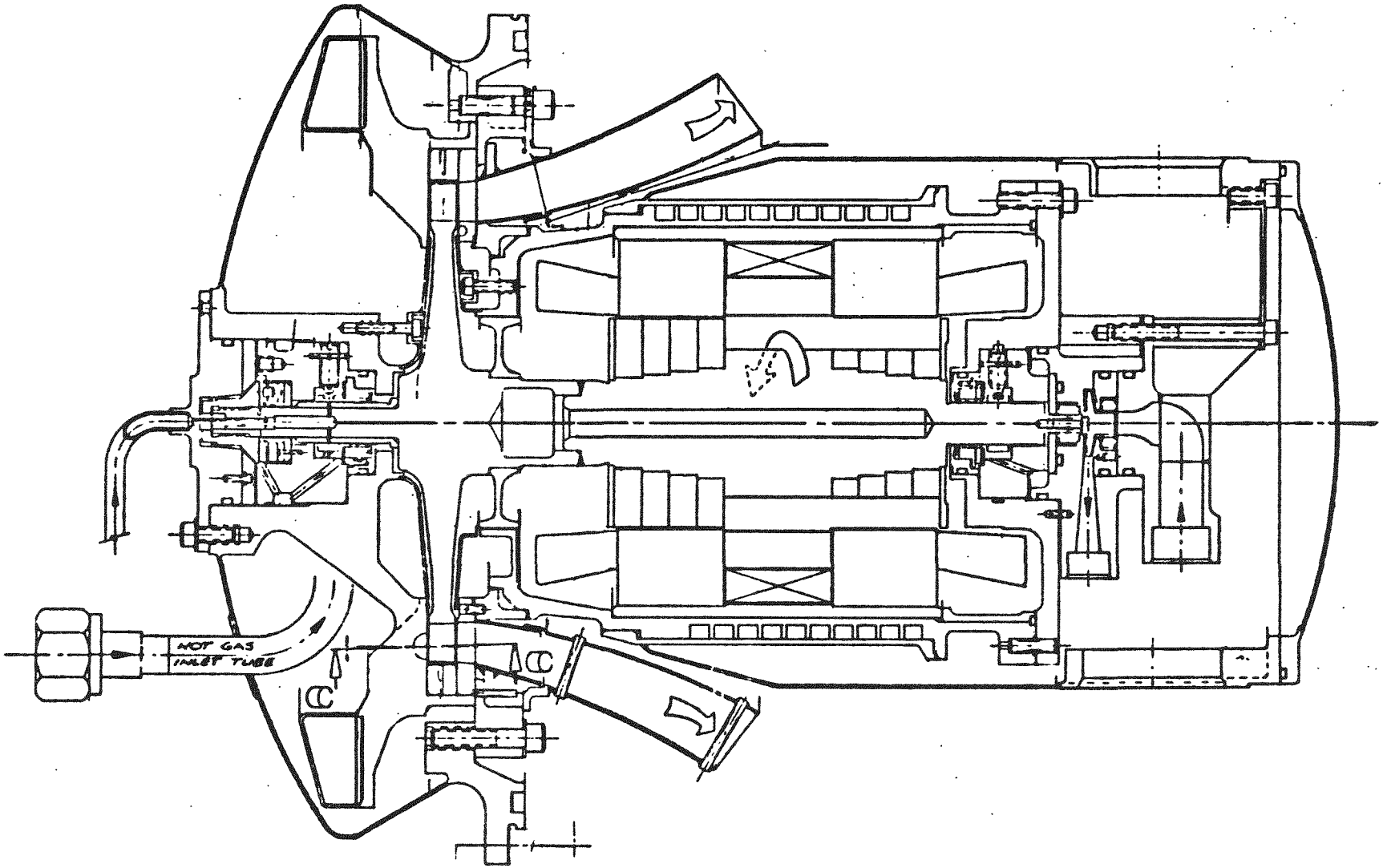

Figure 3.2.1

Nozzle Discharge Coefficient

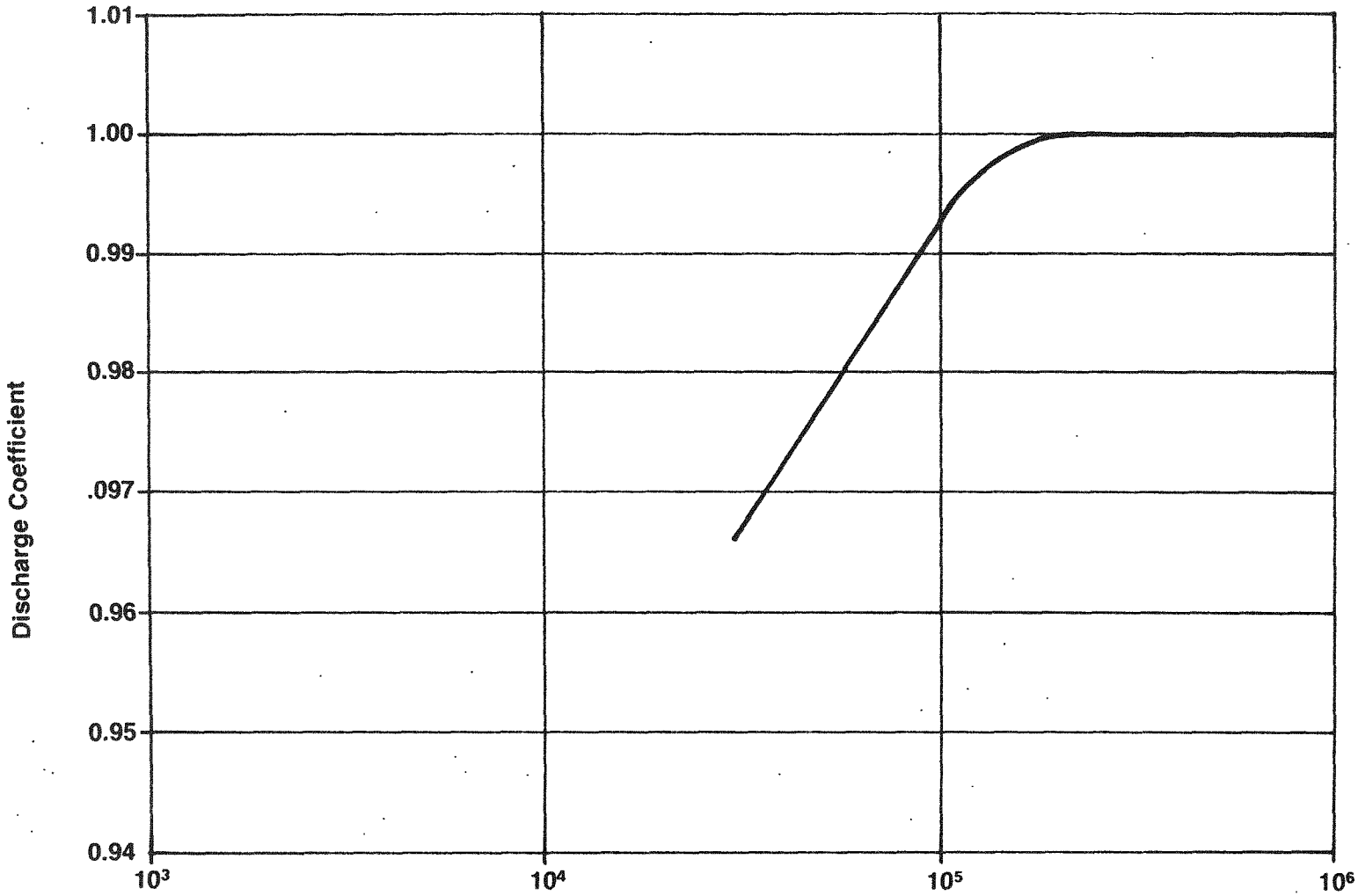

$R_n = \frac{48W}{60\pi d_2 \mu}$; W = lbm/Min , d_2 = .14087" , μ = .0000120 lbm/Ft-Sec

Throat Reynolds Number

Figure 3.2.2

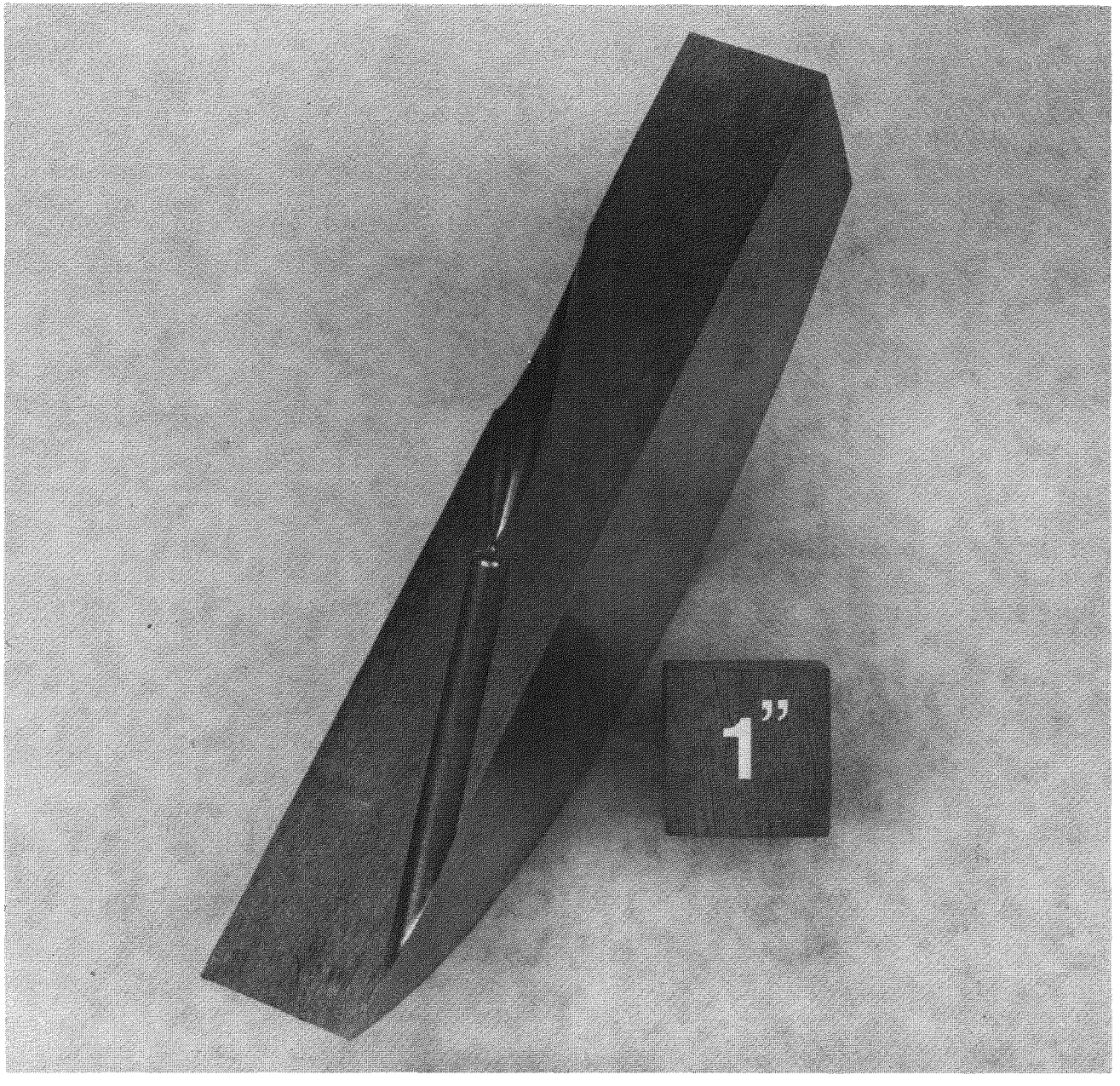

Figure 3.2.3

Turbine Blade Contours

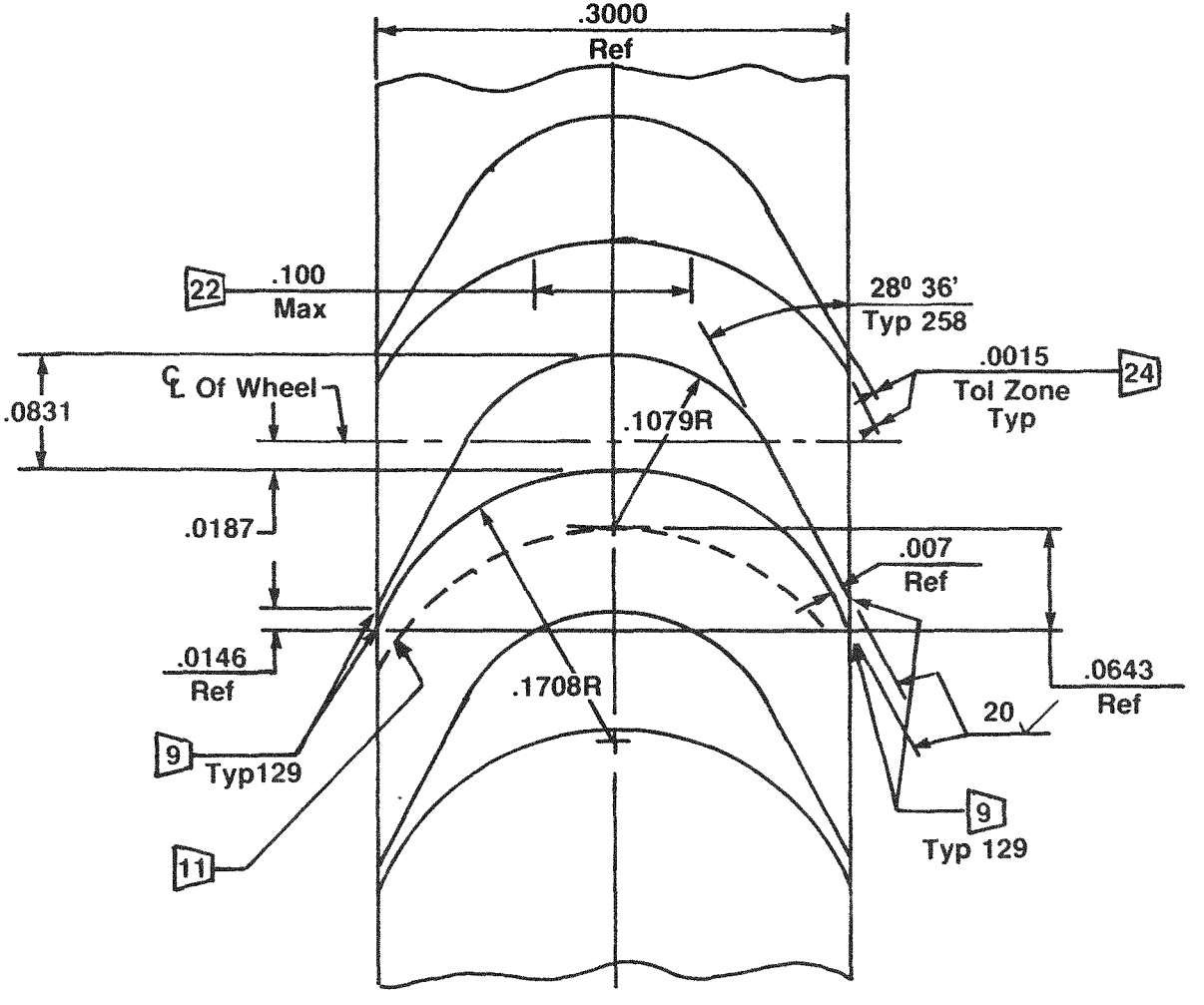

Figure 3.2.4

Turbine Nozzle Contours

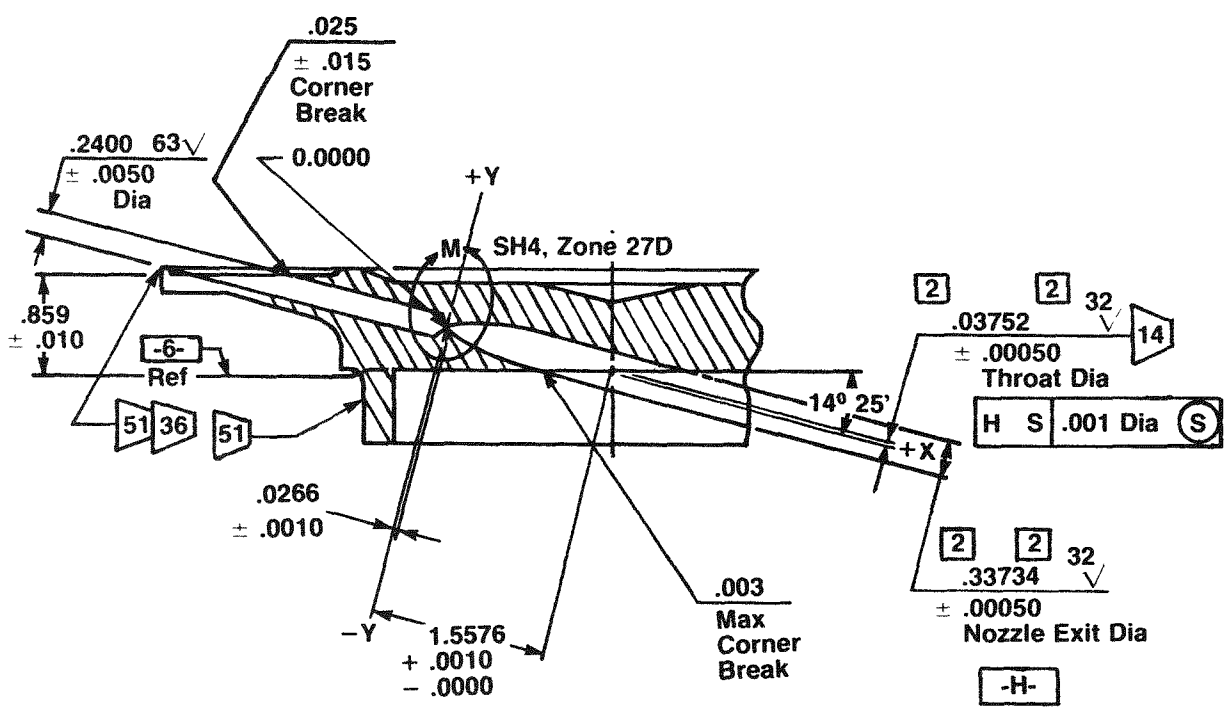

Nozzle Contour Configuration Data	
x ± .00100	± y Datum Radius
.04243	.02272
.07191	.03851
.07896	.04215
.08680	.04592
.09553	.04984
.10525	.05392
.11607	.05816
.12811	.06257
.14153	.06716
.15650	.07194
.17319	.07690
.19183	.08205
.21268	.08739
.23602	.09293
.26219	.09864
.29159	.10454
.32469	.11061
.36205	.11683
.40432	.12319
.45230	.12967
.50697	.13624
.56954	.14287
.64149	.14952
.72473	.15613
.82172	.16267
.92817	.16867 (Ref)

Figure 3.2.5

System Centrifugal Pump

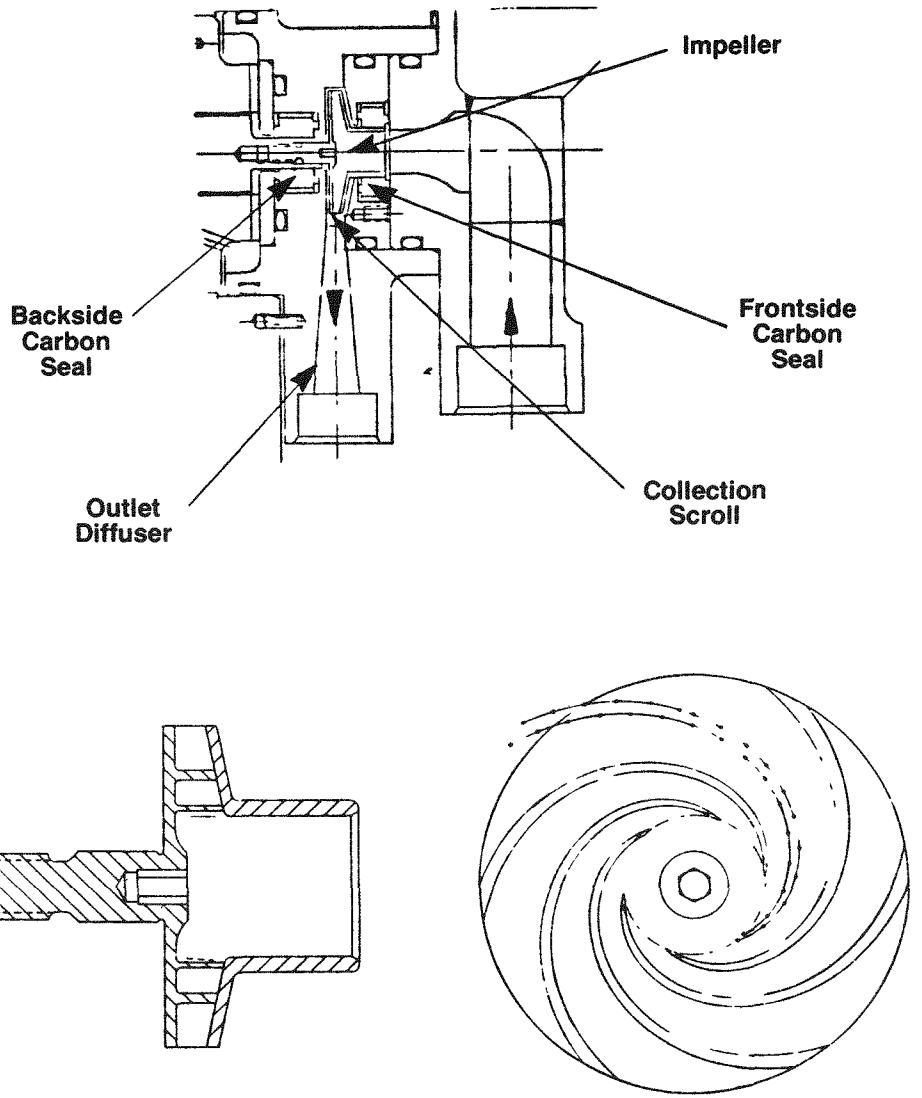

Figure 3.2.6

Pump Pressure Rise Characteristics

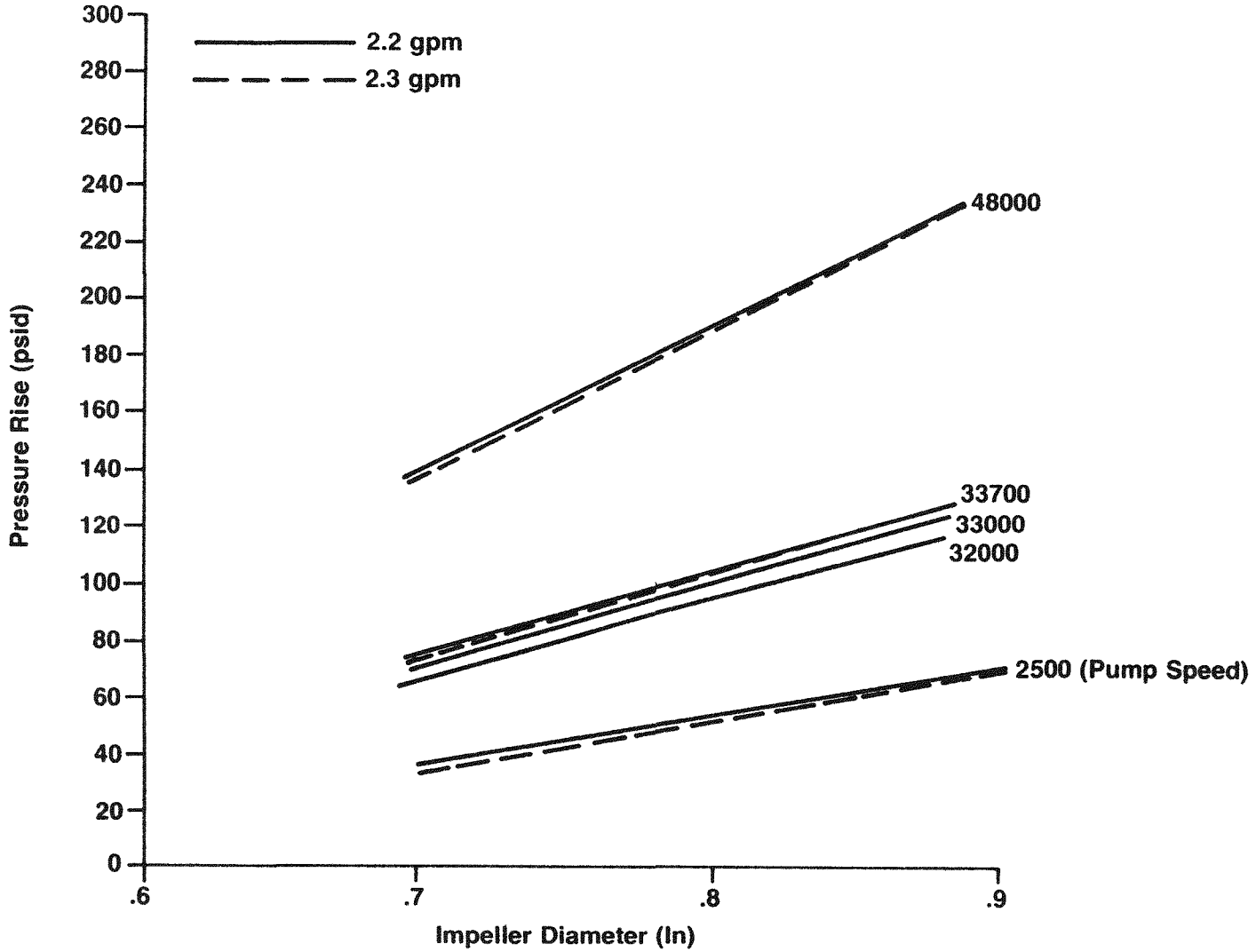

Figure 3.2.7

Pump Head
Flow Characteristics

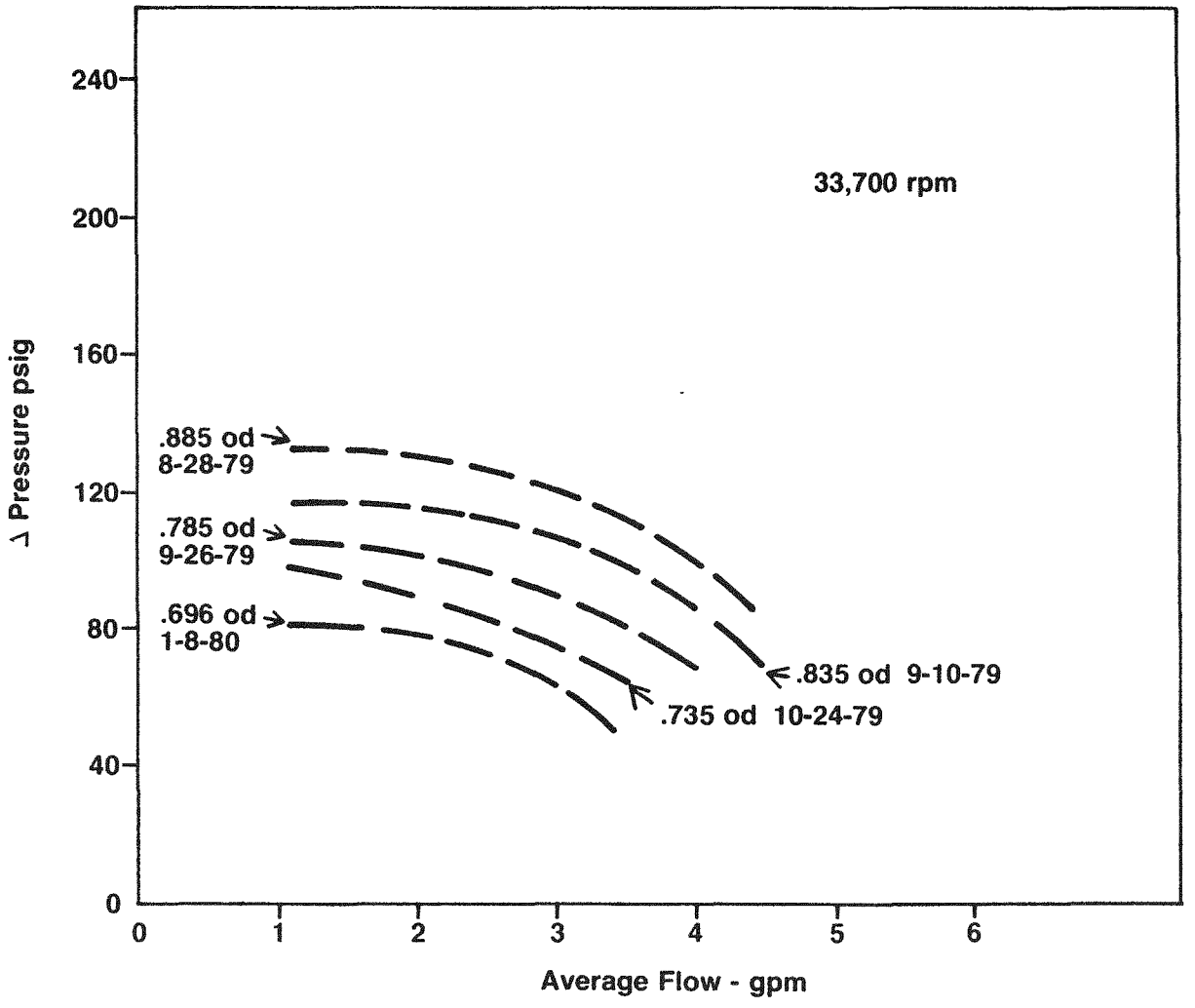

Figure 3.2.8

Measured Pump Performance
Inch
(.696/Diameter)

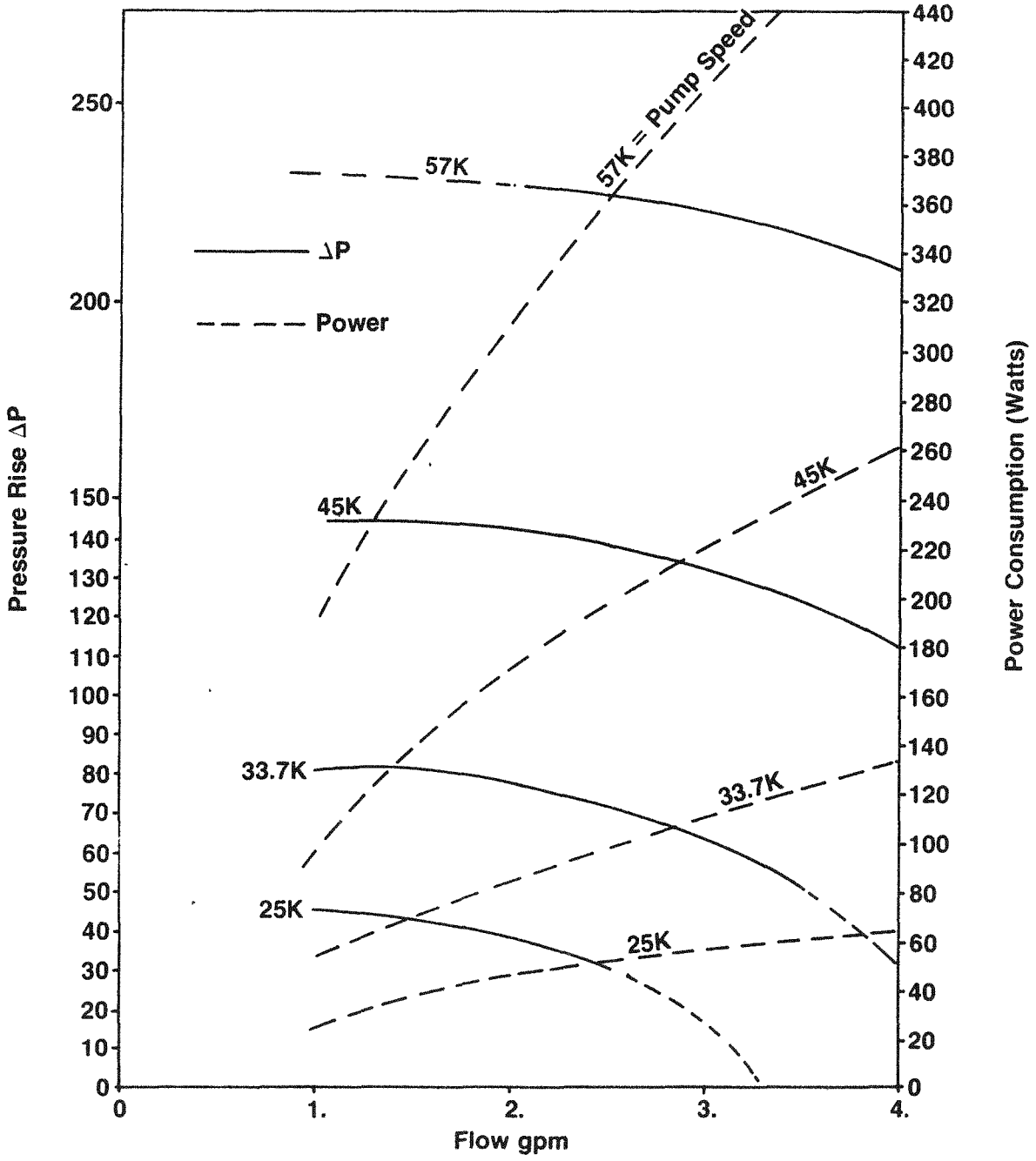

Figure 3.2.9

GDS Pressure Levels

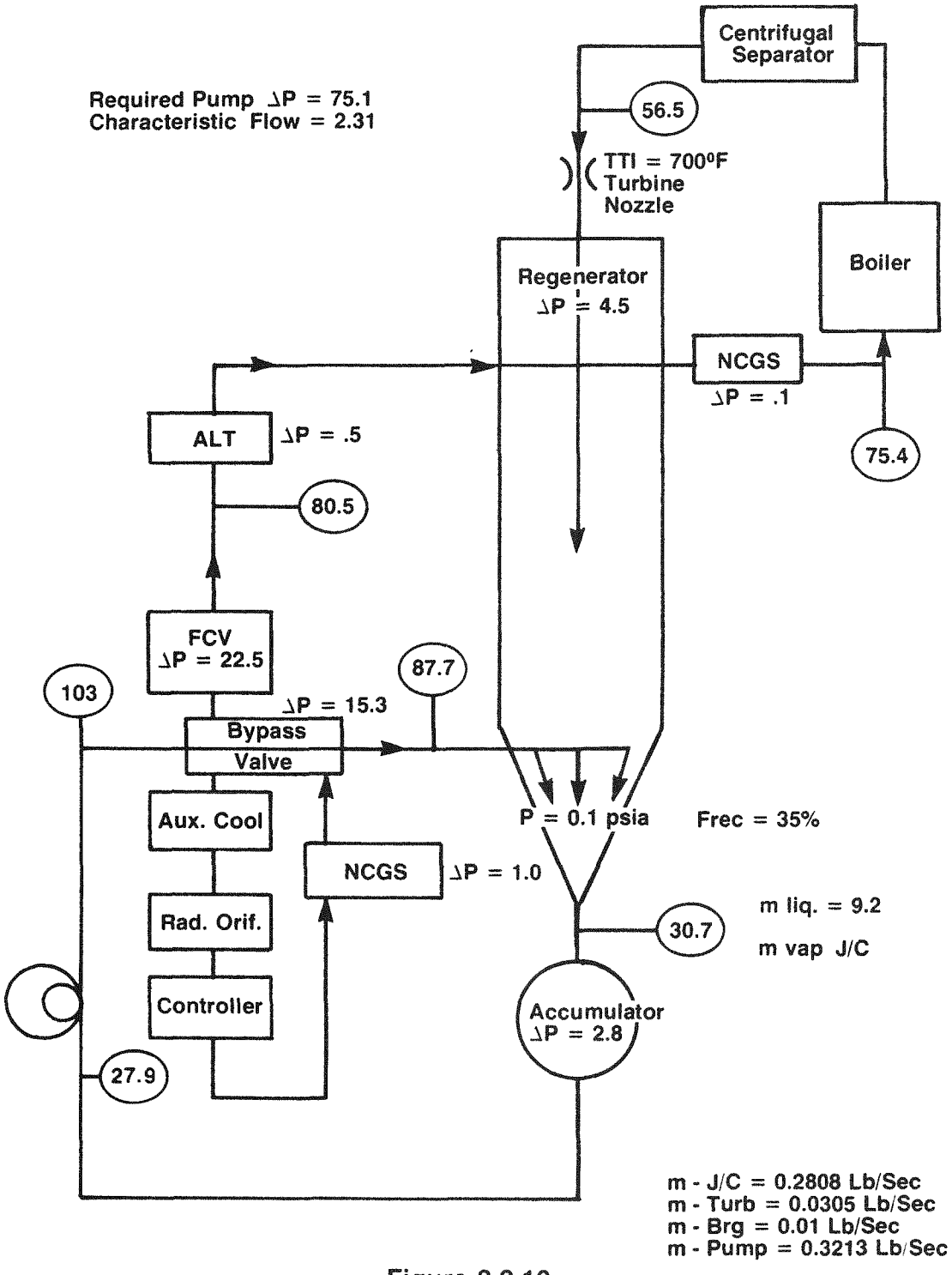

Figure 3.2.10

Homopolar Alternator

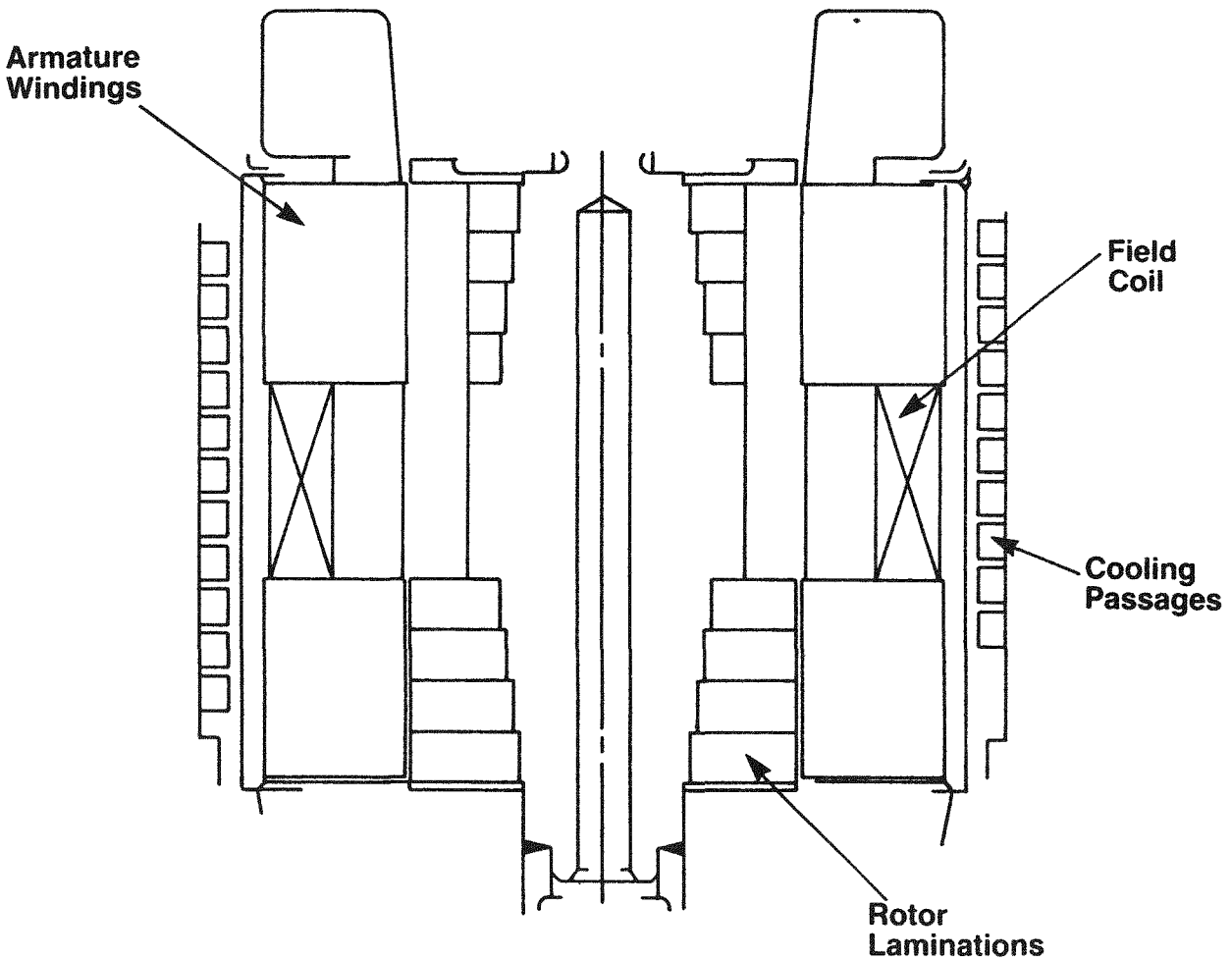

Figure 3.2.11

DIPS Alternator Efficiency Vs Air Gap

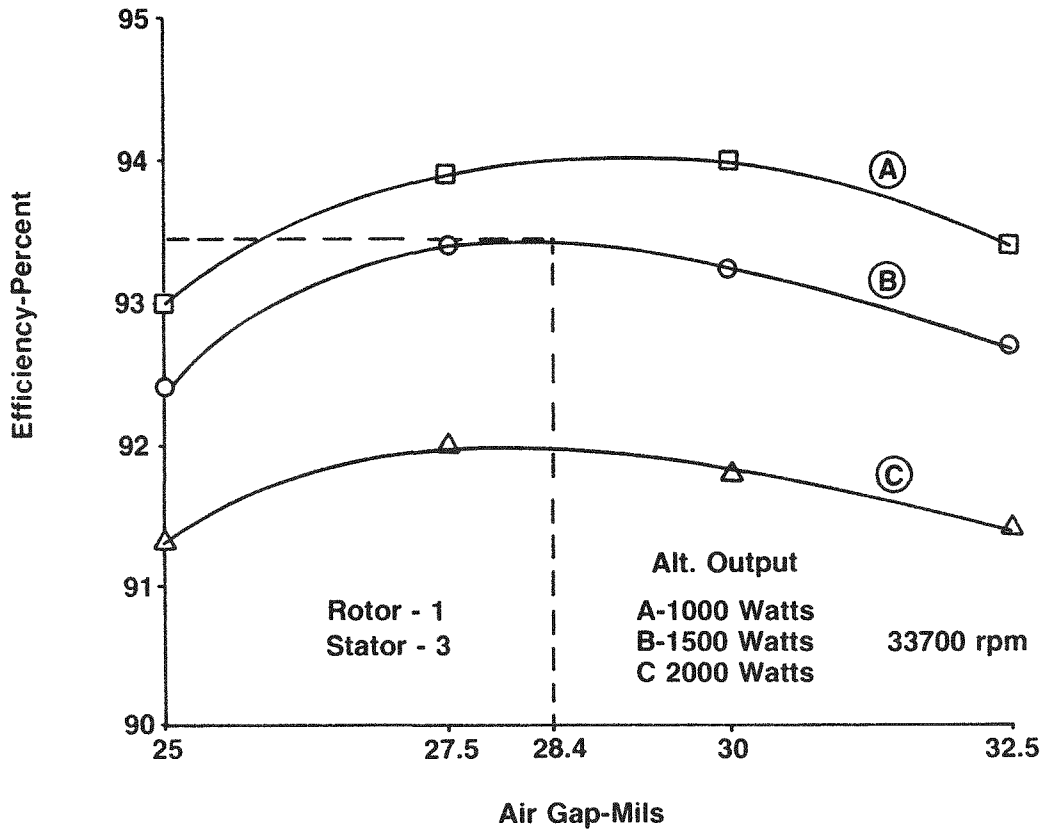

Figure 3.2.12

Bearing Geometries

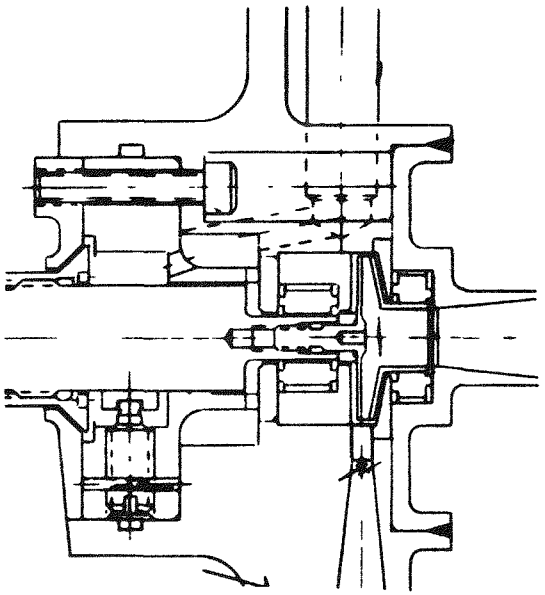

Pump Bearing

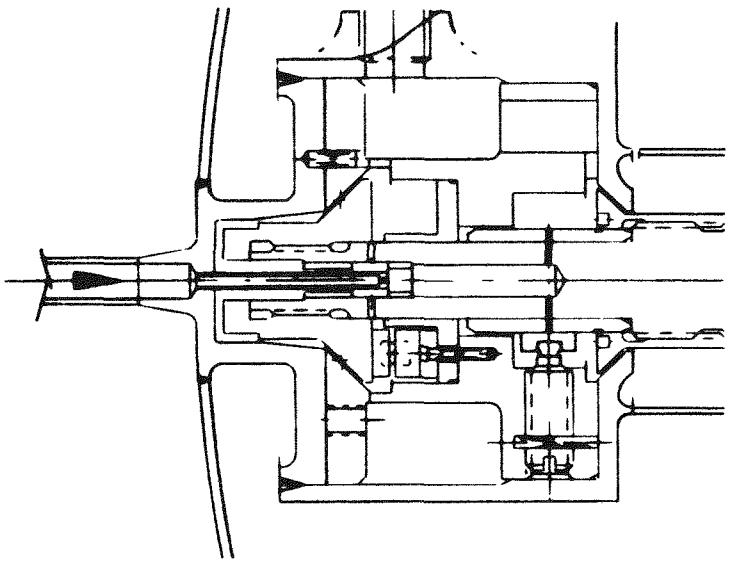

Turbine Bearing

Figure 3.2.13

Seal Configurations Tested

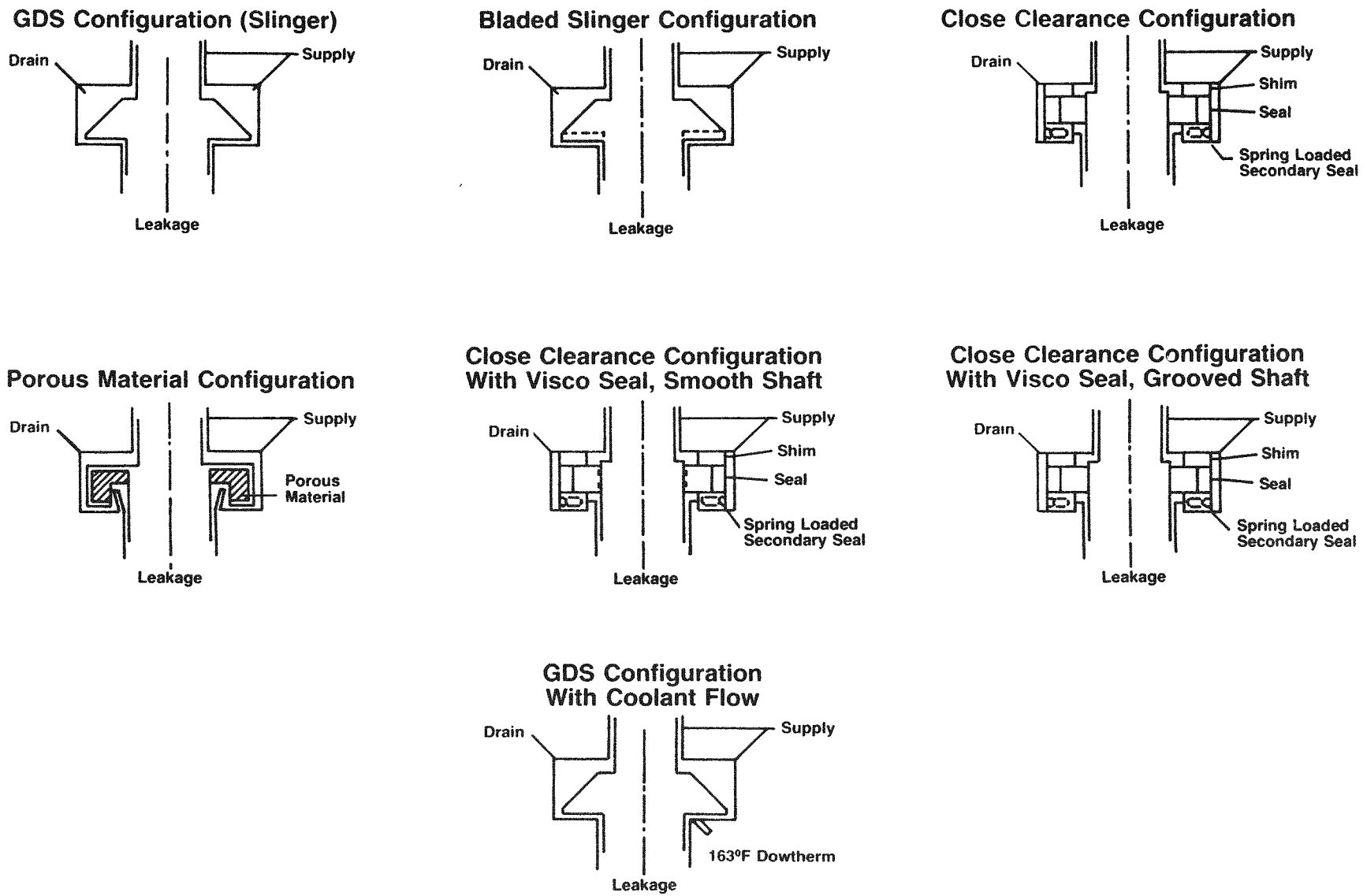

Figure 3.2.14

Hybrid Visco Seal

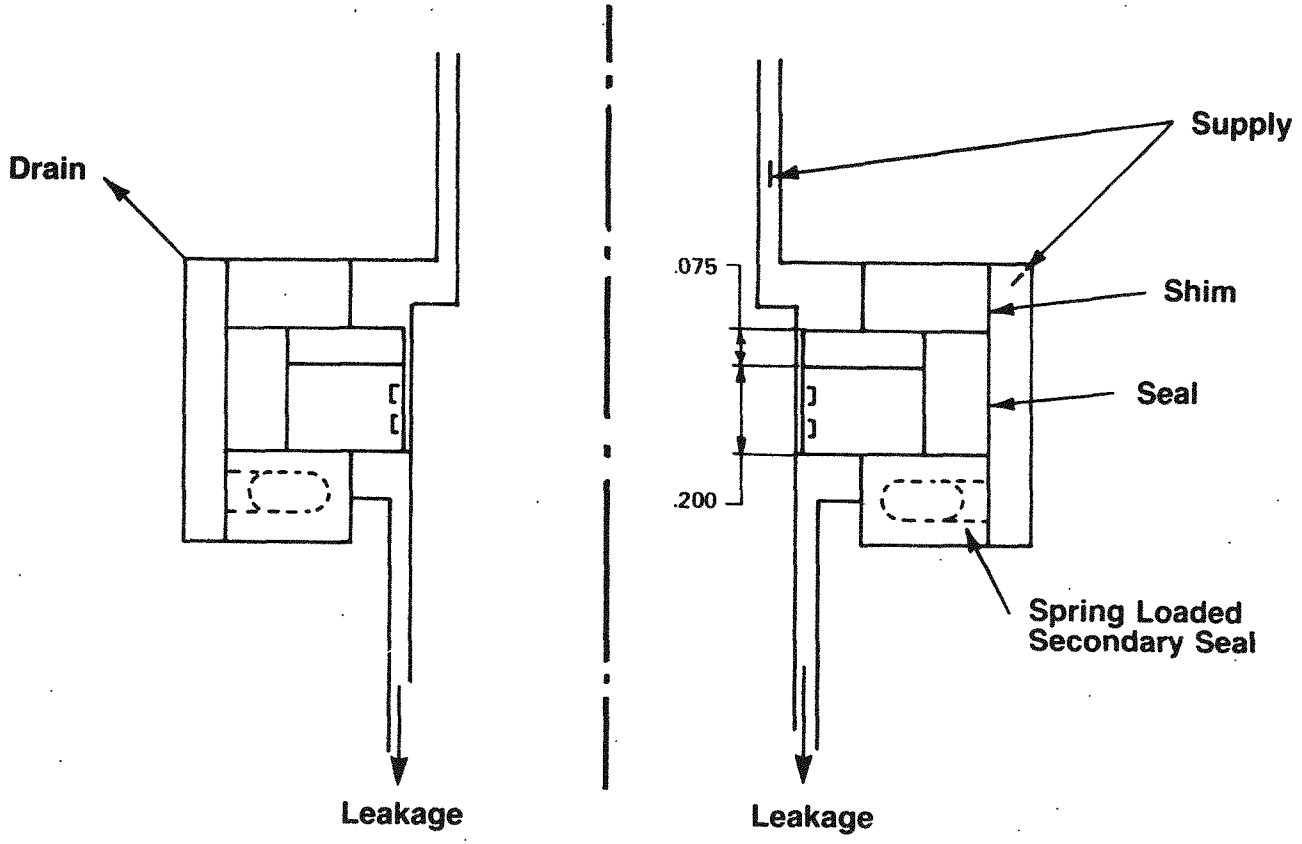

Figure 3.2.15

Hybrid Visco Seal

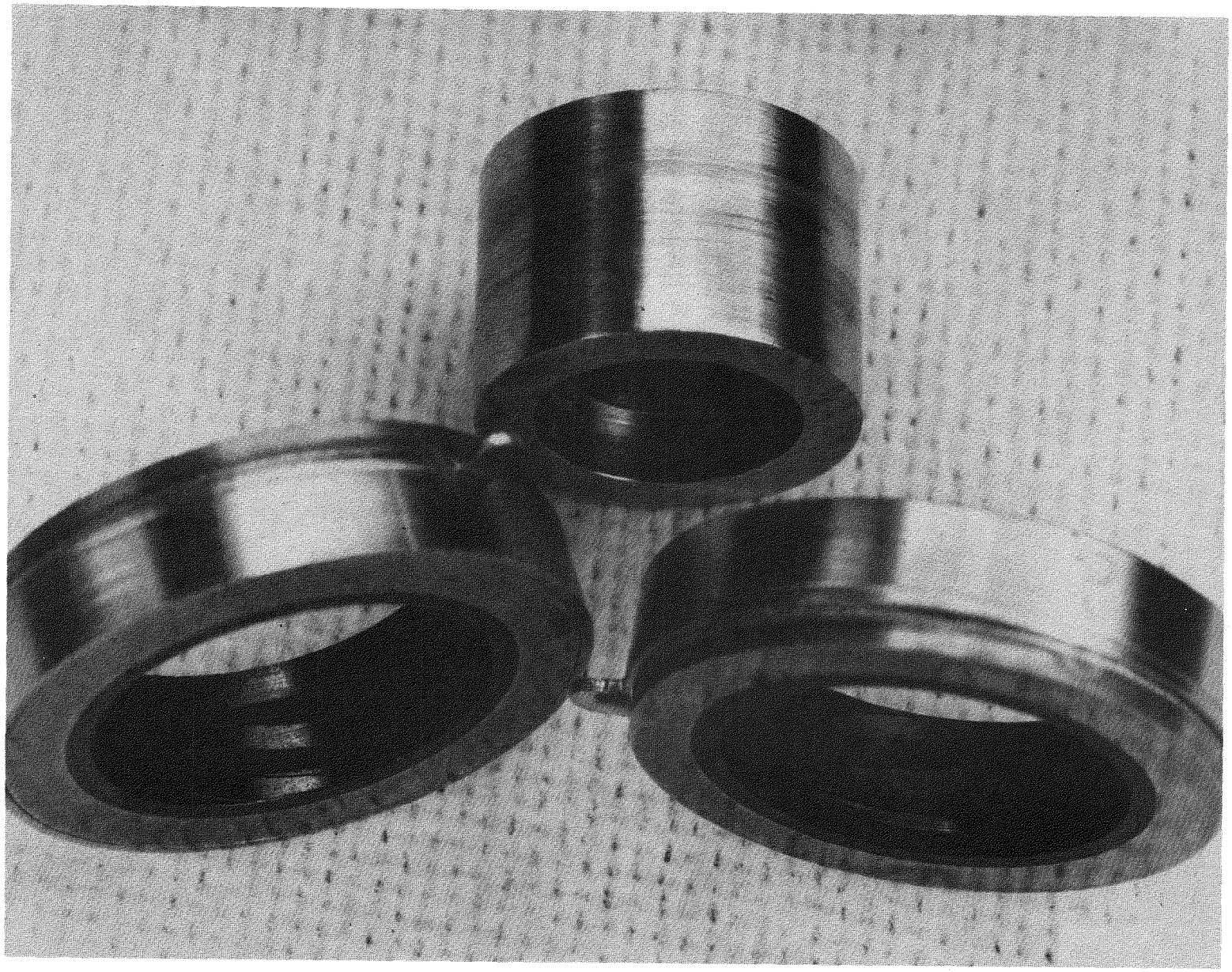

Figure 3.2.16

GDS Pump End Seal Leakage (.55 In. D.A.)

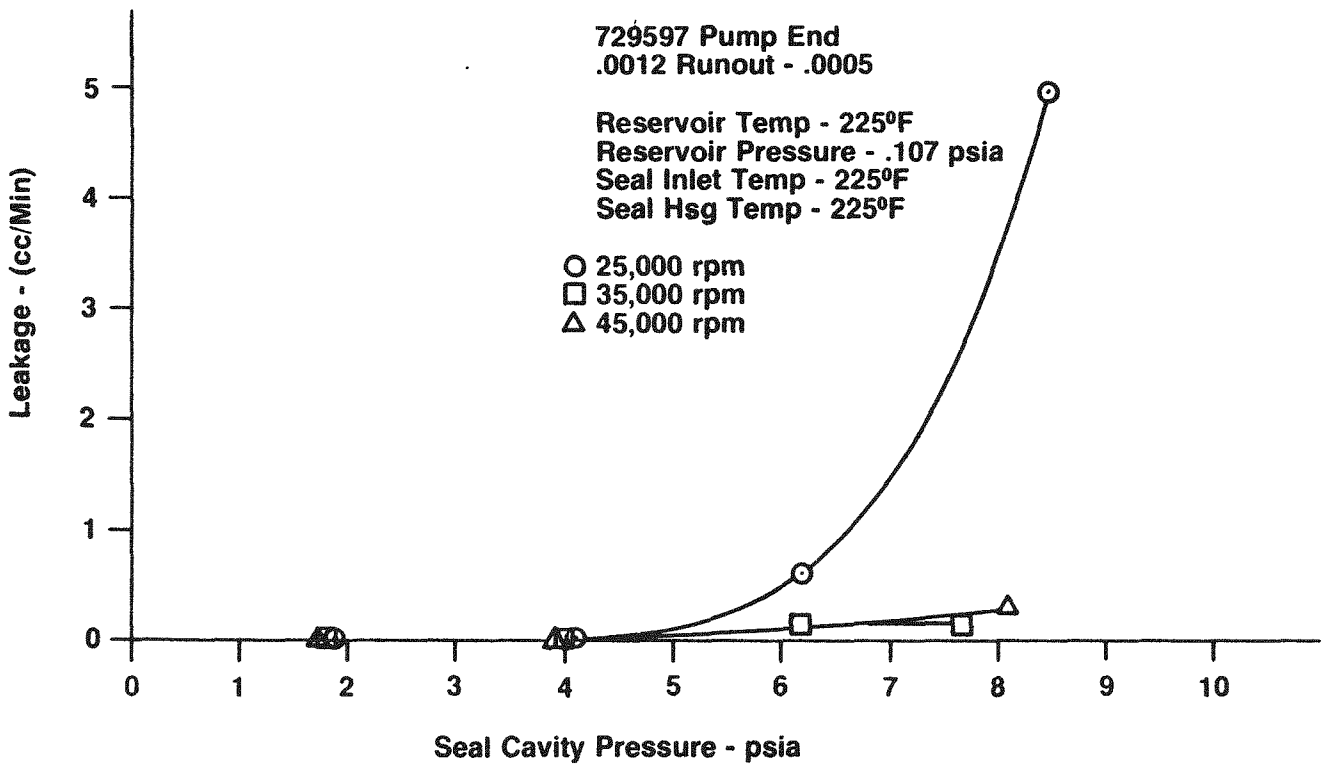

Figure 3.2.17

GDS Pump End Seal Power Loss (.55 In. Dia.)

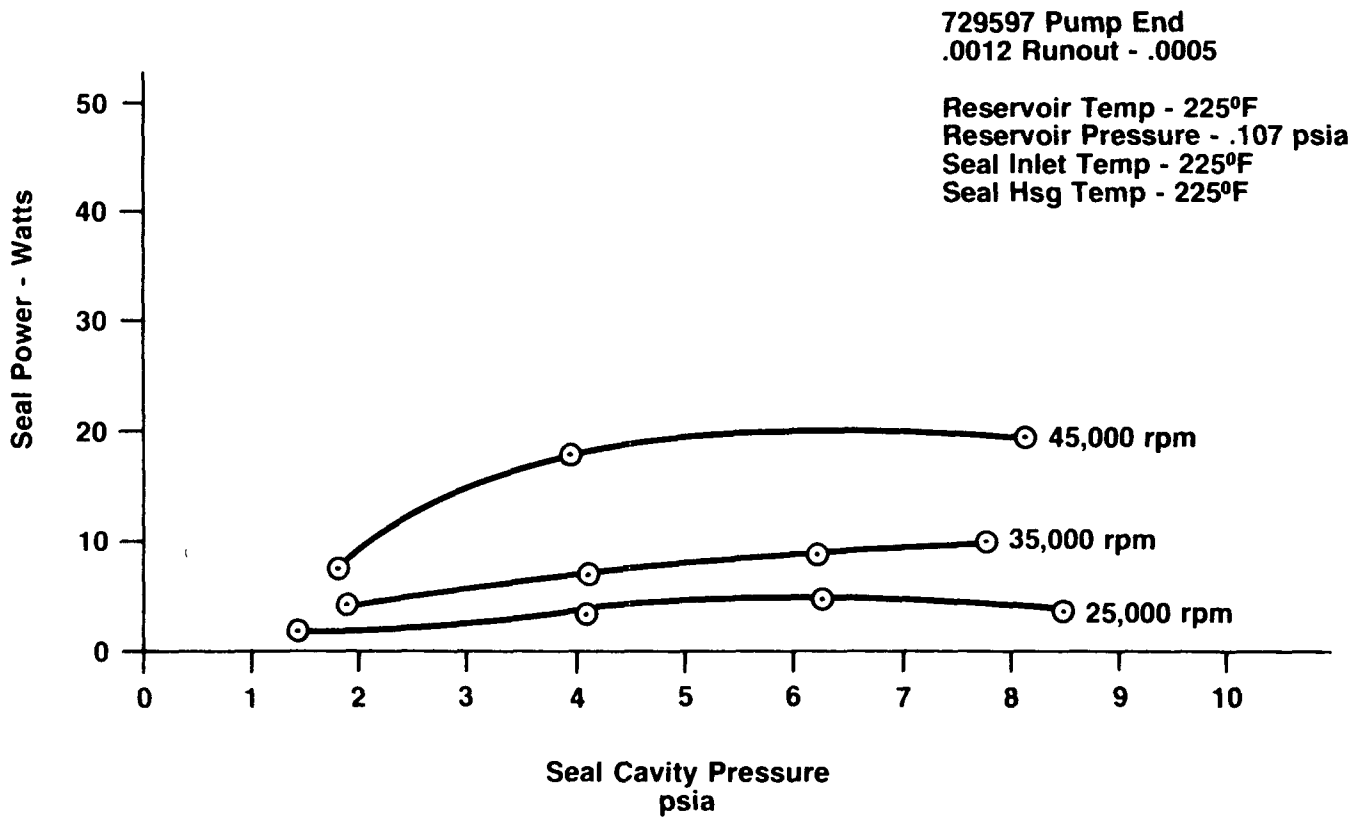

Figure 3.2.18

GDS Seal Power Loss (.725 In. Dia.)

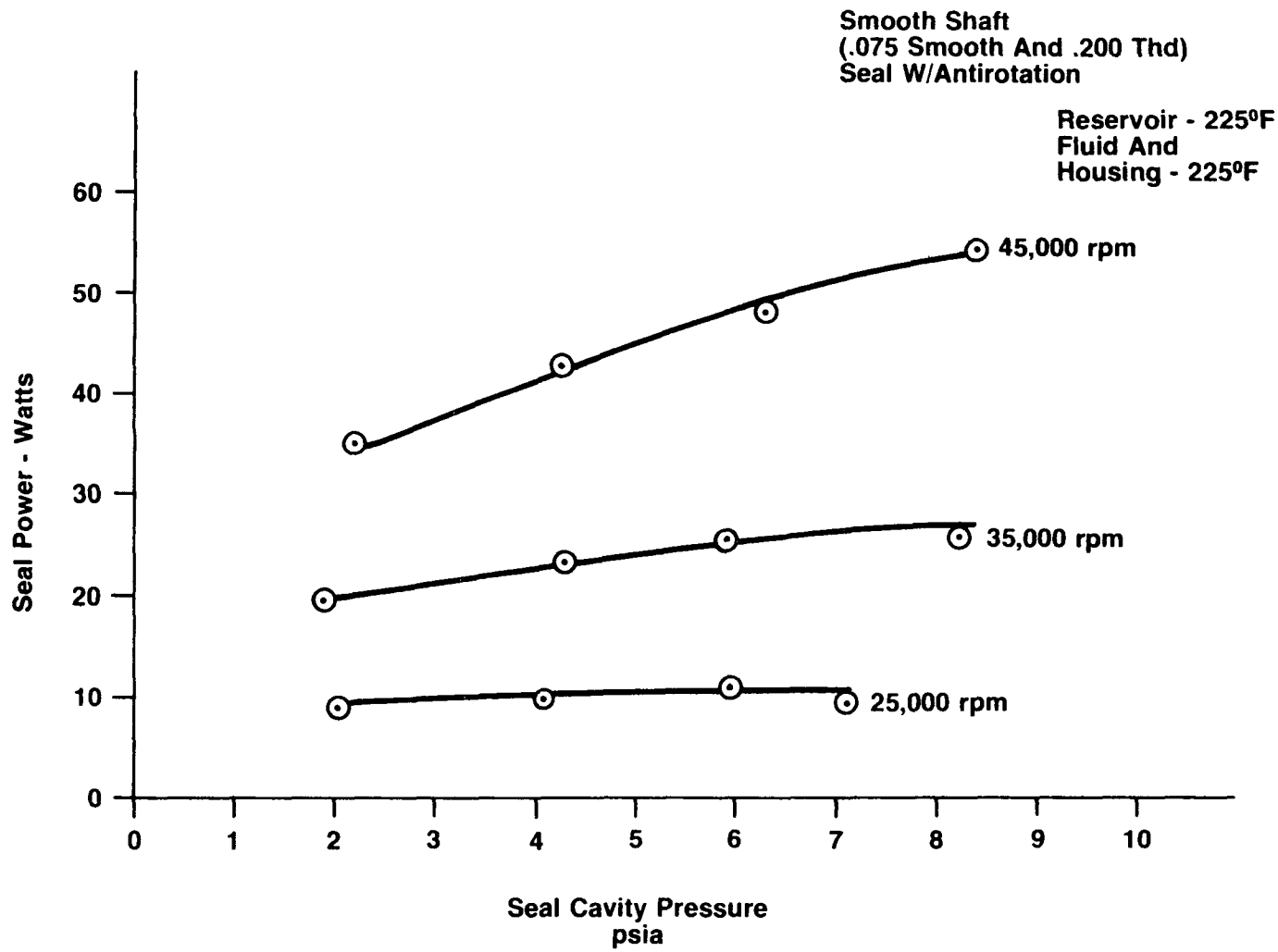

Figure 3.2.19

3.3 REGENERATOR

The regenerator is an overall counterflow, spirally wound, aluminum finned-tube configuration, mounted coaxially around the combined rotating unit. The heat exchanger is split into two separate cores as shown in Figure 3.3.1 to provide space for two ducts to carry plumbing to the CRU. This in turn provides a vacuum over the alternator and pump housings, thus precluding vapor condensation on these surfaces. This arrangement can be seen in Figure 3.3.2.

The spiral coils are stacked and joined together with 180° return bends for liquid transfer and are spaced and supported by means of .018 inch stainless steel baffle plates. This can be seen in Figure 3.3.3. The baffle plate assemblies are made by welding an inner and outer baffle to six equally spaced radial support channels. By machining grooves in the fins to correspond to the radial spokes the plates nest between fins thus ensuring at least six fins are contacting from coil-to-coil and providing a rigid structure. The baffle plates were shaped to match the spiral form of the coil and thus prevent vapor blow-by at ID and OD. A stiff plate was provided at the turbine end (see Figure 3.3.4) to support the complete assembly and allow it to be mounted to the transition housing with six tie bolts which preload the assembly. Excessive torsional distortion is prevented by keying the turbine end baffle plate to the outer housing, while the close fit of the baffle plates provides radial location.

Two different regenerator designs were tested during Phase II. The first configuration employed an integral, extrusion formed fin-tube design which eliminated the brazed joints of fin-to-tube that had been employed in Phase I. There was evidence in Phase I of potential corrosion at the braze joint from residual flux left after cleaning which could limit the life. Unfortunately, the integrally finned tube could not be obtained with the same fin density or tube size as the original brazed design. This led to considerably reduced area and hence reduction in performance although

the lower fin density did also reduce the vapor side pressure drop.

A development effort in Phase II demonstrated that with special techniques the higher fin density could be obtained in an integral fin-tube by machining rather than extrusion forming.

At the first disassembly in Phase II a brazed tube configuration was reinstalled to recover the performance capability of the high fin density, with the knowledge that the geometry could be duplicated for a flight design using appropriate machining techniques. This geometry was retained through the end of Phase II.

Table 3.3.1 summarizes the main geometry and performance differences of the two heat exchangers.

TABLE 3.3.1 REGENERATOR SUMMARY

TYPE	INTEGRAL FIN	BRAZED FIN
NO. OF ROWS	14	16
FINS PER INCH	11	14
FIN THICKNESS (in)	.018	.015
TUBE O.D. (in)	.375	.3125
EFFECTIVENSS (%)	92	97
CALCULATED/ ΔP (psid)	.007	.015
MEASURED/ ΔP (psid)	-	.021

An electric, in-line heat exchanger was incorporated into the regenerator liquid inlet line during Phase I in order to preheat the regenerator during start-up. This precluded jet condenser flood-out failures during start-up with the 45 nozzle jet condenser. After installation of the 90 nozzle jet condenser in Phase II it was found that the preheater was no longer necessary since system starts could be made without it. On the final build it was deleted to save the associated pressure drop of at least 8 psi.

A thermal shunt between liquid outlet and liquid inlet was also included in Phase I to preheat the first row of the regenerator above the local saturation temperature to prevent condensation. During experiments to measure the alternator temperature rise it was found that this also was not necessary for GDS operation since when the shunt was removed no jet condenser problems were experienced. However, the shunt was reinstalled in the final build since it is believed to be necessary in a flight system to maintain system inventory control. Some difficulties were experienced in the final build with jet condenser operation (see Section 4.2) indicating that the shunt may have been undersized. External electrical heating was applied to overcome the problem - a redesign would incorporate a larger shunt. It is believed that the problem resulted from cooler turbine outlet vapor temperatures due to the more efficient turbine.

The original design analysis of the regenerator indicated that 140 feet or 14 coils of high fin density tubing would be required to obtain an effectiveness of 0.95.

Sixteen (16) coils or 176 feet of high fin density tubing were installed in the final build. The indicated effectiveness of 97% appears to be consistent with the increase in area.

Split Regenerator Design

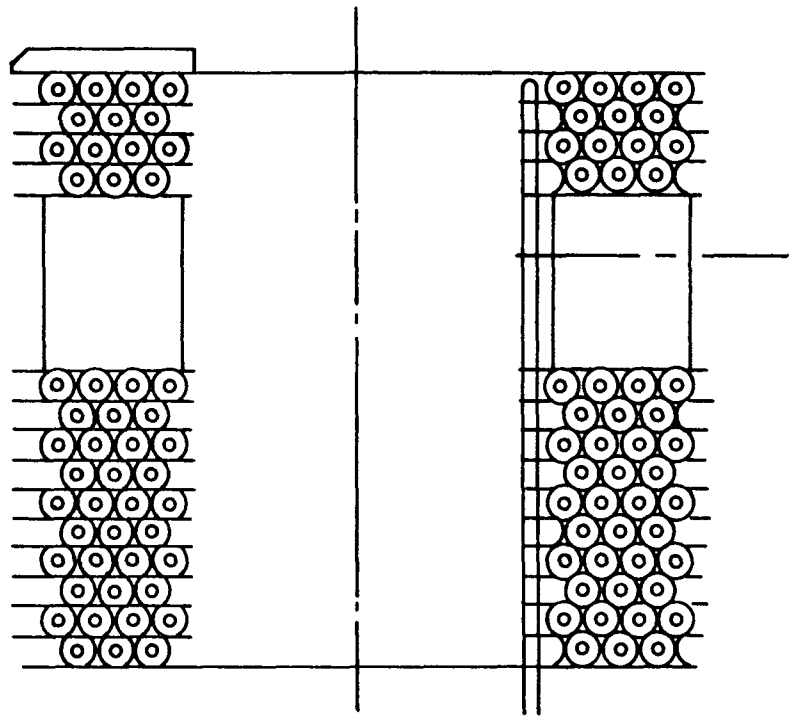

Figure 3.3.1

CRU/Regenerator Package

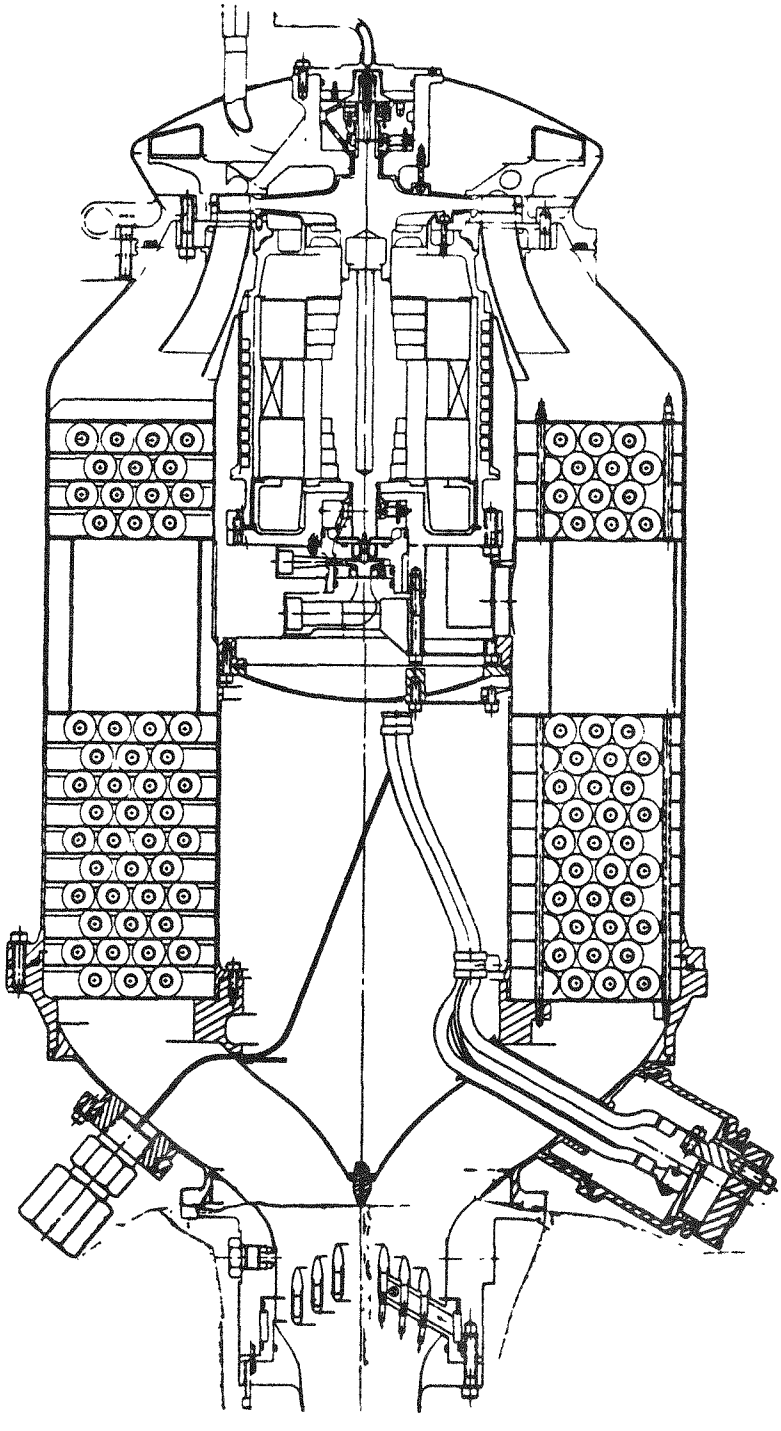

Figure 3.3.2

Regenerator

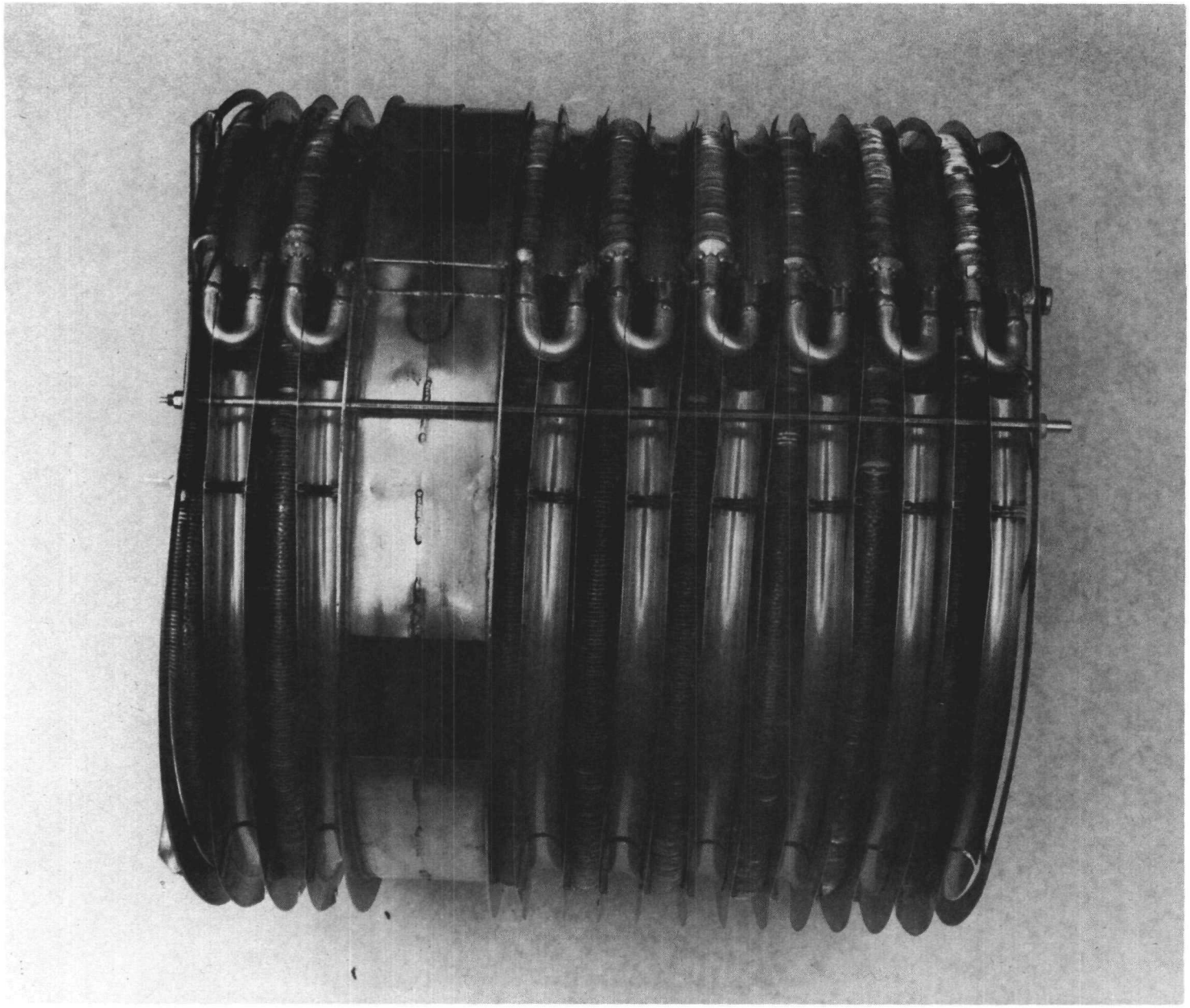

Figure 3.3.3

Regenerator

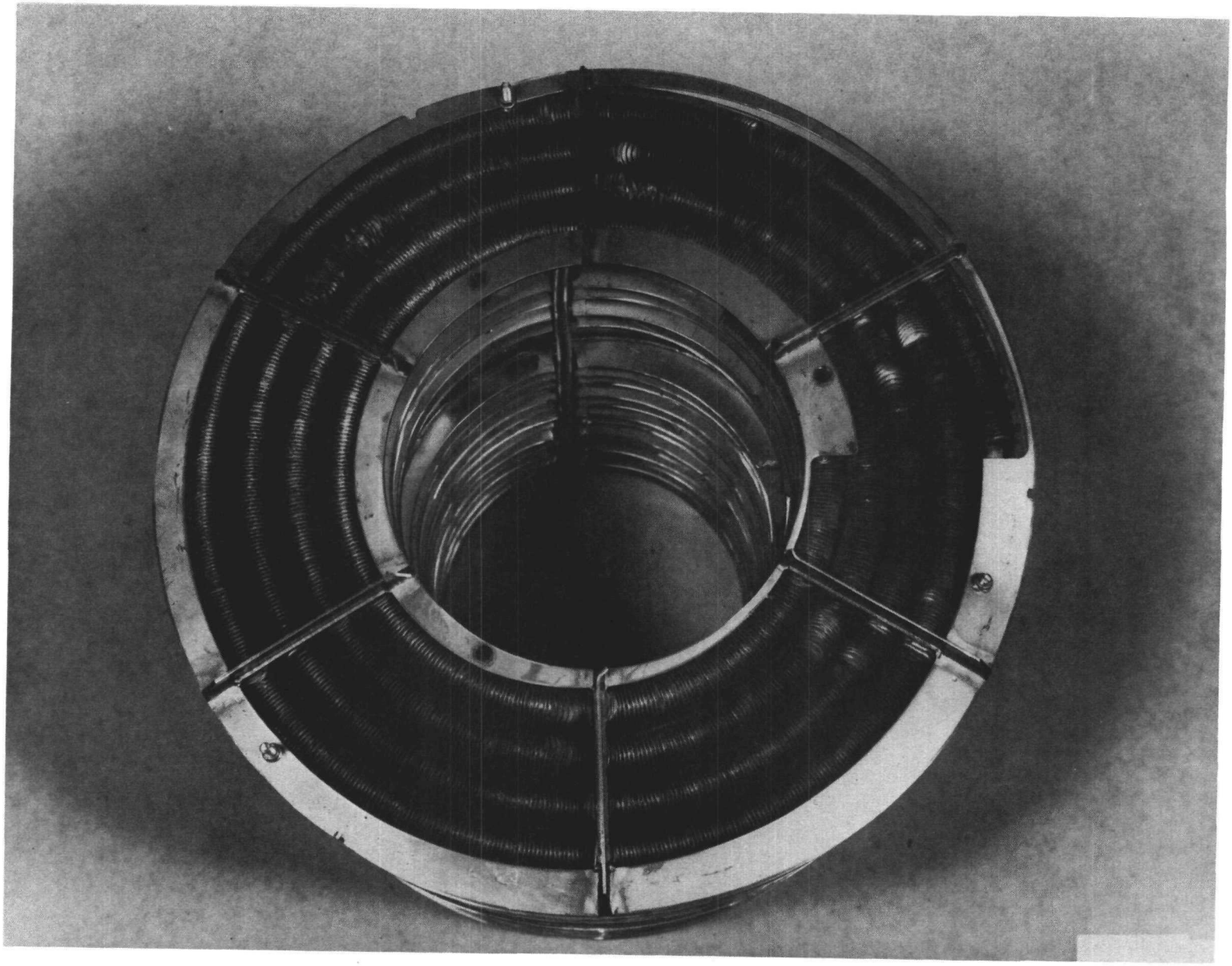

Figure 3.3.4

3.4 System Electrical Performance Analysis

The specification requirements of the DIPS system dictate the generation of 28V DC electric power to satisfy the needs of satellite users. In addition, the use of an isotope heat source leads to the requirement for very high efficiency to minimize the fuel requirements and hence cost for a given mission. For this reason considerable effort has been directed towards improving the overall system electrical efficiency, defined as:

$$\eta_{elec} = \frac{\text{useful DC output}}{\text{alternator shaft power}}$$

Figure 3.4.1 shows a schematic of the electrical system comprised of the alternator, which generates alternating current, and the controller which rectifies the AC and performs various control functions such as voltage regulation, speed control and filtering of the DC output to meet specified ripple levels.

Table 3.4.1 summarizes the electrical performance as the system evolved from the original flight conceptual design through Phase I GDS, development in Phase II to the final Phase II GDS testing.

Phase II development of the alternator was directed at recovering the efficiency back to the original value. This was achieved by optimizing the air gap and developing a manufacturing technique to prevent smearing of the rotor pole tip laminations, thereby reducing eddy current losses.

Another effect of removing the capacitors was to reduce the feeder losses in the cables which ran from the alternator to the controller. During Phase I these cables brought the power outside the vacuum chamber wall to allow AC current measurement with current transformers and then re-entered to return to the controller. Figure 3.4.2 shows the feeder losses obtained by measuring AC power both at the controller and the alternator output connector. The first measurement was made at the end of Phase I and was used to determine effective DC output. It was theorized that a flight design feeder loss could be held to about 7 watts and that the difference between the measured loss and 7 watts could therefore be added to the useful output after being corrected for controller efficiency.

In order to simplify controller development in Phase II the controller was moved outside the chamber. As a result of the move, the cables were shortened. The external cables also operated at lower temperatures. This resulted in the lower loss value measured on 8/14/79, with tuning capacitors included. Also shown in Figure 3.4.2 is the feeder loss as a function of AC power with no tuning capacitors. These data were used for feeder loss correction for

Table 3.4.1 Electrical Performance Summary

	Original FCD Low Speed Rectifiers	GDS Phase I Low Speed Rectifiers	FCD Phase I Ion-Implant Rectifiers	High Speed Rectifiers With Capacitors	High Speed Rectifiers w/o Capacitors	Ion-Implant Rectifiers	Projection Of Heated Ion-Implant Rect.*	(12) Ion-Implant Reduced Ripple	Final GDS Phase II
Shaft Power	1523	1365	1524	1331	1345	1343	1343	1359	1470
AC Out	1456	1285	1425	1249	1254	1252	1252	1268	1387
Tuning Capacitors	Yes	Yes	Yes	Yes	No	No	No	No	No
Field Power	25	11*	8	5	11	11	11	13	12
Alt. Eff.	.94*	.934*	.93*	.935*	.925*	.925*	.925*	.924*	.936*
Feeder Loss	0	107*	7	84	62	67	67	74	95.⁰
Controller In	1456	1178	1418	1165	1192	1185	1185	1194	1292
No. Of Rectifiers	6	6	6	6	6	6	6	12	18
Rectif. Loss	106	76	80	85	79	64	54	54	63
Rectif. Eff.	.927	.935	.944	.927	.934	.946	.954	.955	.951
Choke Loss	0	0	0	0	0	0	0	30	34
Ripple	0.1%	10%	0.1%	10%	10%	10%	10%	0.1%	0.1%
Filter & Controller	25	5‡*	30	16	11	20	20	7	25
Controller DC Output (Useful O/P & Field Power)	1325	1097	1308	1064	1102	1101	1111	1103	1170
Controller Loss	131	81	110	101	90	84	74	91	122
Controller Eff.	.91	.931	.922	.913	.924	.929	.938	.924	.906
Useful O/P	1300	1086	1300	1059	1091	1090	1100	1090	1158
Effective Feeder DC†	0	101	0	70	51	56	56	62	81
Total Customer 28V DC	1300	1187	1300	1129	1142	1146	1156	1152	1239
Overall Elec Eff	.854	.870	.853	.848	.849	.853	.861	.848	.843

† Based On FCD Feeder Loss Of 7W
‡ Most Of Controller De-Activated
* Estimated
⁰ New Feeder Installation

all the development testing in Phase II. The final build of the GDS had the cables rearranged again and the losses were measured to be slightly higher. This result was probably due to the changed heat dissipation characteristics of the cables since the resistance changes with temperature.

Feeder losses have to be known accurately in order to determine the effective DC output. This is calculated by presuming a 7 watt loss for a flight system feeder and subtracting that value from the measured loss. The remainder is multiplied by the apparent controller efficiency and added to the measured DC output.

One projected performance improvement noted at the end of Phase I was the increase of rectification efficiency. During Phase II development rectifier improvement was investigated carefully. The original rectifiers used in Phase I were of the slow speed type. High speed rectifiers were next investigated and finally the ion-implant type. The results of these tests are shown in Table 3.4.1.

The "slow-speed" rectifier has a relatively long "recovery time" between the point where current begins to flow in the reverse direction and the time that the rectifier switches to the non-conductive state. The "snap-off" time, however, from this point to zero current flow is very rapid and voltage spikes are induced as a result. The high speed rectifiers on the other hand have a very short recovery time but relatively long snap-off time and voltage spikes are greatly reduced. This results in an improvement in long term rectifier efficiency. The voltage spikes of the slow speed rectifiers can cause problems requiring capacitors for correction. The ion-implant rectifier is a 'high-speed' type with an improved doping technique which reduces forward voltage drop and hence improves efficiency. The data shows the low and the high speed rectifiers to have about the same efficiency while the ion-implant type showed a significant improvement.

Investigation of the manufacturer's data on the rectifiers showed potential improvement to be gained from heating the rectifiers.

The development tests were performed outside the vacuum chamber and the junction temperatures were relatively low. The projected improvement is shown in Table 3.4.1. Tests were performed to try to heat the rectifiers to 100°C (the design operating temperature) but the claimed improvement did not materialize. It is suspected that the junction temperature did not reach the desired value because of the heat dissipation through the large cables. Temperatures were measured on the support plate rather than at the junction. It was found during this development that doubling the number of rectifiers resulted in reduced rectifier losses due to reduced current, but when 18 were used the losses increased slightly. It was believed that the slightly higher losses resulted from less self-heating. The final design employed 18 relatively low temperature ion-implanted rectifiers. The decision to use 18 was based on the presumption that the temperature of the rectifiers in the FSCD could be kept high and the losses minimized.

In Phase II the controller was modified to reduce the ripple in the DC output. The DC output from the Phase I controller had almost 10% ripple content while the specification was for 0.1%. Large chokes and capacitors were added to reduce the ripple. Several iterations were needed to achieve low ripple without excessively high losses. The final GDS configuration attained a level of less than 0.1%.

The controller was outside the chamber during the final operation so its waste heat was not available for recovery by the system (a slight performance penalty). During the development testing, considerable instrumentation difficulty was experienced when trying to differentiate component losses in the controller. Power in and power out of the controller was measured reliably, but there is some doubt on the reported controller component losses.

Electrical System Schematic

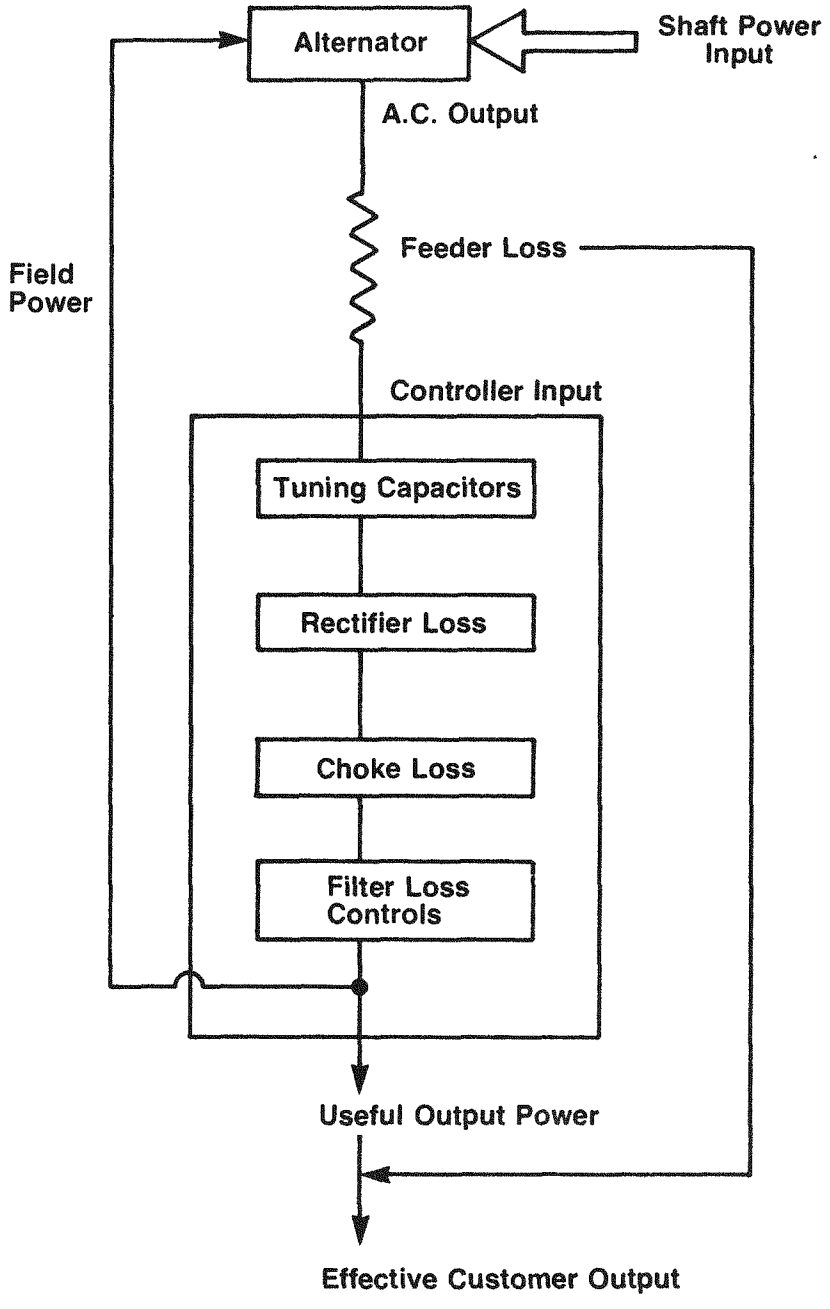

Figure 3.4.1

Feeder Losses

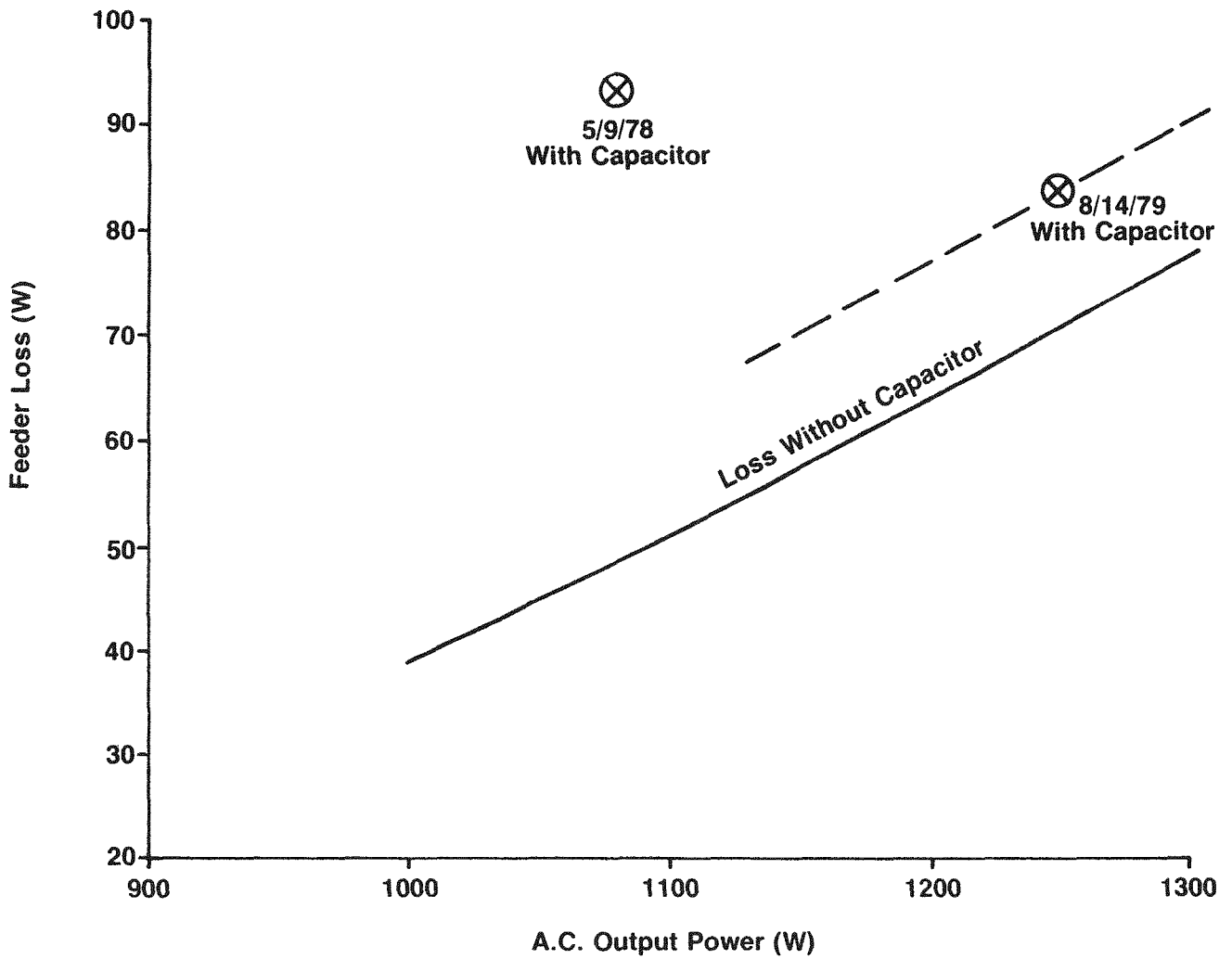

Figure 3.4.2

3.5 System Insulation

Theoretical calculations of the insulation requirements of the Power Conversion System (PCS) showed that one layer of HITCO TG15000 bulk insulation with a thickness of 0.65 inches, covered with three aluminum radiation foils would limit the PCS heat loss to 24 Btu/hr. The use of 2 inches of TG15000 and three foils on the high temperature plumbing would limit that heat loss to an additional 22 Btu/hr.

TG 15000 insulation was not available during Phase I and the only readily available alternate was Carborundum 'Lo-Con' Fibrefrax. This material has a manufacturer's value of conductivity of 0.011 Btu/hr. ft. ^{o}F compared to 0.0078 for TG15000. Aluminum foils were added as radiation shields.

As reported in the Phase I test report (70 KIPS-33 (AER 1516)), excessive turbine temperature drop was noted in the Phase I configuration. This was thought to be mainly due to seal leakage, though lower insulation performance than design was suspected.

At the first rebuild in Phase II, when new seals were installed, TG15000 with multiple radiation foils was installed as in the flight configuration. It was found that the large turbine temperature drop still existed even though the seals were no longer leaking. This lead to the suspicion that significant heat was being lost through the insulation and two additional layers of TG15000 were added. Some improvement was noted. Since all the available TG15000 had been used, eight additional layers of Fibrefrax were added. The turbine temperature drop was reduced from about 177°F to about 149°F, though this value was still considerably higher than the anticipated value of about 122°F.

As a consequence of these results, an insulation investigation was embarked upon and is reported in detail in report 80-DIPS-31 (AER 1833). The outcome of the investigation was the installation of ten layers of TG15000 on the final build of the GDS because of poor success with demonstrating the application of radiation foils. The final assembly of the GDS unit with insulation is shown in Figure 3.5.1. Test results for measured values of TG15000 and Fibrefrax thermal conductivity are shown in Figure 3.5.2.

GDS Insulation Installation

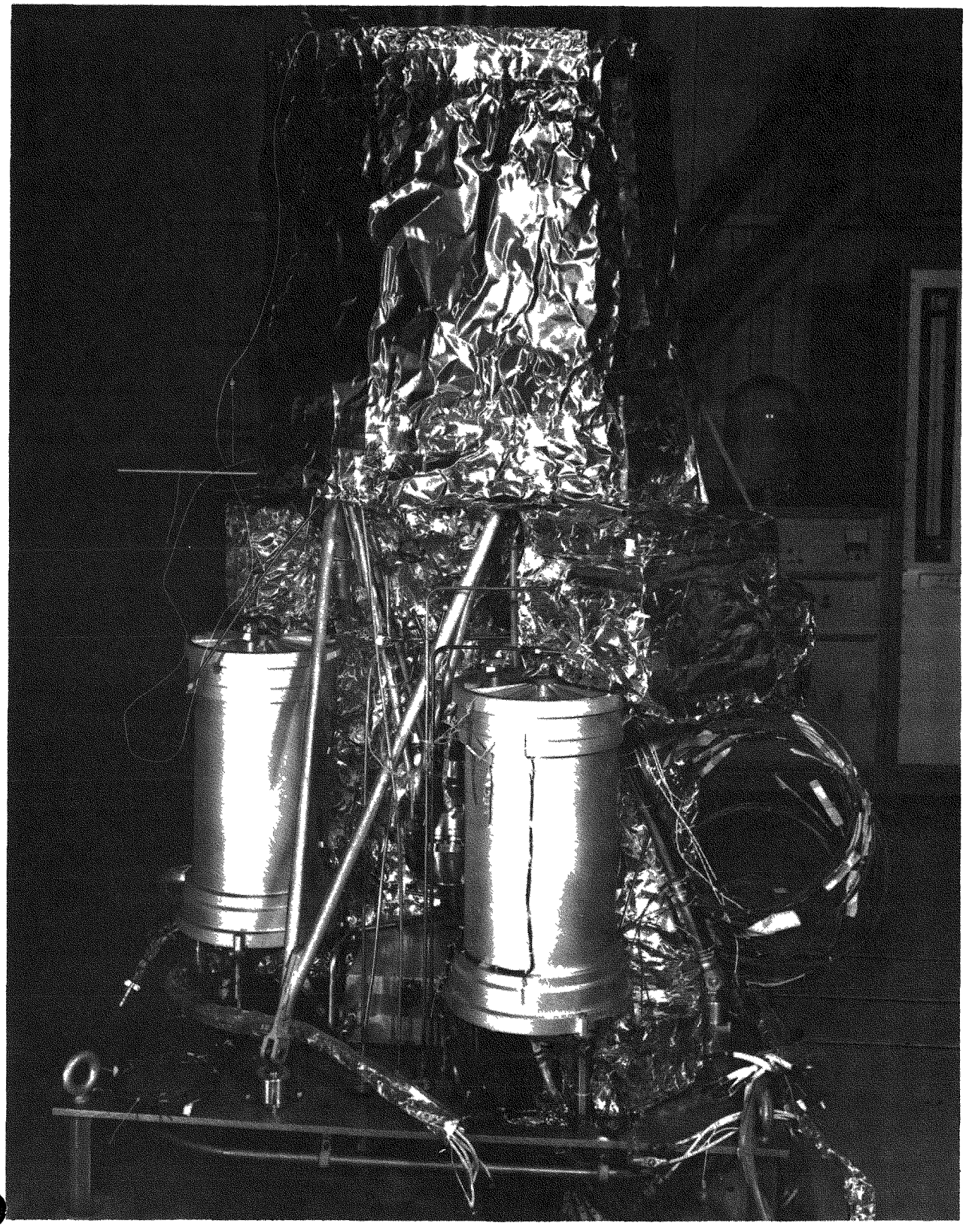

Figure 3.5.1

Measured Conductivity For Fibrefrax And TG15000

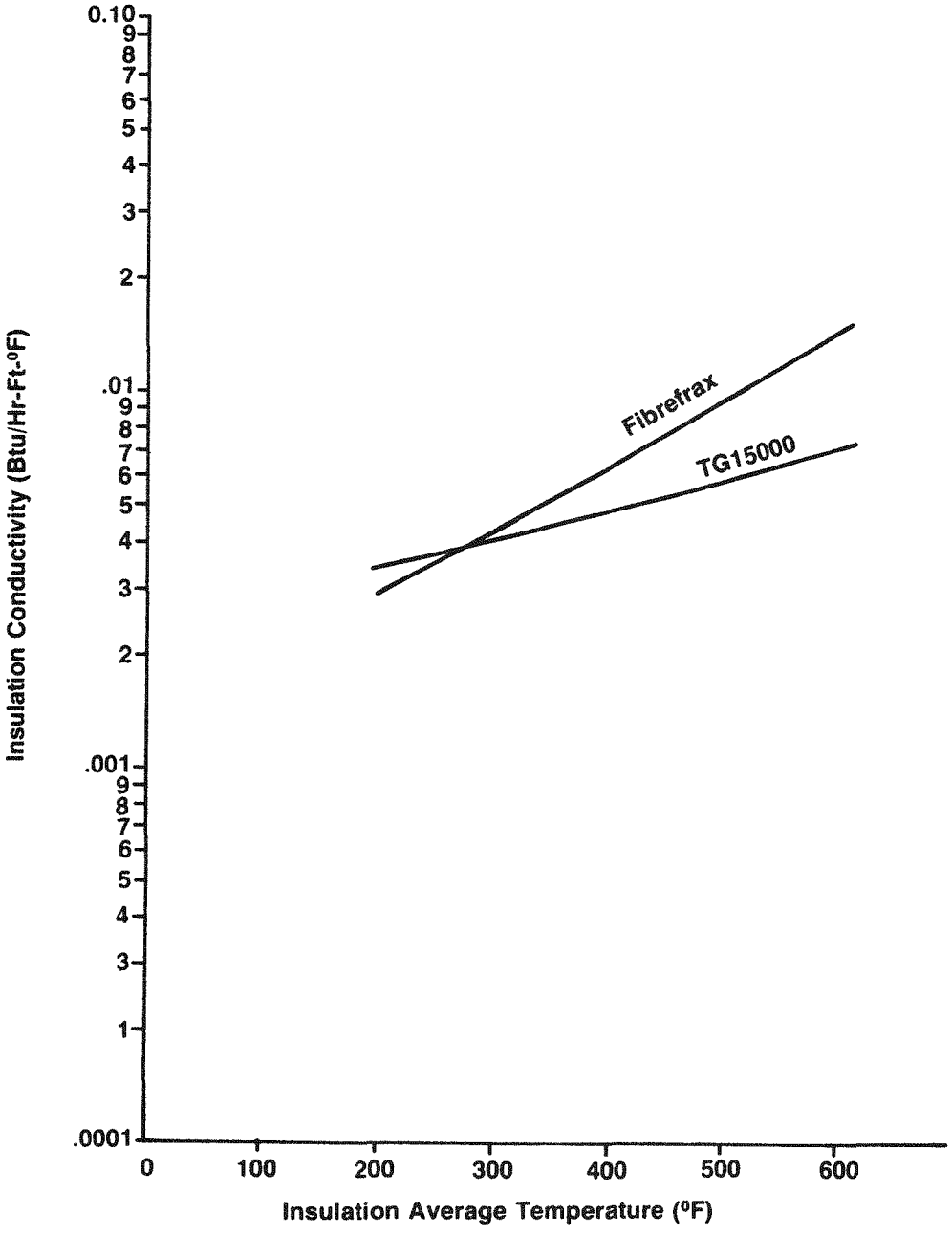

Figure 3.5.2

3.6 Condensing Heat Exchanger

System waste heat is rejected by condensing the slightly superheated regenerator exhaust vapor on the surface of subcooled liquid jets in the jet condenser. A liquid radiator is then used in the flight design to reject the waste heat to space; in the GDS a liquid-to-liquid heat exchanger was used.

A jet condenser is employed to allow satisfactory liquid-vapor interface control in all attitudes and in zero-g conditions and minimal vapor side pressure drop. In this type of condenser the low pressure vapor is ducted into a funnel where multiple subcooled higher velocity liquid jets aimed at the throat of the vapor funnel are injected into the vapor. The vapor condenses on the subcooled jets which are heated by the vapor condensation but remain subcooled. The jets combine into one stream at the focal point and pass through the throat and into the diffuser. In the diffuser the high velocity stream undergoes a sudden expansion and fills the entire cross section. There is a loss of total pressure in the sudden expansion but a gain in static pressure as some of the dynamic pressure is recovered. Further static pressure recovery occurs as the liquid passes through the diffuser. The amount of dynamic pressure recovery obtainable is determined by the diameter ratio of the combined liquid jets and throat diameter as well as the diameter ratio of the diffuser. At maximum recovery, the sudden expansion occurs just downstream of the throat while at minimum recovery the sudden expansion occurs far downstream at the end of the diffuser. The static outlet pressure is determined by the system accumulator located downstream of the jet condenser and is set for the worst case operating conditions to provide sufficient margin to preclude the interface passing backwards through the throat. If the interface does pass upstream through the throat, the sudden expansion occurs in a converging section and the condenser suffers from a "flood-out" failure.

The jet condenser consists of three major sections; the liquid injector, the vapor funnel and the throat/diffuser section. These are combined into the jet condenser assembly shown in Figure 3.6.1. This assembly, in turn, is mounted at the outlet end of the transition housing connecting the regenerator to the jet condenser. At the diffuser outlet the diffuser is connected to the system accumulator. This can be seen in the system layout shown in Figure 3.6.2.

The liquid injector is made up of three hollow concentric rings supported by three equally-spaced, elliptically shaped, hollow, radial struts. These transport the cold inlet flow from ring-to-ring and in turn are fed from an annulus on the inside of the housing. The injector nozzles are threaded into the annular rings and epoxied in place to provide a seal. The number of nozzles in each ring is selected to give equal condensing area around each jet.

The vapor funnel provides a boundary for the mixing and condensation process. The funnel is smoothly blended from the transition housing and provides a vapor flow area at the nozzle exit plane to give a Mach 0.6 vapor velocity at design point conditions. This requirement was based upon testing performed with the AEC loop jet condenser. The funnel wall then transitions into two simple cones, sized to allow adequate space between the outer circle of liquid jets and the wall.

The jet condenser throat is located at the end of the funnel just downstream of the focal point of the liquid jets. The liquid jets combine into a single stream to pass through the throat which is .133 inches in diameter; the focal point can be clearly seen in Figure 3.6.3 which shows a 90 nozzle jet condenser after each nozzle has been individually focused. The throat is a straight section .050 inches long followed immediately downstream by a narrow .029 inch wide slot through which the bearing scavenge fluid flows. The scavenge flows from turbine and pump bearing cavities enter separately to preclude any interaction. Downstream of the scavenge port is the compound diffuser; the primary diffuser is 0.700 inches long with a 2° included angle and the secondary diffuser is 2.90 inches long with a 6° included angle giving a total diffuser area ratio of about 12:1.

The initial Phase I design was based upon extrapolation of data from the 6 Kwe jet condenser and employed 45 sharp edged orifices which gave a well collimated, easily focused stream. Although high recoveries were obtained because of the high velocity coefficient of the nozzles, performance was well below the design value. Increased jet Reynold's numbers resulted in improved performance and it was concluded

that the jet surface from the sharp edged orifice was too smooth for effective liquid-vapor interaction.

As a consequence, nozzles with a length to diameter ratio (L/D) of about 4 were tested to generate a rougher surfaced jet and performance improvements over the sharp edged orifice design were obtained. Vapor pressures were still higher then design and the nozzle discharge coefficients were lower than expected. The results for the 45 nozzle showerhead with nozzles having an L/D = 4 are shown in Table 3.6.1.

These data were obtained by using a manometer poisoned by non-condensible gases for measuring pressure, since at that time reliable pressure transducers were not available.

Air sensitivity tests were also performed at this time on the 45 nozzle jet condenser and showed critical concentrations before flood-outs of about 7×10^{-5} moles air/mole Dowtherm.

A mathematical model of the condensation process was developed along with an experimental investigation of single nozzle designs operating with steam. This development has been reported in detail in Appendix A to Volume II and III of the Phase II plan (AER 1579). The ultimate outcome was a design employing 90 nozzles with a diameter of 0.010 inches and an L/D=4. The nozzle length was selected to minimize frictional pressure drop while being long enough to prevent instability associated with the jet reattaching to the nozzle wall.

The 90 nozzle design is summarized in Table 3.6.2.

Table 3.6.1 45 Nozzle Test Results

	m_{vapor} (lb/sec)	m_{liquid} (lb/sec)	P_{liquid} (psia)	P_{vap} (psia)
Design	.0306	.2754	80	.10
Test	.0306	.2754	100	.118

Table 3.6.2 Jet Condenser Geometry

Length	L	= 10 In.
Mixture Chamber Pressure	P_{mix}	= 0.083 psia
Number Of Nozzles	N	= 90
Orifice Diameter	D_o	= 0.100 In.
Effective Vapor Diameter At The Liquid Injector	D_{mix}	= 3.14 In.
Diameter At Liquid Injector	D_l	= 4.00 In.
Number Of Rings	n	= 3
Throat Diameter	d_t	= 0.133 In.

Distribution (By Ring)	No. Of Nozzles	Diameter (In.)	Angle To Axis (Degrees)
Outer	42	2.808	8^0 12'
Middle	30	1.932	5^0 31'
Inner	18	1.014	2^0 49'

Vapor Velocity At Liquid Injector	V_v	= 278.3 Ft/Sec (M=.6)
Liquid Velocity	V_l	= 103.0 Ft/sec (Re_D=8140)

Diffuser	Length (In.)	Half Angle (Degrees)
Primary	0.700	1
Secondary	2.900	3

Pressure Recovery	= 35%
Liquid Side Pressure Drop	= 1.9 psid

The original single nozzles used for steam testing were manufactured in aluminum using a drilling technique. This technique could not be duplicated in stainless steel and Electrical Discharge Machining (EDM) was employed. Although the hole was tapered and rough, equivalent performance to the drilled aluminum nozzles was obtained on the single nozzle rig. Laser drilling was also tried but the test pieces had very poor surface finishes and rough inlet and outlet diameters.

Late in Phase I a 90 nozzle injector was installed in the GDS using EDM type .010 inch nozzles. Repeated start attempts were unsuccessful and the 45 nozzle assembly was reinstalled. Although the individual nozzles of the 90 nozzle assembly had been checked there was some directional instability in some of the nozzles, making adequate focus impossible.

It was realized that the manufacturing technique for the .010 inch nozzles was inadequate and that an improved reliable method was needed. A Phase II development effort addressed this problem.

3.6.1 Jet Condenser Development

The Phase II development was directed mainly at machining .010 inch nozzles. The final selected technique employed artificial sapphire inserts from a commercial vendor. Sample orifices of 0.0085 inches were sectioned for inspection and mounted in nozzle assemblies for testing. The single nozzle test rig was converted for use with Dowtherm so that direct heat transfer data could be obtained. The sapphire sample nozzles were tested on this rig, Figure 3.6.4 and found to be thermally and hydraulically very good. On this basis 300 nozzles with jewels installed were ordered. The nozzles were manufactured by pressing the jewel into the end of a threaded tube followed by a swaging operation to hold the jewel in place. See Figure 3.6.5. Pressure tests indicated no liquid leakage around the o.d. of the jewel.

Each individual nozzle was flow-checked and had its thermal performance measured before installation into a nozzle ring. Two complete nozzle rings were assembled, one for use in the GDS and one for use in the jet condenser vibration test.

A complete nozzle assembly is shown in Figure 3.6.6 and a close-up individual nozzles in Figure 3.6.7.

Single nozzles of different configurations were tested on the Dowtherm rig to re-evaluate their thermal and hydraulic performance. Results on the jet condenser test rig in Phase I had indicated superior thermal performance for long L/D nozzles at the expense of hydraulic pressure drop. Limited steam testing had indicated the possibility that a sharp-edge orifice jet was about the same if not marginally better than a jet of the same size issuing from an .0145 inch long L/D nozzle.

Testing of a .0145 inch sharp edged orifice (.0114 jet diameter) on the Dowtherm rig indicated worse thermal performance than the .010 inch long L/D nozzles but sharp edged orifices having a jet diameter of .010 inch (.0127 inch hole diameter) were not tested on Dowtherm to allow a direct comparison of thermal performance.

The discharge coefficients of the long L/D nozzles were quite low due to the frictional losses in the nozzles. The measured discharge coefficients indicated pressure losses of close to 20 psi for the .010 inch nozzles which is consistant with calculated losses for internal friction. This 20 psi additional pressure drop is equivalent to about 0.14% points in system efficiency. Since the sharp edged orifices of the same jet diameter were not tested, it is known whether the trade-off between pump work and condenser pressure was made correctly. The 0.14% points in system efficiency would be equivalent to about 0.008 psia in jet condenser vapor pressure, so this represents the minimum improvement necessary to justify the long L/D nozzles. It was apparent from jet condenser component testing that the selection of .010 nozzles over .0145 inch nozzles was beneficial. There was a slight increase in liquid side pressure drop but the vapor pressure, as indicated by a manometer, dropped from 0.118 to 0.1 psia at the same flow ratio; this represents a 0.27% points improvement in efficiency. It is recommended that any future design include a thorough evaluation of the benefits of the two types of nozzle to ensure that the optimum version is incorporated.

Consideration of the hydraulic characteristics of the injector indicate significant improvement by changing nozzle configuration.

The 90 nozzle jet condenser with jewel nozzles was installed on the GDS in November 1979 and showed operating characteristics superior to the 45 nozzle configuration. Maximum recovery capabilities were higher with values as high as 44% being measured before flood-out. The condenser was never run at recoveries higher than 35% during system operation to provide adequate margin for worst case operating conditions which occurs after the CRU has slowed down to design speed from overspeed operation. This operating condition results in the maximum required recovery because of the volumetric expansion of the fluid resulting from the higher operating temperatures at overspeed.

Flood-out failure of the 45 nozzle jet condenser had invariably occurred during system flow initiation; the apparent cause of this phenomenon was condensate dripping from the initially cold regenerator and interrupting the nozzle flows. An electrical preheater had been added to preclude this problem. The 90 nozzle jet condenser was found to be capable of a start cycle without the necessity of a regenerator preheater.

Simulated flight system starts, in which all the valves were left open before the start pump was activated, were also repeatedly made with the 90 nozzle condenser. These demonstrations allowed the regenerator preheater to be removed for the final build, thus saving an excess pressure drop of 8 psid.

Considerable effort was spent trying to establish the sensitivity of the 90 nozzle jet condenser to non-condensable gases. Measurement of gas concentrations performed in Phase I on the jet condenser test rig used a condensation bottle scheme for levels of 30-100 ppm. This scheme allowed vapor condensation to occur in a bottle of known volume at system pressure until the inflow of non-condensables poisoned the condensation process and condensation ceased. Measurement of resultant liquid volumes allowed inlet gas concentration to be calculated.

For the GDS, however, operation inside a vacuum chamber with isolation valves on all potential air in-leakage lines meant that residual gas levels

were expected to be low, resulting only from component outgassing, imperfectly de-aerated fluid, and thermal degradation. In addition, it was expected that the jet condenser operation would be sensitive to hydrogen concentrations of less than 10 ppm, and the testing was aimed at measurements of 10 ppm or less.

It was felt at the onset of the testing that the bottle method of measurement would be insufficiently accurate for measurements of concentrations perhaps as low as 1-2 ppm. A McLeod gauge was therefore incorporated in place of the condensing bottle in order to provide a magnification effect on the non-condensable gases collected during condensation. The test schematic is shown in Figure 3.6.8. All lines from the system to the McLeod gauge were trace-heated to prevent any condensation in uncontrolled areas. The de-aeration tank was to be used as a source of gas-free liquid for backfilling purposes while the spent Dowtherm reservoir was used for the collection of used backfilling liquid and condensed system fluid. The Hydrogen bottle was to be used for injection of gas, whose level in the system could then be determined as described. The Residual Gas Analyzer (RGA) was installed to determine the degradation species from the working fluid during the endurance operation.

Numerous difficulties were encountered with the testing scheme. After taking a sample it was extremely difficult to remove the residual Dowtherm from the surfaces of the McLeod gauge, especially from the small capillary tubes. An infra-red heating system was installed to help speed up the process. It was first attempted to measure the background level of gas in the McLeod after evacuation. This was accomplished by evacuating the McLeod and then backfilling with Dowtherm from the de-aeration tank. It was found that the background levels had variations greater than the expected levels to be measured in the system and that the residual gas pressures after removal of the Dowtherm from the McLeod were invariably too high to allow accurate measurement. It was felt that the gauge was probably contaminated by backfilling from the de-aeration tank which, although subjected to a relatively hard vacuum, suffered from the problem of having plumbing with joints through which air could leak.

The use of mercury as a backfilling medium was considered but not implemented because of schedule constraints and potential hazard.

After several months non-productive testing the McLeod gauge was removed and replaced with a straight glass tube, thus reverting to the initial condensing bottle scheme. This is shown in Figure 3.6.9 . After initial problems the system background level with deaerated Dowtherm was determined to be in the range 7-10 ppm. These tests were performed before the installation of the non-condensable gas separator and gas concentrations therefore increased slowly with time. At that time no reliable low pressure measurement transducers were available and the only indication of an increase in gas concentration, and hence rise in condenser pressure, was a drop in electrical output as the turbine isentropic head was reduced.

The jet condenser Phase II effort also included vibration testing. Vibration testing of the jet condenser assembly was performed to dispel fears that the component could not continue to operate through the high vibrational environment of a space launch. To this end a jet condenser-accumulator assembly was mounted to a vibration platform with flexible connections for the vapor and liquid lines. Separate resonance tests had been performed on the injector assembly to show that no potential problem existed from individual nozzle excitation.

With the jet condenser operating, lateral vibrations were imposed at frequencies varying from 5 to 500 HZ, with the input excitation level increasing until condenser flood-out occurred or 30 g's was reached. These tests have been reported in detail in report 80 DIPS-28 (AER 1504-16). Figure 3.6.10 shows a photograph of the jet condenser with the hydraulic actuator attached. Tests were run at different injection pressures to include the higher injection pressure associated with the higher CRU rotational speed during the launch phase.

It should be noted that with higher injection pressures and a fixed reference pressure in the system accumulator the jet condenser operates at a lower recovery and is therefore less susceptible to disturbances in the combined stream passing through the throat.

Measurements of non-condensable concentration during the tests showed a range of 5-20 ppm air which is consistent with levels anticipated in the GDS with an operating non-condensable gas separator designed for 1 ppm hydrogen.

Floodout occurs when the vibration level is sufficient to cause the combined stream to contact the side of the throat and thus to disturb the flow to such an extent that flow through the throat is no longer possible. Figure 3.6.11 summarizes the vibration test results, showing that the condenser could sustain more than 10 g's for all frequencies.

GDS Jet Condenser

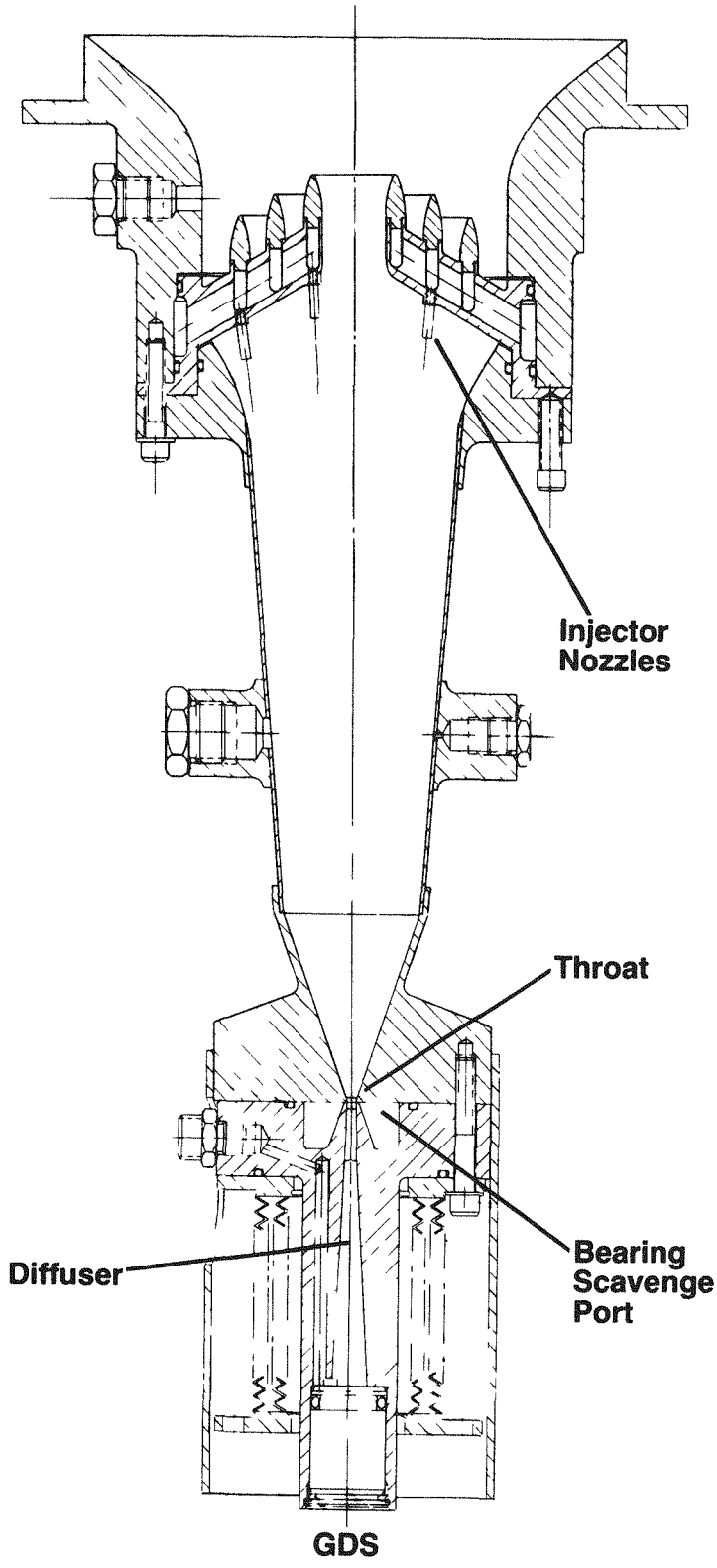

Figure 3.6.1

GDS System Configuration

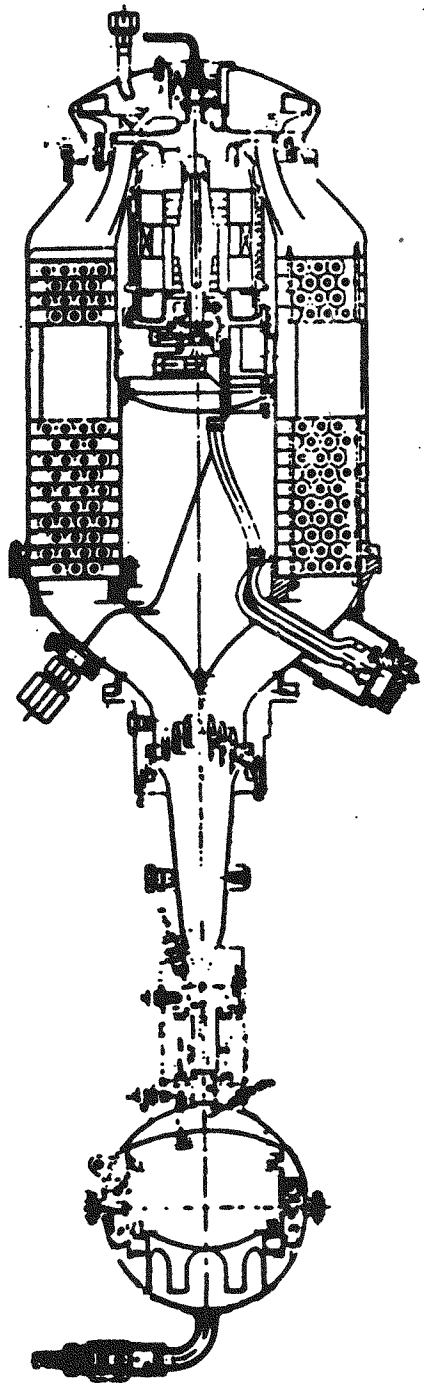

Figure 3.6.2

Focused Stream Of Jet Condenser Liquid Jets

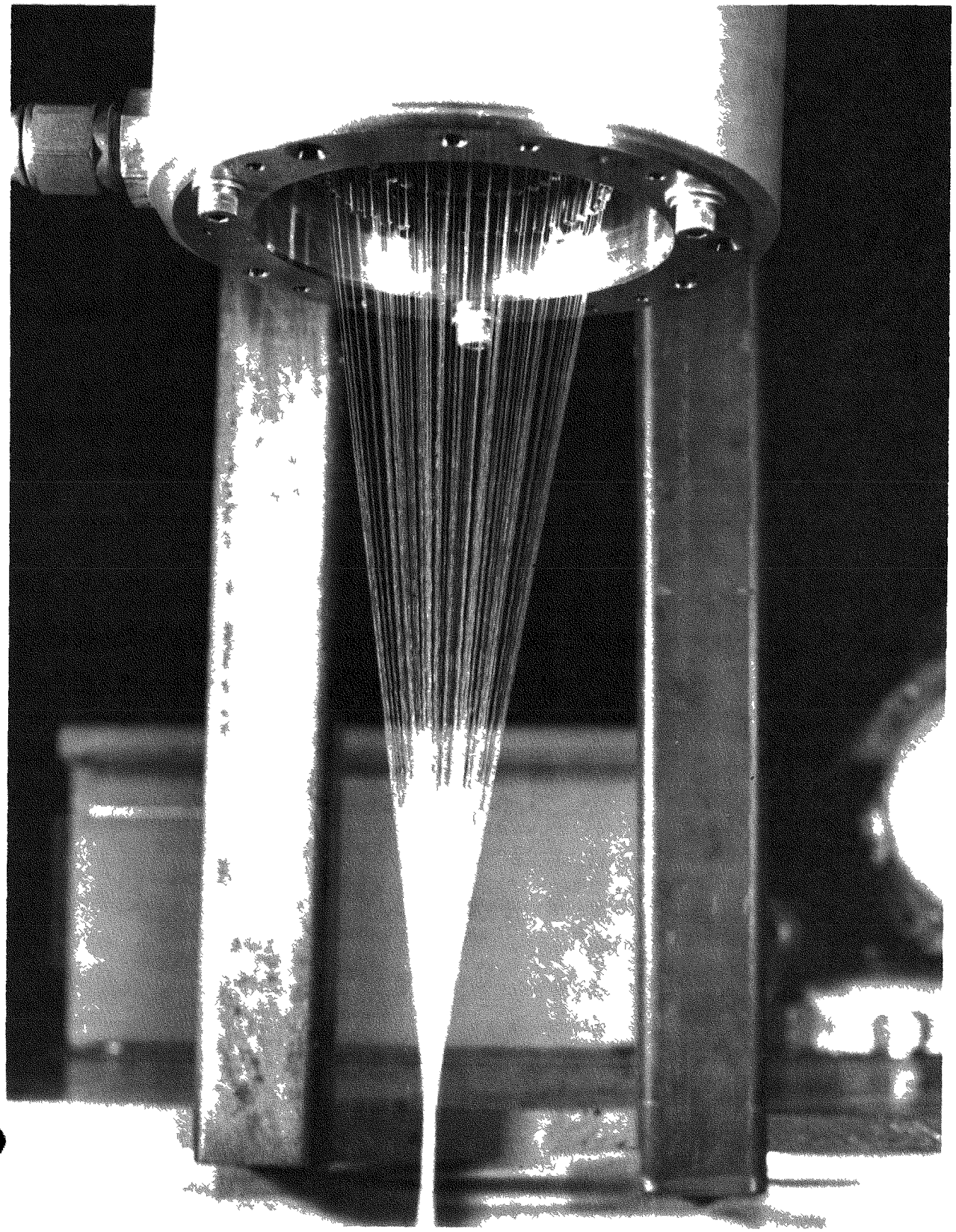

Figure 3.6.3

Single Nozzle Test Rig (Dowtherm A Operation)

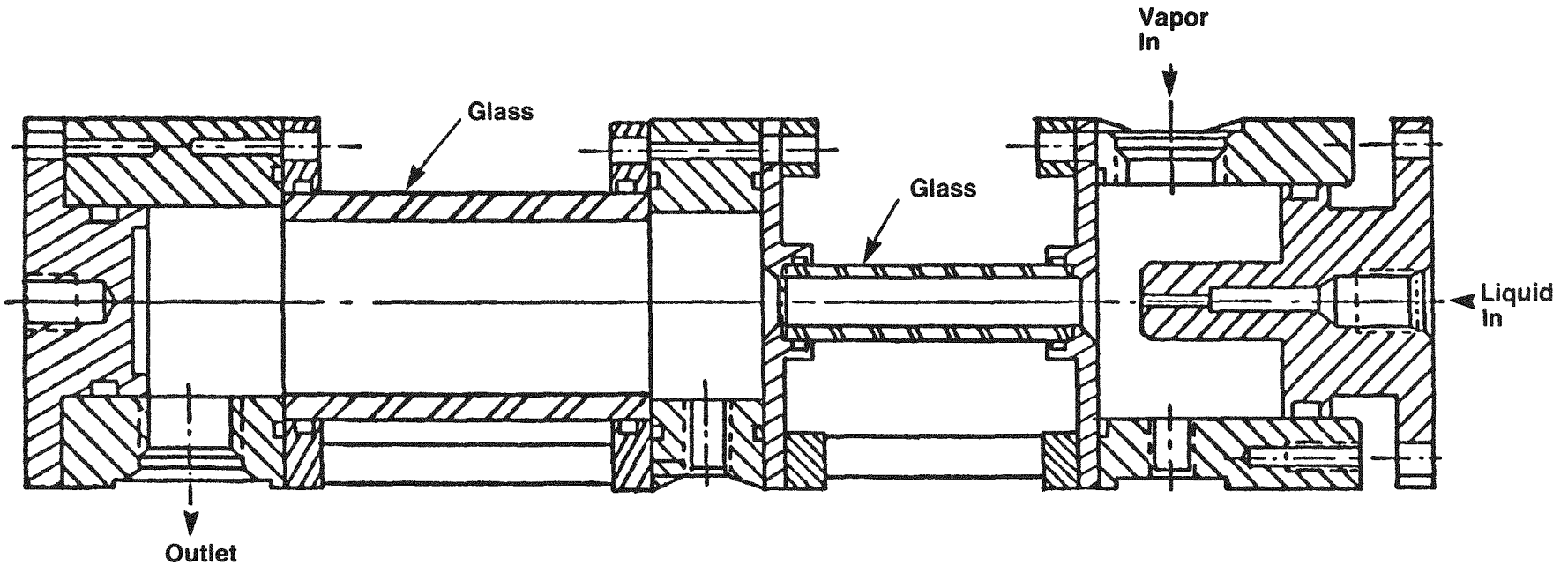

Figure 3.6.4

Jewel Orifice Configuration

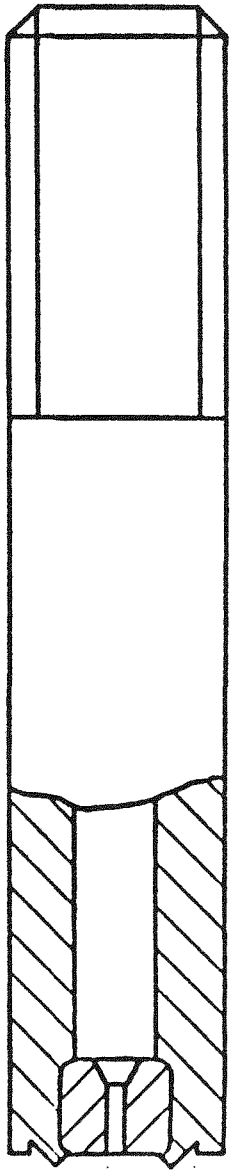

Characteristics

Orifice Diameter	.010 In.
Orifice Length	.040 In.
Surface Finish	16
Exit Corner Break	.001 In. Max.

Figure 3.6.5

Ninety Nozzle Jet Condenser Shower Head

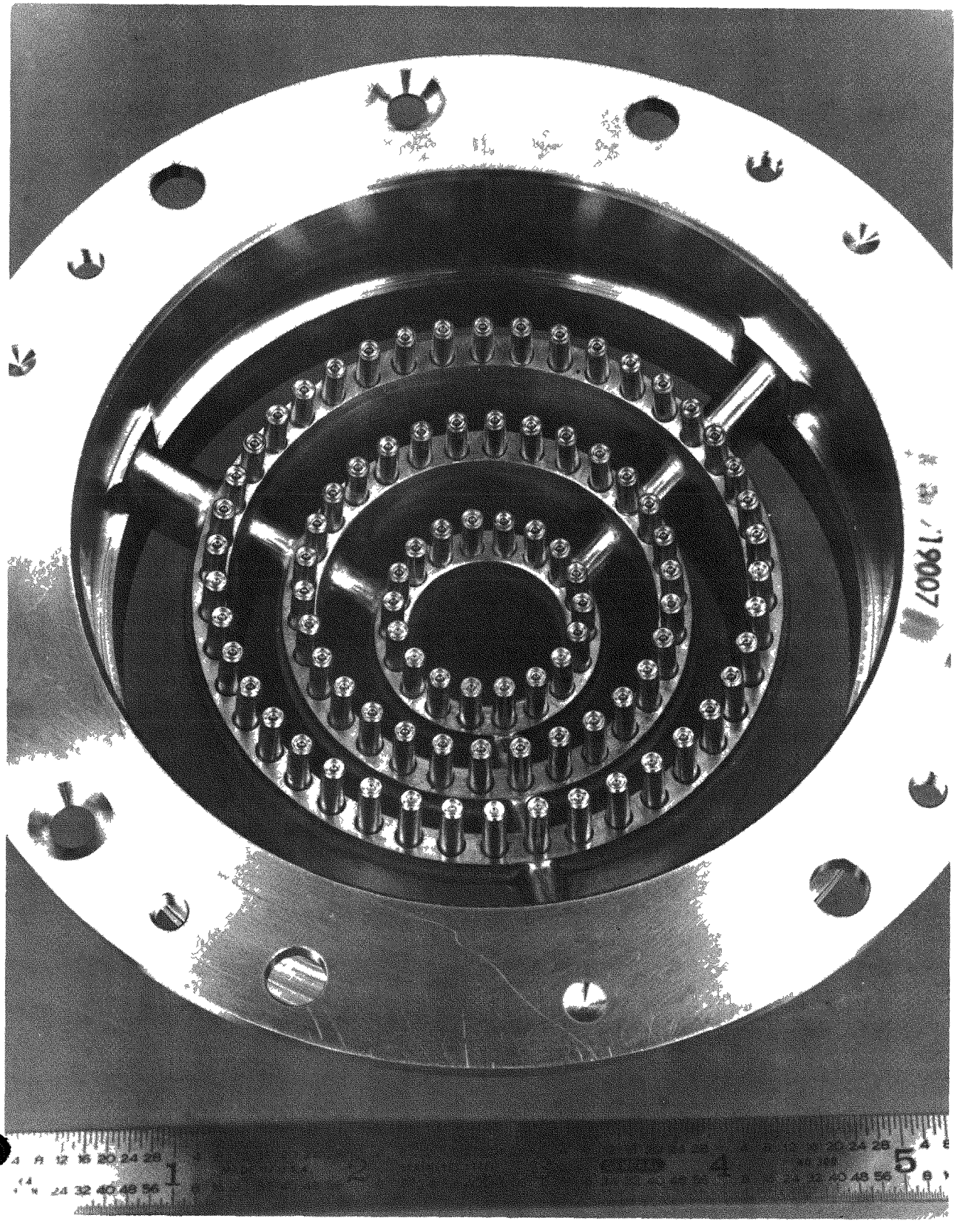

Figure 3.6.6

Jet Condenser Jewel Nozzles

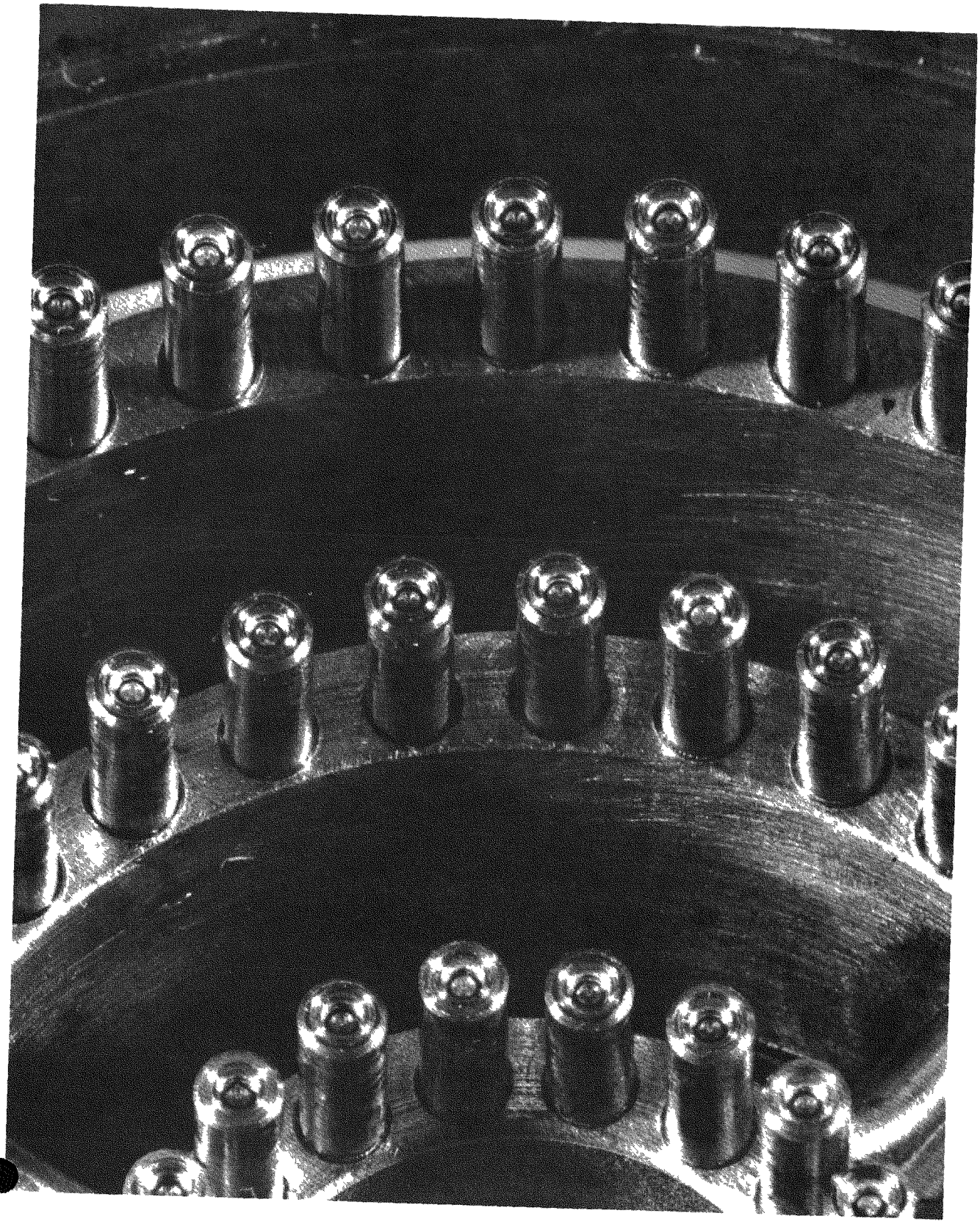

Figure 3.6.7

Schematic For Jet Condenser Gas Sensitivity Tests

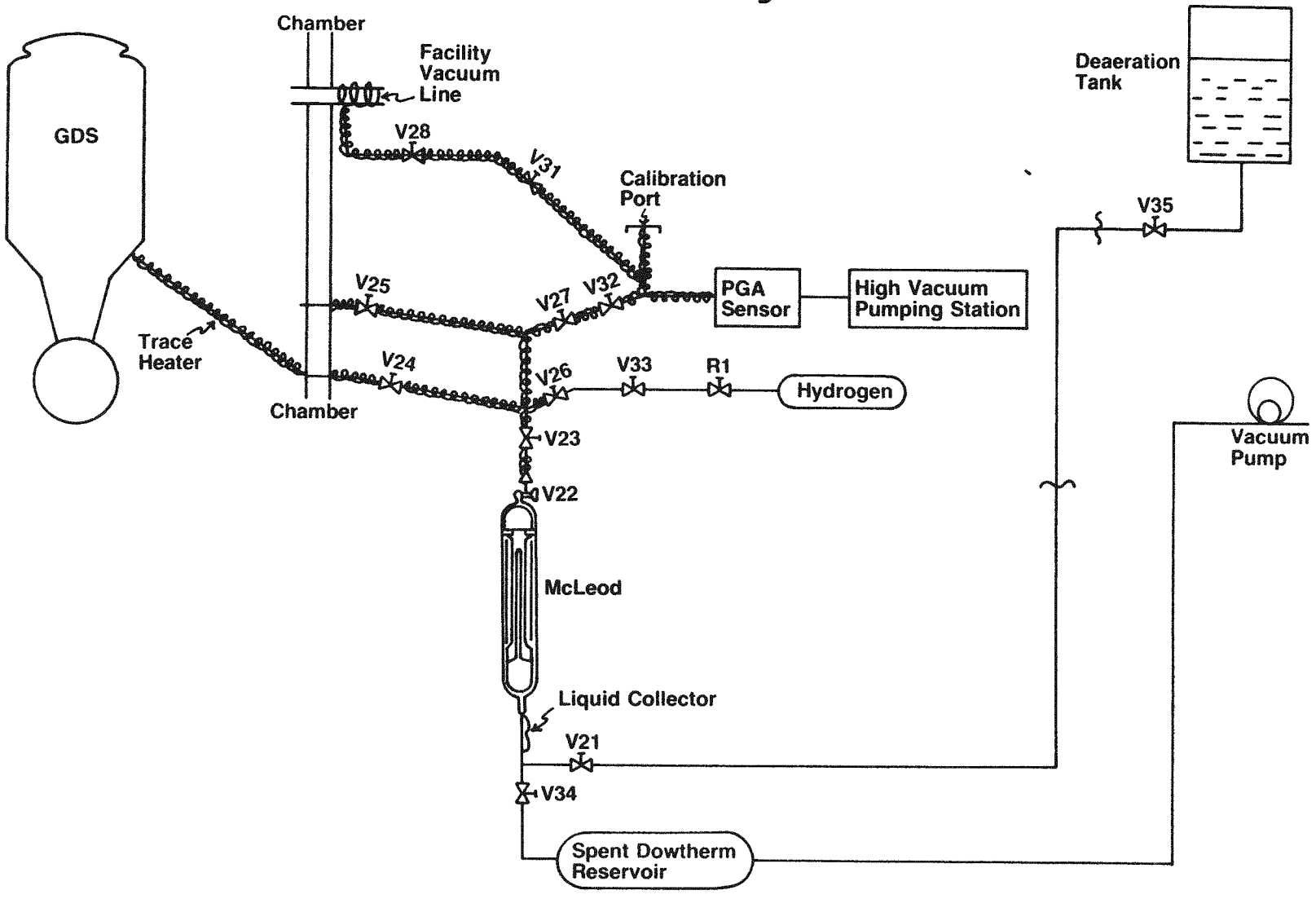

Figure 3.6.8

Jet Condenser Sensitivity Bottle Test System

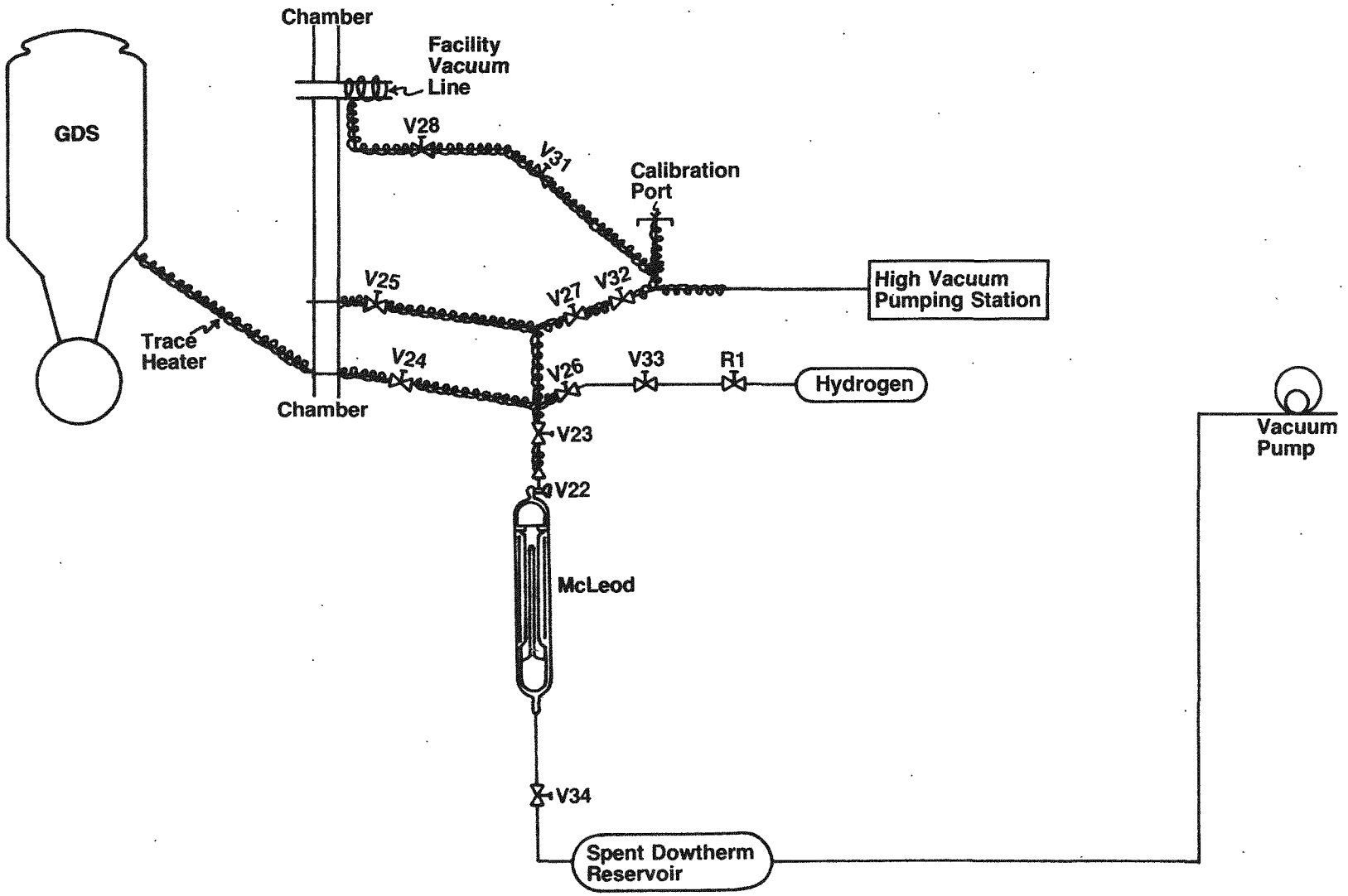

Figure 3.6.9

Jet Condenser Vibrator Test Rig

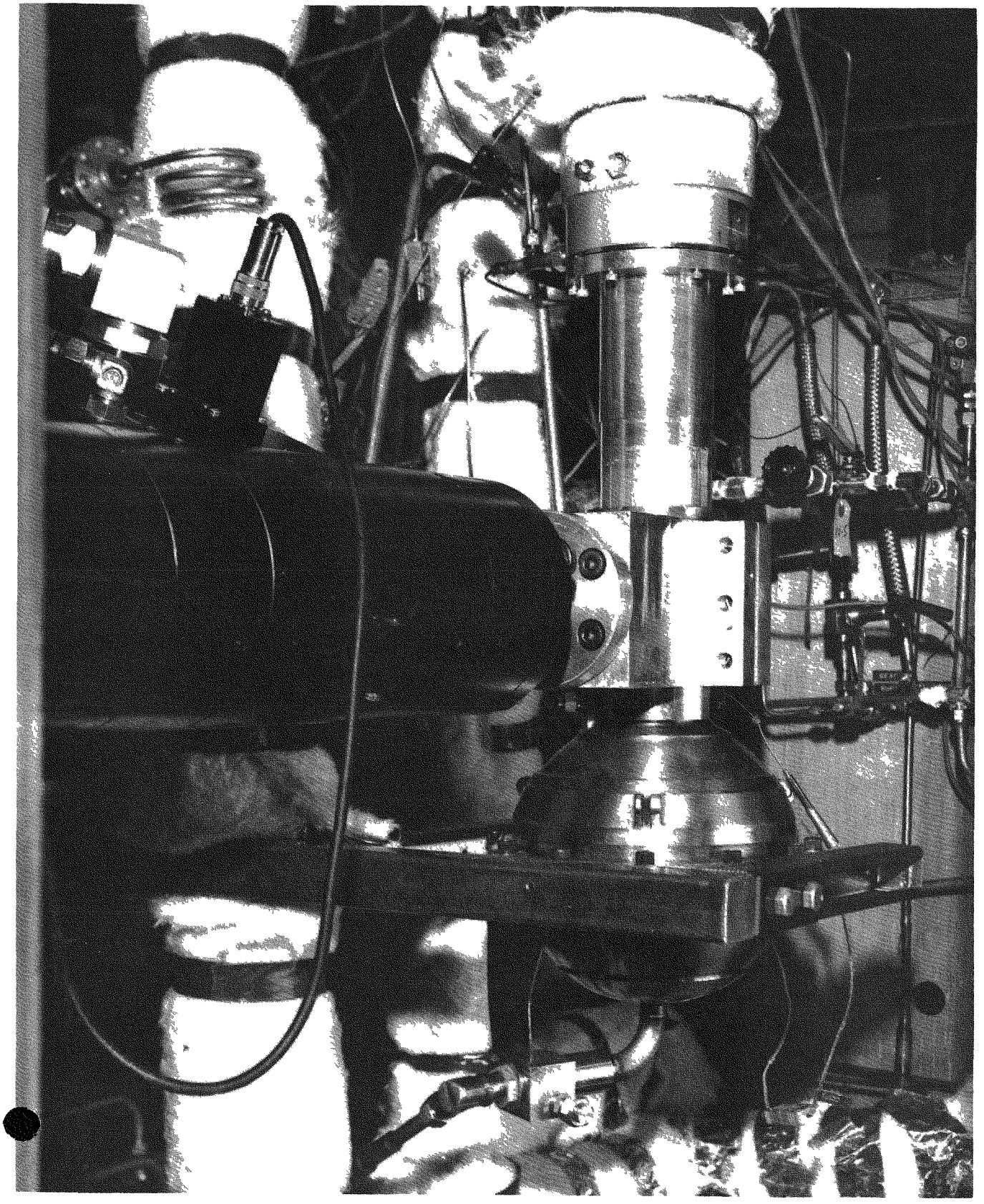

Figure 3.6.10

Jet Condenser Vibration Data

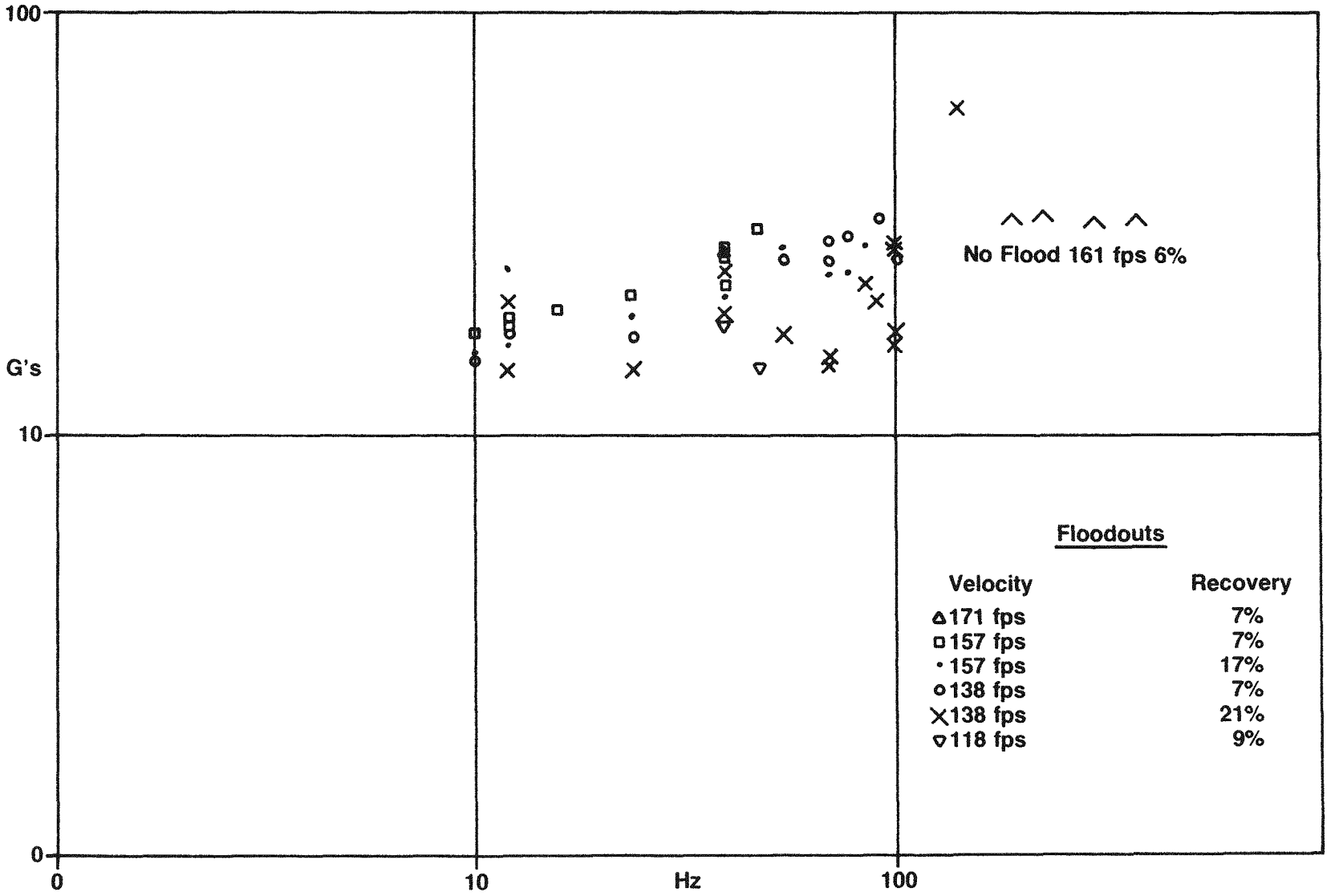

Figure 3.6.11

3.7 Fluid Degradation Products Removal System

Organic fluids undergo pyrolytic decomposition when subjected to elevated temperatures. Extensive thermal stability testing of the Dowtherm A working fluid by Sundstrand under Atomic Energy Commission contact and further testing by Battelle Memorial Institute during Phase I led to the conclusion that positive non-condensable gas removal would be required. This conclusion resulted from experiments performed on the susceptibility of the jet condenser to the presence of non-condensable gases. These gases tend to be concentrated in the jet condenser and cause occlusion of the subcooled liquid jets and subsequent degraded performance. At higher concentrations of the gas in the liquid, defocusing of the liquid jets occurs due to the sudden expansion of the gas as it passes through the jet condenser liquid nozzles. This results in a condenser failure.

3.7.1 Non-Condensable Gas Removal System

Experimental results from Phase I jet condenser testing with different air concentrations showed that air concentrations in excess of 30 parts per million (ppm) would degrade performance, i.e., condenser pressure rises with gas concentration as shown in Figure 3.7.1. Concentrations in excess of 90 ppm caused condenser "flood-out" failures as shown by the dramatic rise in bearing scavenge pressure, indicative of the liquid interface moving into the throat region. Based upon relative gas solubilities it was determined that if hydrogen were the non-condensable gas,

solubilities it was determined that if hydrogen were the non-condensable gas, concentrations lower than 10 ppm would be necessary to prevent failure.

The Phase I scheme for gas removal employed a combination of a palladium diffusion cell for hydrogen removal and a non-condensable gas separator (NCGS) to remove the other non-condensable gases which were presumed to be mostly methane. The design goal for the NCGS was a system gas concentration of 1 ppm of methane, based upon AEC degradation loop test data with considerable derating factors.

A palladium diffusion cell is a widely accepted method of removing hydrogen from process loops in industry. The diffusion cell consisted of a palladium-silver diffusion material in the form of a tube, 0.062 in. OD x 0.003 in. wall thickness. The tube was 26 in. long with one end sealed and the other brazed to a nickel tube. The diffusion tube was coiled into a helix 1.125 in. diameter by 1.75 in. long and supported by a "bird cage" constraint system. This constraint protects the diffusion tube from damage by handling or dynamic environment. The palladium diffusion cell assembly was placed at the regenerator vapor exit with the constraint welded to the wall interior and the nickel extension tube brazed through the wall. Analysis during Phase I indicated that, with one cell, a maximum concentration of only 3% of the maximum tolerable level would occur. This would be reached at approximately 200 hours.

The non-condensable gas separator concept was based on the gas controlled heat pipe principal. Its two major sections are the condenser and the evaporator. The heart of the device is a section of extruded, ID grooved aluminum tube upon which the vapor condenses and is collected. It is then wicked through the grooves to the evaporator where the fluid is vaporized and returned to the system. The non-condensable gases are concentrated at the end of the condenser and are removed through a capillary tube vented to space. The cooling fluid for the NCGS condenser is the jet condenser inlet flow. The heating fluid for the NCGS evaporator is the regenerator liquid outlet fluid.

A small portion of the vapor from the regenerator outlet is circulated into the NCGS where the non-condensable gases are removed and the vapor outlet

is discharged to the jet condenser mixing chamber. This configuration provides a net "driving potential" of 0.017 psi through the separator to ensure continuous, steady flow.

The heat pipe consists of a long section of grooved tubing extruded from 6063 aluminum. This heat pipe material has been the workhorse of many NASA heat pipe applications, is well characterized and has been space qualified. Its main advantage is the high film coefficient achievable with low conductivity fluids.

During Phase I a non-condensable gas separator was designed, built and tested as a component but not incorporated on the GDS. The palladium diffusion cell was incorporated.

The NCGS design that was tested is shown schematically in Figure 3.7.2 and in more detail in Figure 3.7.3 along with the integration scheme into the GDS. This unit was designated Serial No. 001. The heat pipe was made from a 14 inch length of extruded, grooved aluminum tube with a 15 inch length of capillary tubing having an O.D. of .010 inch and an I.D. of .005 inch.

Thermal connection between evaporator and condenser jackets with the heat pipe was through different thickness gas gaps, thus providing a high thermal resistance. Some variation of this resistance was feasible by varying gas composition and hence molecular weight and conductivity. Evaporator and condenser lengths were chosen to be six inches each, with a two inch adiabatic section separating them. The six inch lengths were selected to yield adequate separation of non-condensable gas. At the evaporator end, the heat pipe was closed by a stainless steel end plug which was penetrated by the capillary. The capillary was designed to reject a volume flow rate of 6×10^{-8} ft^3/sec at the system pressure of 0.1 psia. This corresponds to a non-condensable gas flow rate of 3×10^{-12} lbm/sec and a Dowtherm flow rate of 1×10^{-10} lbm/sec passing through the capillary. The condenser end closure was wicked with a single layer of wire mesh in order to return any liquid which condensed there to the grooves.

The seal between condenser and evaporator consisted of a 1 in. long stainless steel plug which was interference fitted into the grooved aluminum tube.

A 0.250 in. OD x 0.020 in. wall stainless steel tube connected the condenser to the vapor source. The flow resistance of the tube (assuming a 6 inch length) was 0.023 psi-hr/lbm. Thus, for the nominal flow rate of 0.16 lbm/hr, the pressure loss in this tube would be 0.004 psi and the pressure drop across the seal between the condenser and evaporator would be (0.017-0.004) = 0.013 psi. The maximum delta P which the wick could sustain without blow-through is 0.015 psi, which exceeds the existing pressure. Thus, in zero g, no vapor would bypass from the condenser to the evaporator. However, during vertical operation on the ground, the grooves partially drain and some vapor can bypass the seal. The flow resistance of the seal is 0.288 psi hr/lbm. This was estimated to result in a bypass flow of approximately 15% of the nominal vapor flow rate. It should be noted that this bypass flow occurs in addition to the useful flow and does not detract from it.

Initial testing of the NCGS as a component in the vertical orientation showed encouraging results as shown in Figure 3.7.4. 100% separation was not achieved however, and this was probably attributable to vapor blow-by through the plug separating condenser and evaporator.

However, at the end of Phase I the device was turned horizontally and the test results showed a cyclic gas ejection behavior, as shown in Figure 3.7.5 which was thought to be due to the intermittent plugging of the capillary inlet.

This instability led to the decision to include the NCGS in the Phase II Technology Verification Phase with the major objective being to stabilize the operation and demonstrate acceptable gas separation.

Significant test rig improvements were made and a Residual Gas Analyzer (RGA) added to the capillary exit to improve the understanding of the operational mode. A simplified schematic of the test rig is shown in Figure 3.7.6. Further testing of S/N 001, shown in Figure 3.7.7, resulted in anomalous results and indicated severe operational problems. As a result, it was decided to build a modified version of the heat pipe, S/N 002, incorporating modifications which were expected to alleviate most of the problems, including vapor inlet modifications, gas gap baffling to preclude natural convection,

reduced conduction area in the aluminum tubing, the wick thermally shorted to the capillary inlet and other minor modifications. In addition, it was decided to design an experimental separator (designated S/N EX) which would allow installation of appropriate thermocouples and pressure transducers, have a geometry flexible enough to allow reversing of vapor and capillary flow directions, allow the fixed gas gaps to be replaced by variable conductance paths, have the capillary inlet shielded and to allow incorporation of a centerbody to maintain high vapor velocities. This version is shown in Figure 3.7.8.

Testing of S/N 002 led to the discovery of a through leak around the back of the aluminum wick structure which in turn led to a development effort aimed at obtaining a satisfactory shrink fit of the aluminum into the stainless steel housing. S/N 002 was tested with Loktite sealant to plug the leak with some good test data obtained, but the main outcome was to build another heat pipe, S/N 3M, with an adequate interference fit. This version also exhibited periodic gas ejection in the horizontal position and subsequently, based on S/N EX testing, another pipe S/N 3M-2 was built with a .010 inch diameter capillary to increase ejection capability.

In order to obtain a better understanding of the operation of the separator a detailed mathematical model was initiated. The model used the SINDA thermal network analyzer to simulate the heat pipe, combined with a stepwise integration of the momentum, energy and continuity equations along the length of the heat pipe, incorporating non-condensable gas mass-fraction changes, gas diffusion and two phase flow where appropriate. This detailed model was applied to the S/N EX configuration, with a simplified version used to model the S/N 001 and the later versions S/N 002 and S/N 003.

The initial version of the S/N EX separator also exhibited periodic ejection in the horizontal orientation and also suffered low vapor throughput. The addition of a larger (.010 inch) diameter) capillary and the incorporation of a liquid eliminator at the capillary inlet appeared to eliminate all problems associated with periodic operation. The liquid eliminator employed a porous Teflon cover which, being non-wetting,

prevented the through flow of liquid while allowing passage of non-condensable gas. The mathematical model predicted that Liedenfrost boiling was occuring in the evaporator due to the high evaporator temperatures. This necessitated the addition of a demister, shown in Figure 3.7.9 at the vapor outlet from the device since liquid droplets in the outflow could lead to inventory control problems in a zero-g environment and also possibly could impact jet condenser operation. Analysis also indicated that a center-body should be added to the condenser to obtain the vapor velocities of the non-EX configurations. However, when the center-body was added, the oscillations returned, perhaps due to high vapor-liquid shear along the wick surface.

Further developments were made to the S/N EX configuration. These included a smaller center-body, the capillary was passed down the center to eliminate electrical heating requirements, and also conductances were changed. The final configuration of S/N EX is shown in Figure 3.7.10. This configuration operated satisfactorily in the vertical mode but with somewhat lower vapor flow rates horizontally and some instability at low helium injection rates. The final version of the EX separator did operate satisfactorily at the gas removal rates required for DIPS in both horizontal and vertical orientations.

Figure 3.7.11 shows a summary of the test results obtained from the modified S/N EX configuration. The dashed line represents an average performance curve for the separator based on a multiplicity of tests. The oscillations in the horizontal mode are indicated by the wide range of ejection rates at low injection. In all cases the separator shows less than 100% separation and asymptotically approaches the calculated limit for the .010 inch diameter capillary. The various projected requirements are shown on this figure and summarized in Table 3.7.1.

A detailed report of the results of the mathematical model have been submitted separately in report 80-DIPS-27 (AER 1816). One figure from that report is partially reproduced in Figure 3.7.12 to show comparison between analysis and experimental results. It can be seen that good temperature correlation exists in the condenser (up to Z = 0.6 feet) while the model shows much higher

Table 3.7.1 NCGS Performance Summary

	Ejection (Scc/Sec)	Efficiency (%)	Flow (Lb/Hr)	Concentrate (PPM)
Design	2.75×10^{-6}	100	.16	1
Test	3.25×10^{-6}	50	.20	2
S/N EX	7.5×10^{-6}*	50**	.20***	4
Worst Case	25×10^{-6}****	100	.20	~8

* GDS Analysis
** Demonstrated Efficiency
*** Current Test Flow Rate Horizontal
**** Worst Case Battelle Data

evaporator metal temperatures (T_M) than measured. The test was performed in the vertical mode and this may have had an effect on the boil-off and Leidenfrost heat transfer process in the evaporator, resulting in cooler metal temperatures.

After a thorough cleaning, the modified S/N EX configuration, shown in Figure 3.7.13, was mounted to the GDS in the vertical orientation. A preliminary test was performed to determine whether any negative impact on GDS operation occurred and then it was installed as part of the final GDS rebuild. Initial results indicated inadequate operation, with system pressures rising at a steady rate during operation Figure 3.7.14. A larger capillary (.015 inch diameter) was installed but with no major improvement while instrumentation indicated that the separator appeared to be superheated throughout its length. The problem was ultimately traced to poor contact between the condenser cooling jacket and the heat pipe; when vacuum grease was applied to the conduction rings the device began operating and then maintained a constant system pressure.

3.7.2 Centrifugal Separator

The Dowtherm A organic working fluid undergoes a slight pyrolytic decomposition under long term thermal cycling at high temperatures, forming high molecular weight substances (liquid droplets) at the boiler outlet conditions. It is desirable to separate these droplets from the vapor stream to prevent their deposition and subsequent buildup on the low pressure turbine nozzle surfaces. A centrifugal separator is located between the boiler and the turbine nozzle plenum. Its function is to prevent the buildup of any substance on the nozzle surfaces by swirling the vapor, causing the entrained higher density droplets to accumulate inside the swirl chamber.

A cross-sectional view of the centrifugal separator is presented in Figure 3.7.15. The separator consists of a rectangular-tangential inlet nozzle which accelerates the stream to a velocity of 50 ft/sec. The main body is comprised of three sections: an annular inlet and transition funnel, particle trap, and vapor exit nozzle.

The vapor enters the separator tangentially in the annular section and is forced in upon itself resulting in an axial acceleration toward the particle trap. This swirling axial motion continues through the straight section of the body and into the tapered section where the axial velocity is again accelerated to the throat. At the throat, a small carry-over of the vortex occurs, sweeping with it the separated particles and droplets and forcing them to the outer walls of the separator trap. At the throat, the primary vapor flow undergoes a reversal in axial direction and begins to swirl toward the vapor exit nozzle.

Effects Of Non-Condensable Air On Jet Condenser Performance

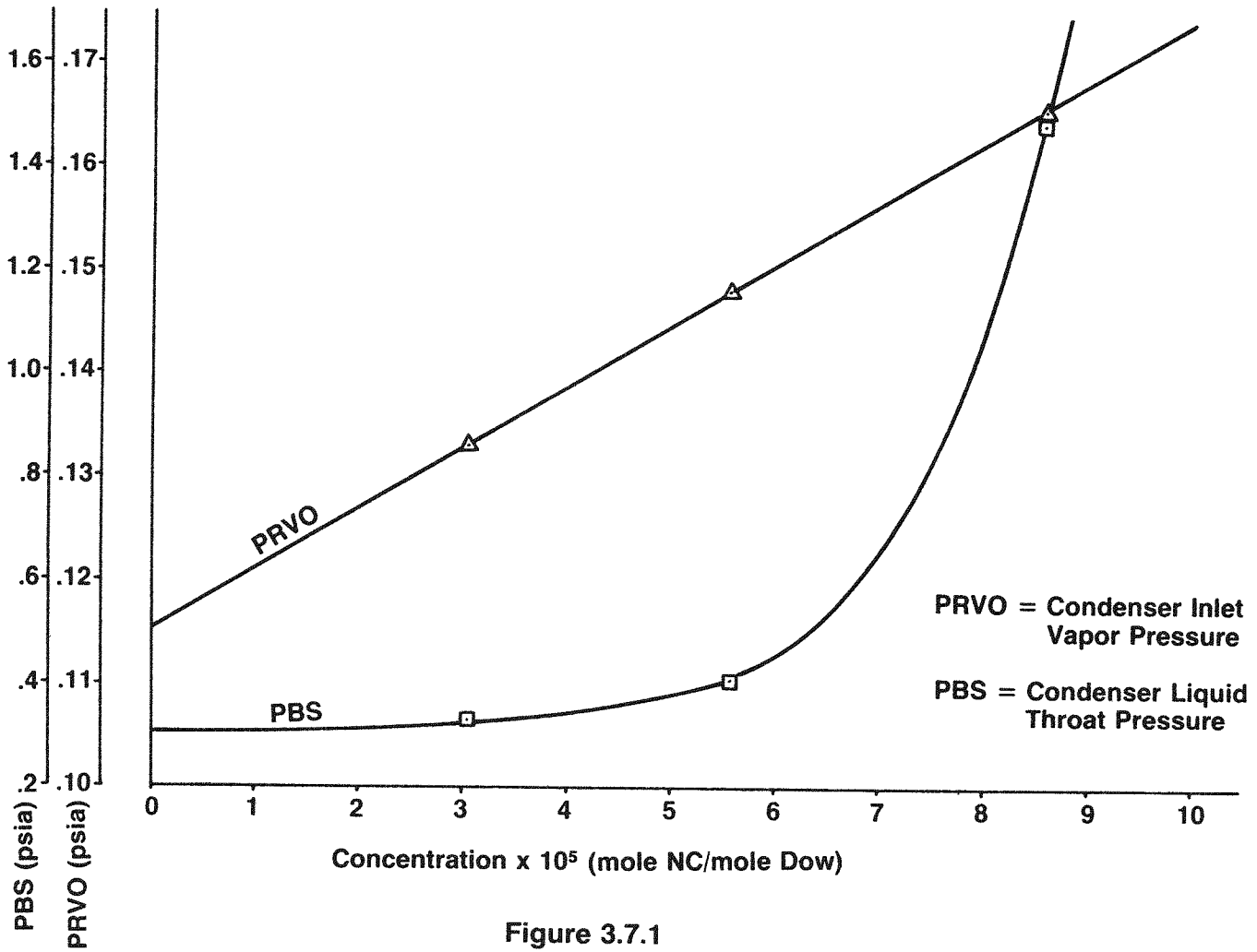

Figure 3.7.1

Noncondensable Gas Separator

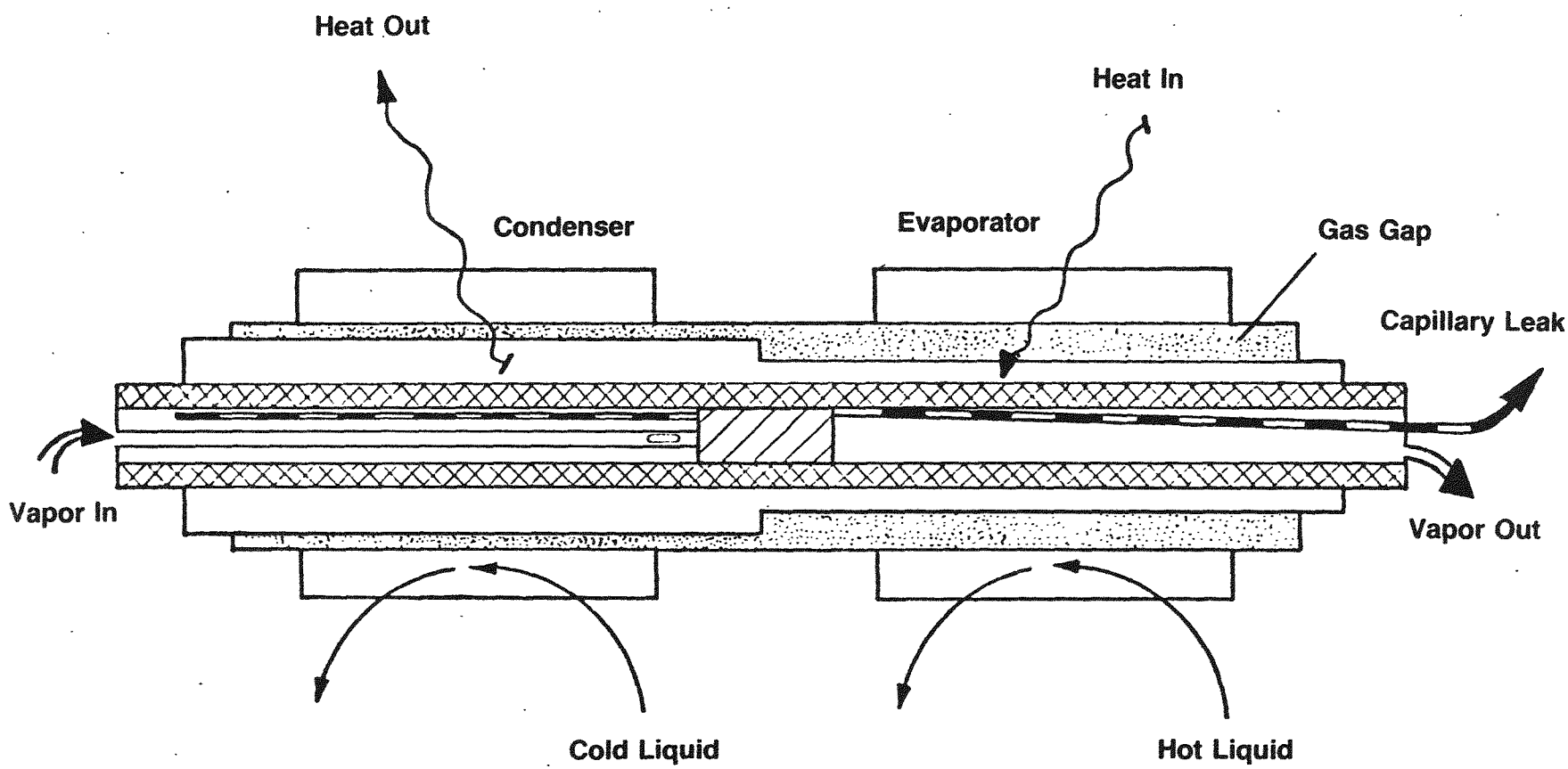

Figure 3.7.2

Noncondensable Gas Separator

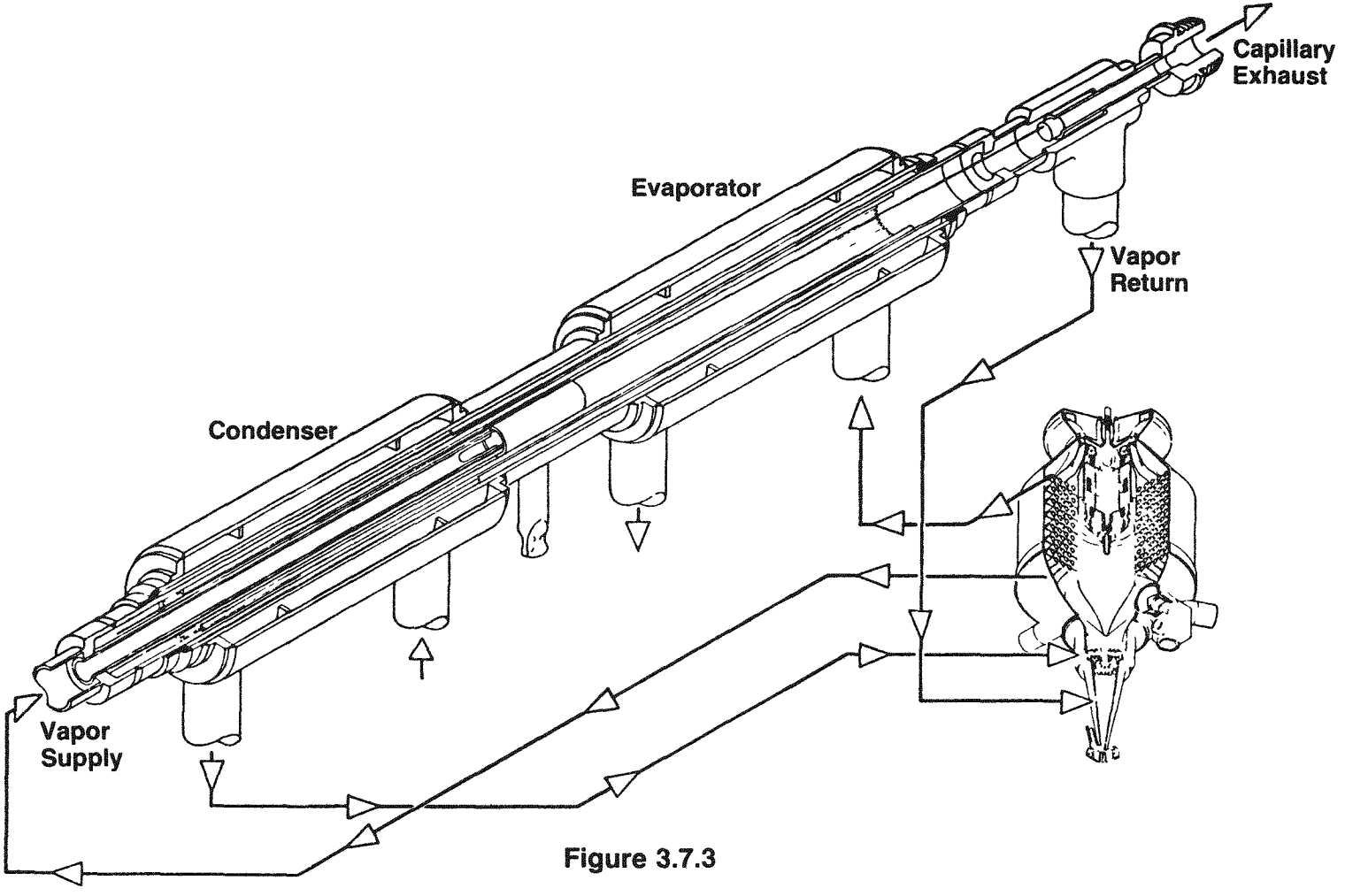

Figure 3.7.3

Theoretical And Measured Performance Of NCGS (Vertical)

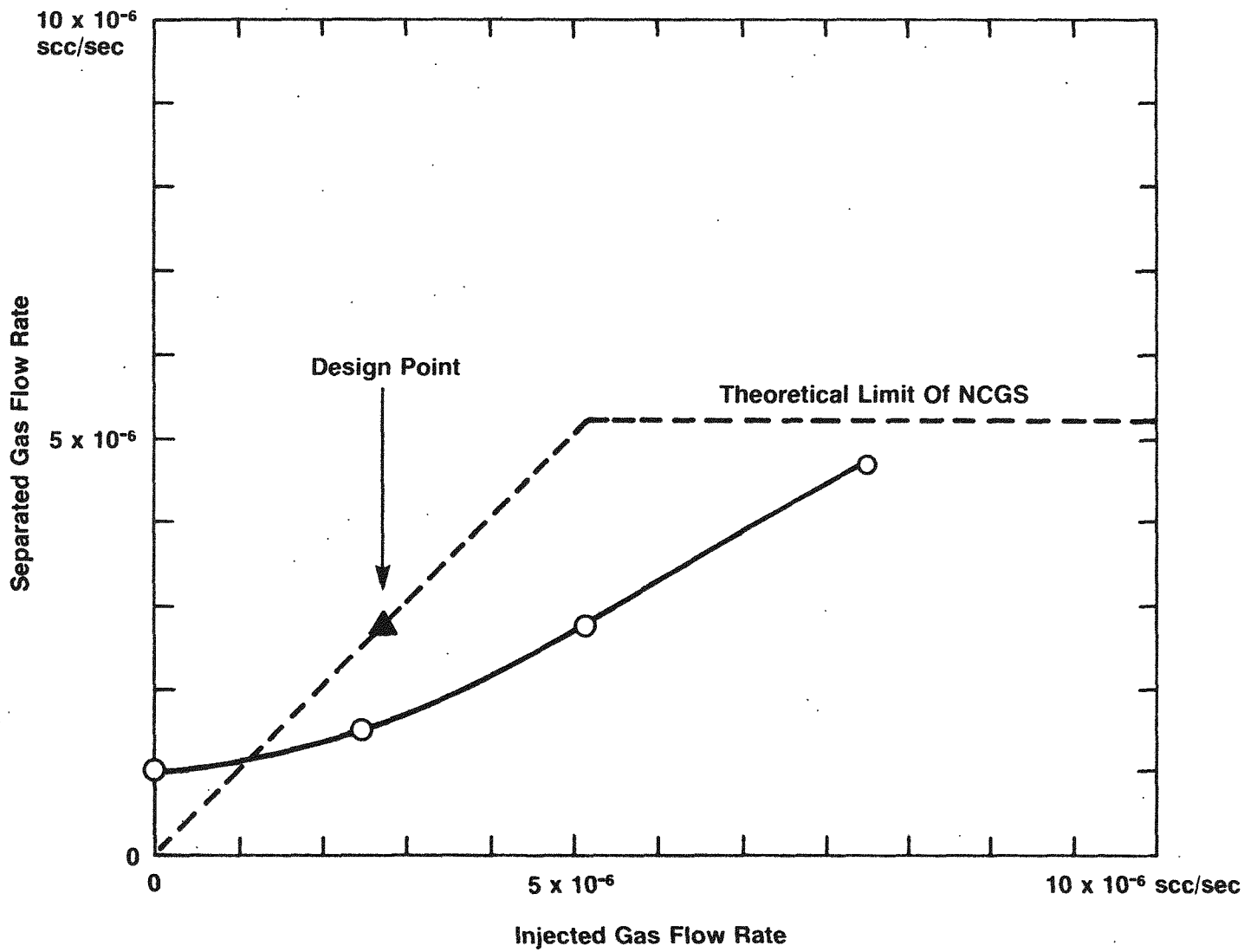

Figure 3.7.4

NCGS Performance Instability

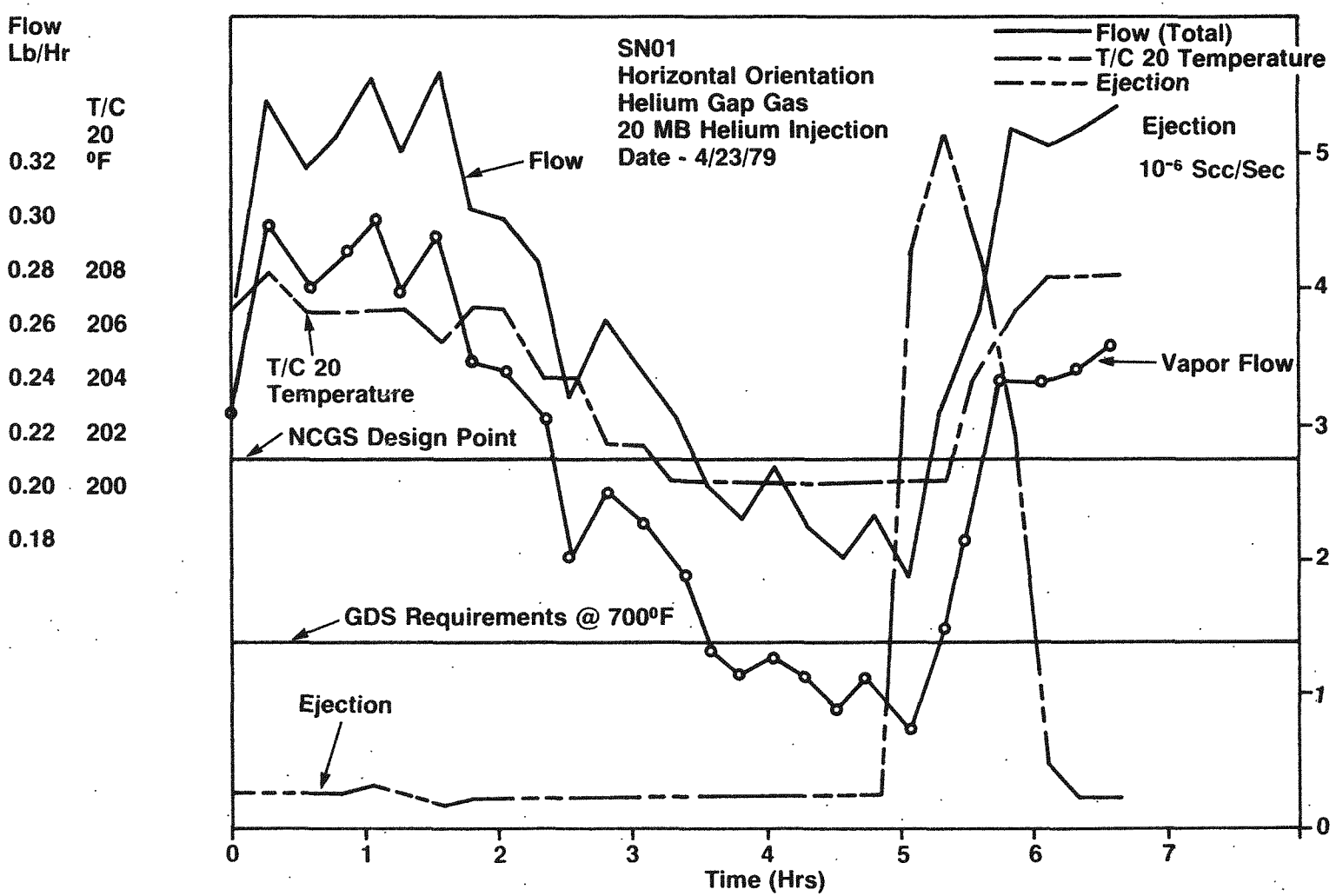

Figure 3.7.5

Simplified Test Rig Schematic

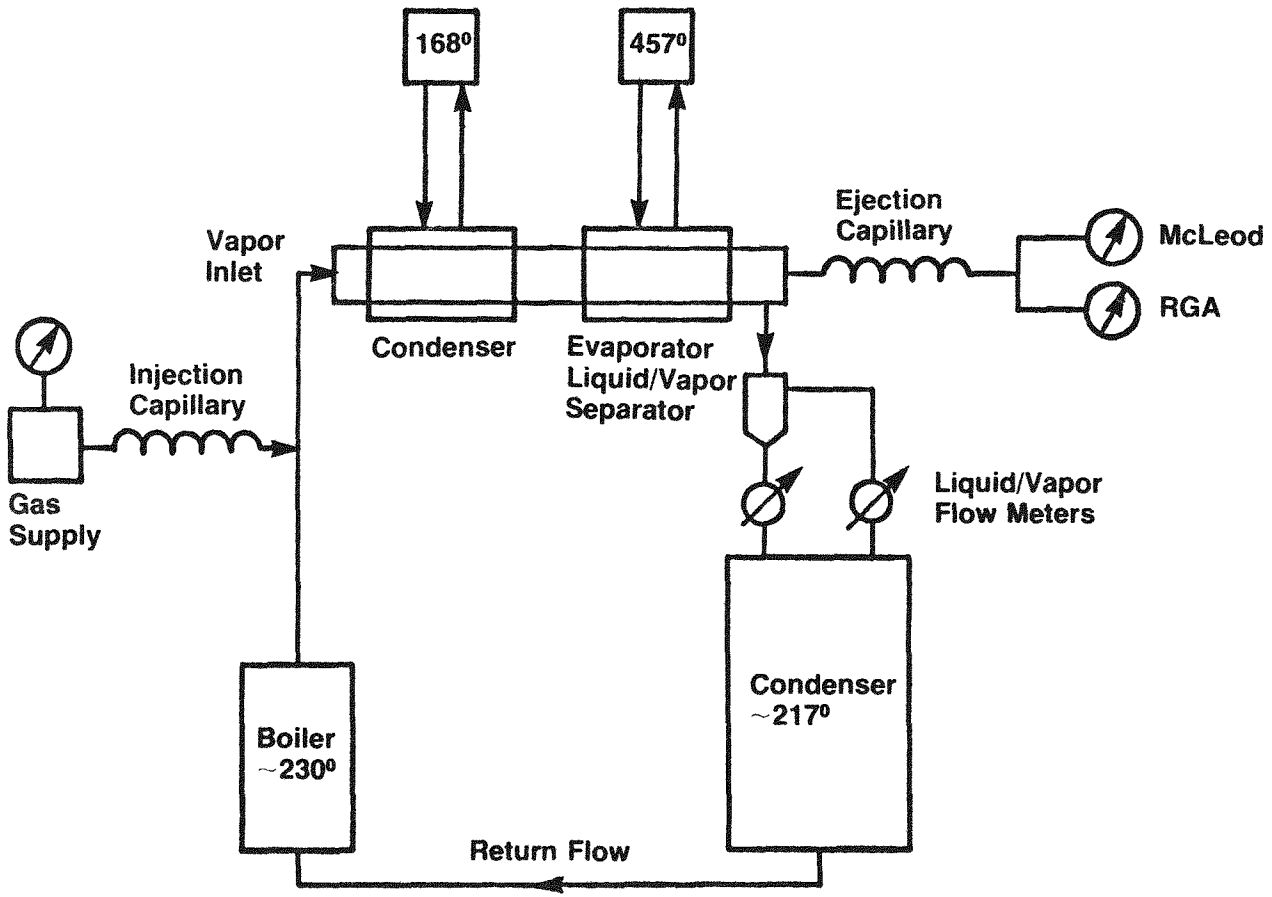

Figure 3.7.6

NCGS
Serial No. 001

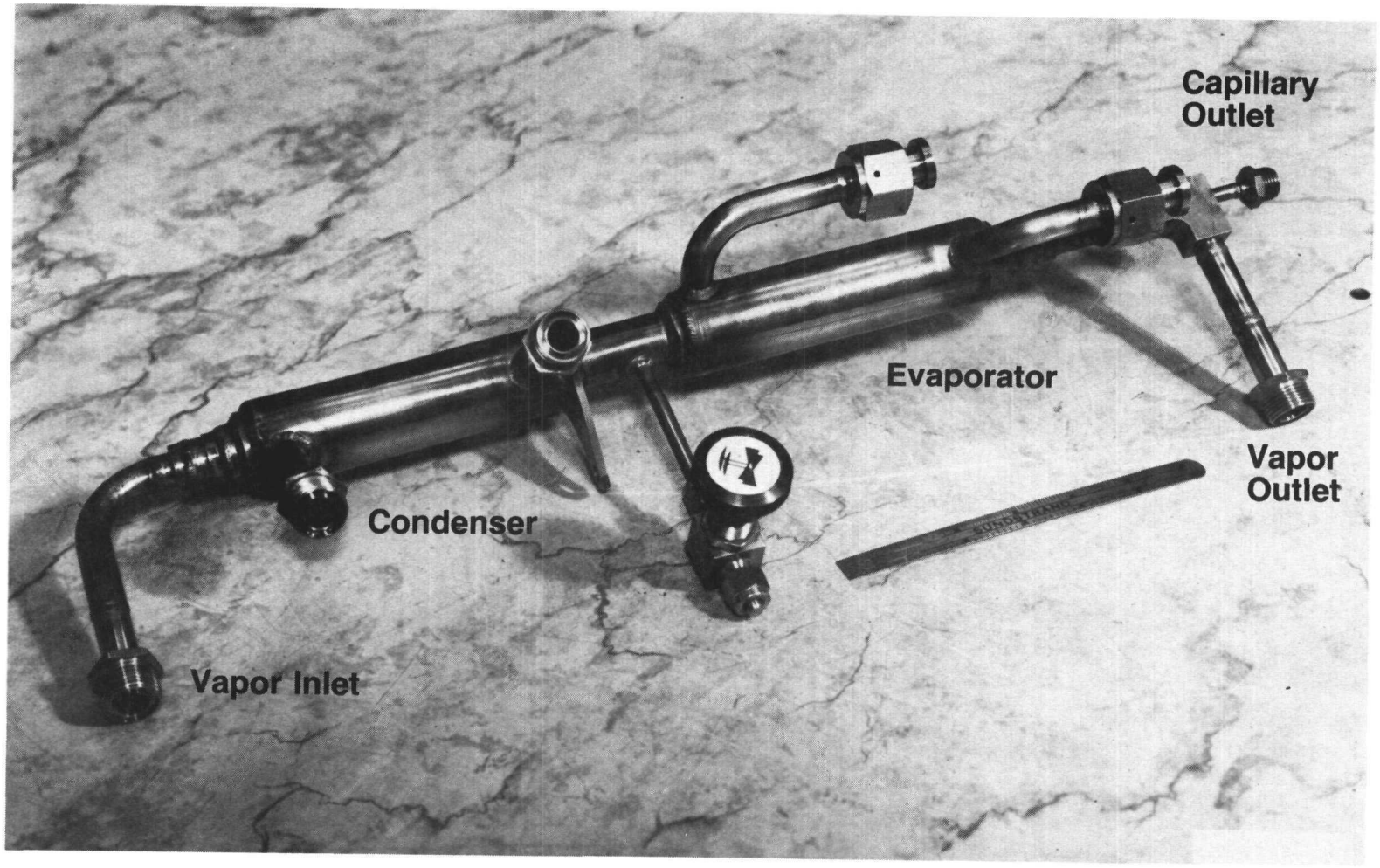

Figure 3.7.7

NCGS
Serial No. EX

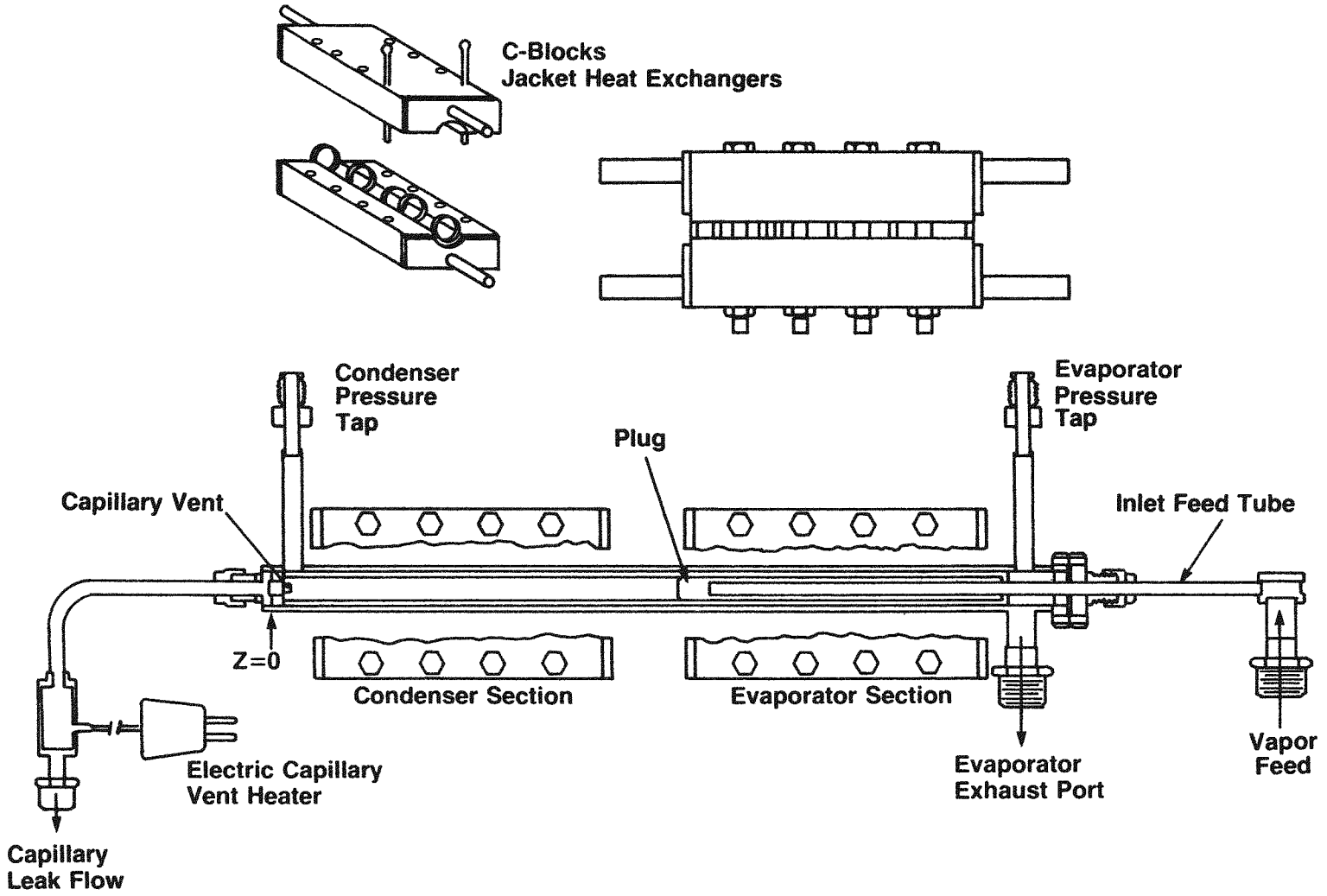

Figure 3.7.8

Demister/Evaporator

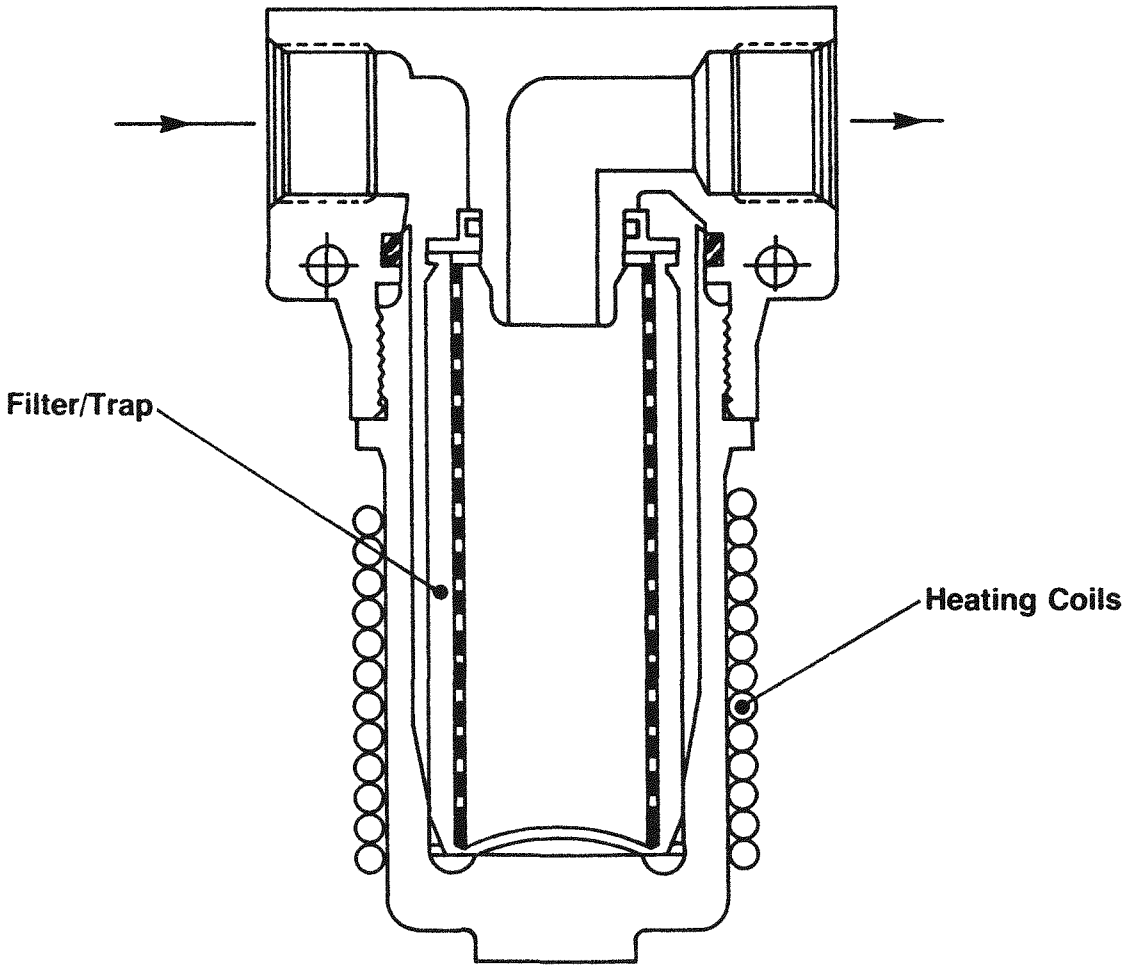

Figure 3.7.9

Modified Serial No. EX As Installed On GDS

*Liquid Jackets Not Shown

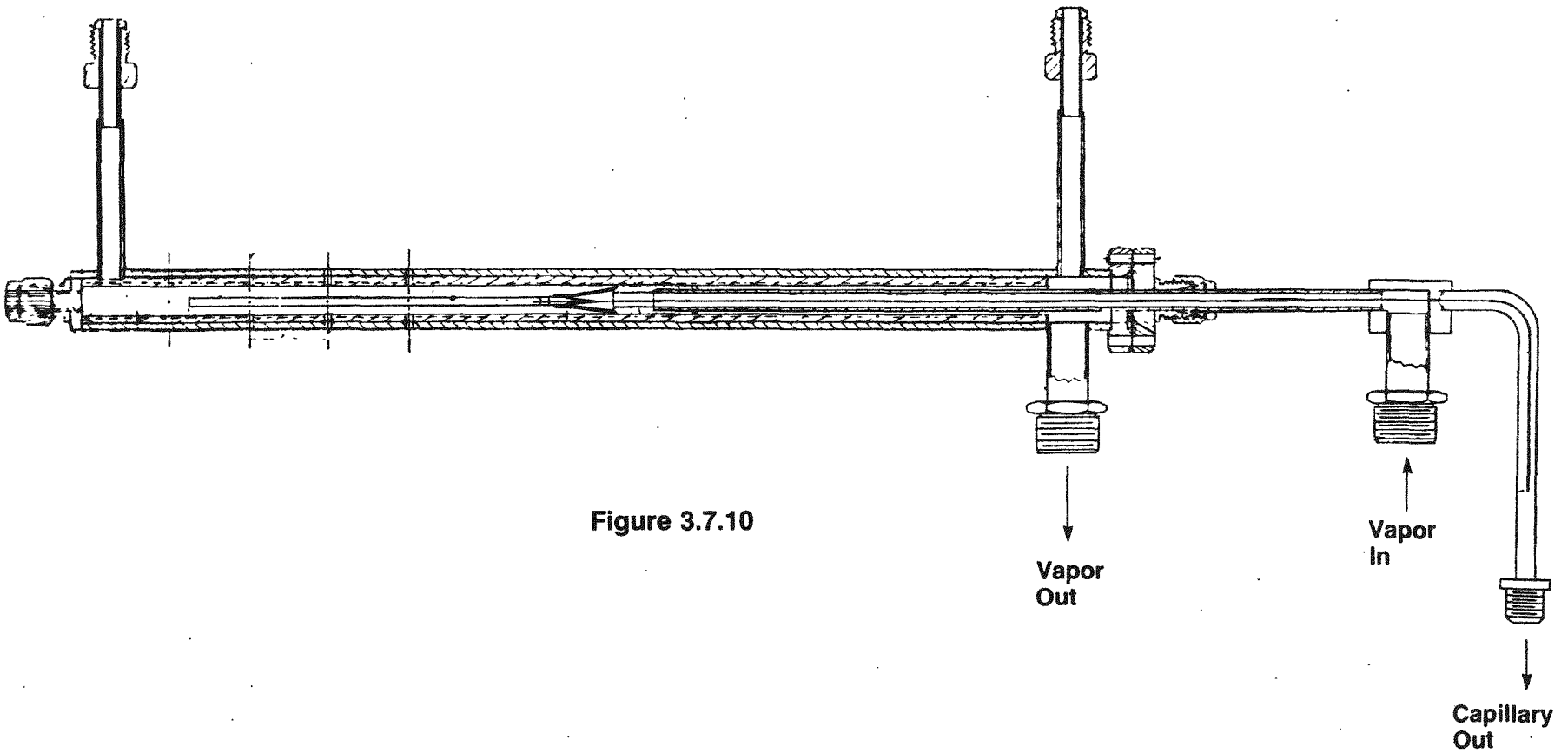

Figure 3.7.10

Serial No. EX
Test Result Summary

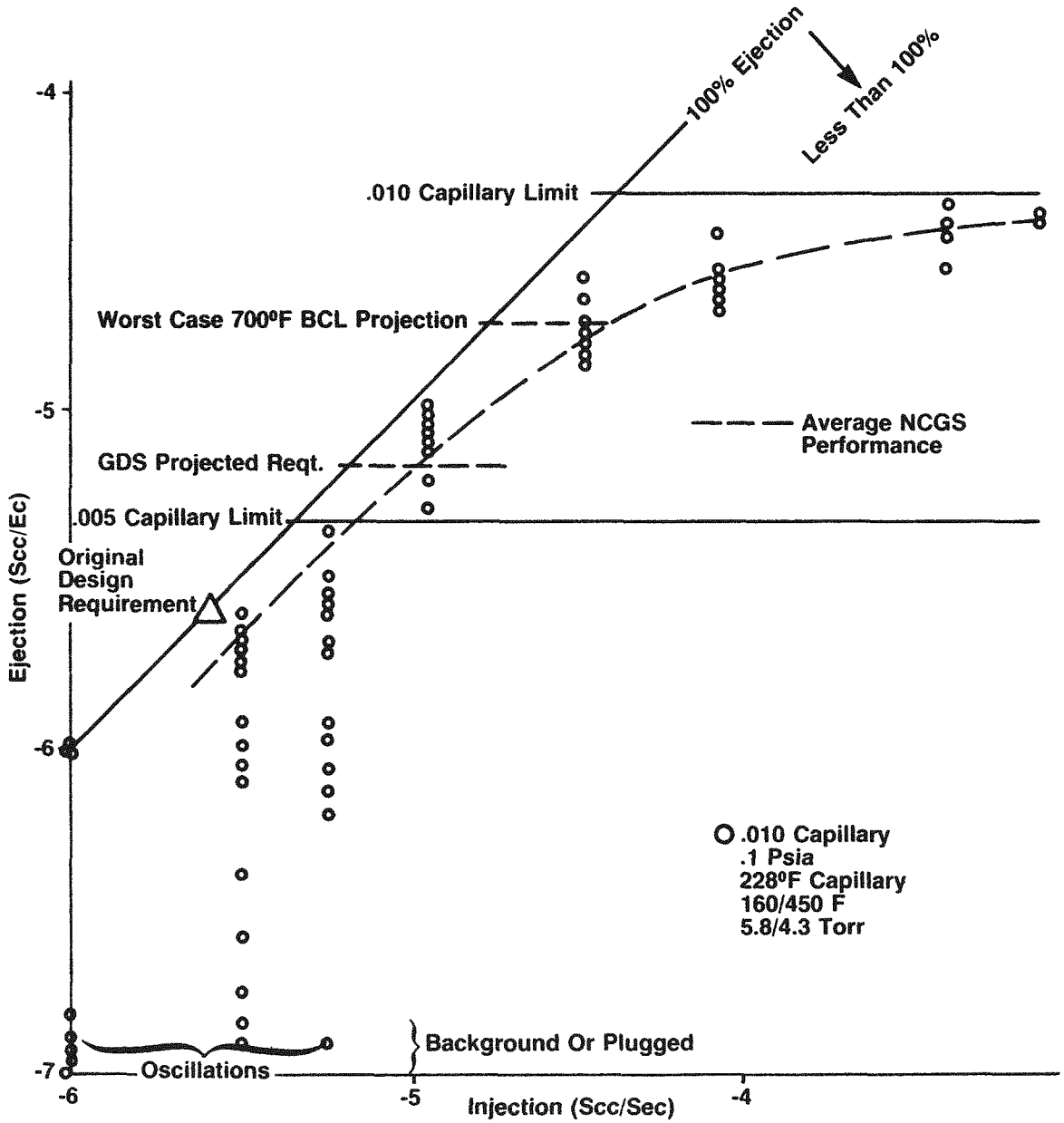

Figure 3.7.11

Analytical And Experimental Comparison

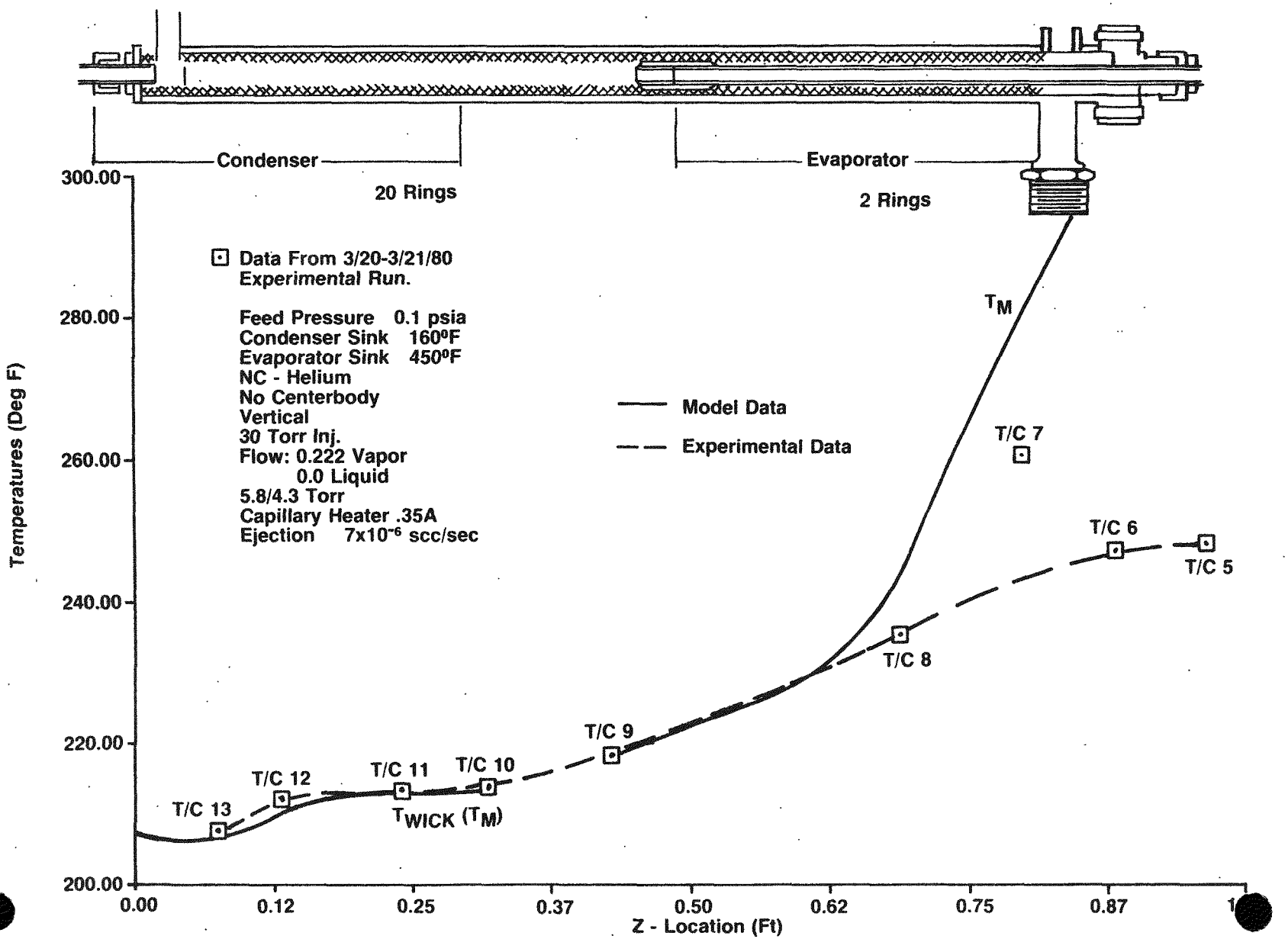

18.09.52 03/28/80

Figure 3.7.12

Modified Serial No. EX NCGS Prior To Installation On GDS

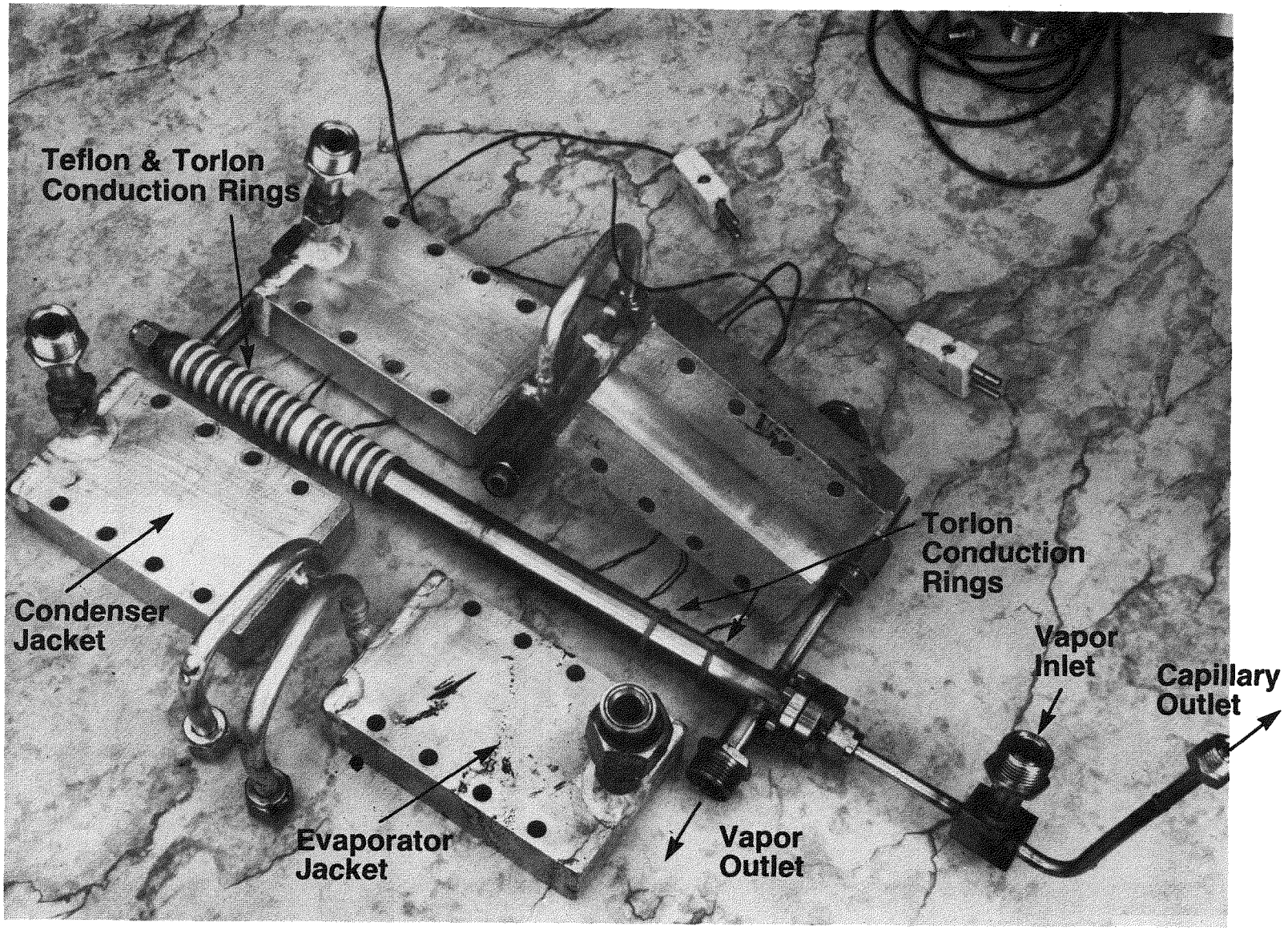

Figure 3.7.13

Turbine Back Pressure Variation

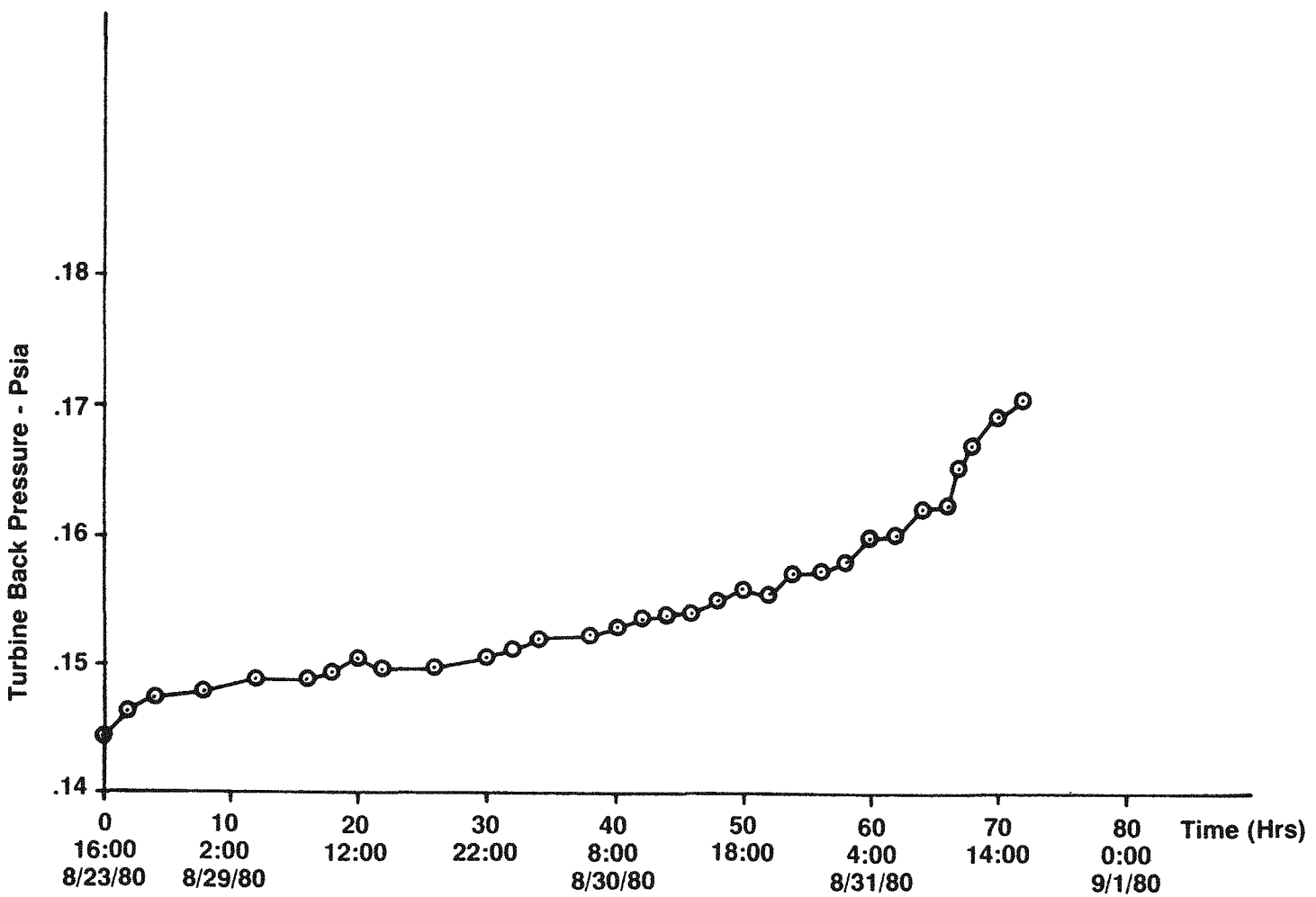

Figure 3.7.14

Centrifugal Separator

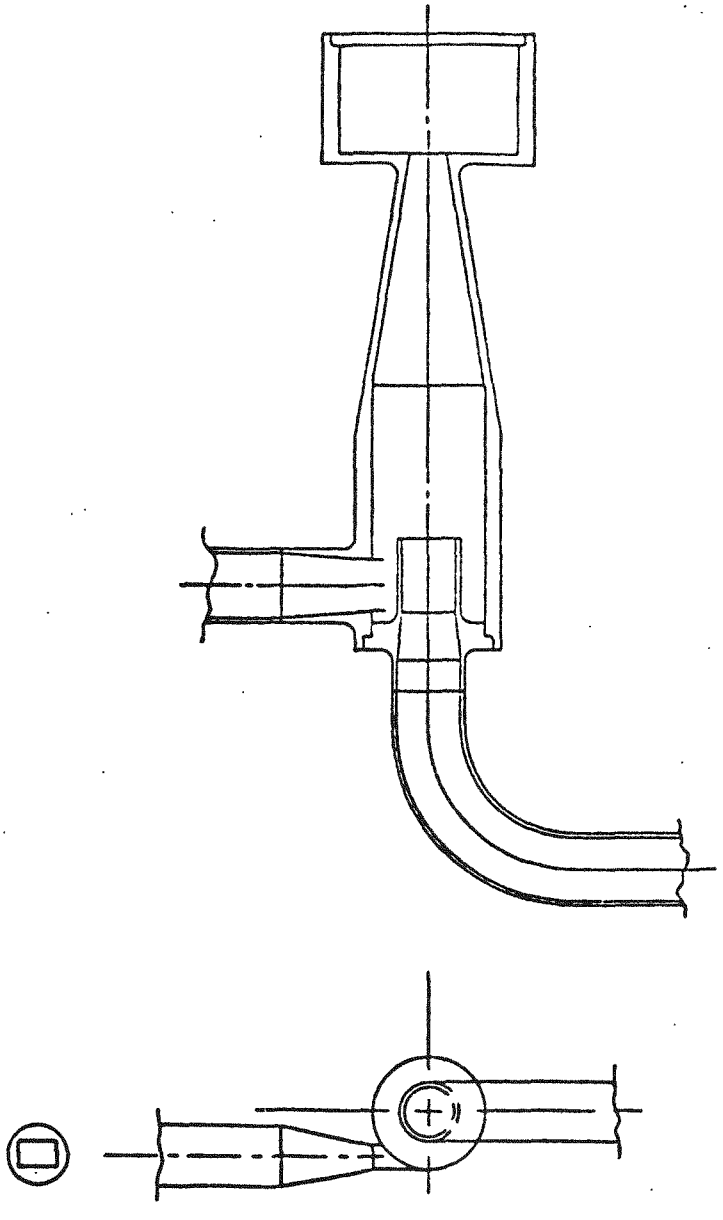

Figure 3.7.15

3.8 Control System

The DIPS control system is designed to accommodate a wide variety of requirements. Some of these are fundamental control functions required on any organic Rankine cycle system, some are necessitated by the particular requirements of the changing thermal output of the isotope heat source used in the DIPS system, and additional functions are necessitated by spacecraft requirements for a flight system.

The basic control functions include turbine loop flow control, turbine inlet temperature control, combined rotating unit (CRU) speed control, electrical overload protection, output voltage regulation, and system heat rejection control.

The control functions are performed by two separate modules: a "valve pack" and an electronic controller. The valve pack contains the turbine loop flow and temperature controls as well as the radiator bypass valve. The electronic controller provides voltage regulation, overload protection, and speed control.

The fluid loop controls are powered directly by mechanical and hydraulic forces and require no internal or external electrical power for operation. Because of this, the DIPS system can continue to operate safely under conditions of electrical overload.

The DIPS CRU is structurally designed to withstand continuous operation in a frequency wild (no speed control) mode. This allows disabling the speed control system when desired. This capability

provides the ability to run the CRU at higher speed during launch and orbital maneuvers resulting in added bearing load capability and jet condenser jet stiffness during periods of high shock and vibration.

A block diagram showing the location of the control components in the system is shown in Figure 3.8.1.

3.8.1 Turbine Flow Control

A Rankine cycle system utilizes a control system to maintain turbine inlet conditions at the selected design point. Keeping turbine inlet conditions relatively close to the design point ensures that the system will be able to produce the required power and that the turbine will always be supplied with superheated vapor. This will avoid erosion damage from partially vaporized working fluid. The flow control method employed in KIPS adjusts the boiler flow rate to maintain nearly constant turbine inlet temperature.

A cross section of the integrated valve pack including the turbine loop flow control valve is shown in Figure 3.8.2. The inlet receives flow from the system pump and the regulated outlet flow enters the turbine loop. The pressure regulator bellows assembly senses valve chamber pressure on the side facing the valve chamber. The other side of the bellows is connected via internal porting to the valve outlet. The bellows therefore moves in response to pressure drop across the temperature control orifice. When turbine inlet temperature is constant, the temperature control flapper remains in a fixed position and the effective orifice area of the temperature control orifice is constant. With the pressure regulator controlling the pressure drop across the orifice, system flow is kept constant regardless of inlet pressure. The pressure regulator performs this function by actuating the pressure regulator flapper which throttles inlet flow as required to keep the temperature control orifice pressure drop constant. Changes in valve inlet pressure are therefore prevented from affecting the flow rate through the valve.

The resulting valve performance characteristic curves are shown on Figure 3.8.3 where it can be noted that flow remains essentially constant

(for constant turbine inlet temperature) as overall valve delta P varies from 20 to 160 psi.

With the pressure drop across the temperature control orifice held nearly constant, as turbine inlet temperature increases, expansion of the NaK in the thermal sensor moves the temperature control flapper away from the temperature control orifice, thus increasing the area and the system flow rate. This effect is shown for several steady state temperatures on Figure 3.8.2.

The flow control valve was designed with redundant bellows in the pressure regulator assembly. These were sized such that a failure of either bellows would have only a minor effect on system operation. The effect of a cracked or failed bellows is a shift of turbine inlet temperature of less than 2°F. Dual thermal sensor assemblies are utilized to provide redundancy in the event of a bellows failure in the temperature sensing portion of the valve.

At the conclusion of Phase I of the program the flow control valve was fully operational with a functioning NaK filled temperature sensor. During the interval between the conclusion of Phase I and the start of Phase II however, a flow shift was observed to occur. Since the flow shift was in the decreasing flow direction, it was hypothesized that the flow shift was caused by a bubble of gas migrating from the hot temperature bulb end of the temperature sensor to the cooler transition capillary or actuator end of the sensor. The resulting contraction of the bubble would cause the flow control valve to reduce turbine loop flow and consequently increase the turbine inlet temperature. As a result of this occurance, Phase II included an effort to investigate the problem and to define and test a solution.

It was believed that the most likely source of a trapped bubble was a deficiency in the filling procedure. Another possible source of gas is hydrogen absorbed into the temperature sensor materials during heat treating and gradually accumulating in the sensor as it is given off from the internal surfaces. It was decided to open the temperature sensor which had exhibited

the shift in the examination stage of a mass spectrometer. The NaK was expelled from the sensor using helium and the mass spectrometer used to determine if a gas bubble was expelled with the NaK and, if so, what was its composition. By this means it was determined that the sensor contained argon. Since argon was used to prevent oxygen contamination of the NaK during filling it was concluded that the temperature sensor shift resulted from an inadequate filling procedure. This test was carried out at Battelle Columbus Laboratories.

It was decided to contract with Battelle Columbus Laboratories to develop a filling procedure. The Battelle report describing the filling procedure development is presented as Appendix A. The temperature sensors were solid filled with NaK at Battelle with the entire sensor assembly maintained at an elevated temperature. The temperature sensor was then installed on a flow control valve and operated under conditions closely simulating those seen in the DIPS on the hot flow stand at Sundstrand. The temperature sensor was then calibrated to begin to stroke at the desired temperature and the tube extensions left on the assembly for filling were removed. The temperature sensor tubes were resealed using a crimp and weld procedure identical to that used at Battelle. The flow control valve was then installed on the GDS and shimming adjustments were made to obtain the desired turbine inlet temperature. The valve maintained a steady turbine inlet temperature throughout many startup/shutdown cycles thereafter. The flow control valve with temperature sensor achieved over 2000 hours of operation.

3.8.2 Radiator Bypass Flow Control

The primary means of GDS heat rejection is via the auxiliary heat exchanger. The heat exchanger is large enough to reject system waste heat at no load and the highest heat sink temperature. At other operating conditions, the heat exchanger is oversized and it is desirable to limit the heat rejected to maximize GDS efficiency. To this end tight control of the jet condenser inlet temperature is required and is obtained by controlling

a bypass loop around the heat rejection heat exchanger.

A thermal bulb type valve is used for the radiator bypass valve. A cross section of the valve is shown in Figure 3.8.2. The bulb is integrated into the valve block and filter assembly. Warm fluid from the pump passes through a controlled orifice and mixes with cooler radiator outlet fluid. The mixed fluid is circulated around the thermal bulb and then exits to the jet condenser. When the mixed fluid temperature is excessive, expansion of the fluid in the thermal bulb moves the valve poppet closer to the orifice restricting the influx of warm fluid to reduce the mixed fluid temperature. The actuation bellows free length is sufficiently shorter than its operating length so that a leak in the thermal bulb or bellows will cause the bellows to contract pulling the auxiliary poppet against the seat to completely shut off the bypass flow.

The radiator bypass valve has only two flexing parts, the two bellows in the thermal bulb assembly. These bellows were designed such that cyclic fatigue would not occur, although a failure here is not critical to continued system operation. The working fluid in the thermal bulb is Dowtherm A, identical to the system working fluid, so there is no ill effect on the system fluid from a leaking bellows. Redundancy was therefore not provided on the radiator bypass valve bellows.

3.8.3 Electrical Controls

The controller provides output power conditioning, voltage regulation and speed control. The controller is powered by the alternator and needs no external power supply. Power conditioning includes rectifiers and filters to attain a voltage ripple of less than 0.1%. Voltage regulation provides 28V DC $\pm$ 2% and the speed is controlled within 2% of design speed.

The Phase I controller was built to simulate the flight system controller and was actively cooled by the radiator outlet liquid. The radiator outlet liquid is at the coldest temperature in the system. Figure 3.8.4 shows the Phase I controller block diagram.

Speed control for the Phase I controller was accomplished by a frequency discriminator which monitored the alternator output frequency (which is proportional to speed), a comparator (pulse width modulator), and the parasitic load resistor.

The parasitic load is comprised of three parasitic load resistors (PLRs), each capable of drawing 50% of the load. Thus, two PLRs are capable of providing full load. Having three PLRs with any two capable of handling full load greatly increases the reliability of the system.

The frequency discriminator consisted of a passive, tuned circuit which produced a DC output voltage proportional to system frequency near the resonant frequency of the tuned circuit.

The Pulse Width Modulator (PWM) comparator was set at a 50% duty cycle at a voltage proportional to 1122 Hz (33,700 rpm). The PWM rate was controlled by the carrier frequency which is the ripple frequency of the three phase, full wave bridge rectifier. The PWM comparator turned the power switches on or off, applying or removing power to the PLRs. Since the carrier frequency is high (6 x 1122 = 6732 Hz), the time averaged effect is a steady load determined by the PLR duty cycle. The duty cycle changed in response to system capability and customer loading.

The voltage regulator was pulse width modulated to minimize the regulating losses. The switching point of the PWM regulator was set at the 50% duty cycle of the carrier frequency. When the output voltage was low, the PWM duty cycle went toward 100% causing maximum field current to flow in the field winding, thereby increasing the generator voltage. When the output was high, the PWM duty cycle tended toward zero, allowing the field current and generator output voltage to decay.

The overload protection circuit used a frequency discriminator similar to the speed control frequency discriminator and a comparator to detect when turbine speed falls below 95%. When this was detected, the switching amplifier was turned off, decreasing the generator output voltage and lowering the generator load. The generator output voltage would not decrease below a small residual voltage which was sufficient to operate the frequency discriminator, comparator and switching amplifier.

The Phase I controller schematic is shown in Figure 3.8.5 and a drawing of the component arrangement in Figure 3.8.6 with predicted operating temperatures.

Controller Development

During Phase II it became necessary to perform significant development on the controller, firstly to improve rectifier performance and secondly to meet the 0.1% ripple requirement. In order to facilitate this development the Phase II controller was located outside the vacuum chamber and was air cooled instead of liquid cooled. In addition, the ripple requirements necessitated considerable redesign and the decision was made to build a breadboard version rather than a simulated flight design controller. Figure 3.8.7 shows the block diagram for the final Phase II controller and Figure 3.8.8 the controller schematic.

The controller circuitry can be divided into three functional groups, the speed regulator, power conditioning and the voltage regulator. The speed regulator controlled alternator field current to provide constant torque on the shaft and constant power output. Since the output voltage is regulated to 28 volts the generator is essentially a constant current source and the current either goes to the customer load or is diverted to the PLRs. The voltage regulator acts as a shunt regulator providing a constant 28V DC by shunting the right amount of current to the PLRs. Because of these changes in controller logic the rotational speed became essentially independent of customer load. Customer load could be changed from 0 to 100% of system capacity with resulting speed changes of less than 60 rpm.

Power conditioning is attained by a full wave bridge rectifier circuit. In Phase I this comprised six rectifiers. During development twelve and eighteen rectifiers were incorporated in the bridge to improve rectifier performance.

Filtering of the output power was necessary to obtain the 0.1% voltage ripple. This was obtained using a large inductor combined with capacitors.

KIPS Block Diagram

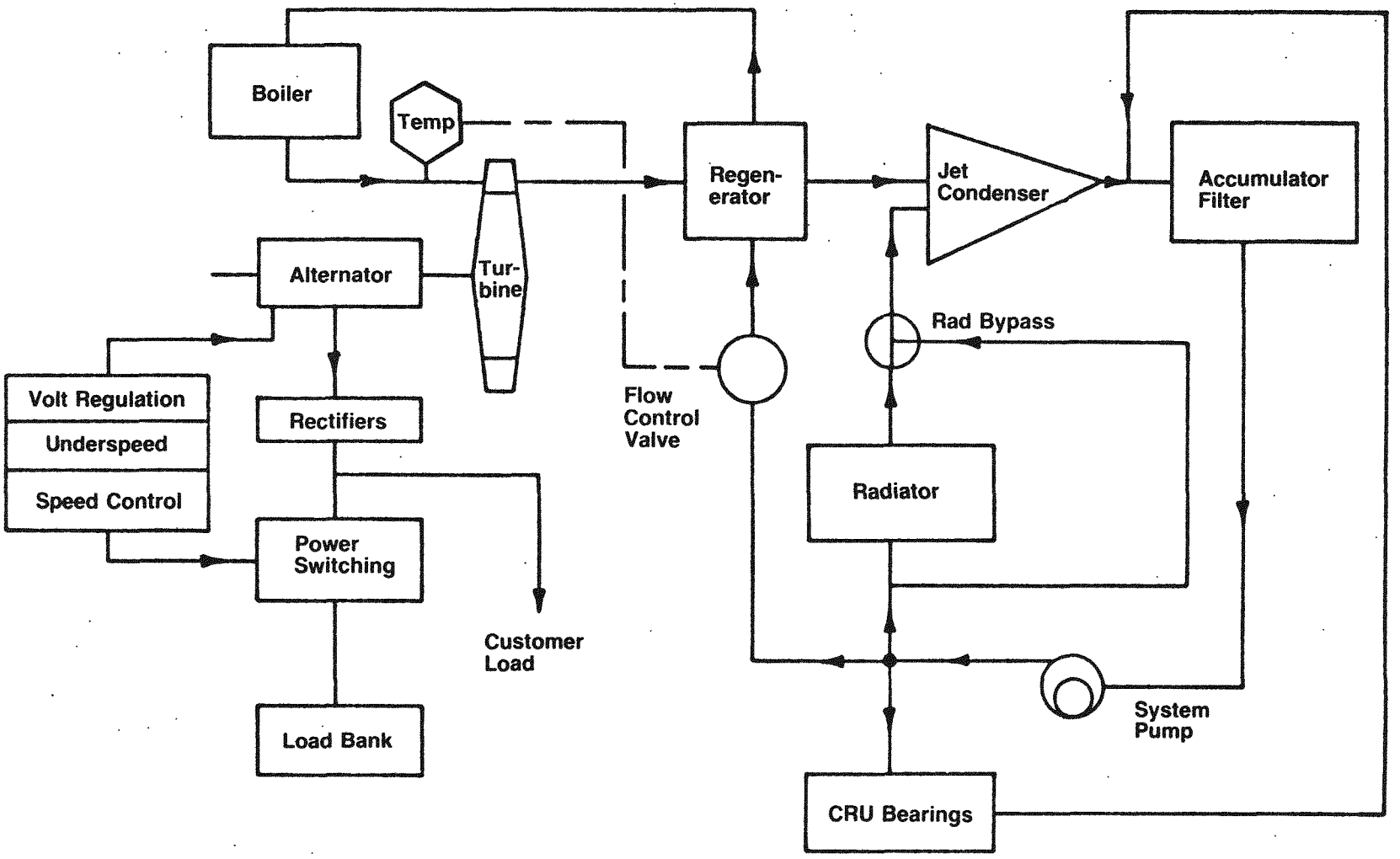

Figure 3.8.1

GDS Fluid Loop Controls

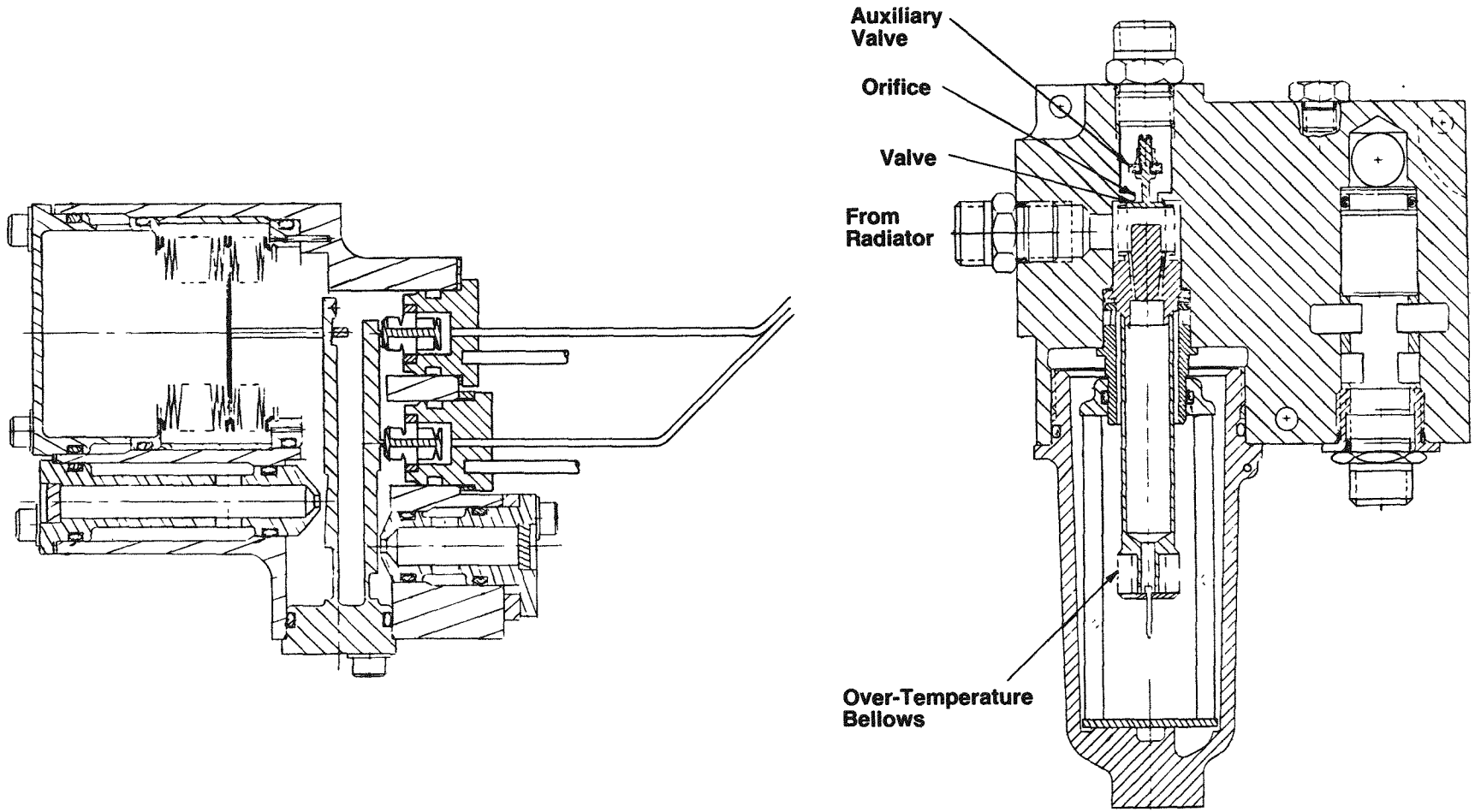

Figure 3.8.2

KIPS Turbine Loop Flow Control Valve

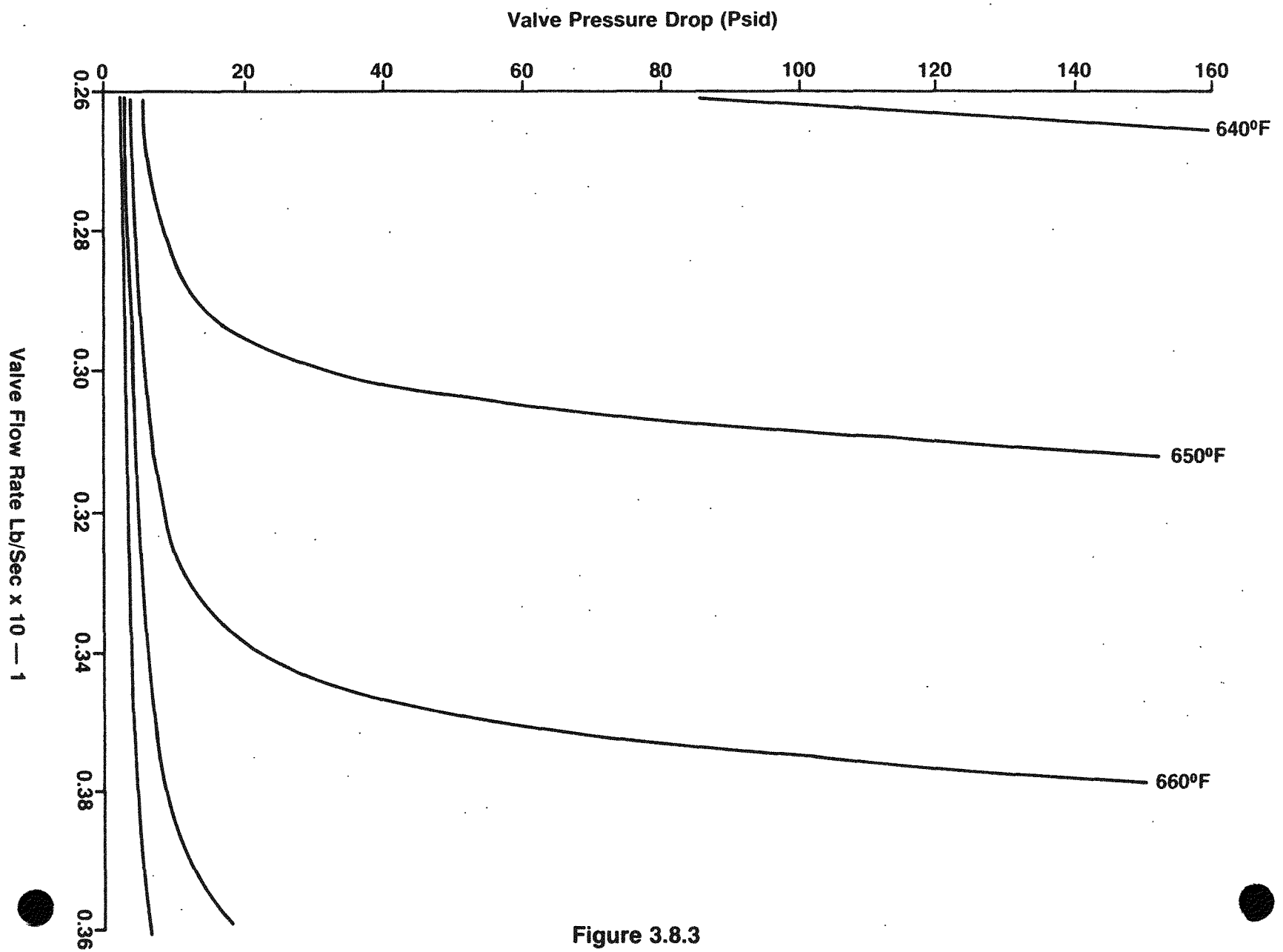

Figure 3.8.3

Phase I Control System Block Diagram

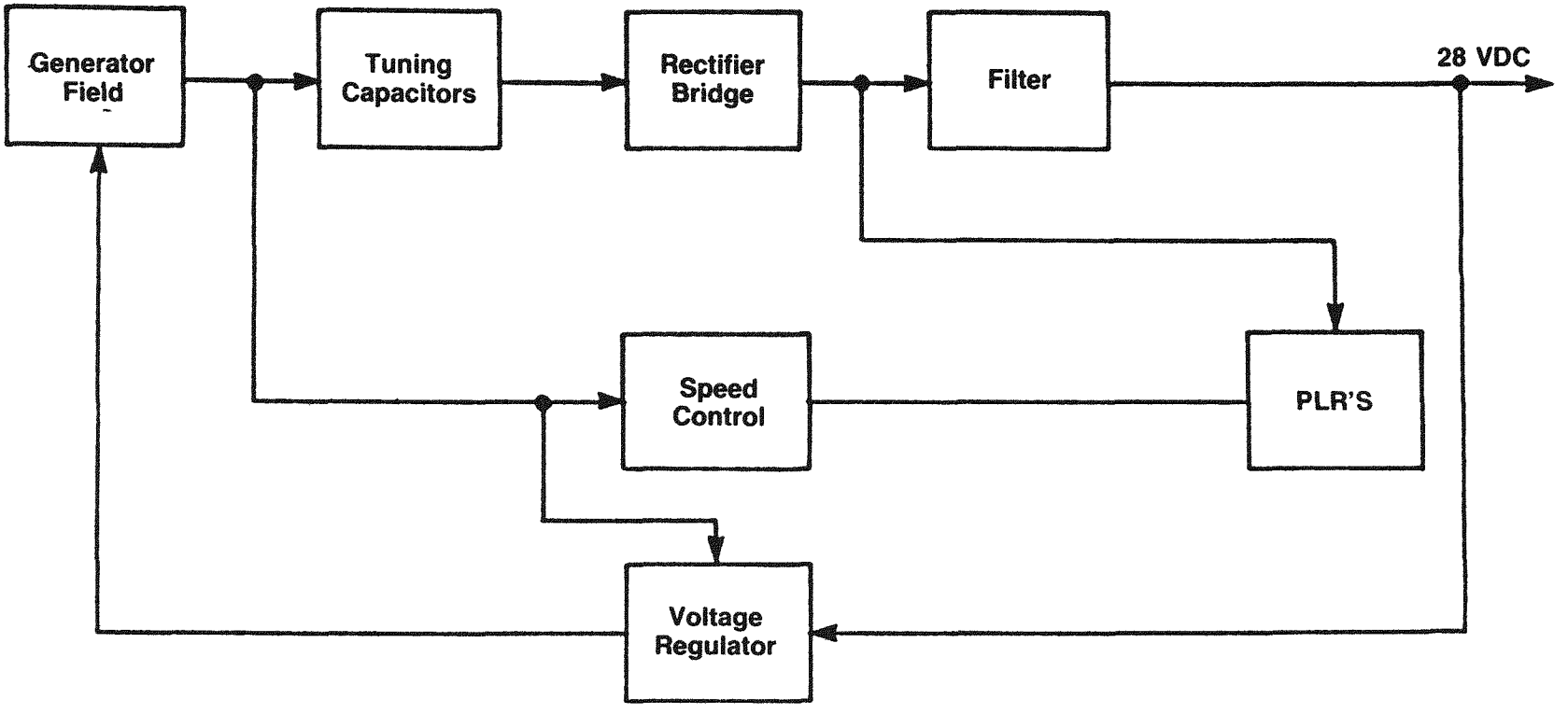

Figure 3.8.4

Alternator Controller Schematic Phase I

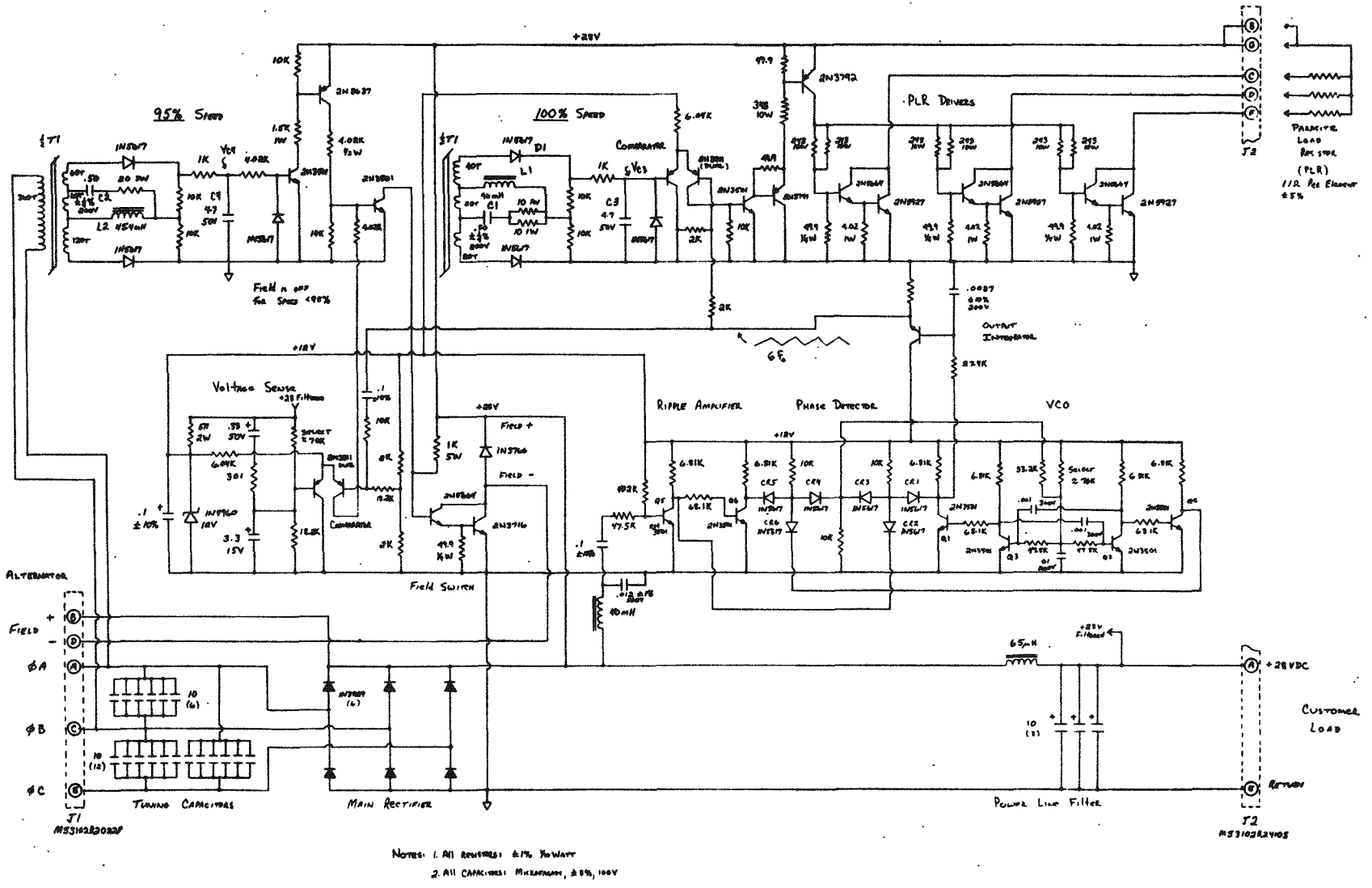

Figure 3.8.5

GDS Controller - Phase I

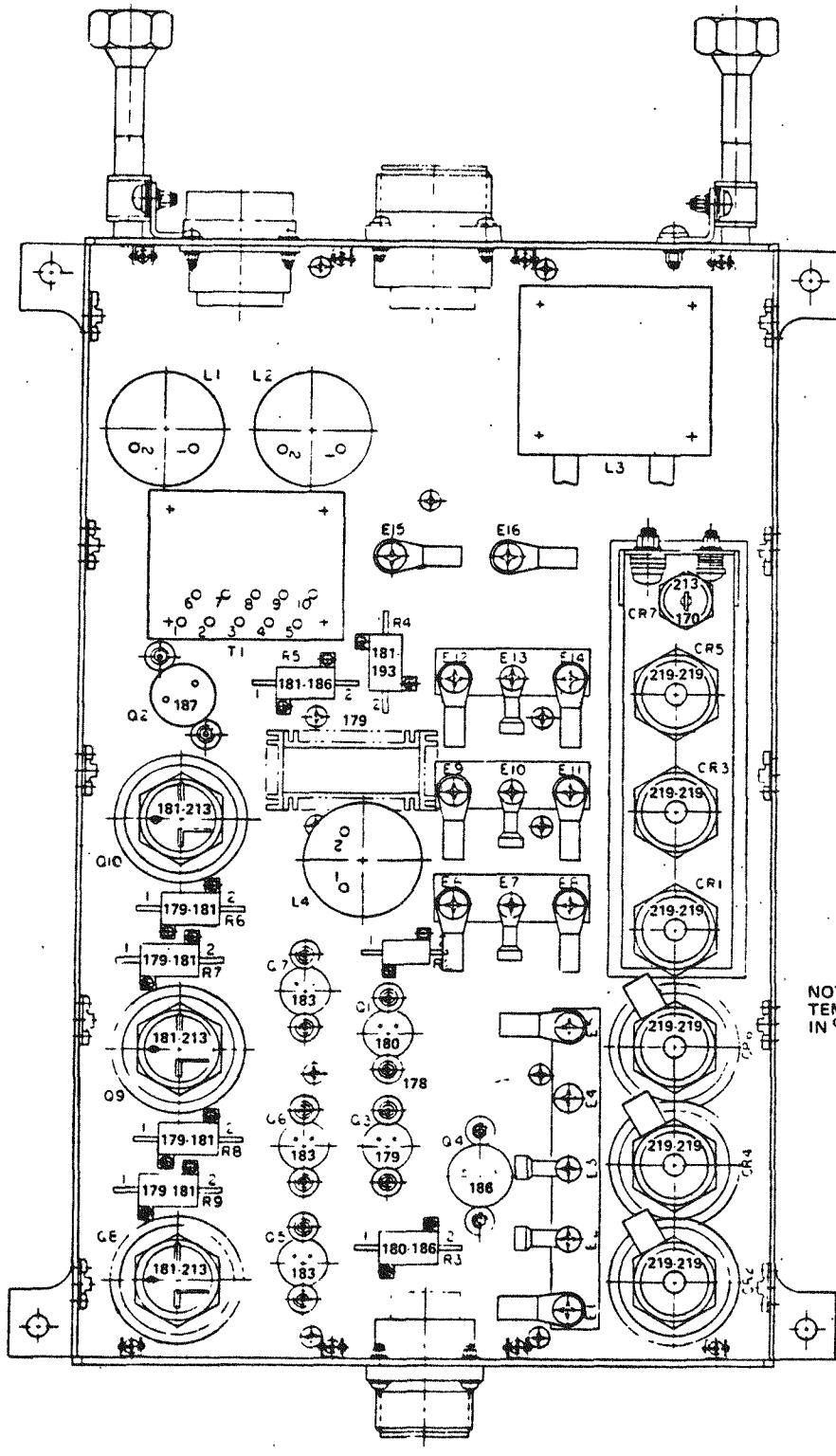

Figure 3.8.6

Phase II Controller Block Diagram

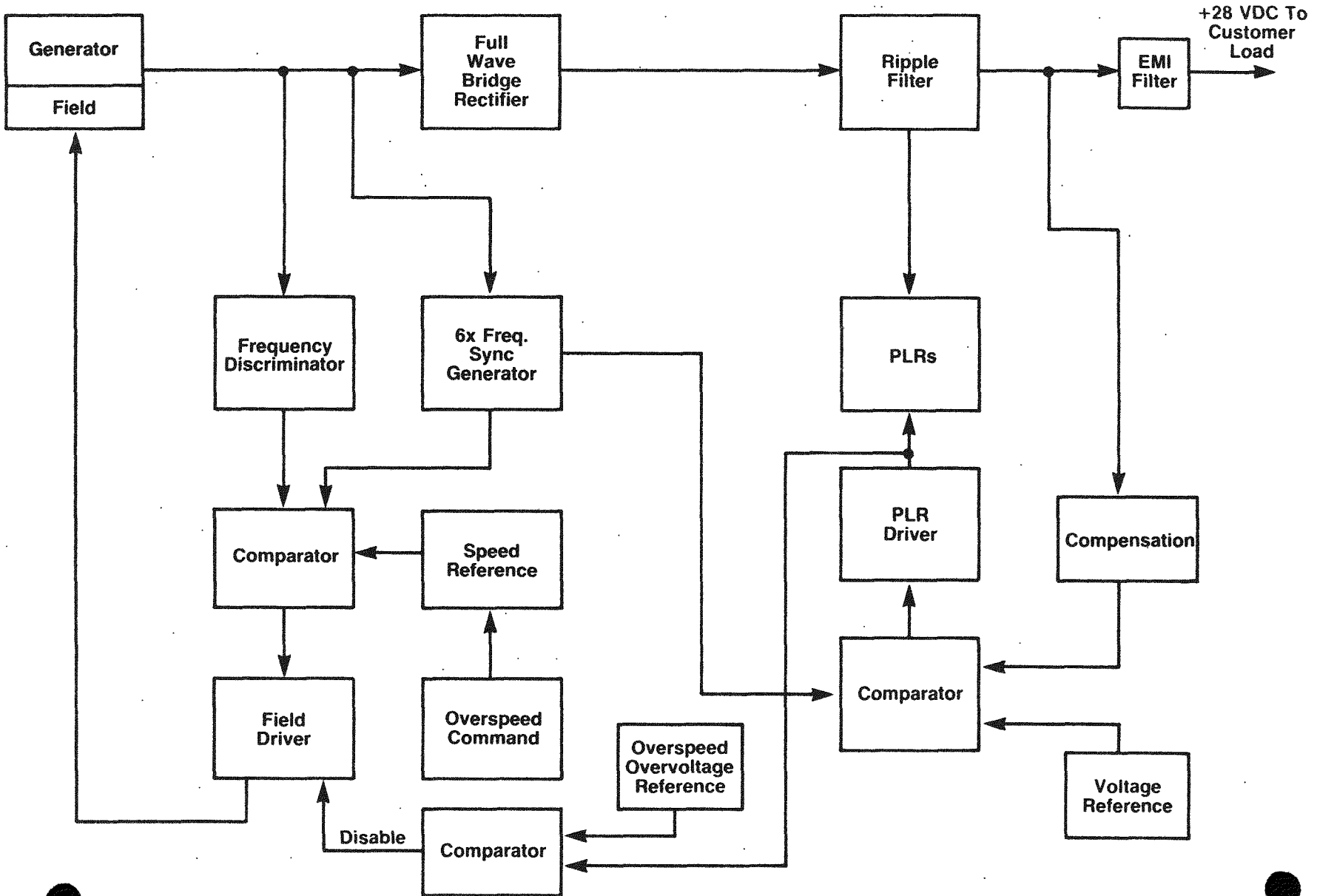

Figure 3.8.7

Controller Schematic - Phase II

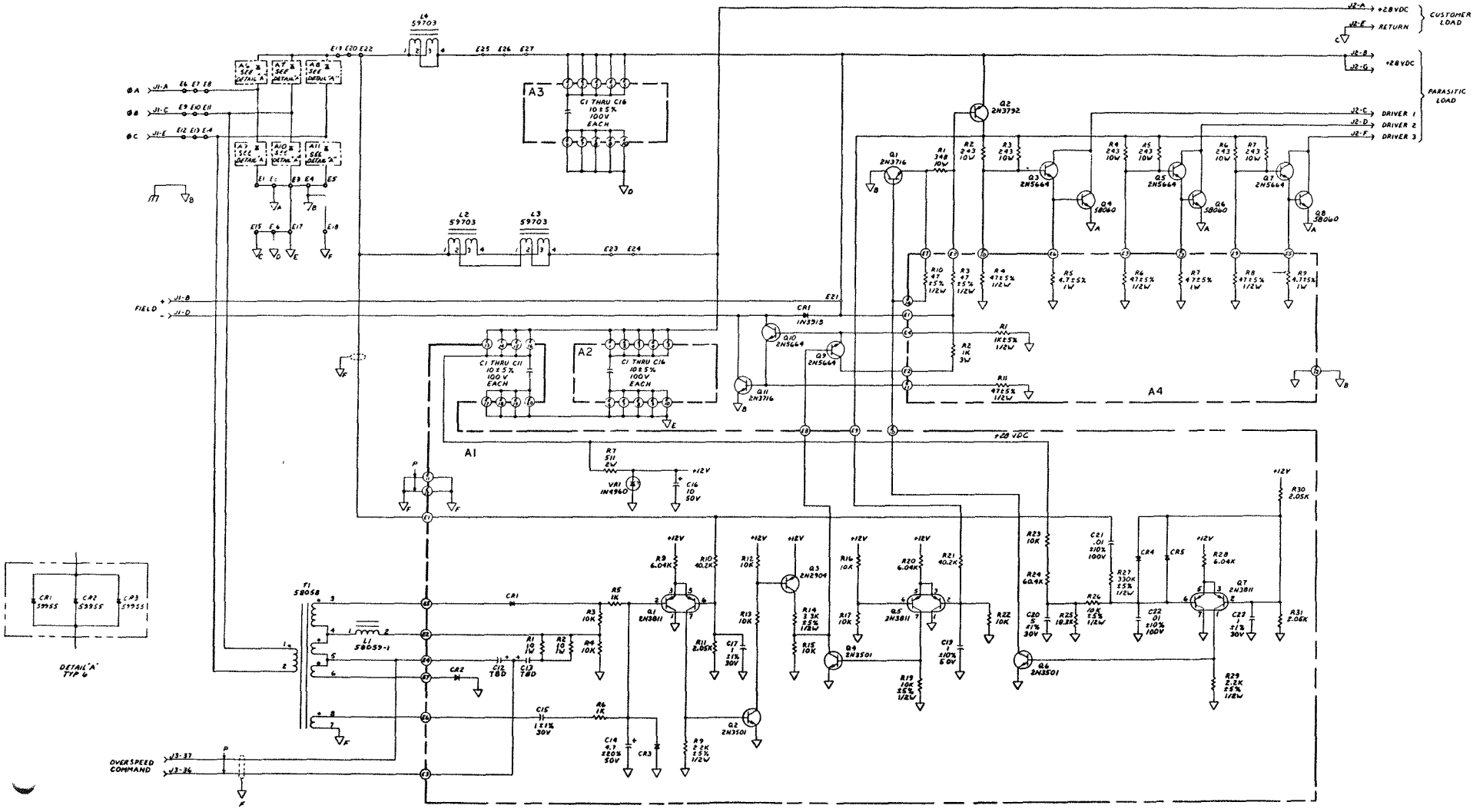

Figure 3.8.8

Profilometer Traces

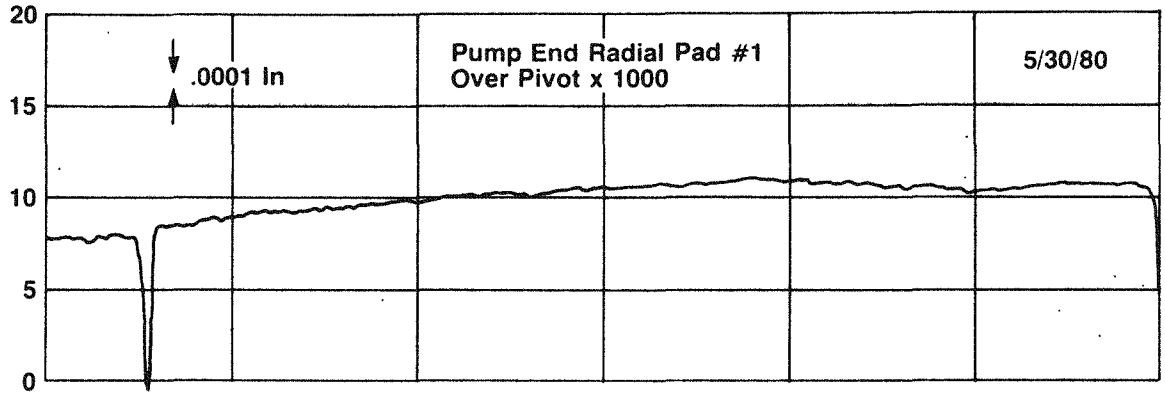

(a) Pump End Radial Bearing Pad

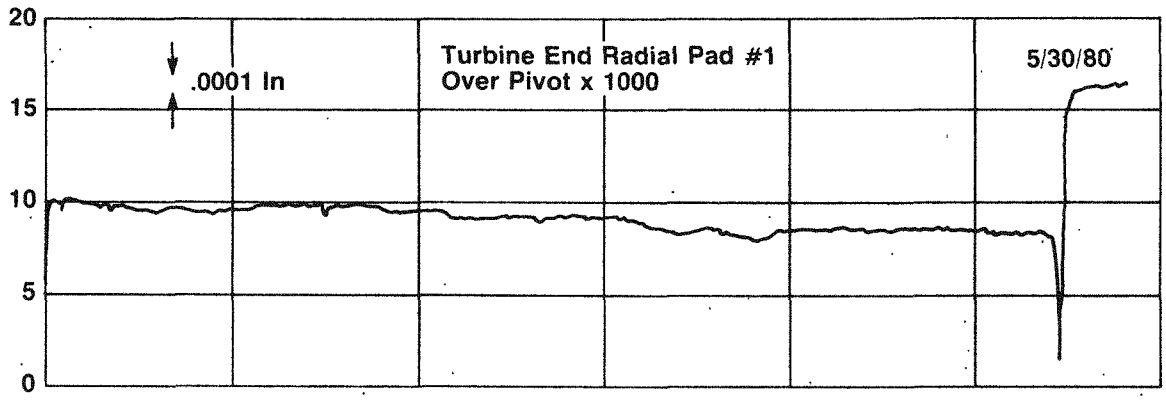

(b) Turbine End Radial Bearing Pad

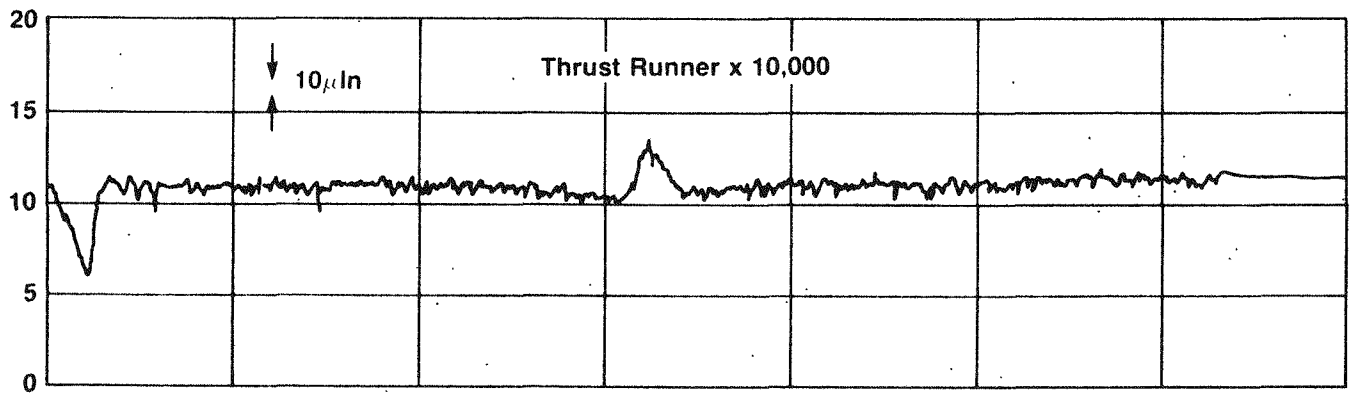

(c) Thrust Runner

Figure 10

Radial Pivot Surfaces
Pump End

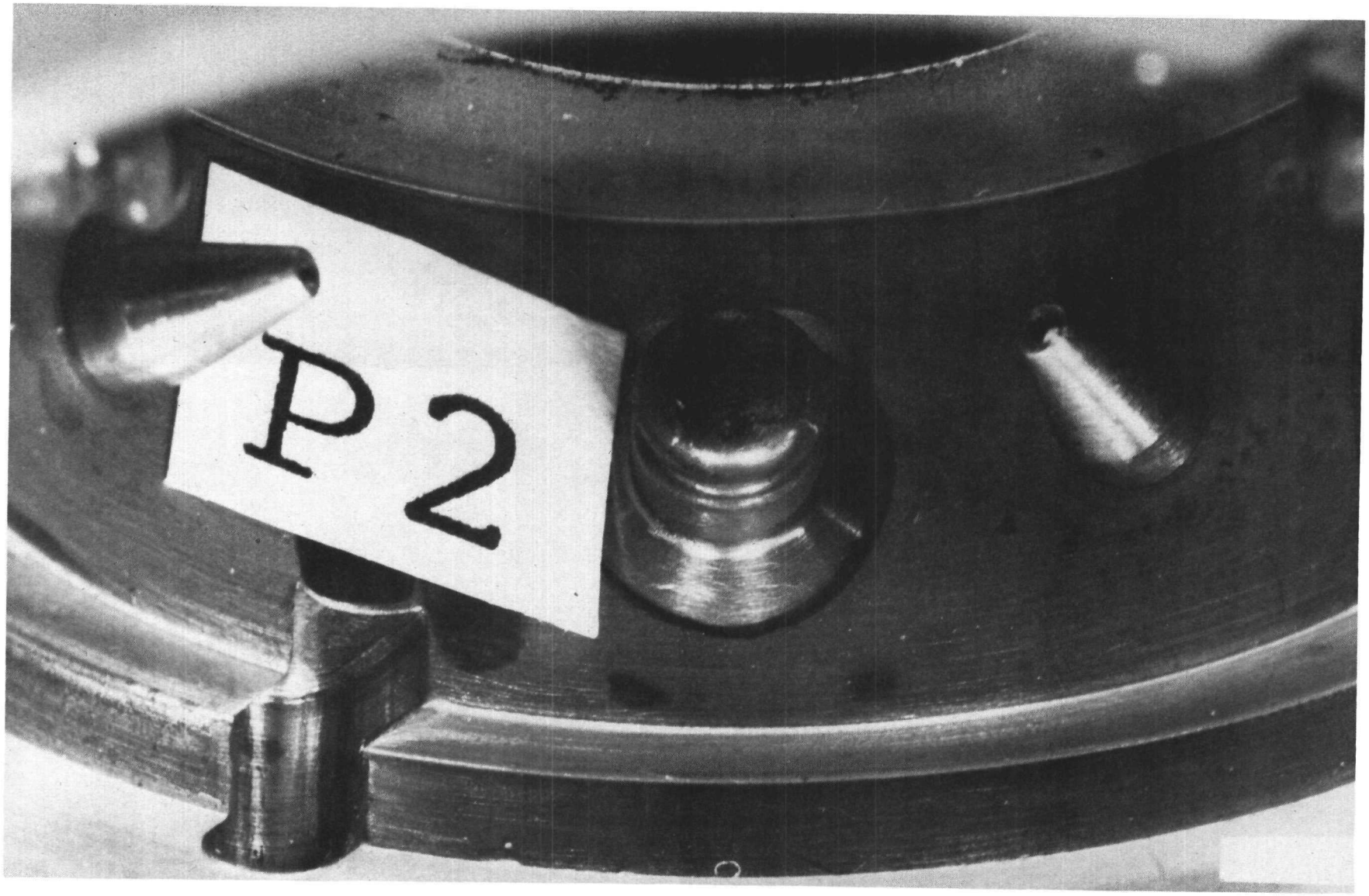

Figure 9

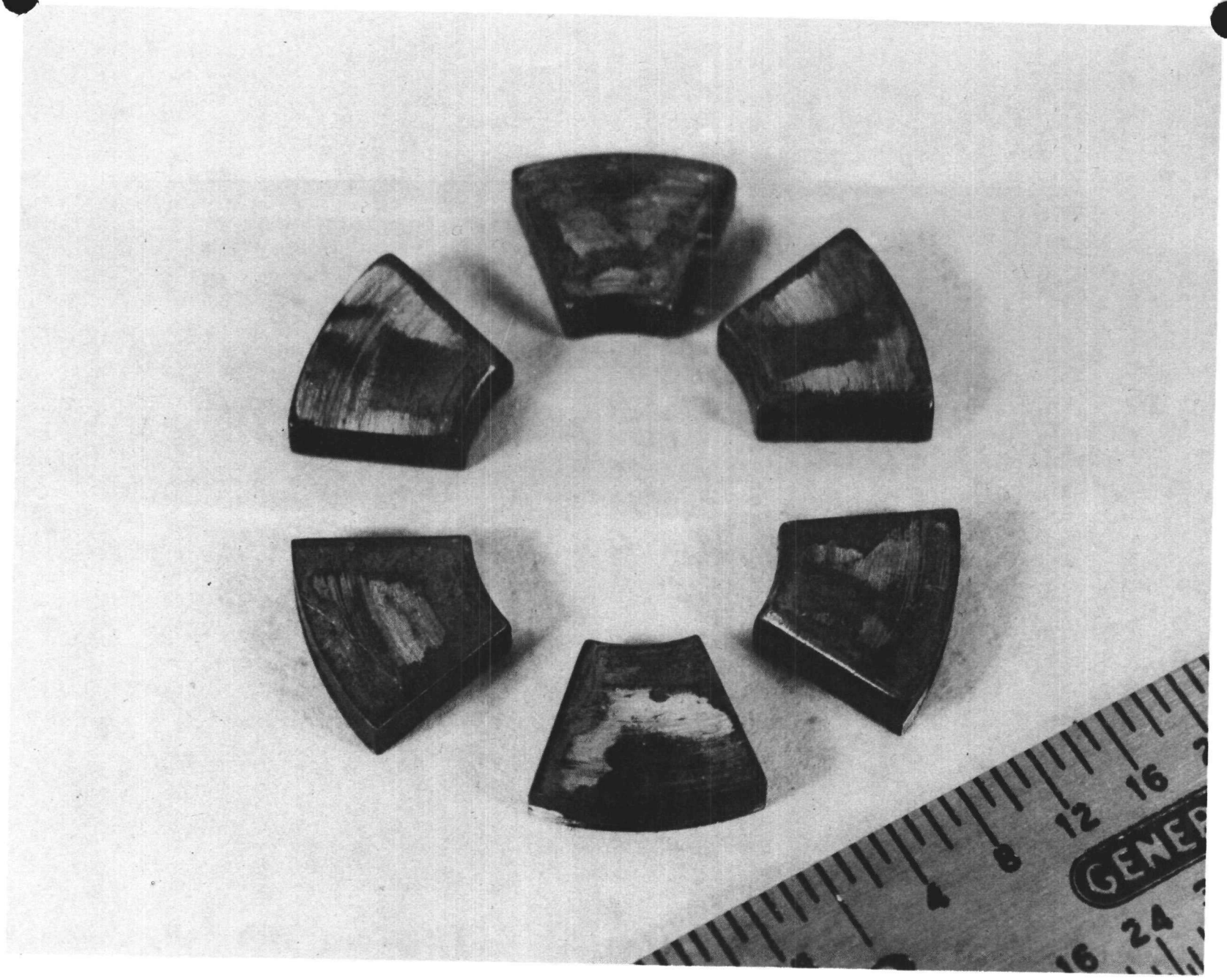

Figure 8

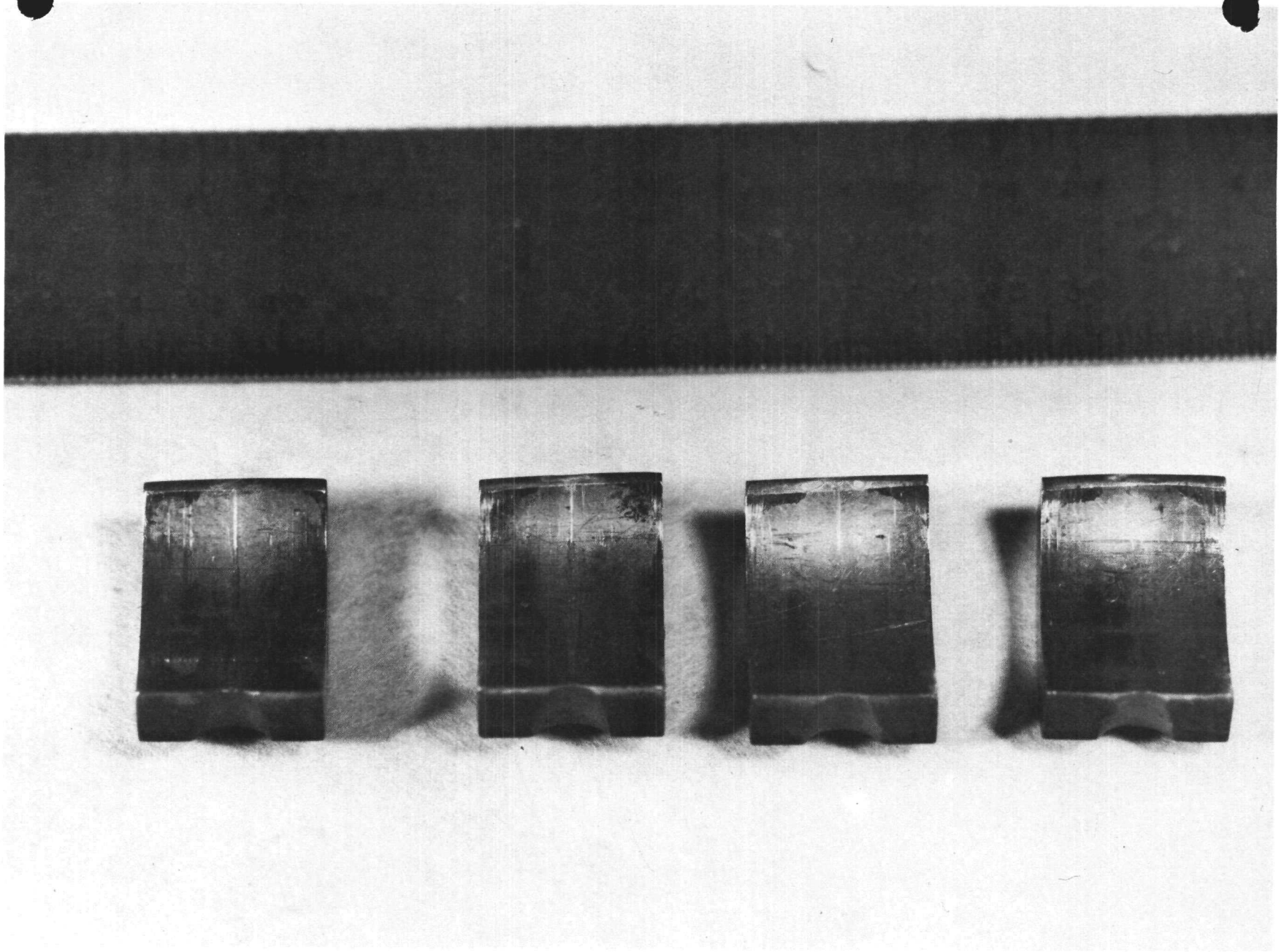

Figure 7

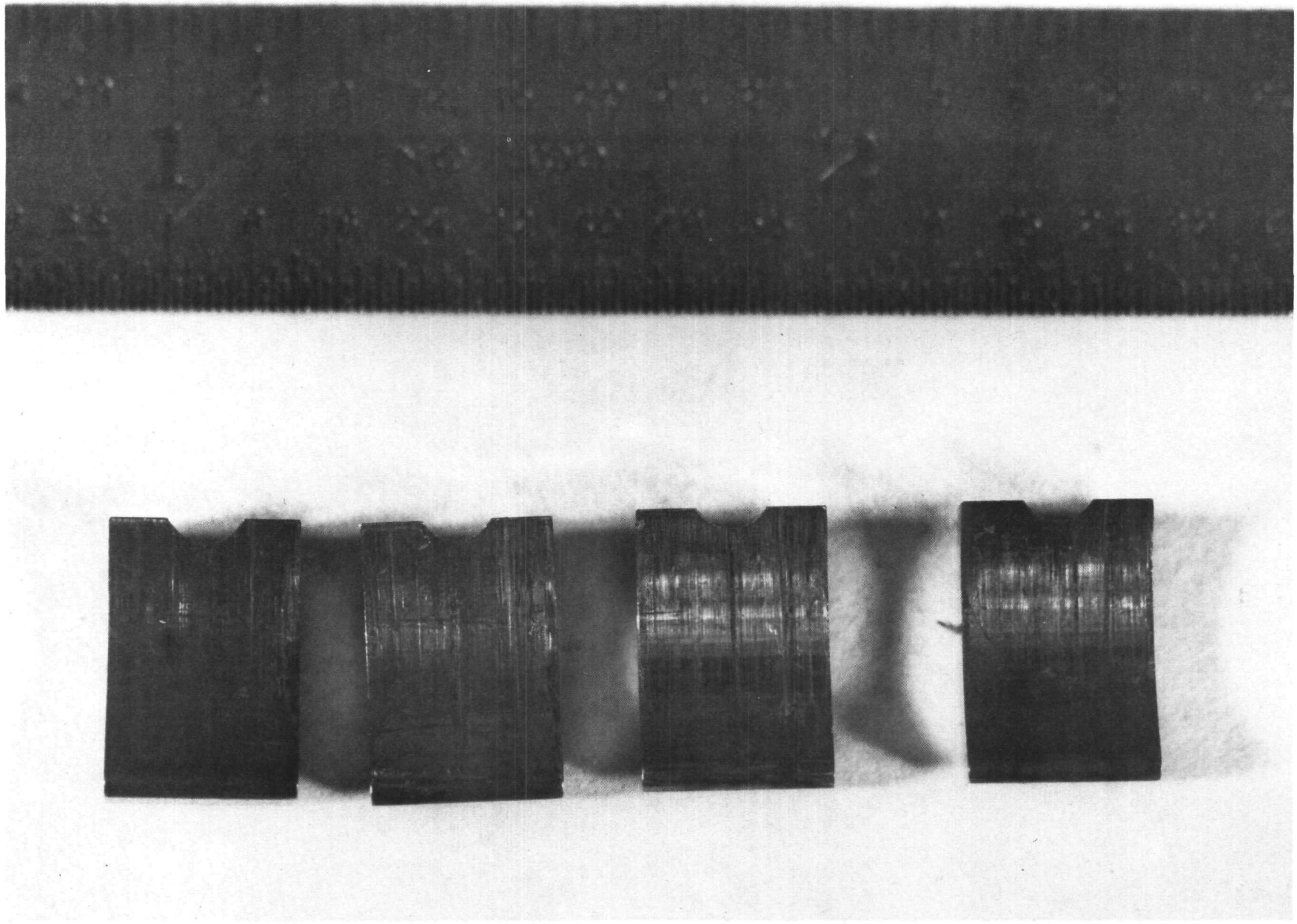

Figure 6

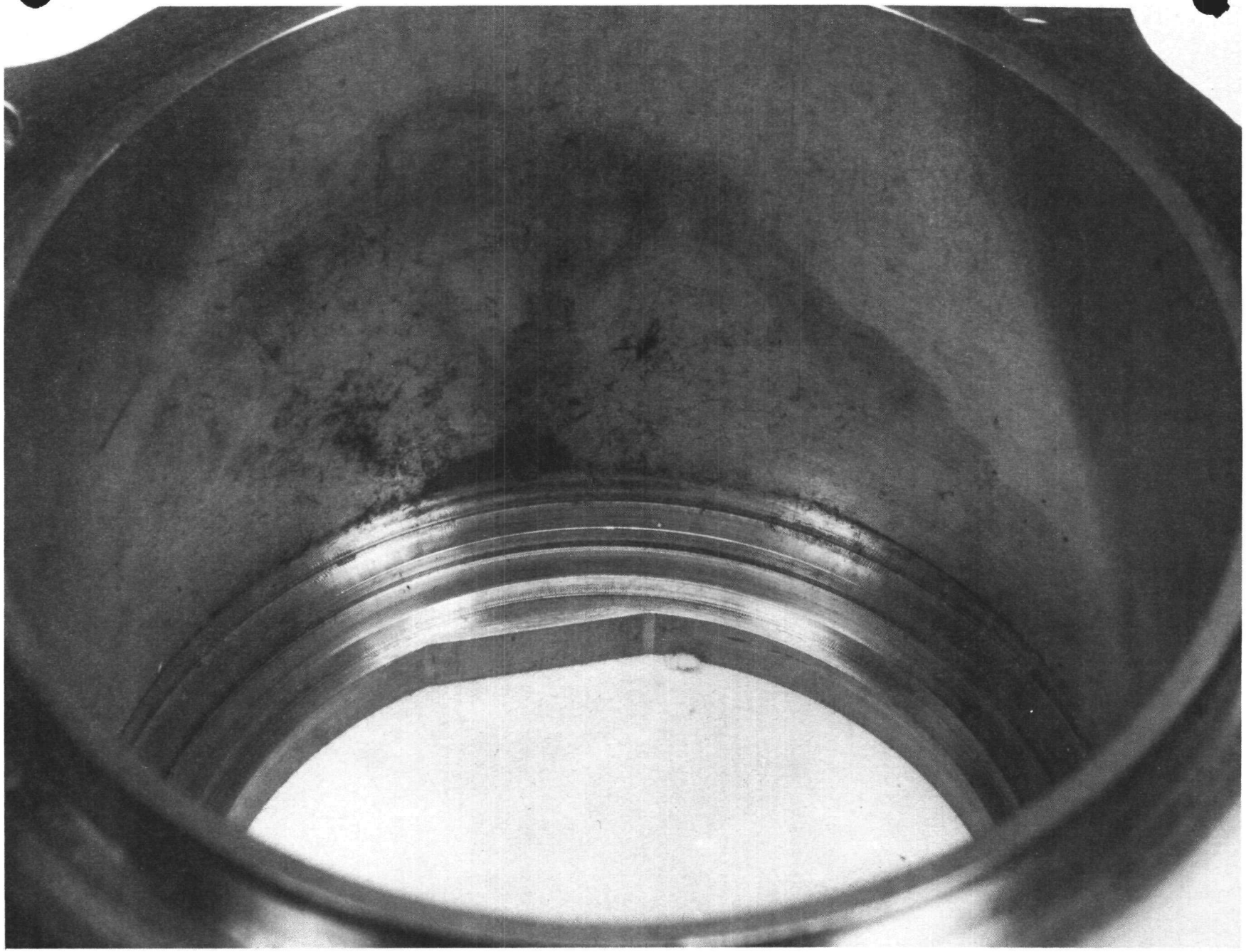

Figure 5

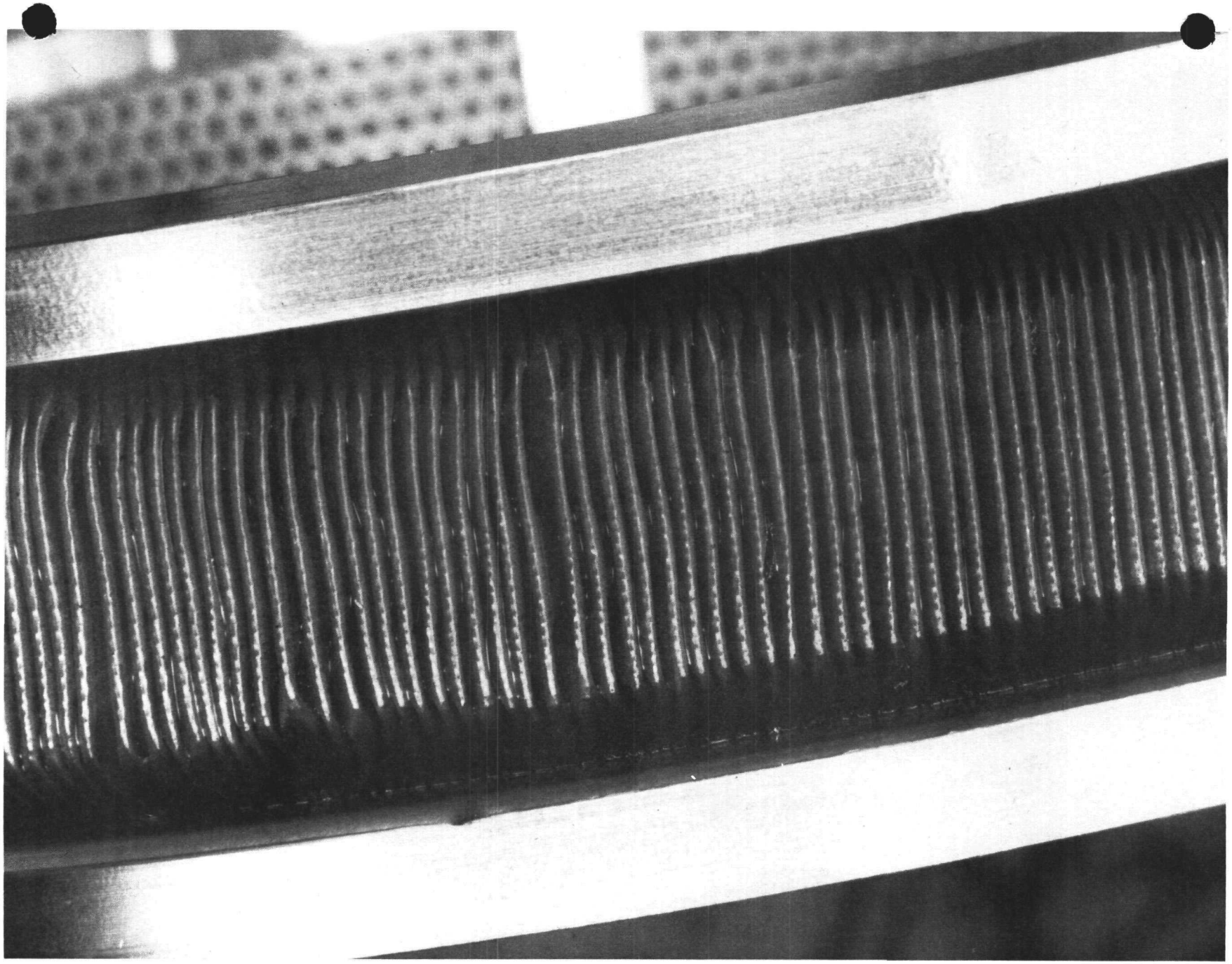

Figure 4

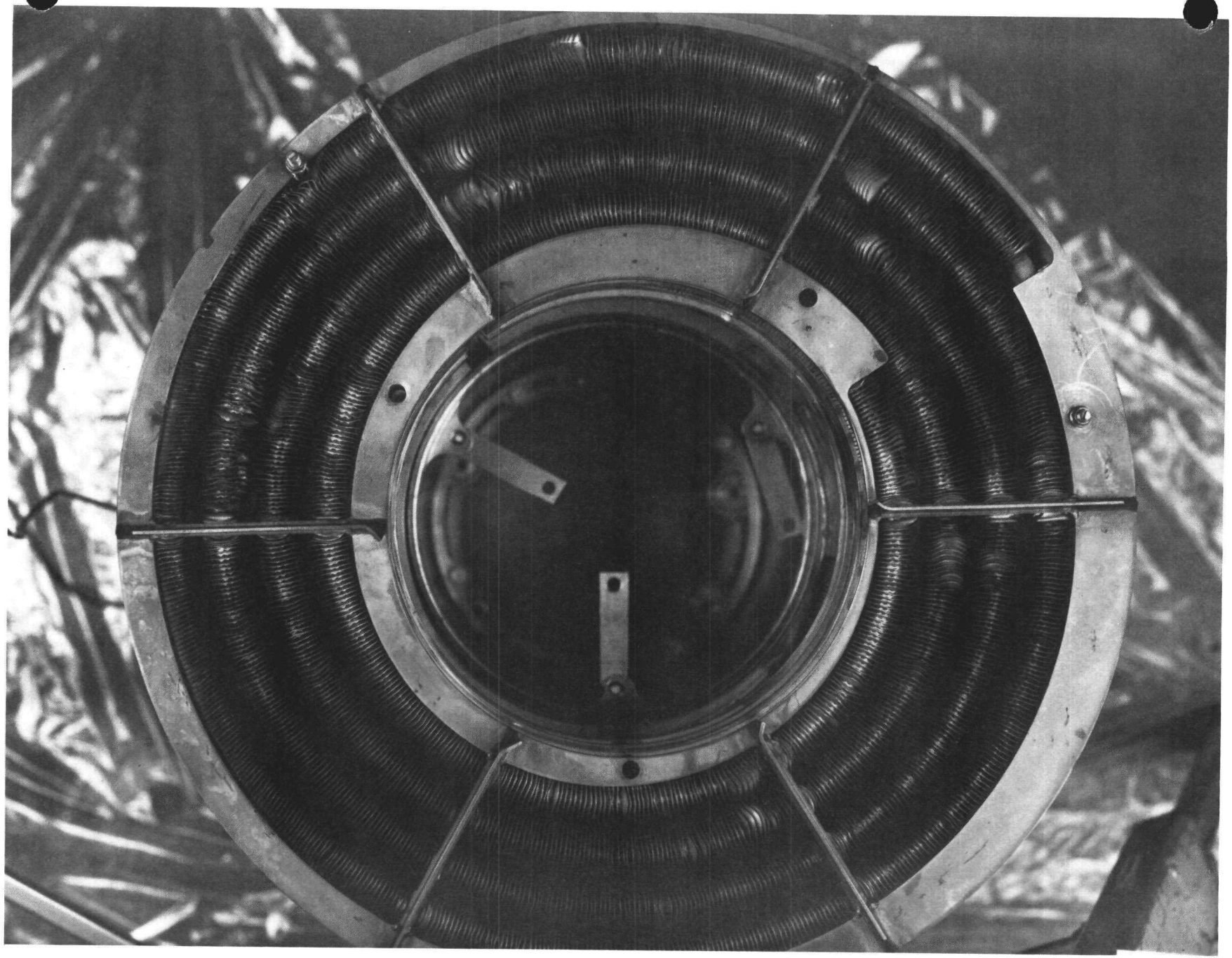

Figure 3

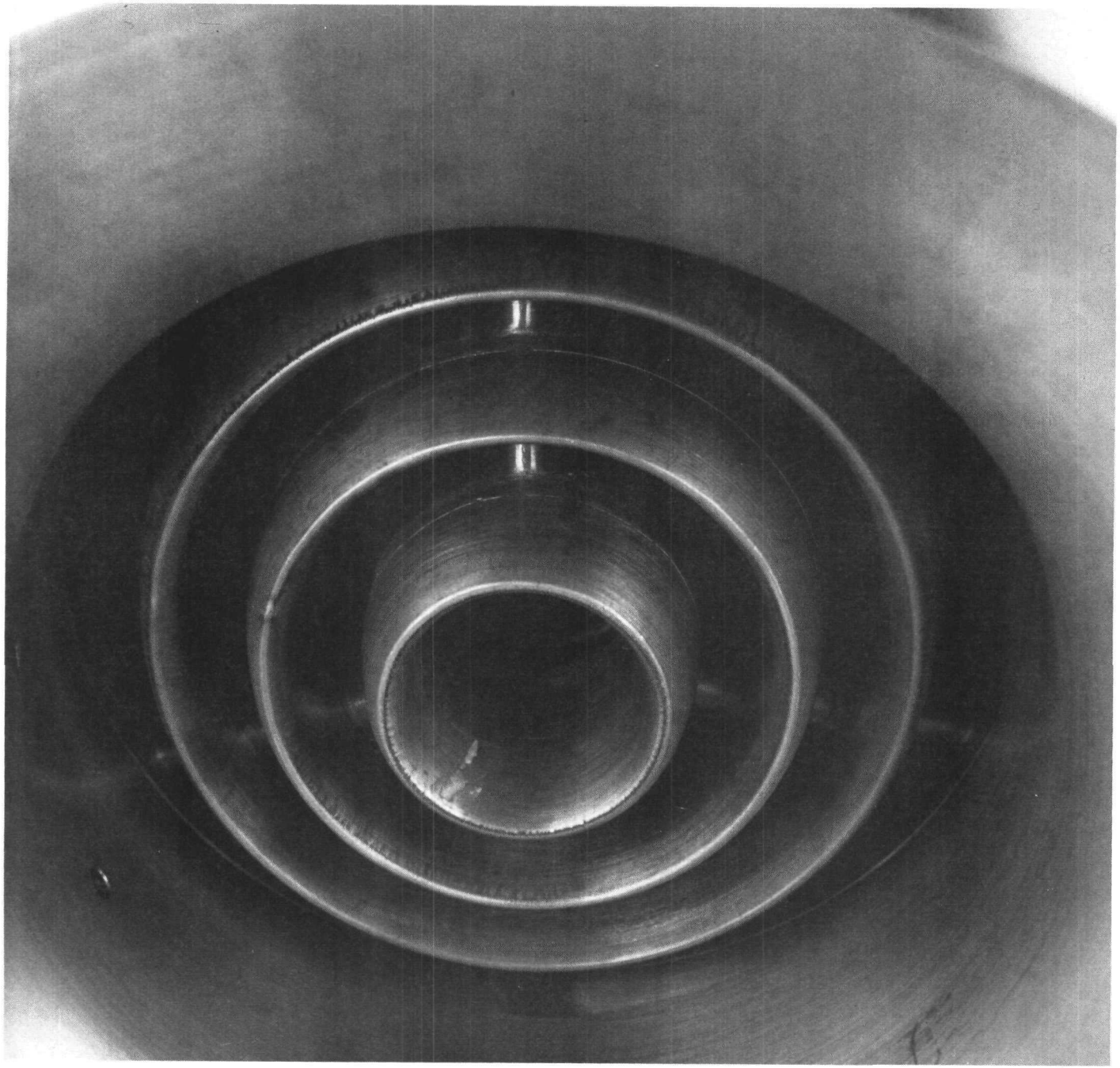

Figure 2

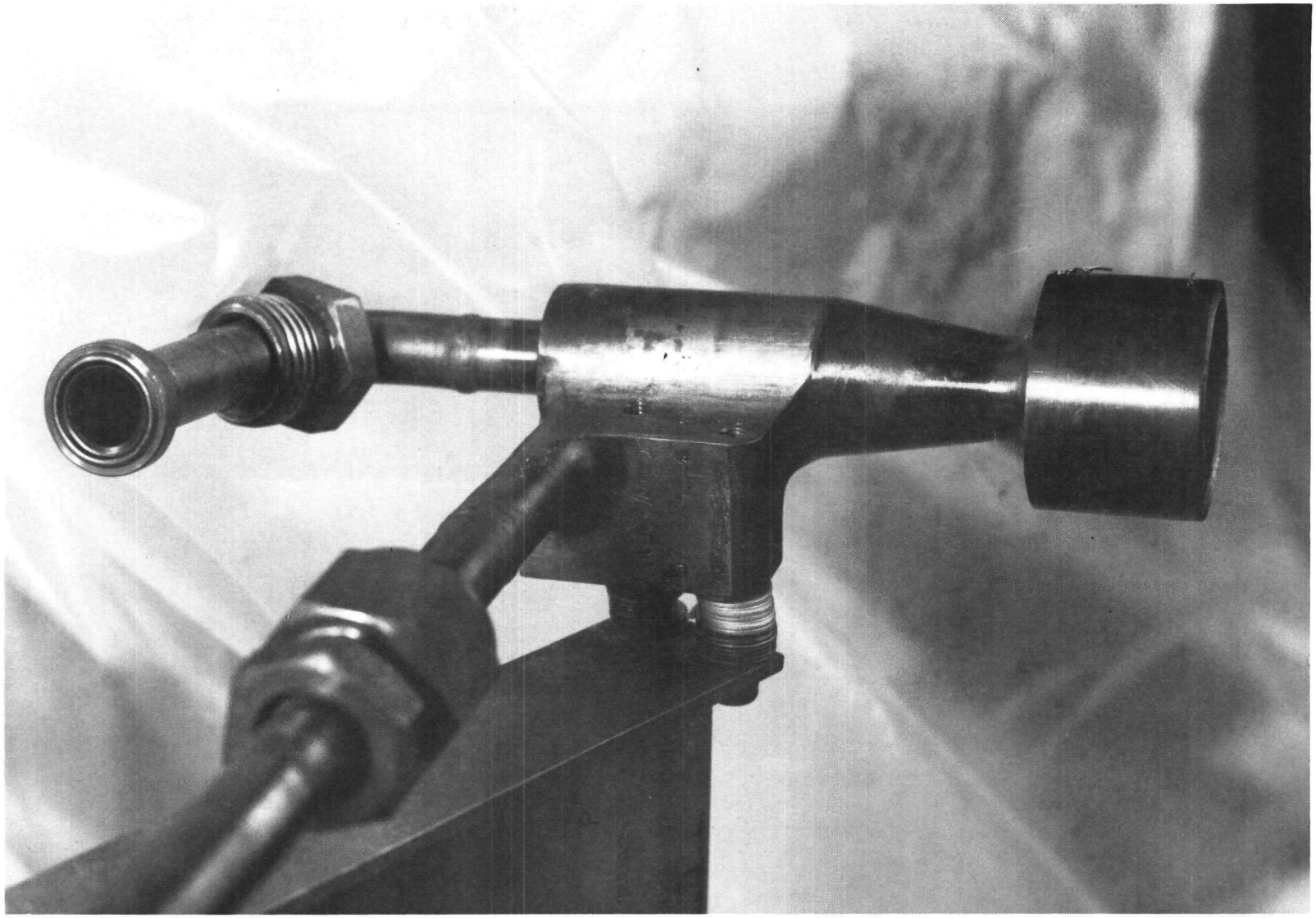

Figure 1

The burnish marks on the turbine radial pads were uneven axially across the surface. This was traced to a small step on the shaft, originating from the first balancing procedure. Residual grinding dust had escaped from the radial feed holes and entered the balance bearing clearance space causing localized machining of the surface.

The thrust pad bearing surfaces (Figure 8) appeared unchanged from their assembly condition. All the pivot surfaces of both thrust and radial bearings were undamaged. A pump-end pivot is shown as an example in Figure 9.

Examples of profilometer traces taken from radial pads and the thrust runner surface are shown in Figure 10. Bearing radial clearances were measured before and after assembly using the special fixturing previously referred to. The pump-end bearing, which had accumulated 4306 hours on the previous build had clearances which measured within $\pm$ .0002 inch of the installed values, depending on the measurement direction.

Initial measurement of the turbine bearing clearance gave values much less than the installed value. After de-magnetization and ultrasonic cleaning the measured clearance showed an increase of about .0005 inch over the installed value, indicating the presence of contamination during the first measurement, either in the bearing clearance or on the pivot.

The noted increase in clearance may have resulted from contaminent particle or may represent a "running-in" process associated with the silver plating on the bearing pivots. The silver plate has an initial value of .0002 inch and local deformation under load is likely to occur during initial operation. Since this was the first successful technique for accurately measuring clearances it is the first evidence that this process may occur.

The fact that the pump bearing showed no change in clearance during the 4298 hours operation of this build gives credence to the fact that a change may only occur during initial operation.

TABLE 1 BEARING OPERATIONAL SUMMARY

			CUMULATIVE BEARING DATA					
BUILD	BUILD DATE	BUILD HOURS	TURBINE RADIAL		PUMP RADIAL		THRUST	
Development Unit	Nov. 1977	540	Hours 540	Starts 118	Hours 540	Starts 118	Hours 540	Starts 118
Mod I	April 1978	1124	1124	41	1124	41	1124	41
A	September 1978	3182	4306	62	4306	62	4306	62
B	May 1979	4298	4298	111	8604	173	8604	173

degradation occured. The amount of particle contaminant was significantly less than has been seen at previous disassemblies.

2.2.1 The accumulator was disassembled. The accumulator has seen 4298.4 hours of operation. A fluid sample was taken from the fluid remaining in the accumulator. The fluid was found to be in good condition (see Appendix A).

Particulate matter was found in the accumulator/filter as detailed below. (Figure 4)

2.2.1.1 The machining chips were primarily stainless steel with some aluminum. The chips were generally small. The approximate size of a typical chip was a few thousandths thick by .050 wide by .100 long. The aluminum shavings are most likely from the regenerator coils. The stainless chips are probably machining chips trapped in hard-to-clean areas like the turbine cavity of the nozzle housing.

2.2.1.2 Particles of alternator thermocouple insulation material were found.

2.2.1.3 Other materials present in smaller amounts were silicon, kapton and varnish. The alternator is the most probable source of these materials.

2.2.2 Silver flakes form the silver plated screws and O-ring material were found in the electrical connector cover (Figure 5).

2.3 Disassembly Problems

2.3.1 The non-condensable gas separator vapor supply line meet was seized on the transition housing fitting.

2.3.2 One of the CRU attachment bolts stripped on disassembly.

2.4 Bearings

The bearings were disassembled and inspected. Photographs were taken of bearing components, measurements made of clearances and profile meter traces taken of bearing surfaces.

2.4.1 Background

The previous two teardown reports made reference to circumferential scratching of the radial bearing

surfaces and postulated that this was due to contamination. It was suspected that the scratching resulted from contaminant particles generated during assembly. A new assembly technique was introduced on this build to reduce generation of contaminant particles. This entailed de-magnetization of the bearing module prior to assembly, and a shrink fit installation process instead of a press-fit process.

An additional technique employed for this build was the development of a more reliable radial bearing clearance measurement, in which the bearing modules were mounted in a "Vee" block and the clearance measured using a mandrel of a known size. This technique allows comparison of clearances before and after testing.

This build was made with the thrust bearing assembly and pump-end radial bearing from the previous build. A new turbine radial bearing was installed because of burnishing from operation at low scavenge pressures on the previous build. Bearing operational hours and start/stop cycle history is summarized in Table 1.

2.4.2 Current Teardown

The circumferential scratching of previous builds was greatly alleviated. The pump-end radial bearing pads appeared to have no new scratches. The turbine end pads all had one scratch in approximately the centre of the pad (see Figure 6). Since the turbine bearing lubricant injection tube showed signs of rubbing, it is postulated that this was the origin of the contaminant particle that caused the scratch.

The radial pads were otherwise in very good condition. Some burnishing of the bearing surfaces was evident (Figure 7), a result of the large number of start/stop cycles. During each shutdown sequence, a large electrical load is applied to the generator to cause a rapid spin-down. Eccentricity between the rotor and stator causes a radial load on the bearing which can be high at low speeds. At both turbine and pump ends only two of the four pads showed burnish marks. Inspection of the installation orientation showed that the apparent loading on the pads was consistent with a unidirectional magnetic load during the spin-down transient.

1.0 Introduction

The technology verification phase of the Dynamic Isotope Power System Program requires an endurance test on the Ground Demonstration System (GDS) with improved components to meet an 18% system efficiency goal. This report covers the teardown and inspection of a prior GDS build after completion of over 4200 accumulated hours at 15.5% peak system efficiency. This test is in support of and in addition to the endurance test as many components will remain unchanged in the improved GDS.

1.1 Summary

After 4298.4 hours of operation, the GDS was torn down and inspected. The longest continuous run was 748.8 hours. The CRU for this build was the one in the system for the last build except for turbine end radial bearings and turbine shaft seals (8604 total CRU hours). The total system hours accumulated are 9100.8 hours. This total applies to two of the three Electric Heat Source Assemblies (EHSA) to the accumulator and to the radiator bypass valve. Upon inspection, the hardware was found to be in excellent condition. The radial bearings exhibited slight burnishing, but in general appear to be in the as-built condition.

The overall condition of the bearings after this disassembly was very good and the combination of many thousands of hours of operation and multiple start/stop cycles bears no doubt that a 60,000 hour mission capacity exists for this system.

Cases where discrepancies were noted are detailed below.

The degree of O-ring damage at this split was reduced from previous builds. Individual notation of O-ring damage will not be included in this report. It should be noted that O-rings are unique to the GDS and will not be utilized in a flight system.

The surface discolorations are felt to be associated with the fluid degradation. Attempts at measuring the thickness of the deposit on previous builds showed it to be on the order of Angstroms in thickness. Analysis of the fluid in the system showed it to be indestinguishable from fresh fluid. Details of the analysis are presented in Appendix A of this report.

Sources for the contamination found are discussed in other sections of this report.

2.0 Findings of Discrepancies

2.1 Discoloration

Several areas were found to be discolored. This discoloration was not heavy enough to allow a conventional scraped sample for analysis. Sandia Labs and Battelle analyzed similar deposits on previous disassemblies. The reports of these analyses can be found in GDS disassembly report #2. In general, the discolorations noted were categorized as follows:

Blue - Heat

Black - Degradation

2.1.1 The top half of the regenerator housing was discolored dark gold.

2.1.2 A thin black deposit covered the VCR gasket on the turbine inlet tube.

2.1.3 The VCR gasket nearest the turbine inlet was greenish in color.

2.1.4 The turbine inlet tube ID had a charcoal black discoloration.

2.1.5 A dull black deposit was found on the boiler outlet thermocouple.

2.1.6 The outside of the centrifugal separator was blued similar to a rifle barrel. (Figure 1)

2.1.7 A dull black streaked deposit was found on the leading edge of the jet condenser injector (Figure 2).

2.1.8 The diffusers showed signs of bluing.

2.1.9 A dark band was found on regenerator ID at the top corresponding to emission arc.

2.1.10 The top coils of the regenerator were tinted dark brown (Figure 3).

2.2 Particulate Contaminations

Particles were found in several parts of the system upon disassembly. No damage or discernable power

SUNDSTRAND ENERGY SYSTEMS

Rockford, Illinois

GDS TEARDOWN REPORT

CONTENTS

1.0 Introduction

2.0 Findings of Discrepancies

3.0 Appendices

SUNDSTRAND ENERGY SYSTEMS

Rockford, Illinois

LIST OF FIGURES

FIGURE NUMBER	TITLE
1	Regenerator Housing
2	Centrifical Separator
3	Jet Condenser Liquid Injector
4	Regenerator Housing
5	Regenerator
6	Accumulator Filter
7	Electrical Connector Cover

APPENDIX D

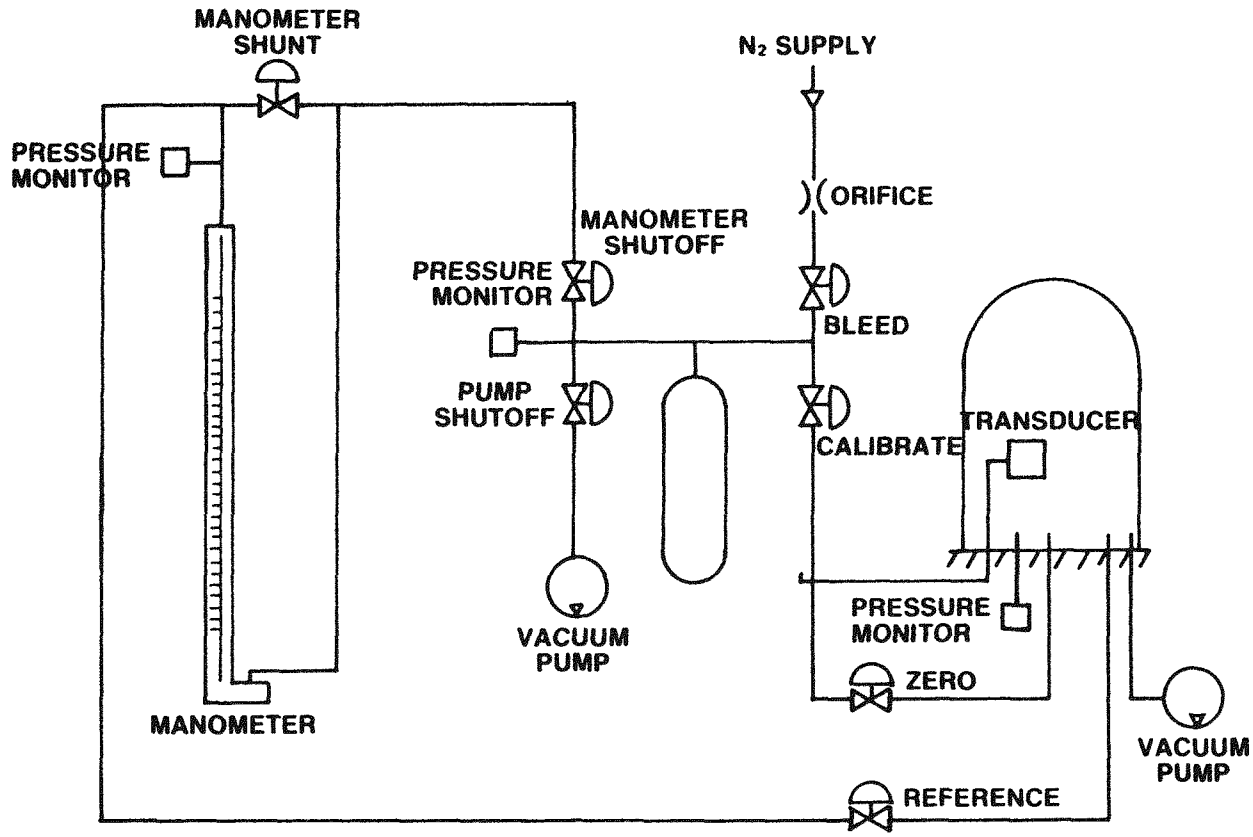

Figure 2A - Calibration System Diagram

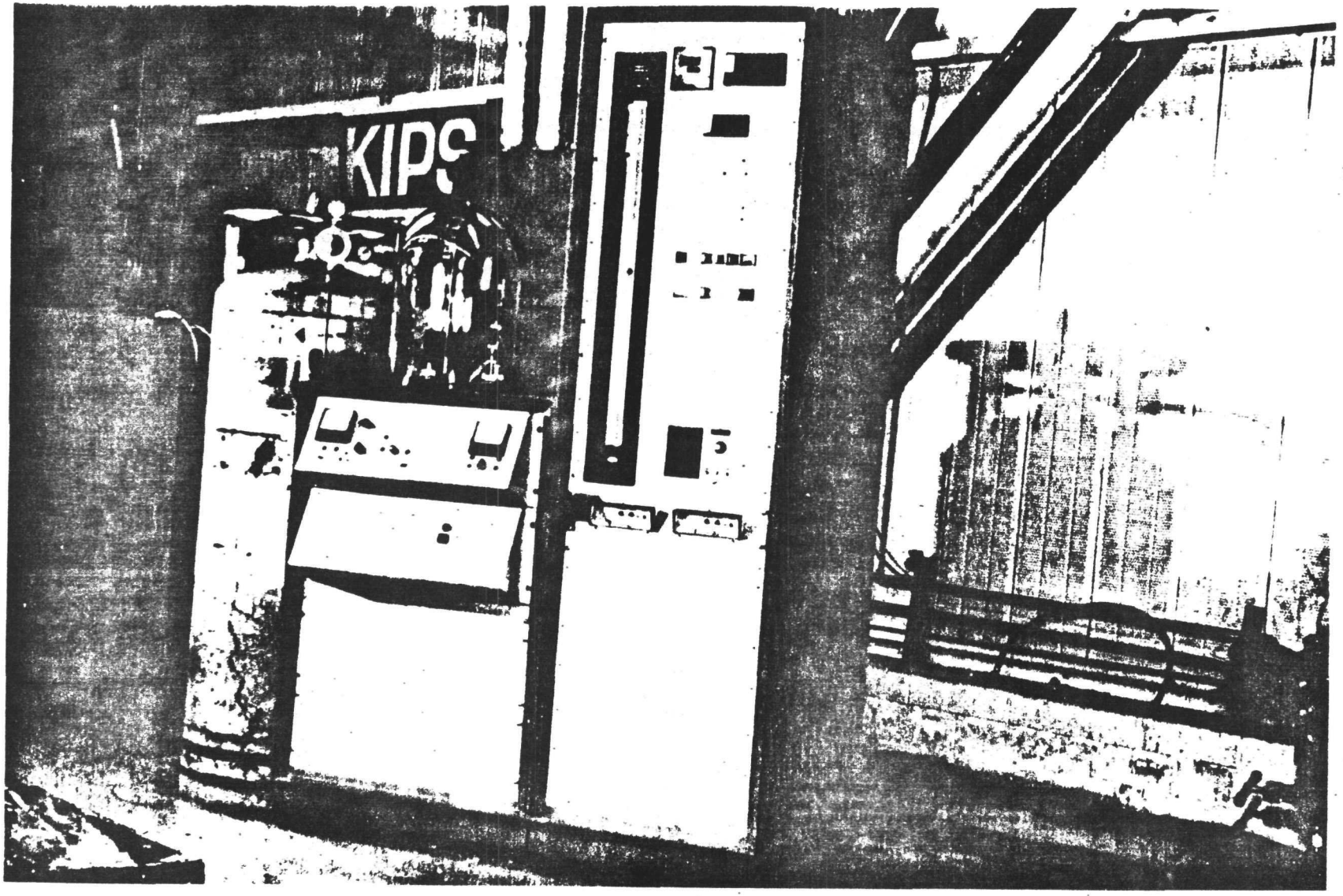

Figure 1A - Low Pressure Calibration System

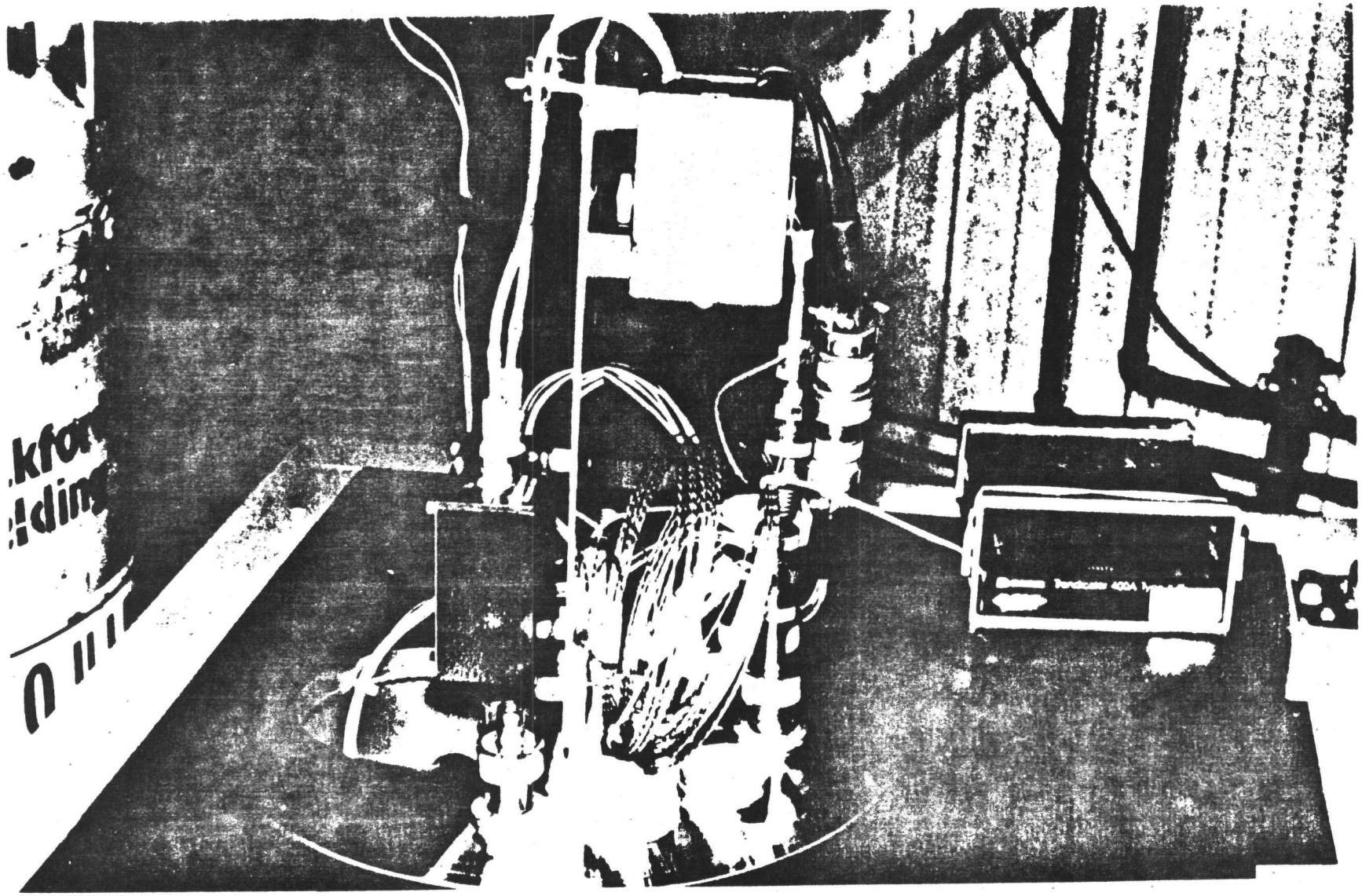

Figure 8 - Transducer Installed on Calibration System

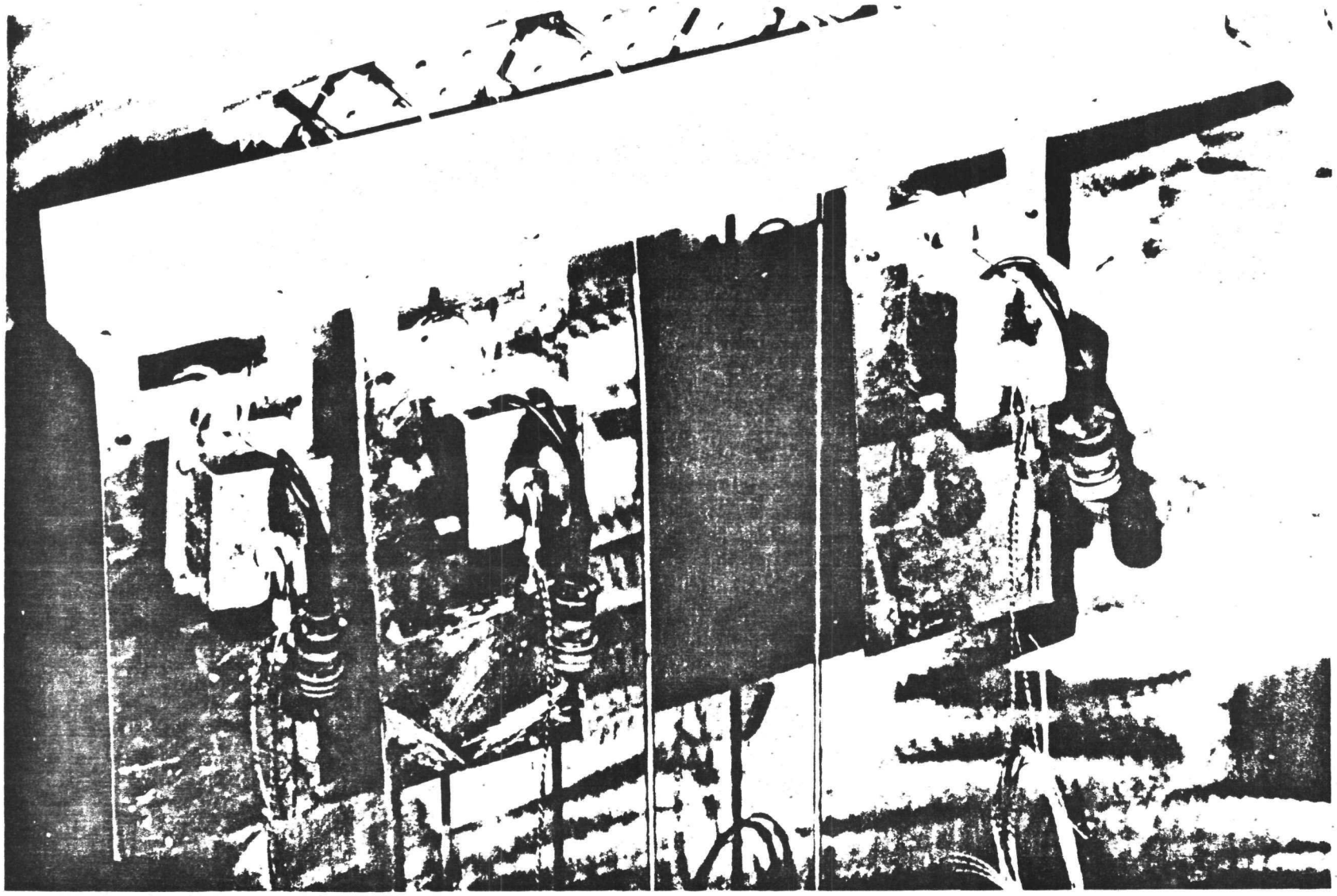

Figure 7 - Transducers Installed in Vacuum Chamber

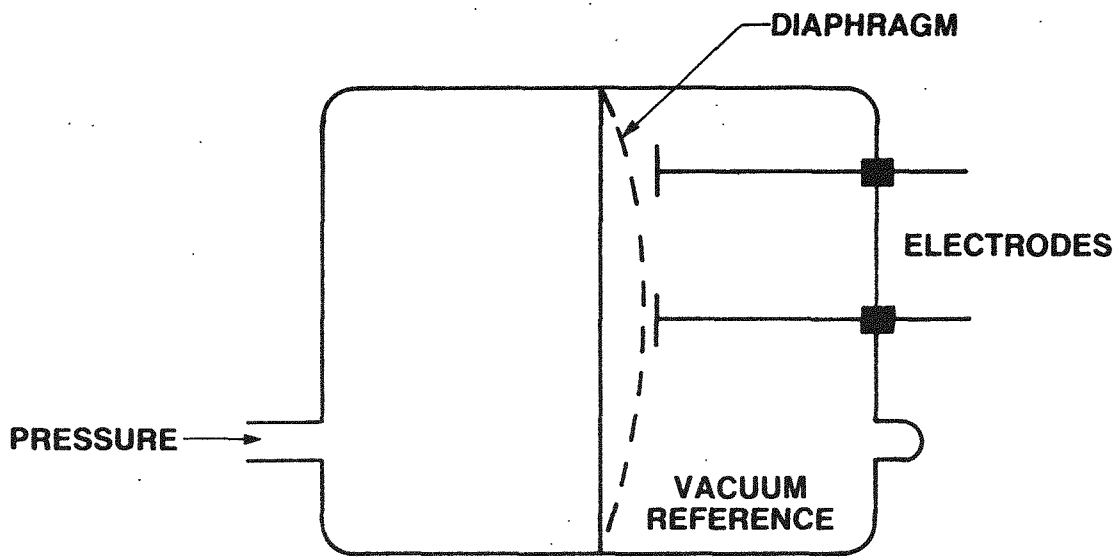

Figure 5 - Capacitive Pressure Transducer, Single-Sided

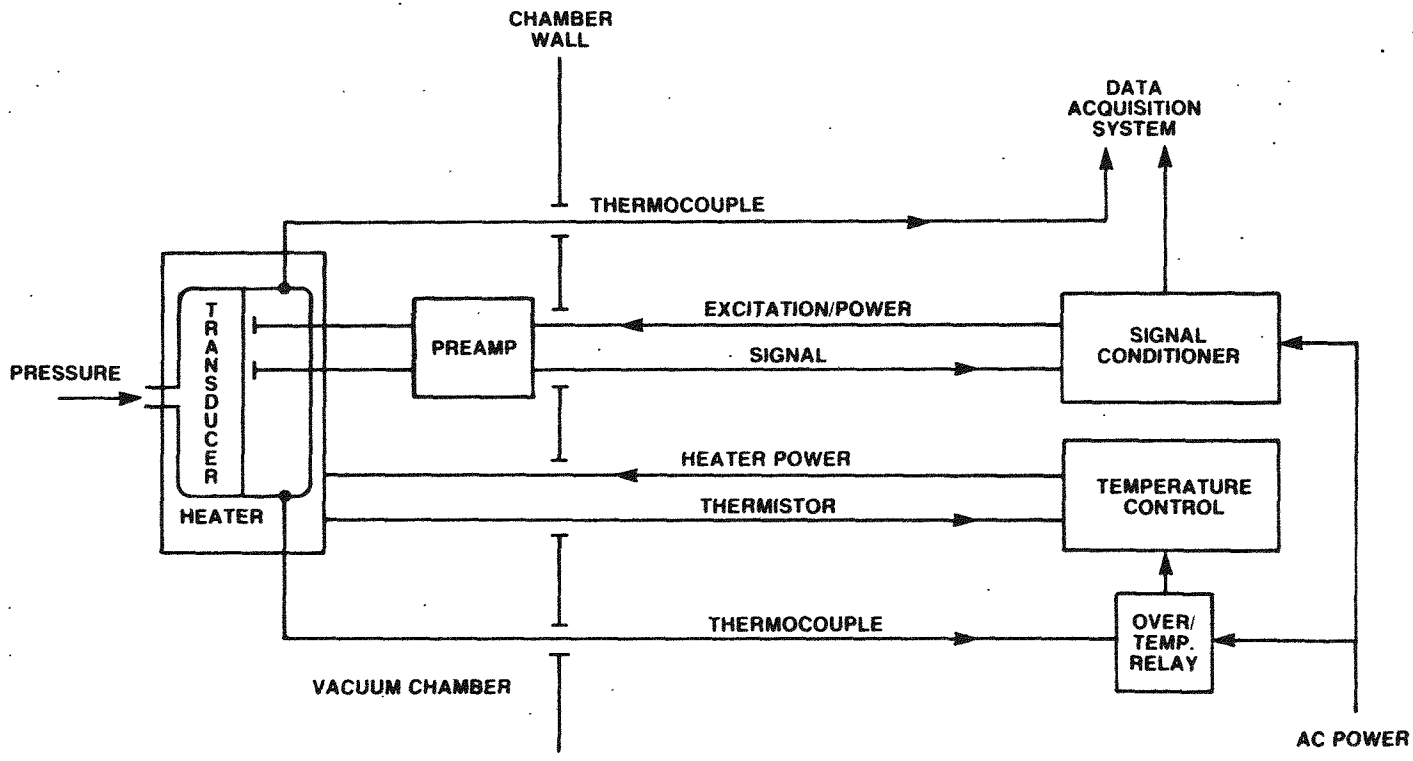

Figure 6 - Pressure Measurement System Block Diagram

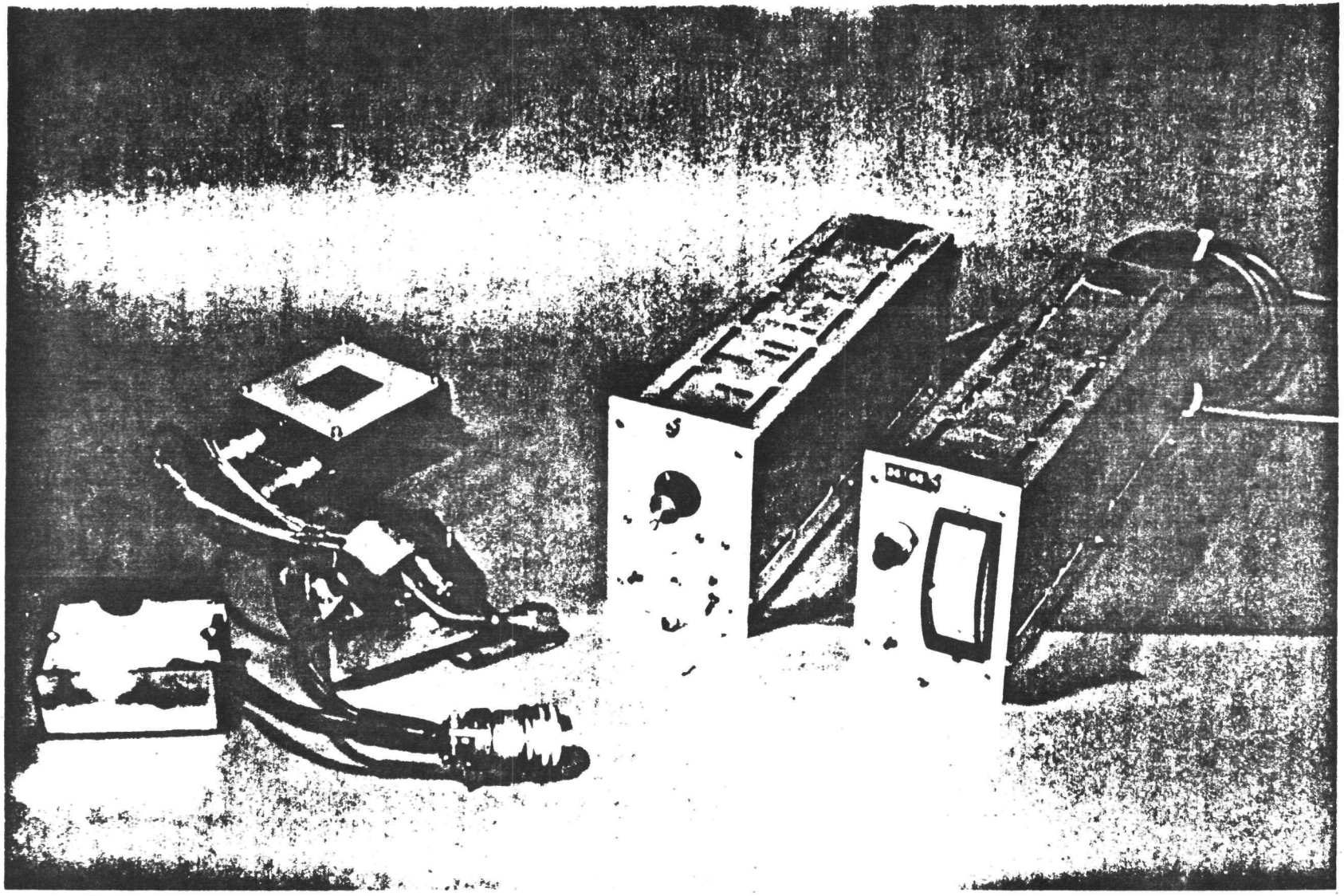

Figure 4 - Low Pressure Measurement System

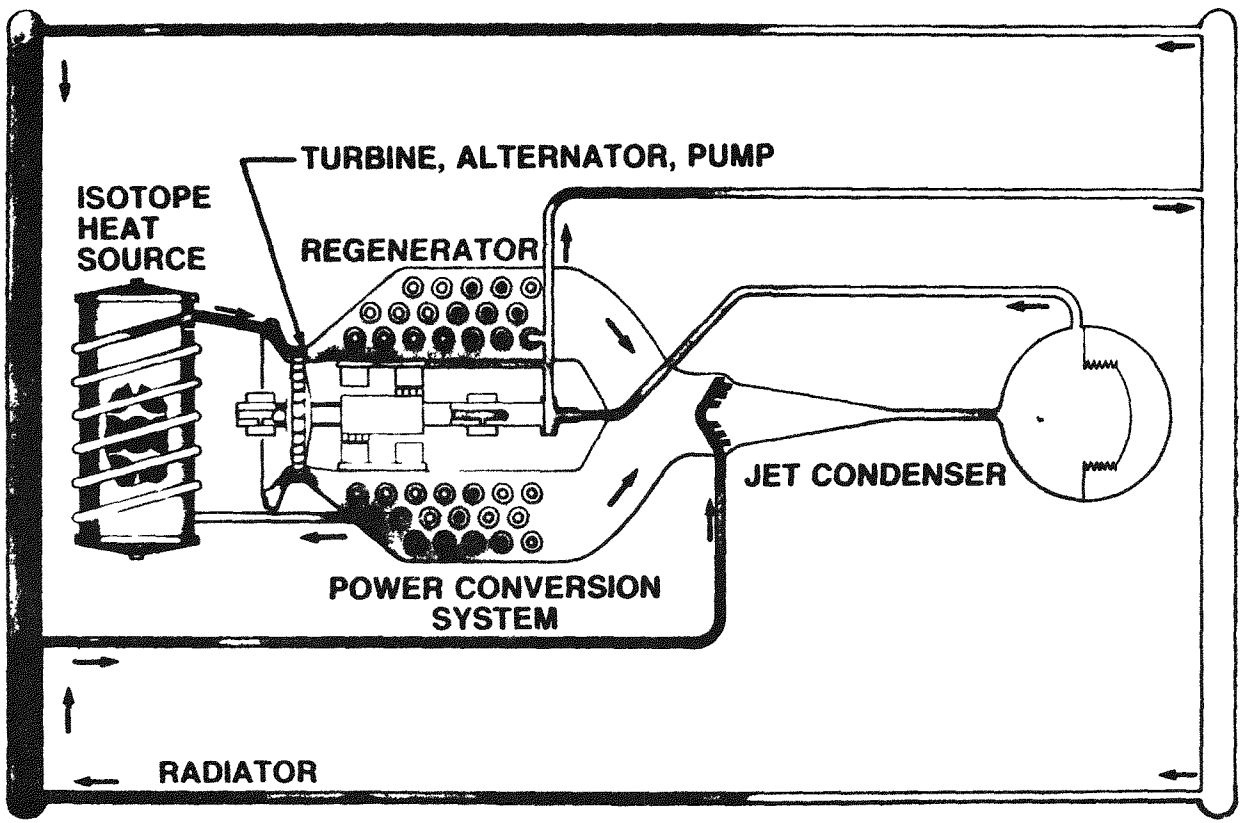

Figure 2 - DIPS Flow Diagram

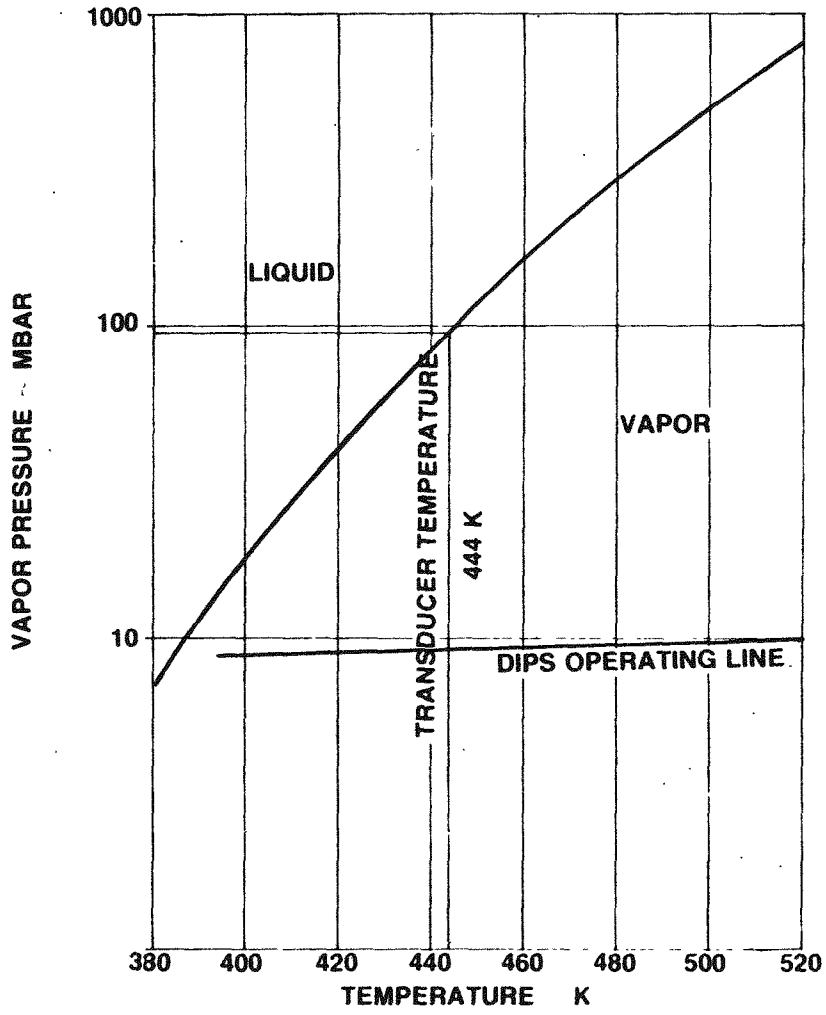

Figure 3 - Dowtherm A Vapor Pressure

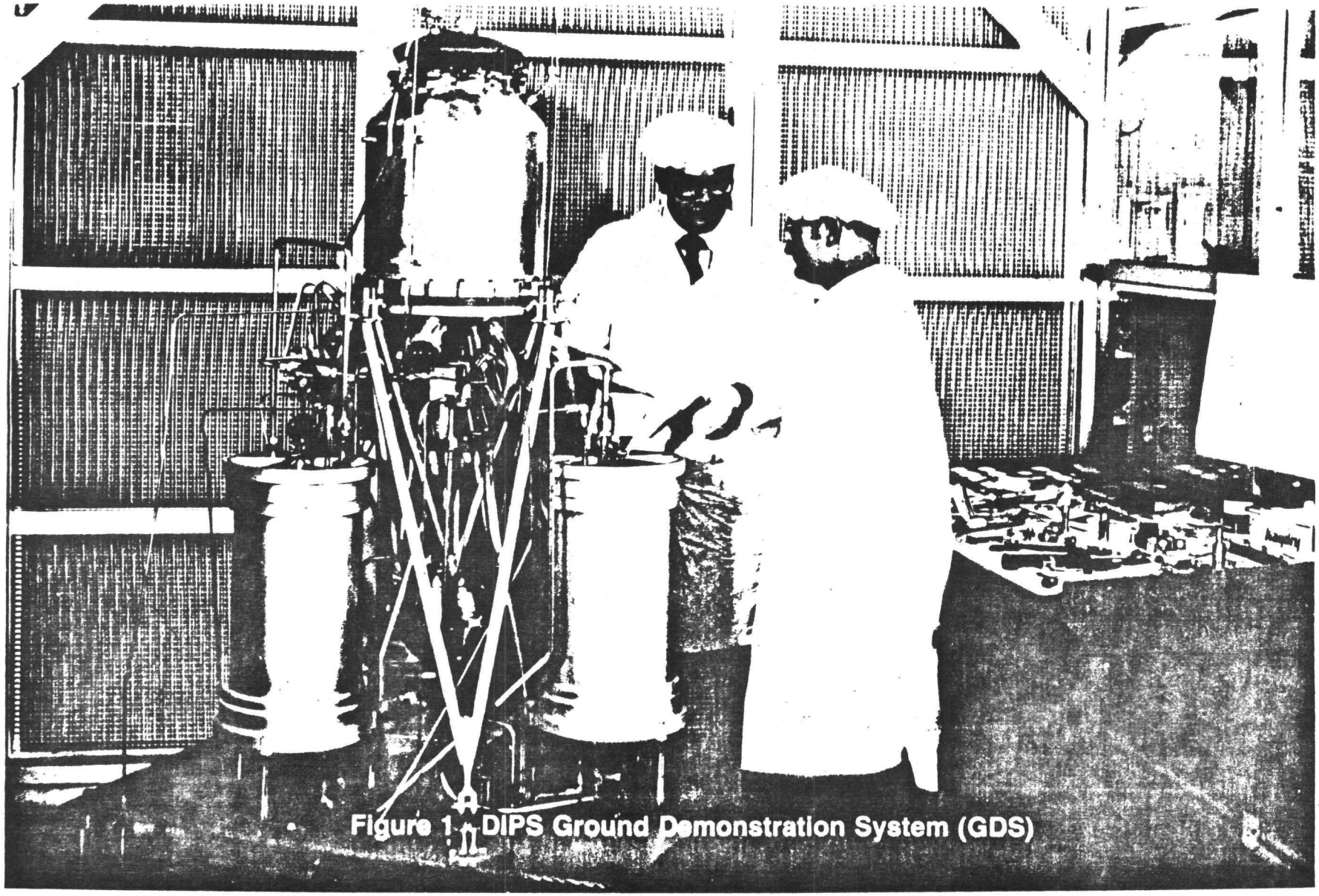

Figure 1. DIPS Ground Demonstration System (GDS)

and heaters, a final check was made of system wiring integrity by the use of preamplifier and heater simulators. This simplified trouble shooting and averted possible component damage due to miswiring.

ON-SITE CALIBRATION

Confidence was enhanced by, as nearly as possible, duplicating operating conditions with an on-site calibration. A special calibration system was constructed and is described in more detail in the Appendix. It consists of a bell jar, two vacuum pumps, a manometer with vernier scale and associated control valves. The cables from the vacuum chamber feedthrough to the preamplifiers were made long enough to reach the calibration system. With the transducer-heater-preamplifier assembly mounted on the calibration system (Figure 8), the transducer temperature was allowed to stabilize at 444K (340°F) for four hours while a vacuum was pulled on the pressure port. Each transducer was calibrated with the same cables, signal conditioner and temperature controller to be used in operation. Once stabilized, coarse zero adjustments were made on the preamplifier and the bell jar was set in place over the transducer. The bell jar was evacuated, and the pressure measurement system was calibrated against the manometer. The output was read directly from the data acquisition system display. The calibration data was used to apply corrections rather than making preamplifier sensitivity adjustments. The calibration system has demonstrated uncertainties of less than ± 0.20% of reading.

Although this is higher than the measurement system specification of 0.08% of reading, it is better than the ± 0.34mbar (0.005 psi) requirement (± 0.5% of full scale for the 69mbar (1 psia) systems used).

RESULTS

The measurement systems operated quite reliably at the elevated temperature, enclosed in a vacuum. They demonstrated excellent repeatability over the three month period (approximately 1000 hours of operation) of an abbreviated endurance test. The system accuracy was evidenced by the close correlation of pressure data with thermodynamic calculations and other related parameters measured in the DIPS.

The project was not without problems, however. The most costly was damage to three transducers and heaters due to overheating. This was a result of faulty wiring, heater feedback failure and failure of a temperature controller, on three separate occasions. The transducers only required replacement of cables and recalibration. The heaters had to be replaced. Careful wiring checkout for integrity and ground loops and the addition of heatsinks to the temperature controller output transistors eliminated further overheating. An additional precaution was the installation of overtemperature relays to disconnect heater power should a failure occur.

It was also observed that liquid Dowtherm would occassionally collect in connecting tubing and transducers when the DIPS was shutdown for service and allowed to cool. This condition was recognized by zero offset or reduced sensitivity and always rectified itself within a few hours after the DIPS again reached operating temperature.

Most perplexing was a zero offset beyond the adjustment range on several transducers. This was observed during calibration of the systems for the endurance test. Transducer zero was very sensitive to movement of the triaxial cables, expecially near their attachment to the transducer. This attachment was in the form of a coil on a post (similar to wire-wrap), which was suspect due to loose fit on some units. A little tinkering with this connection sometimes reduced the mysterious offset. The manufacturer had used this type of connection to minimize stress on the electrode metal-to-glass seal, which might be damaged by welding. Another possible explanation for the offset would be a leak in the reference side of the transducer, resulting in a loss of the absolute reference over an extended period of time.

CONCLUSIONS

This project presented a unique combination of challenging requirements:
*condensable vapor.
*elevated temperature.
*vacuum environment.
Making a successful measurement in these circumstances demands careful planning and follow-through. The most important considerations for making this pressure measurement with confidence are as follows.

Manufacturer's Instructions - The manufacturer usually has a great deal of experience with his product and his recommendations should be heeded. He can often supply the names of other customers who may have similar applications.

Calibration - Uncertainty can be greatly reduced by calibrating the transducer in its operating environment. Any

transducer has some sensitivity to temperature, external pressure, orientation and other factors which can invalidate the calibration if left to chance.

Temperature Control - The transducers were calibrated at the operating temperature and it was important to maintain them at that temperature within a reasonable tolerance.

Zero Checking - Periodic checking of the transducer zeroes was impossible due to constraints on this test. However, experience demonstrated that such a provision in an installation is to be highly recommended.

Mounting - It is important to design the transducer mounting to account for vibration, strain and liquid entrapment.

The DIPS pressure measurement project has demonstrated that capacitive pressure measurement systems can successfully meet the above requirements with proper planning, installation and calibration.

ACKNOWLEDGEMENTS

This work has been accomplished by Sundstrand Advanced Technology Group under contract to the U.S. Department of Energy. The author also acknowledges the significant contributions of MKS Instruments, Inc., Datametrics, Inc., and many associates within Sundstrand and throughout the instrumentation community.

APPENDIX - THE CALIBRATION SYSTEM

The DIPS low pressure calibration system was designed to be a totally self-contained unit, having a pressure standard, vacuum pumps and bell jar (Figure 1A). The system contains separate vacuum systems for the bell jar and for the transducer calibration pressure (Figure 2A). The pressure standard, a manometer, is connected between the two systems. In operation the transducer is placed in the bell jar which is then evacuated to about 0.00013mbar (1.9×10^{-6}psia). This provides an environment for the transducer as well as a reference for the manometer. The transducer pressure is reduced to a similar level for a zero reading. Nitrogen is then admitted to the transducer through an orifice until the desired reading is obtained on the manometer. After a short period of stabilization, the manometer and transducer output are recorded. This is repeated for five pressures.

Development of the calibration system centered on the choice of a standard. It was required to measure pressures from 6.9 to 69mbar (0.1 to 1.0 psia), provide a continuous indication, and be a mechanical system. This last requirement was a result of distrust of electronic systems which had developed from attempts to make the pressure measurement in the first place. A 76 centimeter manometer with a vernier scale was finally chosen. Resolution was 0.1 millimeter. Dibutyl Phthalate was the fluid chosen, having a specific gravity of 1.04 and temperature versus density documentation available. After several calibration attempts on one transducer showed poor repeatability, a trend was noted in the data indicating that the fluid was absorbing nitrogen and growing less dense as pressure was increased. The search for another fluid resulted in the use of Invoil-S (specific gravity about 0.91), an oil designed for use in diffusion pumps. The specific gravity of the Invoil-S as a function of temperature was measured by an independent laboratory so that corrections could be applied to the manometer readings. Several tests run on the same transducer proved successful with a combined transducer-manometer repeatability of $\pm$ 0.2% of reading.

REFERENCES

1. "Dowtherm Heat Transfer Fluids." The Dow Chemical Company, Midland, Michigan, 1969.

2. "Instruction Manual." MKS Instruments, Inc., Burlington, Massachusetts, July, 1978.

For endurance testing inside a vacuum chamber, the DIPS could tolerate no leakage or contamination of the working fluid. Therefore, any additional valves or connections to permit periodic transducer calibrations were prohibited. Feeding the low pressure lines through the vacuum chamber wall to transducers on the outside would have created condensation in the lines due to the heat sinking effect of the feedthrough plate. Therefore, the entire unit, including the low pressure transducers, had to be enclosed in the vacuum chamber, making access during a 5000 hour endurance test impossible. Because of this, pressure transducers with good long term stability were imperative.

All performance parameters were to be recorded by a digital data acquisition system to facilitate quick turnaround on performance calculations. This defined the pressure transducer analog output requirement of 10 volts D.C. full scale. Additionally, the vibration and electrical noise (1123 hertz) from the generator could not be ignored.

Providing a valid pressure measurement required careful consideration of all the above requirements and influences. The first step was choosing a dependable transducer compatible with the range, accuracy and temperature requirements. The installation was carefully planned to minimize uncertainties due to condensation, vibration and electrical noise. Finally, a calibration system was designed to permit duplication of the transducer environment during calibration. The real test was the operational checkout. Most problems encountered were associated with transducer temperature control. Transducer malfunction and Dowtherm condensation did occur, but did not compromise the test results.

PRESSURE MEASUREMENT SYSTEM

A commercially available capacitive pressure measurement system was chosen based on its specifications and reputation for good stability. Figure 4 shows the transducer, preamplifier, signal conditioner, heater and temperature controller which make up each pressure measurement system. A 133mbar (1.93 psia) absolute transducer was chosen and the system was scaled by the manufacturer to provide a 10 volt D.C. output for 69mbar (1.0 psia). System accuracy was specified to be $\pm$ 0.08% of reading with a temperature coefficient less than 15 ppm of full scale per degree kelvin. Maximum allowable transducer temperature was 473K (392°F) and could be controlled within $\pm$ 0.1K (0.2°F) for a $\pm$ 3.0K (5.4°F) change in ambient temperature.(2) Each of the ten systems purchased were factory calibrated at the anticipated operating temperature of 444 K (340°F). This temperature corresponds to 96mbar, allowing operation over the full range of the transducer, and is below the upper limit of 473K (392°F).

The transducer was a single-sided design with two sensing electrodes on one side of the diaphragm as shown in Figure 5. In this type transducer, the diaphragm curvature is sensed.(2) This allows the pressure side of the transducer to be constructed of corrosion resistant materials. The signal conditioning is a 10 kilohertz carrier system, providing good immunity to the 1123 hertz generator noise. The carrier is modulated by the varying capacitance of the transducer and amplified by the preamplifier which is connected to the transducer by two 0.33 meter (12 inch) triaxial cables (Figure 6). The amplified signal is demodulated and scaled by the signal conditioner, which also provides range switching, zero and span adjustment.

INSTALLATION IN THE VACUUM CHAMBER

The transducers and preamplifiers were mounted inside the vacuum chamber to eliminate the need for pressure feedthroughs in the chamber wall which might collect condensation. The transducers were instrumented with thermocouples for temperature monitoring and wrapped with stainless steel mesh material to promote conductive heat transfer in the vacuum. The heaters, split aluminum castings with impedded cartridge heaters, were firmly clamped around the transducers. The transducer-heater assemblies and preamplifiers were mounted on aluminum plates, and the interconnecting triaxial cables were installed and clamped in place to prevent zero shifts due to cable motion. These assemblies were then attached to the chamber wall, where they would be isolated from vibration (Figure 7). The pressure tubing sloped up from the DIPS to the transducers to keep liquid Dowtherm from entering. The tubing was coupled to the transducers with vibration isolating bellows, then wrapped with resistance heaters and instrumented with thermocouples. The tubing temperatures were adjusted by power rheostats since precise regulation was not necessary. Cables from the preamplifiers penetrated the chamber wall and were connected to the signal conditioners about 10 meters (33 feet) away. Power cables from the generator were shielded to reduce EMI.

A Total of eight systems were installed; four in the vacuum chamber and four on a similar test setup used for testing at atmospheric pressure. Before making electrical connections to the preamplifiers

LOW PRESSURE MEASUREMENT OF CONDENSABLE VAPORS

David W. Miller
Sundstrand Corp., Advanced Technology Group
4747 Harrison Ave., Rockford, IL 61101

ABSTRACT

Accurate pressure measurement in the medium vacuum range, 6.9 to 69 millibars (0.1 to 1.0 psia), a normally difficult task, was complicated in recent tests by elevated temperatures and the presence of condensable vapor. The tests were associated with the Dynamic Isotope Power System (DIPS), a U.S. Department of Energy program which Sundstrand Energy Systems was contracted to develop. This paper discusses the pressure measurement system selection and calibration rationale and some operational problems encountered.

A commercially available capacitive pressure measurement system was selected for this application because of its high performance and stability at high temperature. Since the transducer had to be operated at 444K (340°F) in a hard vacuum, a special system was constructed to allow calibration under these conditions. Eight systems were installed and provided the ± 0.34mbar (0.005psi) accuracy required.

INTRODUCTION

To meet the power requirements of satellites of the 1980's and beyond, the Department of Energy established the Dynamic Isotope Power System (DIPS) program. Sundstrand Energy Systems developed a DIPS (Figure 1) under contract to DOE. The DIPS produces electric power by use of a Sundstrand organic Rankine cycle power conversion system and the proven plutonium oxide heat source. The organic Rankine cycle hardware is composed of a turbine-alternator-pump on a common shaft, boiler, regenerator, jet condenser and radiator (Figure 2). During operation, the Dowtherm A working fluid is vaporized in the isotope boiler and expanded through the turbine, driving the alternator and pump. The vapor gives up remaining useable heat to the regenerator before being condensed by the jet condenser. Liquid from the reservoir is then sent by the pump through the regenerator for the addition of heat and to the boiler to continue the cycle.

During development, the DIPS was heavily instrumented for electric power, temperature, flow and pressure in order to determine performance of the individual components. One very important parameter was the pressure on the low-pressure side of the turbine. This measurement, along with other low pressures in the regenerator and jet condenser, were required by the data acquisition system for performance calculations. The low working pressures in this area, 8.3mbar (0.12 psia), and the sensitivity of calculations to these parameters led to an uncertainty requirement of ± 0.34mbar (0.005 psi).

First attempts to measure these pressures using conventional (strain-gage and variable reluctance) absolute pressure transducers proved the difficulty of the task. Inspection of the transducers, as a result of severe zero shifts, revealed deposits of Dowtherm in the pressure cavities. An examination of Dowtherm A properties for the conditions predicted at the points of interest showed a high probability of condensation, especially on the cooler transducer diaphragms.(1) The presence of a viscous liquid on the diaphragm could have a significant effect on the output of a low range, 69mbar (1 psia), transducer. To prevent this, the pressure transducer had to be maintained at a temperature significantly higher than the saturated vapor temperature as a function of pressure in Figure 3. For 8.3mbar (0.12 psia) this corresponds to 383K (230°F), very near the upper temperature limit of 394K (250°F) for most transducers. It was desired to operate the transducers at 444K (340°F) to insure no condensation at all system operating points, and to speed up bake-out of condensation occurring during periods of shutdown.

APPENDIX C

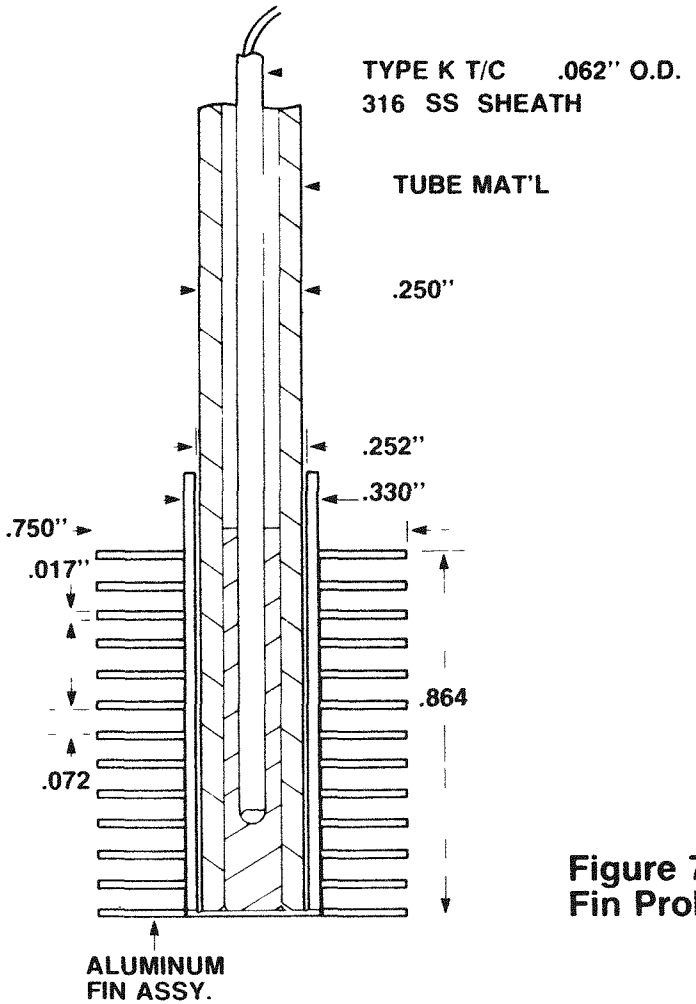

Figure 7
Fin Probe Design

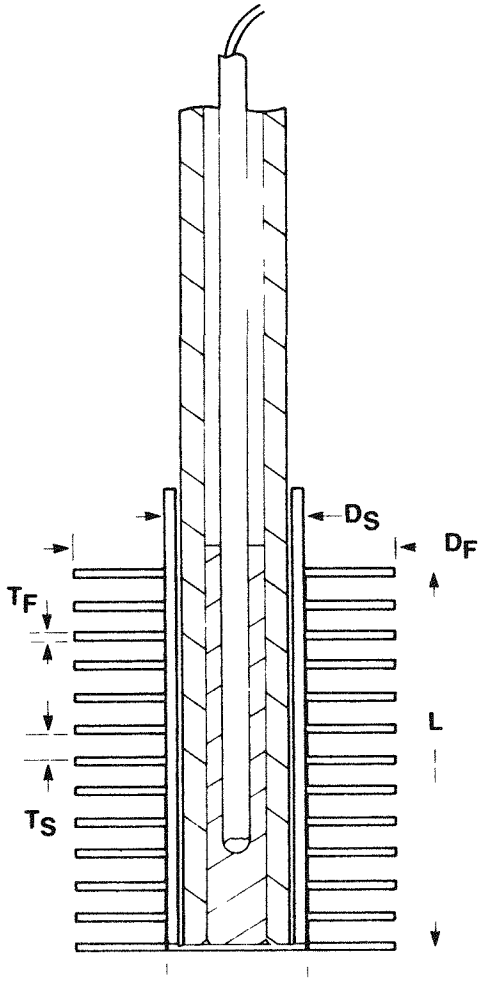

Figure 8
Fin Probe Design

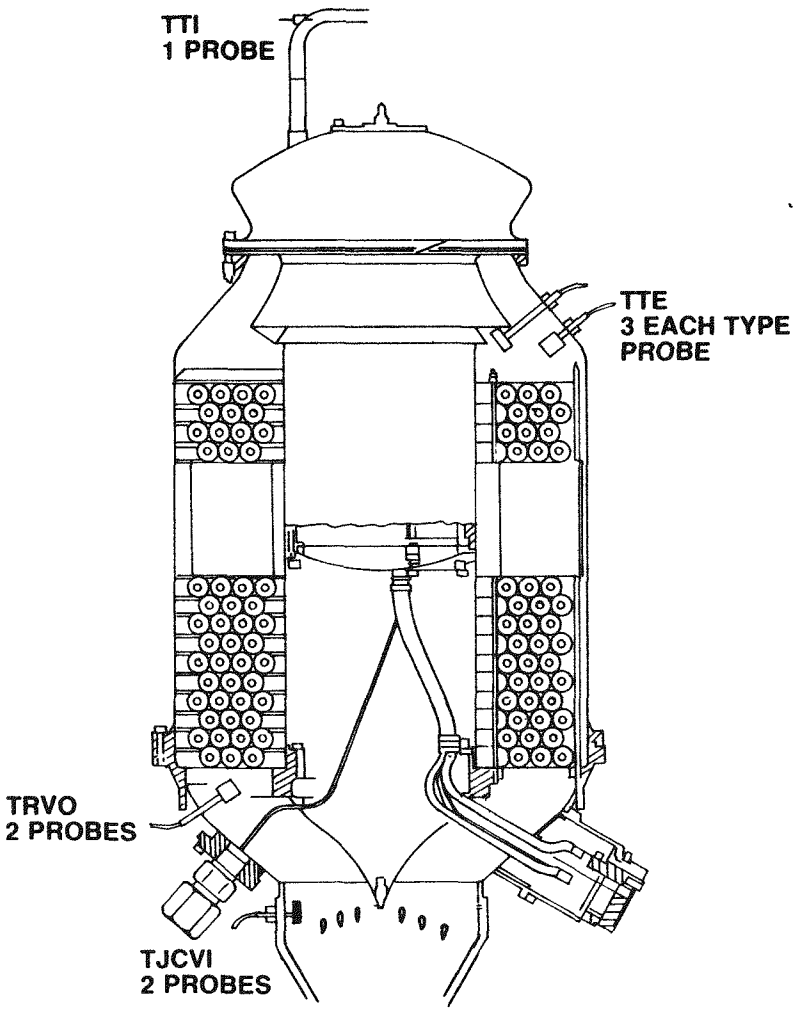

Figure 5
DIPS GDS Special Probe Installation

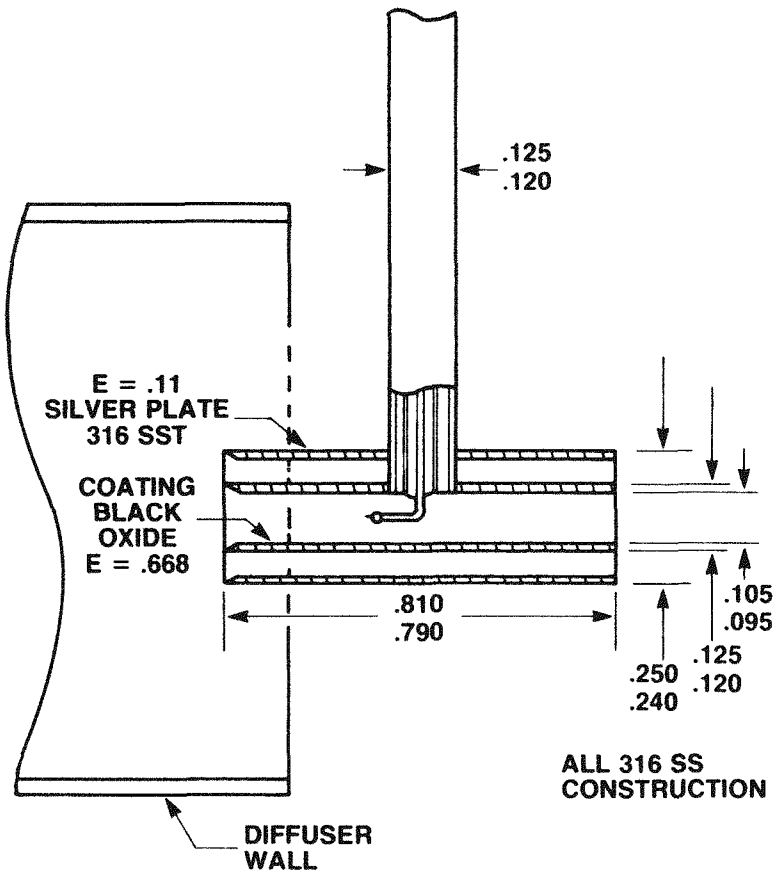

Figure 6 - Two Shield Probe

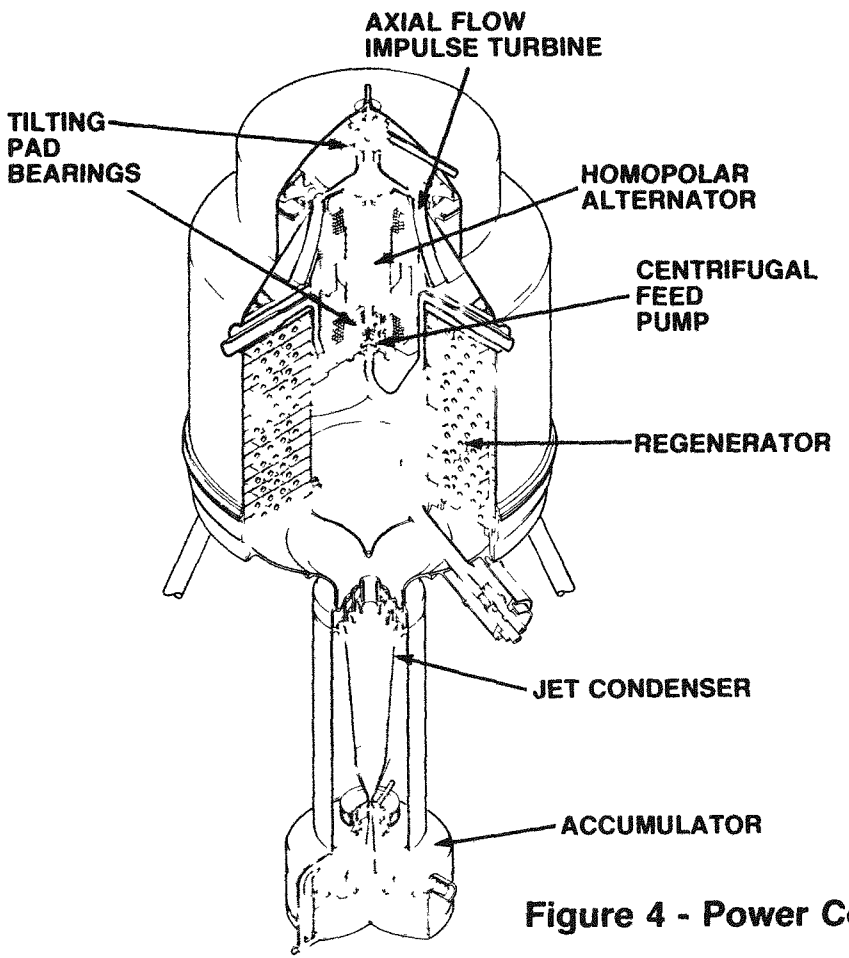

Figure 4 - Power Conversion Unit

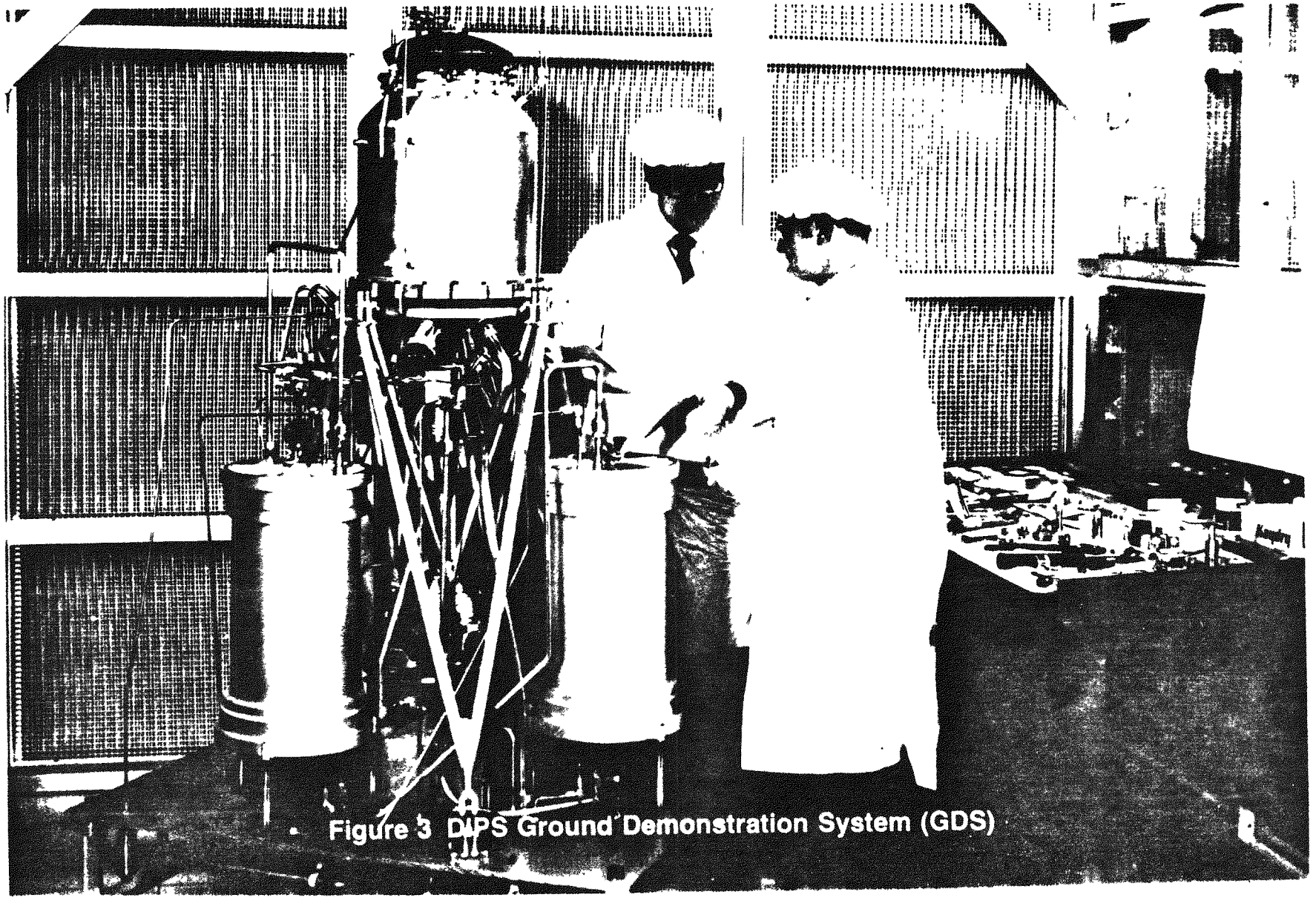

Figure 3 DIPS Ground Demonstration System (GDS)

Dynamic Isotope Power System

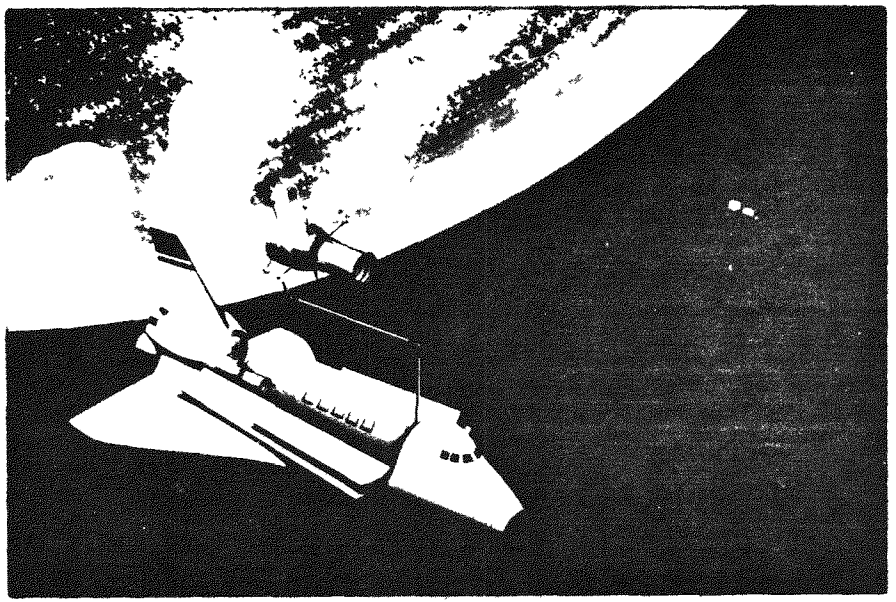

Sundstrand Energy Systems
Under Contract to the
Department of Energy

Figure 1

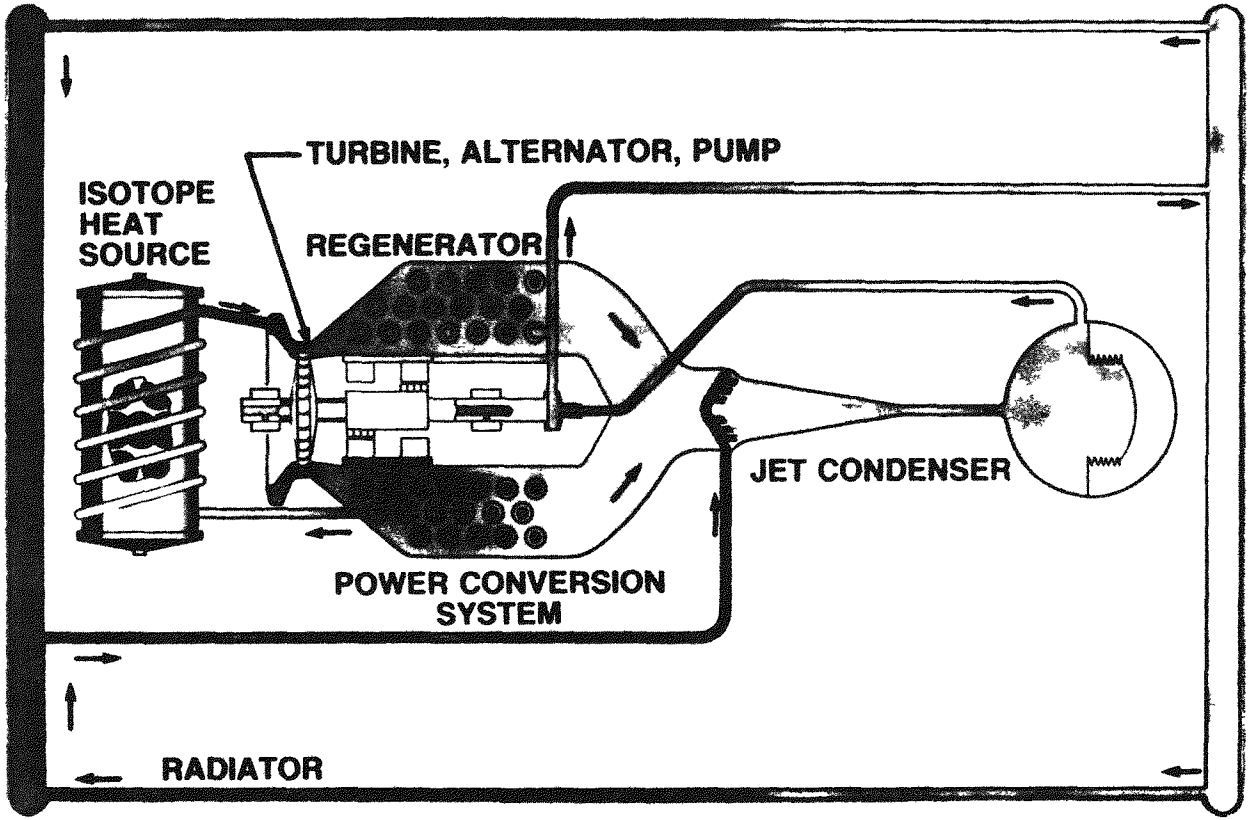

Figure 2 - DIPS Flow Diagram

$$\pm \frac{\left[\left(\frac{1}{2} - \frac{N_{FS}}{4}\right)^2 + D_S^2(R_{CR} - N_{FS} + 1) + 4N_S D_S T_S\right]^{\frac{1}{2}}}{1 - \frac{N_{FS}}{2}}$$

In using the above solution, we suggest the following approach:

1. Establish the desired R_{CR} employing the equation for radiation and convective heat transfer; this requires setting of an error goal.

$$H_c A_c (T_g - T_J) = \sigma \epsilon A_R (J_J^4 - T_W^4) \qquad (10)$$

2. Define the probe envelope with respect to length and some maximum diameter. Take blockage effects into consideration.
3. Survey the probe support structure to determine the minimum spacer diameter.
4. Establish fin and spacer width. Fin thickness is primarily based on structural requirements dictated by material compatibility and emmisivity. Spacer thickness depends on boundary layer analysis as a function of N_{Re}. Generally a ratio of spacer width to fin length.

$$\frac{\frac{D_F - D_S}{2}}{D_S} \leq 4 \qquad (11)$$

will limit the spacer view field.

NOMENCLATURE

A_C - Area of Convection
A_R - Area of Radiation
D_F - Diameter of Fin
D_S - Diameter of Spacer
N_F - Number of Fins
N_{FS} - Number of Fin Sides
N_S - Number of Spacers
R_{CR} - $\frac{A_C}{A_R}$ Area ratio Convection to Radiation
T_F - Thickness of Fin
T_S - Thickness of Spacer
L - Length of Probe Head

Table I

Error (T_{TVAPOR} - T_{PROBE})

Location		TTI	TTE	TRVO	TJCVI	TDE
E_{Total}	°F	+2.0	+19 ± 4	-29 ± 37	-4.9	.01
E_V	°F	.01	+.04	.01	+.07	.01
E_R	°F	+2.00	15 E_R 23	-9 E_R +66	-4.87	.01
E_C	°F	--	+.02	+.10	+.006	.01
α		.97	.95	.95	.95	3.4
V	Ft/Sec	41.3	131.6	18.05	160.7	0.6
c_p	BTU/lb.°F	.4521	.4521	.4521	.4521	.4521
$\dot{m}$	lb/Sec.	.0311	.0311	.0311	.0311	.3319
ρ	lb/Ft.^{3}	0.79	1.39×10^{-3}	2.22×10^{-3}	2.22×10^{-3}	62.4
A	Ft.^{2}	9.87×10^{-4}	0.17	0.758	0.0815	0.35
h_c	BTU/Ft.^{2}HR°F	168	13.1	3.46	20.5	244*
E_{Probe}		0.4	0.4	0.4	0.4	0.4
T_{Wall}	°F	625*	325 → 525	314 → 443	300*	200
N_{Red}		2.1×10^4	135	43.3	373	1.24×10^{-6}
d_{Probe}	in.	.063	.063	.063	.063	.063
ν	Ft.^{2}/Sec.	10.3×10^{-6}	5.03×10^{-3}	2.15×10^{-3}	2.15×10^{-3}	1.1 x 10
N_{Pr}		0.95	0.95	0.95	0.95	11.5
K_{fluid}	BTU/HR Ft°F	.014	.0125	.012	.012	.075
T_{Mount}	°F	625	540	443	300	200
L_{Probe}	in.	4.0	2.0	2.5	2.0	1.0
$K_{s_{Probe}}$	BTU/Ft. Sec°F	12.7	12.7	12.7	12.7	12.7
P	Psia	50.74	0.10	0.10	0.10	23.3
$T_{T_{Vapor}}$	°F	650	511	236	232	203

*These values based on limited instrumentation data and analytical predictions.

± .11 K (0.2°F) when the calibration corrections are applied. For ease of applying the calibration corrections to the data, the individual corrections were grouped into a single correction curve with a maximum dispersion error of ± .17 K (0.3°F).

THERMOCOUPLE LEAKAGE TEST

The GDS has strigent leakage rate allowables due to its 7 year life demonstration. This required that each thermocouple wire be helium leak checked against the allowable of 1.0×10^{-8} standard cu. cm./sec. of Helium (He). The bare wire thermocouple junction showed a leakage rate of 0.8×10^{-9} standard cu. cm./sec which is approximately 0.1 of the allowable rate. No detectable leakage registered on the leak checker for the grounded tip immersion junction.

PROBE INSTALLATION

Three double shielded probes are installed at 120° intervals on the Power Conversion System (PCS) at TTE (see Figure 5). These are canted 7° to parallel the discharge flow. Adjacent to each of these is a finned probe positioned outside the diffuser.

Two finned probes are located in bosses at TRVO. One of these can be removed for examination during test to determine the probe coating which influences the fin emissivity.

Location TJCVI has two single shielded probes installed between the outer liquid injector ring and the jet condenser wall. The mount fitting attaches to the probe shank at least 10 diameters from the shield to reduce heat conduction to the wall.

RESULTS

The GDS, equipted with its new pressure and temperature instrumentation, received final check out in July 1980. During this phase, one discrepant immersion thermocouple had to be replaced. As of November 1980, the 10 thermocouples in the subject probes plus 80 additional thermocouples are all functioning. Initial data analysis indicates the thermocouples readings are stable, repeatable and reasonable. The three probes at TTE inner have only an average ΔT of 1.28 K (2.3°F) circumferentially around the diffuser which is very acceptable. As no system thermodynamic analysis has been done, the validity of the data cannot be assessed at this time.

The over all system error (E_S) is calculated using the Root Sum Square method discussed for instrumentation by Dr. Abernethy in (4). Individual errors are combined in Equation 5 to give an error more statistically correct.

$$E_S = \pm \sqrt{(E_{probe})^2 + (E_{cal.})^2 + (E_{record})^2} \quad (5)$$

For TTE, the error is calculated as follows:

$$E_{S_{TTE}} = \pm \sqrt{(0.86)^2 + (0.3)^2 + (0.8)^2} \quad (6)$$

yielding

$$E_{S_{TTE}} = \pm 0.67 \text{ K } (1.2^{\circ}\text{F}) \quad (7)$$

Based on the above calculation, the system error at TTE comes within ± 0.11 K (0.2°F) of meeting the designed temperature accuracy goal outlined at the start of the program.

CONCLUSION

The new temperature probes now installed in the DIPS GDS indicate that valid temperature measurements can be made in a Dowtherm vapor atmosphere at very low pressures, densities and N_{Re}'s as long as the probes are in the superheated region. Probes can be designed to sense these operating parameters without changing the system operation significantly.

To achieve the desired results when developing an accurate temperature measurement system, the following items must be strictly adhered to:

1. A system allowable temperature error must be established based on the system analysis which closes the thermodynamic loop to within the design goal.
2. Each proposed sensor location must be analyzed for heat transfer and installation errors.
3. Proper probe design selection must be employed to reduce the sensor error to the design goal.
4. Thermocouple wire must be carefully inspected, processed and calibrated to establish a documented base measurement.
5. Probe installation design must be such as to facilitate positioning while minimizing the damage and leakage points.
6. Thermometry system signal handling and recording equipment must control extraneous signals while maintaining the basic system accuracy.

The diligent use of the above premises and controls provided the capability to meet the accuracy goal established for the DIPS GDS.

REFERENCES

1. Sorensen, G. L.; Niggemann, R. E., Reck, M. W.; Kenney, D., "The 1980 Technology Status of the Dynamic Isotope Power System", 15th Inter-Society Energy Conversion Engineering Conference. Seattle, WA, 1980.

2. Moffat, R. J., "Gas Temperature Measurement", Measurements Engineering Vol. I., 6th edition, 1970, Peter K. Stein and contributing authors, Stein Engineering Service, Inc., Phoenix, AZ.

3. Moffat, R. J., "Gas Temperature Measurement: Direct Design of Radiation Shielding", Instrument Society of America, Paper No. 68-517.

4. Abernethy, R. B., "Test Measurement Accuracy", Instrument Society of America, ASI 75203 (47-57).

NOMENCLATURE

1.	T_J	= Junction Temperature	^oR
2.	T_S	= Gas stream static temperature	^oR
3.	T_T	= Gas stream total temperature	^oR
4.	T_M	= Mount temperature	^oR
5.	T_W	= Wall temperature	^oR
6.	E_V	= Velocity error	^oR
7.	E_C	= Conduction error	^oR
8.	E_R	= Radiation error	^oR
9.	K_R	= Radiation form factor	--
10.	k_s	= Coefficient of thermal conductivity, in a solid	BTU Ft.$^{-1}$ Sec.$^{-1}$ $^oR^{-1}$
11.	k_f	= Coefficient of thermal conductivity, in a fluid	BTU ft.$^{-1}$ Sec.$^{-1}$ $^oR^{-1}$
12.	A_C	= Area available for convective heat transfer	Ft.^{2}
13.	A_R	= Area available for radiant heat transfer	Ft.^{2}
14.	ρ	= Density	Lb. Ft.$^{-3}$
15.	c	= Specific heat of the solid	BTU Lb.$^{-1}$ $^oR^{-1}$
16.	c_p	= Sepcific heat of the fluid, at constand pressure	BTU Lb.$^{-1}$ $^oR^{-1}$
17.	g	= Gravitational constant	Ft. Sec.$^{-2}$
18.	J	= Mechanical equivalent of thermal energy	Ft. Lb BTU^{-1}
19.	d	= Diameter	Ft.
20.	α	= Recovery factor	--
21.	ϵ	= Emissivity, compared to blackbody performance	--
22.	h_c	= Coefficient of convection heat transfer	BTU Ft.$^{-2}$ Sec.$^{-1}$ $^oR^{-1}$
23.	V	= Velocity	Ft.Sec.$^{-1}$
24.	N_{Pr}	= Prandtl Number	--
25.	μ	= Dynamic viscosity	Lb. Ft.$^{-1}$ Sec.$^{-1}$
26.	σ	= Stefan-Bolzmann Constant; in seconds	BTU Sec.$^{-1}$ Ft.$^{-2}$ $^oR^{-4}$
27.	$\dot{m}$	= Mass flow	Lb. Sec.$^{-1}$

APPENDIX

General Formula for Development Of Finned Probe Dimensions

The basic assumptions used in this design is that the principle radiation surface is considered to be the outer edges and ends of the fin probe while the convective surface includes all the probe head area. From these assumptions, the following formulas are presented as a means to develop the probe fin diameters based on installation and performance compatibility which dictate probe length or minimum shank diameters. By referring to Figure 8 we can write a general equation.

$$R_{CR} = \frac{A_C}{A_R} = \frac{(\pi/4)(N_{FS}-1)(D_F^2 - D^2) + \pi N_F D_F T_F + \pi N_S D_S T_S + (\pi/4) D_F}{(\pi/4)(D_F^2 - D_S^2) + \pi N_F T_F D_F + (\pi/4) D_F} \quad (1)$$

Now expanding and combining factors on each side leads to:

$$R_{CR}\left(\frac{D_F^2}{2} - \frac{D_S^2}{4} + N_F T_F D_F\right) = \frac{D_F^2 N_{FS}}{4} - \frac{(N_{FS}-1)D_S^2}{2} + N_F D_F T_F + N_S D_S T_S \quad (2)$$

Further grouping like terms gives a final form for solution:

$$\frac{D_F^2}{2}\left(1 - \frac{N_{FS}}{2}\right) + D_F T_F N_F (R_{CR}-1) - \frac{D_S^2}{4}(R_{CR} - N_{FS} + 1) - N_S D_S T_S = 0 \quad (3)$$

For general solution of D_F in term of x in the following equation:

$$ax^2 + bx + c = 0 \quad (4)$$

we set

$$a = 1/2 - \frac{N_{FS}}{4} \quad (5)$$

$$b = T_F N_F (R_{CR}-1) \quad (6)$$

$$c = -\frac{D_S^2}{4}(R_{CR} - N_{FS} + 1) - N_S D_S T_S \quad (7)$$

Now solve for D_F using the second order solution:

$$x = \frac{-b \pm \left[(b^2) - 4ac\right]^{\frac{1}{2}}}{2a} \quad (8)$$

such that

$$D_F = \frac{T_F N_F (1 - R_{CR})}{1 - \frac{N_{FS}}{2}} \quad (9)$$

THERMOCOUPLE ERROR ANALYSIS

In the DIPS vapor cycle there are four locations from which temperature information is required to complete an accurate system thermodynamic evaluation. Along with these four, one liquid point is selected for comparison. The five locations are as follows (see Figure 5).

TTI - Turbine Inlet line vapor temperature
TTE - Turbine Diffuser Exit temperature
TRVO - Regenerator Vapor Out temperature
TJCVI - Jet Condenser Vapor In temperature
TDE - Reservoir In temperature

The initial temperature measurement probes used in Phase I consisted of 1/16 in. Type K immersion thermocouples (T/C's) (no shields) installed at TTI, TTE, TRVO and TDE. Using information recorded from these sensors, a baseline was established from which to conduct the error analysis using the formulas presented below.(2)

Velocity Error

$$E_V = T_T - T_J = (1 - \alpha)V^2/2gJc_p \qquad (1)$$

Conduction Error

$$E_C = T_T - T_J = \frac{T_T - T_M}{\cosh L\left(\frac{4h_c}{dk_s}\right)^{\frac{1}{2}}} \qquad (2)$$

Radiation Error

$$E_R = T_T - T_J = \frac{K_R \sigma \epsilon A_R (T_J^4 - T_W^4)}{h_c A_c} \qquad (3)$$

In order to solve the above equations, various information needed to be developed from the several explanations and graphs presented in (2). This includes such items as (α) and convective heat transfer (h_c) which are based on the relationships of Reynolds No. (N_{Re}), Prandlt No. (N_{Pr}) and Nusselt No. (N_{Nu}). The results of these calculations are listed in Table I. By examining the magnitudes and locations of the various errors, it is readily apparent that the low pressure vapor regions (TTE, TRVO and TJCVI) are prime candidates for possible temperature measurement error, particularly due to radiation. It appears that the T/C's at TTI and TDE have sufficient immersion length to reduce the total conduction (E_C), velocity (E_V) and radiation (E_R) errors to an acceptable level. That is;

$$E_{Total} = E_T = E_C + E_V + E_R \qquad (4)$$

and $E_T <$ the maximum accpetable error based on the system analysis which will produce the desired accuracy.

TEMPERATURE MEASUREMENT GOALS

During the DIPS thermodynamic model analysis, it was established that an overall system accuracy of $\pm$ 0.56 K (1.0°F) is required to meet the goals for efficiency determination of the turbine, regenerator, and jet condenser systems. This constraint included errors in the subsystem units such as;

1. Probe head
2. Thermocouple calibration
3. Thermocouple lead wire
4. Uniform temperature reference (UTR) junction box
5. Vacuum wall feed throughs
6. Extension wire
7. Recording System

It was determined that the overall error could be equally divided between the probe and data acquisition system when reviewed against available recording equipment and possible probe designs. The automatic temperature data recording system has an accuracy of $\pm$ 0.28 K (0.5°F) when used with a separate ice point reference. This established a probe design error of $\pm$ 0.28 K (0.5°F) which provided the basis for utilizing the available analytical design criteria.

PROBE SELECTION

Based on the error analysis listed in Table I, it is apparent that locations TTE, TRVO and TJCVI require probe design work. The thermocouple at TTI has some calculated radiation error (E_R), however, this is based on a wall temperature (T_W) of a fitting exposed to a vacuum in a test chamber. Insulation is scheduled for the GDS Technology Verification build which will greatly reduce the heat loss at TTI. This will allow the wall temperature (T_W) to closely match the vapor temperature (T_T), thereby reducing radiation error. The last sensor, TDE, is in liquid and exhibited little error due to probe design.

By closely examining the conditions at TTE, TRVO and TJCVI, it is noted that all three are in a low pressure area of superheated vapor. However, the flow velocity (V) and the Reynolds Number (N_{Re}) vary by a factor of 3 or greater from TTE to TRVO and from TRVO to TJCVI. Also, by noting the low value of convective heat transfer (h_c) at TRVO, it becomes apparent that conventional flow through probes in this area may not provide sufficient heat at the sensor to balance the radiation loss. Based on the above deductions, it is apparent that two probe designs are in order. The TTE and TJCVI locations are candicates for circular radiation shields as presented in (2) due to the higher N_{Re}. Location TRVO needs a probe which is able to correct for the radiation error utilizing the small value for convective heat transfer.

CIRCULAR SHIELD PROBE DESIGN

In analyzing the various designs for TTE and TJCVI, the aspirated and Dahl & Fiock double shielded probes (2) are not acceptable due to a closed fluid system and insufficient velocity. This left the circular shield design with a bare wire thermocouple (3) as the most reasonable choice.

The circular shielded probe requires more shields as the ΔT between the fluid total temperature (T_T) and the surrounding wall temperature (T_W) becomes greater. This phenomena is covered in (3) where Prof. Moffat presents an analytical method for determining the number of shields needed to maintain E_R within design limits.

The first consideration in the above shield design approach required the vapor to wall ΔT determination. The T_T at TTE is assumed to be 561 K (550°F) with T_W at 505 K (450°F). The value for the T_W is an average of the outer shell, regenerator and inner wall housing of the combined rotating unit (CRU). T_W now becomes the minimum average temperature the outer shield can see while keeping E_R within limits.

Determining the material emmisivity (ϵ) becomes the second consideration in this evaluation. Temperature levels, material compatibilities and probe loading requires the use of 316ss as probe material. Based on the preceding temperatures and 316ss emmisivity values plus a L/D ratio of 8 for the .318cm (.125 in.) inner shield, the full analysis showed that two shields will maintain the bare wire sensor within $\pm$ 0.48 K (0.86°F) of T_T if the average T_W is above 508 K (454°F) (Figure 6). The type K thermocouple has .030cm (.012 in.) wires which are designed within an exposed junction L/D ratio of 15.

The DIPS engineers reviewed the two shield design for the 1.5% blockage effect created by three probes and decided it was an acceptable approach. They believe that any additional shields may affect the operational efficiency goal. This analysis is also applicable to location TJCVI where the velocity is greater, the vapor temperature is lower and the ΔT between the vapor and the wall is less. The probe envelope is constrained by the location of the probe between liquid jet rings and the jet condenser wall. Based on these conditions, a single shield probe is all that can be installed. When analyzed at the reduced temperature, the probe error is $\pm$ 0.33 K (0.6°F).

FIN PROBE DESIGN

The second probe design deals with location TRVO and the region outside the turbine diffuser exit, TTE outer (Figure 5). Location of probes in TTE outer is at the request of the DIPS engineers to coordinate temperature data acquired during Phase I operations.

Reviewing the data in Table I, it is apparent that the low h_c and N_{Re} allow the large E_R plus contribute to the uncertainty. Also, by comparing the conditions at TRVO with TTE outer, it is believed that similiar probe design will satisfy both locations.

Returning to Equation 3, the only variables that can be readily changed to reduce E_R are A_C and A_R. An iterative approach is to increase A_C to 10-20 times A_R through proper probe head selection. Using a A_C/A_R ratio of 20 for TRVO based on T_T = 383 K (230°F) and T_W = 422 K (300°F) yields a calculated E_R less than $\pm$ 0.28 K (.5°F).

Calculations for TTE outer based on a vapor velocity of 40% of the diffuser exit velocity and on A_C/A_R ratio of 20 produce E_R = $\pm$ 0.73 K (1.32°F). Conditions for T_T and T_W are considered the same as for TTE inner.

Since the flow is omni directional in these regions, a fin probe design is selected which is insensitive to flow direction in two planes (Figure 7). For the basic probe fin area analysis, the radiation area includes all end surfaces and fin edges. The convection surface includes all area of the probe head excluding the shank. An algebraic formula is presented in the Appendix which allows for various fin sizes and number of fins.

During the DIPS regenerator development, a length of 1.905cm. (.750 in.) solid aluminum shafting had fins machined on the outer surface with a .68cm. (.27 in.) bore. This fin material closely matched the basic proposed probe design. Using the formula and fin tubing dimensions, the final 12 fin probe head came into being. Since the temperature at TTE outer necessitated the use of a 316ss shank, an adapter section is designed into the head to act as a heat sink for the thermocouple and the transition piece. This also allows the thermocouple to be replaced without disturbing the probe installation.

THERMOCOUPLE CALIBRATION

A thermocouple calibration accuracy goal of $\pm$ .056 K (0.1°F) required the careful control of several factors. The type K 316ss sheath wire received a homenogeniety check, aging at 894 K (1150°F) and individual wire calibration in a new fluidized comparitor bath. Each calibration batch consisted of 8 individual thermocouples whose average assessed error is

APPENDIX B

TEMPERATURE MEASUREMENT OF LOW PRESSURE CONDENSABLE VAPORS

Ronald C. Rice
Sundstrand Corporation
4747 Harrison Ave.
Rockford, Illinois 61101

ABSTRACT

Accurate temperature measurement of condensable vapors is a challenge even in superheated, medium to high velocity systems. Further complications arise requiring special temperature sensors when this is undertaken in a medium vacuum (6 895-68.95 m bar) (0.1-1.0 psia), low velocity (1.22-51.8 m/sec.) (4-170 fps.) flow field. These are the conditions associated with the Dynamic Isotope Power System (DIPS), developed by Sundstrand under a DOE contract. This paper covers the temperature error analysis at selected locations, sensor selection and special probe sensor design analysis.

For this program, special thermocouple probes have been designed, fabricated and installed at selected critical locations within the vapor portion of the DIPS operating cycle. In order to meet the requested probe design error band of ±0.28 K (0.5°F), each location is analyzed for conduction, velocity and radiation errors. This analysis led to two basic probe designs, circular shield and fin styles, both reducing the possible radiation effects to the required error level. A total of ten probes are installed in the 367 K-644 K (200°F-700°F) vapor portion of the DIPS.

INTRODUCTION

The temperature measurement effort described in this paper is associated with the DIPS Technology Verification Phase. (1) This is a follow on of the hardware development phase, Phase I, which the Department of Energy (DOE) initiated in 1975. Under this contract, Sundstrand is developing a plutonium oxide fueled Rankine cycle turbine power system for space use. This system is designed to provide electrical power for earth orbit satellites and interplanetary space probes (Figure 1, 2).

The DIPS working fluid is Dowtherm A, a eutectic mixture of diphenyl and diphenyl oxide which has a freezing point of 285.15 K (53.6°F) and a boiling point of 530.25 K (494.8°F) at ambient pressure conditions. During DIPS operation, liquid Dowtherm A is pumped through the electrically heated boilers which simulate the plutonium oxide boilers, where it is vaporized at 382.2K (720°F). This superheated vapor is expanded across the combined rotating unit (CRU) turbine into the low pressure, 8.274mbar (.120 psia), regenerator housing. Heat is removed from the vapor as it passes over the regenerator yet still remains in the superheated range In the jet condenser, jets of cooled liquid draw the vapor through a venturi into a pressurized reservoir. From the reservoir, the liquid Dowtherm begins another cycle

The Technology Verification Phase is being conducted on a fully instrumented Ground Demonstration System (GDS) (Figure 3). This unit is the power generation portion of the DIPS system. Simulated space conditions for the DIPS GDS are attained in a hard vacuum chamber installed for this program. The major goal of the Technology Verification Phase is to raise the overall GDS efficiency from the demonstrated 15% to over 18%. (1)

During the thermoanalysis of the various component efficiencies, which are required to upgrade the system, it became apparent that the limited Phase I temperature instrumentation in the Power Conversion System (PCS) (Figure 4.) was inadequate. In one case measured temperatures downstream of the turbine deviated 11.1K (20°F) or more from the predicted temperature.

With the help of Prof. R J. Moffat, Standford University, the thermodynamic and temperature analysis conducted on the GDS revealed that the major unknowns lay in the vapor portion of the Rankine cycle. Consequently, a thorough study of the possible temperature measurement errors was undertaken to improve the reliability and validity of the data taken from the GDS performance runs.

PHASE II REPORT

on

DESCRIPTION OF AND DOCUMENTATION OF PROCEDURES FOR NAK LOADING OF SUNDSTRAND BELLOWS-TYPE THERMAL SENSORS

to

SUNDSTRAND ENERGY SYSTEMS
SUNDSTRAND CORPORATION
ROCKFORD, ILLINOIS

March 28, 1980

by

W. J. Zielenbach

BATTELLE
Columbus Laboratories
505 King Avenue
Columbus, Ohio 43201

PHASE II REPORT

on

DESCRIPTION OF AND DOCUMENTATION OF PROCEDURES FOR NAK LOADING OF SUNDSTRAND BELLOWS-TYPE THERMAL SENSORS

to

SUNDSTRAND ENERGY SYSTEMS
SUNDSTRAND CORPORATION
ROCKFORD, ILLINOIS

by

W. J. Zielenbach

BATTELLE
Columbus Laboratories

March 28, 1980

INTRODUCTION

As part of Sundstrand's DOE Program to develop the Kilowatt Isotope Power System (KIPS) for electric generators in satellites, Battelle's Columbus Laboratories has investigated techniques for obtaining an adequate loading of liquid metal in thermal sensor sub-systems. The thermal sensor systems are shown in Figure 1; expansion and contraction of the liquid metal (78 w/o potassium/sodium) in the sealed sensor with changing working fluid temperature was to produce linear motion in a bellows to actuate a valve for control of the flow of the working fluid.

In Sundstrand's development of the sensor system, difficulties were encountered in obtaining expected sensor performance; the trouble was thought to be the result of voids in the sealed, liquid metal systems caused by improper filling procedures. Battelle undertook a study for Sundstrand to develop a NaK filling technique to assure a complete loading with no voids. Several sensor assemblies were supplied by Sundstrand for experimentation;

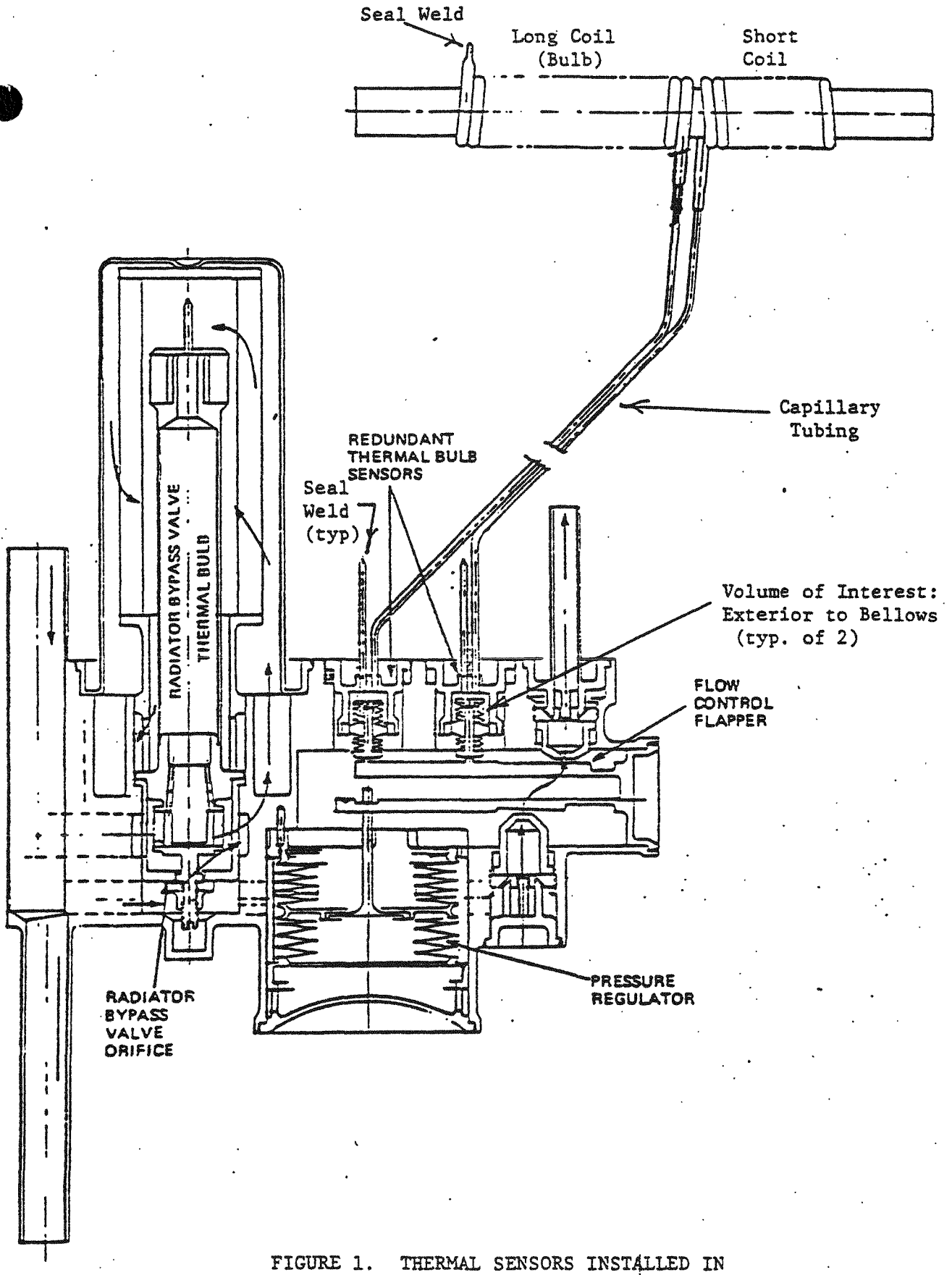

FIGURE 1. THERMAL SENSORS INSTALLED IN FLUID LOOP CONTROL VALVE

it was found that these units were unsuitable for NaK loading experiments since they had been previously loaded with NaK and adequate cleaning of interior surfaces and complete NaK removal were not possible or assured. The results of these Phase I studies were reported to Sundstrand in a Summary Report of August 3, 1979. A primary finding of the study, besides the need for "virgin" surfaces in as-received sensors, was the need to prepare the surfaces for NaK wetting by high temperature vacuum bakeout. It was also suggested that the sensors be hydrogen baked at as high a temperature as possible as defined by sensor material limitations. A limit of 425 C was imposed by the properties of the thin wall bellows.

This report will describe the system for loading NaK into sensors and the method of sensor installation. The step-by-step procedure for obtaining a successful NaK loading as developed in loading seven thermal sensors is documented.

EXPERIMENTAL EQUIPMENT

The experimental equipment used for loading NaK into thermal sensors is shown in Figure 2. The principal system elements are the furnace, NaK supply system and vacuum system. A portion of a multipoint temperature recorder can be seen at the left edge of the picture. The furnace consisted of three sections mounted in line. Electrical power to each 178 mm long furnace section was controlled by separate auto-transformers. The furnace was lined with a segmented alumina tube with a 115 mm inside diameter. When the sensors were installed in the furnace, the furnace ends were covered with fiberglass batting back with metal foil; this insulation was held in place by wires which crossed the outer surfaces of the foil and which were secured to the furnace supports.

The high purity NaK was supplied from a stainless steel pot which nominally holds 1.35 kg of liquid metal when full. The pot also contains zirconium chips to assist in maintaining NaK purity. Overpressure to the NaK pot for transfer of liquid metal was supplied from a cylinder of high

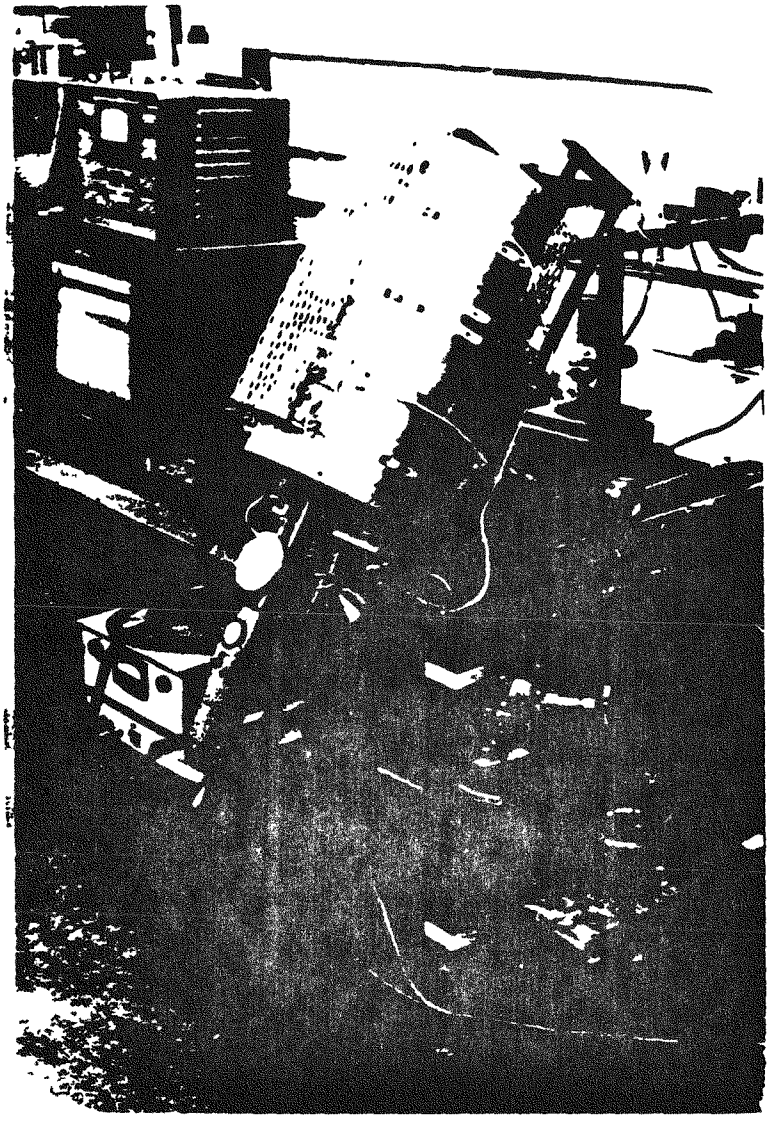

FIGURE 2. EXPERIMENTAL EQUIPMENT SET-UP

purity argon. Great care was exercised in setting up the argon system to assure that air was removed from the system before argon was introduced to the pot. Appropriate valving was installed for venting the argon.

A vacuum system was available for evacuating the sensors as necessary for leak checking and bakeout. A 13 mm diameter manifold system was fabricated, and appropriate valving allowed evacuation of sensor from both ends as well as hydrogen flow end-to-end. Manifold pressure was measured with a thermocouple gage and readout. Manifold pressures of nominally 4 Pa (30 μm) were obtained with a fore pump and small diffusion pump.

A fixture was designed and constructed to measure deflection versus force and deflection versus temperature for the thermal sensor bellows containing NaK at temperature in the furnace. This fixture is shown attached to the furnace structure in Figure 3. A push-pull force gage with an extension rod to contact the bellows was installed in the fixture; this gage would be driven in and out with a crank-handled lead screw. A dial gage was mounted on the extension rod; deflections are measured in reference to a fixed surface which the dial gage probe contacted. This fixture was mounted in position after the NaK was introduced into the sensors.

SENSOR INSTALLATION

There are two thermal sensors in each Sundstrand assembly. The tubings were bent to allow insertion of the assembly into the furnace; the bent configuration required is shown in Figure 4. Each open-ended tube on the bellows housings was bent 180 degrees so that it emerged from the bottom of the furnace; these tubes were connected to the NaK supply system. The connections to valves in the NaK system were made by welding a 6.35 mm OD bushing to the exterior of the 3.18 mm OD tubing at the end to fit into the 6.35 Swagelok fittings on SS bellows-sealed valves. All SS components were used in parts of the system exposed to flowing NaK.

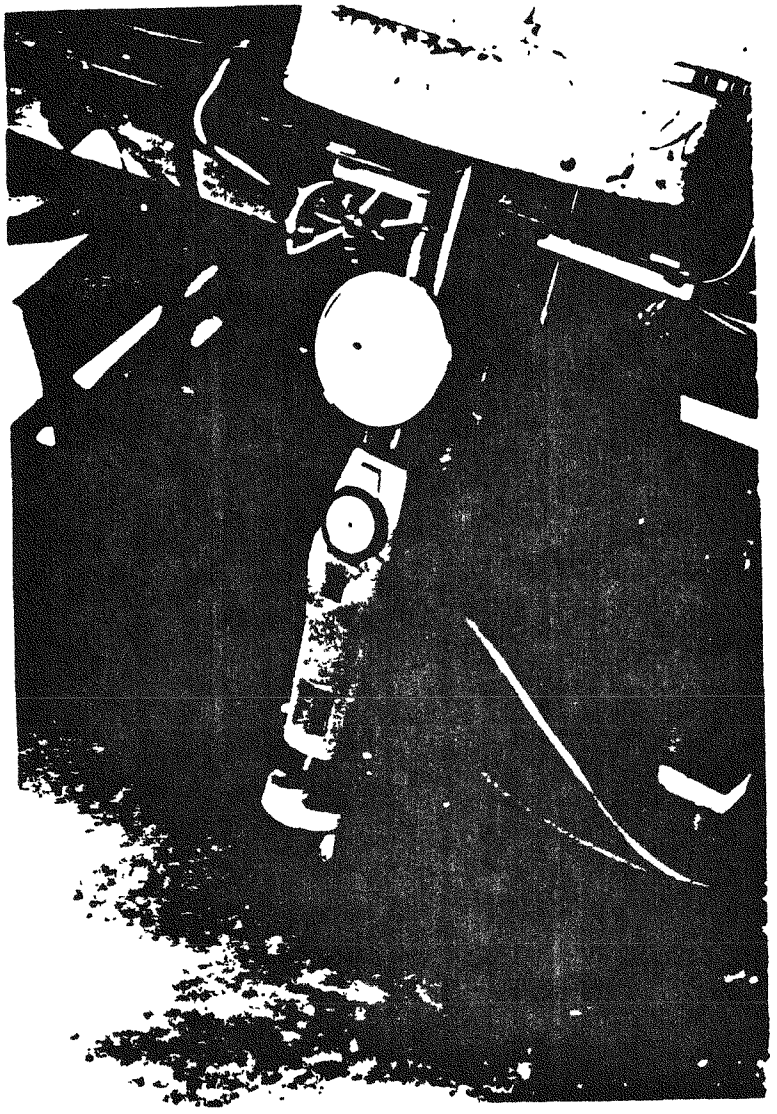

FIGURE 3. BELLOWS DEFLECTION MEASUREMENT FIXTURE

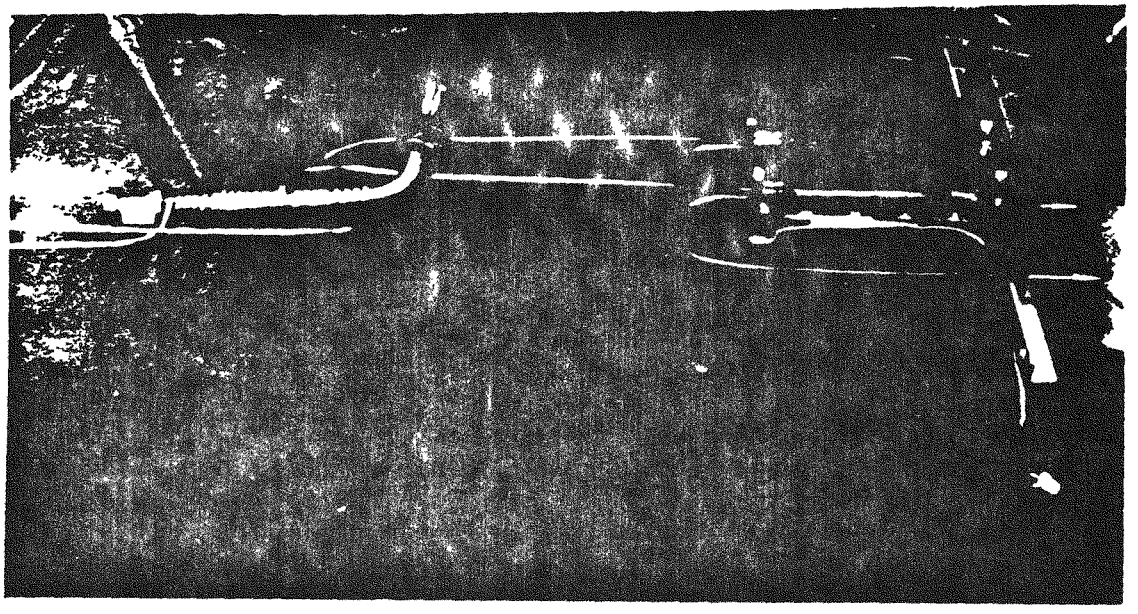

FIGURE 4. THERMAL SENSOR ASSEMBLY PREPARED FOR FURNACE INSERTION

The bellows housings were mounted side by side on a fixture which positioned them inside and about 100 mm above the bottom of the furnace; the bellows faced the open end of the furnace. The mounting fixture had an air cooling line attached to it; air cooling was required to reduce the temperatures of the bellows housing to a low level during the latter stages of the sensor loading. The free bellows lengths were measured before furnace insertion. Each bellows was tied down with a piece of wire to extend the internal bellow convolution exposed to NaK. At an appropriate later time these wires were cut in the furnace. The mounting assembly and bellows tie-down can be seen in Figure 4.

The open-ended tubes from the coils emerged from the top of the furnace, and were also bushed to fit valves as described below. The long coil was connected by a bellows valve to a section of 9.5 mm OD tubing, 180 mm long, to obtain a sample of NaK; each end of the sampler was sealed with a bellows valve. Brass valves were employed in the remainder of the system. In those parts of the system where a valve was exposed to NaK, if the valve was needed for reuse, the valve was aligned such that NaK cleanout of the port occurred only under the seat. Pieces of tubing exposed to NaK were replaced with new material for loading each assembly, and bellows valves were not reused. The ID's of new tubing were rinsed with dilute acid and acetone, and dried at 100 C. Chromel/Alumel thermocouples were tack welded to the exterior of the bellows housings and of the 13 mm diameter tube next to the sensor coils; they were connected to a multipoint chart recorder to monitor temperatures.

NAK LOADING PROCEDURES

General Description

The NaK loading procedure as developed by Battelle consisted of the following major operations:

- System assembly and leak check
- Hydrogen bake at 420 C for 3 hours
- Vacuum bakeout at 360 to 400 C for 3 days
- Introduction of NaK to each sensor sequentially
- NaK wetting exposure at 375 C for 1 day
- Regulation of component temperatures - Bellows, 95 C; Coils, 355 C
- Measure sensor performance with valves closed: deflection versus force; bellows length; thermal cycle bellows deflection
- Crimp and weld seal NaK in sensors
- Repeat sensor performance measurements
- Cool to room temperature
- Optional-reheat to temperature and repeat sensor performance measurements
- Removal of other NaK filled components.

With the experimental set-up used at Battelle, temperatures were found to be very sensitive to furnace electrical settings. Operating experience provided auto-transformer settings which allowed easier, more rapid approaches to desired temperatures; it took many hours for temperatures to stabilize after small adjustments of electrical input. In many cases deflection data was obtained "on the run" as the temperature was changing. The thermal cycle required for the bellows deflection versus temperature measurement was obtained by overpowering the furnace to force a fast temperature rise followed by underpowering to drop the temperatures to the desired level rapidly. The

segmenting of the furnace allowed the low temperature for the housings to be obtained by turning off power in that furnace section.

For sealing the sensors, NaK was cleaned out of the seal areas before welding to assure no contaminants remained which could adversely affect seal life-time performance. This cleanup was done while the sensors were at temperature in the furnace. The tubes were cut as close to the furnace as possible. Before cutting, the tubes were crimped to seal the NaK in the system until the final weld seal could be established. Two crimps were made in each tube at each end of each sensor; two crimps were necessary to seal the NaK in the remaining tube length when the tube was cut. Crimps were made in succession starting at the upper end of the furnace and working toward the NaK supply with the NaK valve open. This was done so that no NaK was trapped in the sensor under a severe overpressure; this behavior had been observed in early experiments and was caused by reduction of internal volume by crimping. The tools for crimping these tubes were developed in experimentation by Sundstrand; they could produce a seal resistant to helium leakage. The crimping tools are shown in Figure 5.

After the tubing was cut, the NaK was washed out of the sensor tubulations. This was originally done with butyl alcohol followed by a water rinse; a sample of rinse water was collected and tested with phenolphthelein for alkali metal content. When the sample showed no indication of alkali metal, the tube was rinsed with acetone to remove water and was dried with hot air. The short length of cleaned tube outside the crimp was flattened, trimmed back, and weld sealed with a plasma torch. Weld integrity was examined visually. The butyl alcohol wash next to the furnace was eliminated owing to the flammability hazard. A water wash of the residual NaK in the tubes was found to be satisfactory; the NaK reaction was violent, but not excessive owing to the small volume of NaK.

Specified methods were established for obtaining bellows deflection data. For the deflection versus force measurements the data set was started with 1 lbf and a dial reading was obtained. Force was increased in 1 lbf increments and dial readings were taken at each increment. This data set

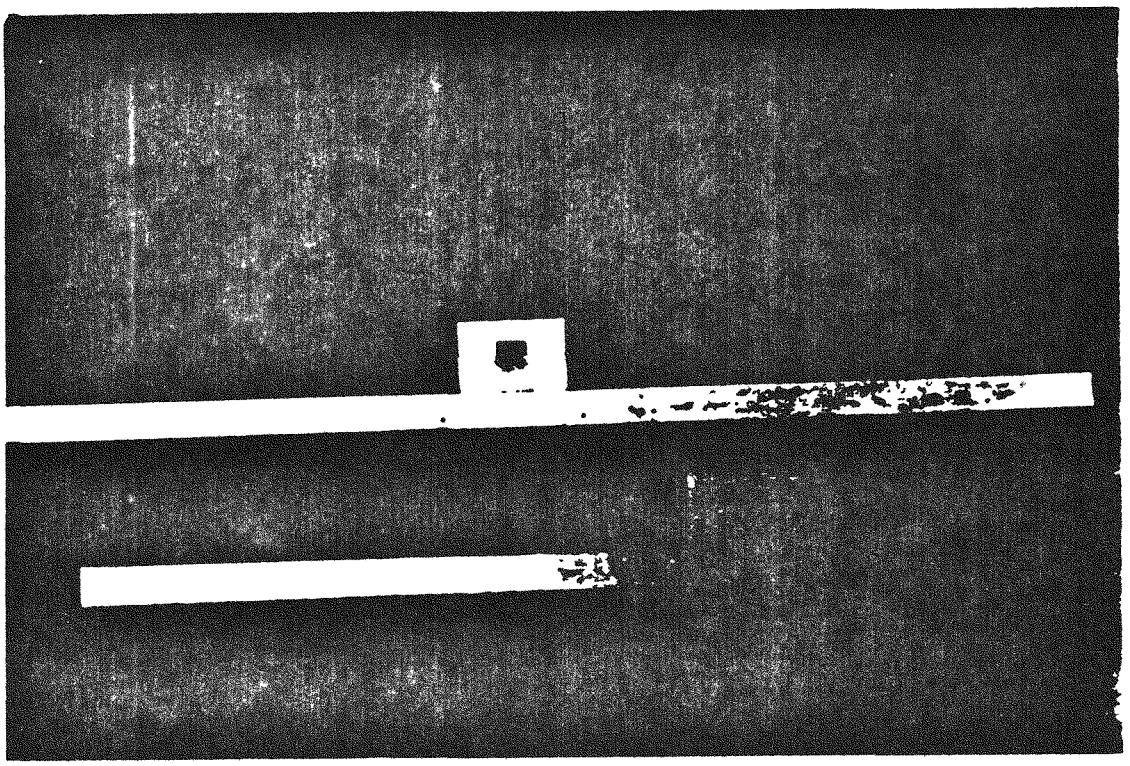

FIGURE 5. CRIMPING TOOL

was taken 3 or 4 times to determine repeatability. Bellows lengths at temperature was obtained by shifting the force gage/extension arm fixture position and cranking it in to contact the shoulder of the housing. Bellows deflection data were obtained by applying a constant 4 lbf to the bellows periodically as the temperature was changing, and taking dial gage readings related to instantaneous temperature readings. Deflections of bellows in both housings could be measured in the same thermal cycle by moving the fixture back and forth between thermal sensors, if a slow heatup rate was used. Data was taken at about each 5 C temperature change up to 395 C.

NaK Loading Procedure

This section presents the step-by-step procedure developed at Battelle for loading NaK into Sundstrand's thermal sensors. Newly fabricated units did not become available until mid-September 1979. The procedural steps here evolved during the loading of thermal sensors. A schematic diagram of the NaK filling system is shown in Figure 6; the valve numbers are used in the procedures. Procedures assume that sensor systems are connected to a vacuum system, and the leak detector is connected and can be valved in when needed.

A. Interior Surface Preparation

1. Open valves 1A, 1B, 2A, 2B, 3, 4, 5, 6 and 15.
2. Helium leak check all weld and Swagelok connections in the system. Tighten and repair as necessary until indicated leak rate of $1 \cdot (10^{-7})$ atm-cc/sec is attained. Check all other valves for closure.
3. Close valve from manifold to helium leak detectors.
4. Close valves 6 and 15.
5. Regulate low pressure in hydrogen supply cylinder.
6. Open valve 13 to allow hydrogen flow into evacuated system.
7. Activate mechanism to burn off exit hydrogen. (A heater cone was used by Battelle).

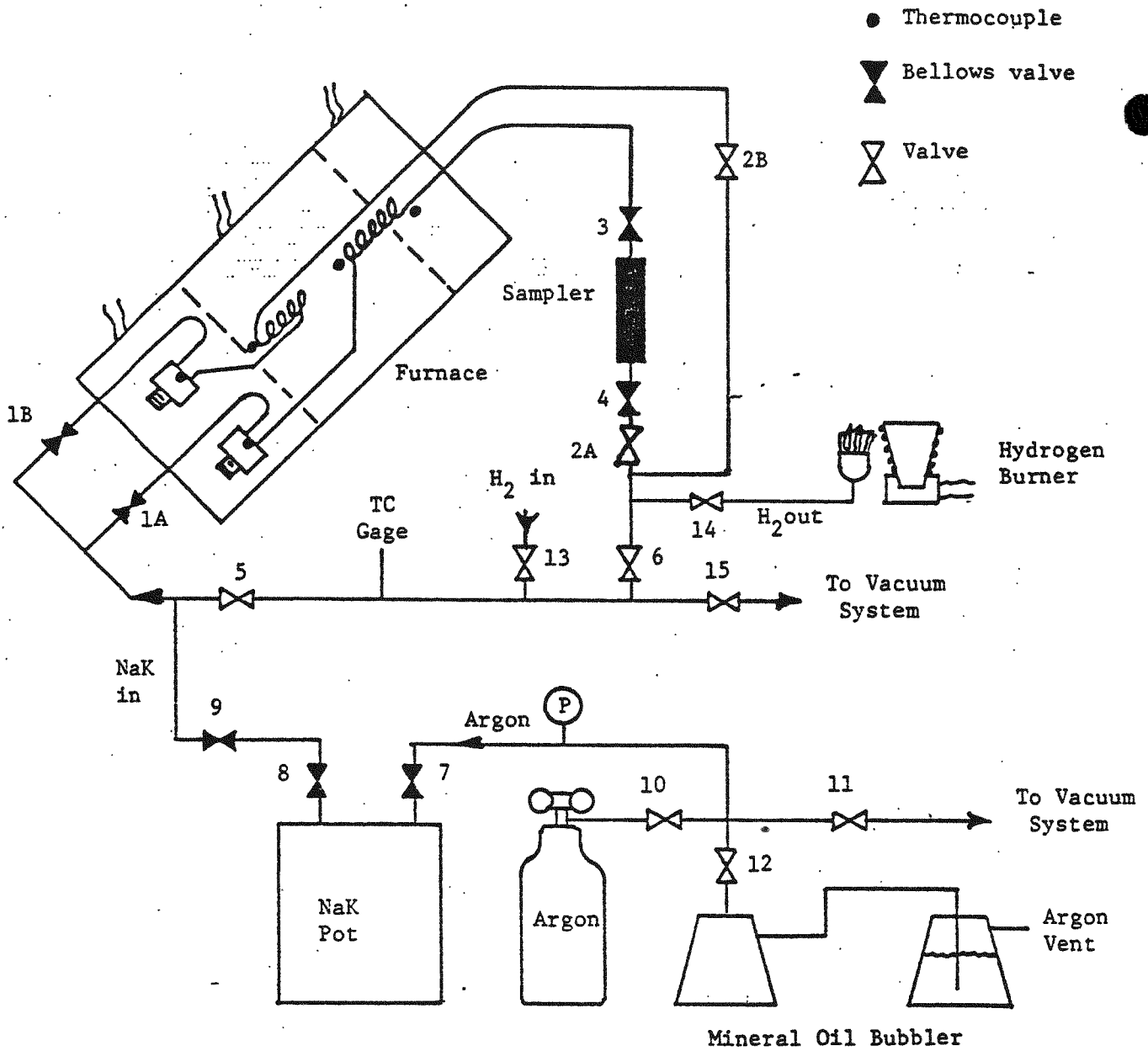

FIGURE 6. SCHEMATIC LAYOUT OF EXPERIMENTAL EQUIPMENT FOR NAK LOADING OF SENSORS

8. Open valve 14, regulate low hydrogen flow rate, and ensure hydrogen burning.
9. Start heating of furnace.
10. When temperatures of sensors are between 400 and 420 C, start hydrogen bake out period.
11. After three hours, reduce electrical input to furnaces slightly.
12. Close valves 13 and 14 to stop hydrogen flow. Turn off hydrogen burner and cylinder valves.
13. Open valves 6 and 15 and initiate high temperature vacuum bake out.
14. Adjust furnace electrical input to obtain sensor temperature of 370 to 380 C.
15. After 72 hours, terminate vacuum bake out.

B. <u>NaK Filling of Sensors</u> (Sensor 1 first)

1. Open valves 10 and 7 and pressurize NaK pot to 15 psig from argon cylinder. Close valve 10.
2. Open valve 8 on NaK pot.
* 3. Close valve 1B to isolate sensor 2 from NaK supply.
* 4. Close valve 2A to close exit of sensor 1 system.
* 5. Close valve 5.
6. Open valve 9 to admit NaK to sensor 1.
7. Observe temperature recorder for significant reduction of bellows temperature (e.g. 60 to 70 C) to indicate NaK flow; check temperature of exit tube for elevated temperature (tactile).
8. Wait until temperatures return to near pre-admittance levels.
9. Close valves 3 and 4 to seal NaK in sampler.
*10. Close valve 2B to close exit of sensor 2 system.
11. Open valve 1B to admit NaK to sensor 2.
12. Observe temperature recorder for bellows temperature reduction (about 30 C) to indicate NaK flow.

---

* Requires one-over-one check before proceeding.

13. Regulate temperatures at about 375 C and hold for 24 hours.

C. Sensor Performance Measurements

1. Remove insulation from bottom of furnace.
2. Turn off power to bottom furnace section.
3. Start air cooling of bellows housing mounting stand.
4. Regulate coil temperature at 355 C $^{+0\ C}_{-10\ C}$ and housing temperature at 95 C.
5. Cut wires tying down bellows.
6. Open valve 12 to reduce argon overpressure on the NaK pot. Close valve when pressure decreases to 2 psig.
7. Close valves 1A and 1B to seal NaK in sensors.
8. Mount deflection/force measurement fixture on bottom of furnace.
9. Measure free length of bellows of sensor 1.
   a. Determine dial gage position at end of bellows at initiation of contact
   b. Determine dial gage position of shoulder of housing.
   c. Determine length by difference and add to housing length from initial measurement
   d. Check to see if this length is in the range specified in note 34 of Sundstrand drawing No. 721262.
10. Measure force versus deflection for bellows of sensor 1.
    a. Apply 1 lbf to bellows and note dial gage reading
    b. Apply force in 1 lbf increments up to 8 lbf and note dial gage reading for each increment
    c. Determine bellows spring rate by $\Delta P/\Delta L$ where $\Delta P = 7$ lbf and ΔL = total measured deflection.
    d. Compare with specifications of note 35 of Sundstrand drawing No. 721262, or most recent expectation
11. Move fixture and repeat steps 9 and 10 for sensor 2.
12. Increase electrical power input to furnace to obtain temperature rate of rise of approximately 5 C per 5 minutes.
13. Measure deflection versus temperature for the bellows in each sensor.

a. Move the measurement fixture back and forth between sensors to obtain a deflection measurement on each sensor every 5 C.

b. Note the dial gage reading at the same time the temperature of the bellows and coil are obtained

c. Reduce heating when coil temperature reaches 395 C.

d. Regulate temperatures at levels of step C4

e. Calculate $\Delta L/\Delta T$ for total movement for total temperature change. Compare to values specified in note 32 of Sundstrand drawing No. 721262 or most recent expectation

f. The above procedure can be run twice to measure each sensor in a separate thermal cycle without having to re-position the fixture constantly. Step C13a was employed to shorten the required time

14. Remove measurement fixture.

D. Sensor Sealing

* 1. Open valve 1A on sensor one.

2. Place a special crimping tool across the top of the furnace as close as possible with the insulation compressed. When the location of this crimp is established on the tubing for sensor 1, crimp this tube with a locking pliers about 13 mm outboard of the special tool; leave the pliers in place.

3. Tighten completely the screws on the special tool, and crimp the NaK tubing.

4. Cut the tubing between the crimps with a jeweler's saw.

5. Clean out the end of the open sensor tube secured in the special crimping tool.

a. Water rinse to react out NaK

b. Phenolphthalein check of water sample for complete alkali metal removal

c. Acetone rinse

d. Hot air dry.

6. Flatten cleaned tubing end with locking pliers.

7. Trim flattened end.

8. Weld flattened end with plasma torch and visually inspect with 10X eyepiece.

9. Place a special crimping tool on the sensor tubing emerging from the bottom of the furnace as close to the furnace as possible.
10. Repeat step C3.
11. Crimp the tubing about 13 mm outboard of the crimping tool with a locking pliers as in step C2.
* 12. Close valve 1A.
13. Repeat steps C4 to C8.
14. Remove the crimping tools from the sealed sensor.
15. Open valve 1B on sensor 2.
16. Repeat steps C2 to C11 for sensor 2.
* 17. Close valve 1B.
18. Repeat steps C13 and C14 for sensor 2.
* 19. Close valves 9 and 8 on the NaK supply system.
20. Open valve 12 and bleed argon pressure off NaK pot through mineral oil bubbler.
* 21. Close valves 12 and 7.

D. Sensor Performance Checkout

1. Repeat steps C8 to C13 for the weld sealed sensor for comparison with earlier performance.
2. Optional cool to room temperature and reheat to operating temperature to re-measure values as in steps C8 to C13.
3. Remove sensor assembly from furnace.
4. Record all data on the data sheet provided for documentation of operation and performance (specimen attached)

E. Removal of Other NaK Filled Components

1. All disconnects from valve ports require:
   a. Reaction of NaK from port with butyl alcohol
   b. Water rinse and phenolphthalein test
   c. Acetone rinse
   d. Hot air drying.

2. Disconnect assembly of tubing containing bellows valves 1A and 1B from valves 5 and 9.
3. Clean out ports of valves 5 and 9 as in step E1.
4. Disassemble tubing from valves 1A and 1B.
5. React NaK in tubing and valves with butyl alcohol.
6. Dispose of tubing and bellows valves. Save SS Swagelok nuts and tee for reuse (non NaK use).
7. Disconnect NaK filled length of tube at valve 2B.
8. Clean out port of valve 2B as in step E1.
9. React NaK in tube with alcohol and dispose of tubing.
10. Disconnect sampler and tubing connection at valve 2A.
11. Clean out port of valve 2A as in step E1.
12. Disconnect tubes from valves 3 and 4 on sampler.
13. Clean out ports of valves 3 and 4 as in step E1.
14. Repeat step E9 for tubing separated in step E12.
15. Seal valve ports on valves 3 and 4 on sampler with Swagelok caps.
16. Send the sampler for analysis of oxygen and carbon contents.

Data obtained in developing the technique is recorded in Battelle Laboratory Record Book No. 34783, pp 38 to 92.

BATTELLE'S COLUMBUS LABORATORIES

PERFORMANCE DATA FOR SUNDSTRAND
THERMAL SENSORS

Assembly No. _____ Sensor No. _____

Sensor Sealing

Date _____ Temperature, C

Sampler _____ Coil _____

Housing _____

Compression Test (dial indicator reading)

Temp, C

) lbf

1

2

3

4

5

6

7

8

ΔL(7 lbf ΔF), in.

Condition

Time, hrs

Hydrogen bake _____ Vacuum bake _____ NaK Exposure _____

Temperature/Deflection Test (4 lbf constant load)

Temp, C	Dial, in.	Temp, C	Dial, in.	Temp, C	Dial, in.

ΔT, C

ΔL, in.

Conditions

Bellows Free Length

Temperatures, C

Housing, in.

Bellows, in.

Total, in.

Conditions

BCL Lab Book No. _____ Pages _____ _____

APPENDIX A

3.9 Potential Performance Improvement

It was apparent from component and system testing that further improvements in system performance are feasible.

3.9.1 Turbine Efficiency

A new design would employ the longer blade height indicated as being optimum from turbine test rig results. This would result in a 1% point turbine efficiency increase. This is a relatively minor improvement and would only be justifiable on a new machine.

3.9.2 Alternator Efficiency

A new PCS design would allow the use of a Samarium Cobalt permanent magnet generator. Development of this type of generator has advanced considerably since the original KIPS design. An efficiency of 95% would be achievable at this power level with an accompanying saving in weight.

3.9.3 Controller Efficiency

It is felt by Sundstrand that the restrictions on quality of power and voltage level are probably unrealistic for a real application. Many spacecraft systems currently operate at 100V DC and users often recondition electric power. In addition, some power is sure to be usable with a relatively high ripple content (e.g. for heating). To illustrate the potential benefits of relaxing the current constraints, calculations were made for a controller delivering 100V DC with only one third of the current filtering losses. For these assumptions the controller efficiency rose from 90.6 to 96.3%. A concomitant effect of reducing the filtering requirements is weight saving since the current filters weigh about 4 lbs.

3.9.4 Turbine Inlet Temperature

Results from Battelle testing indicate that a further increase in turbine inlet temperature to 725°F is probably possible. This would result in about .36% points increase in system efficiency.

3.9.5 Turbine Inlet Vapor

The hypothesis of wet turbine inlet vapor is based upon a correspondence in magnitude of apparent

Table 3.9.1 Component Performance Improvement

Component	Current Performance	Projected Performance	System Improvement	Improvement Method
Turbine Efficiency (%)	68	69	.23	Blade Height Selection
Alternator Efficiency (%)	93.5	95	.27	Samarium Cobalt Design
Controller Efficiency (%)	90.6	96.3	1.14	Reduced Quality Output Higher Voltage
Turbine Inlet Temperature (^{0}F)	700	725	.36	Further Fluid Testing Required
Wet Vapor (Btu/Hr)	950	—	0.7	Boiler Redesign

heat loss in the turbine and negative heat loss in the heat sources. If this is correct a significant performance gain is feasible. The apparent heat loss of 950 Btu/hr would represent a gain of about 0.7% points in system efficiency.

3.9.6 Jet Condenser Vapor Pressure

Component testing with the 90 nozzle jet condenser indicated that the design pressure of .105 psia would be obtained with a liquid/vapor mass flow ratio of about 8.5. The system was operated at flow ratios slightly less than this value during the last build but operating condenser vapor pressures were about 0.126 psia. The discrepancy likely results from the previous inability to measure the low pressures accurately. Further increases in liquid flow were feasible, and indeed were obtained, by running at higher jet condenser pressure recovery. However, the additional pumping power associated with the increased flow compensates for the reduction in back pressure and no net system performance gains accrue. Table 3.9.1 summarizes potential system performance gains from improved components.

4. GDS TESTING

4.1 Operating Hours

During Phase II 9482 hours of GDS operating time were accumulated. The final build of the GDS accumulated 2002 hours of operation. The final run of the GDS was terminated by an intentional shutdown. The total number of hours of GDS operation accumulated during both phases of the program was 10606. The teardown report for the build prior to the final build is presented in Appendix D. A summary of operational hours including the development unit is given in Table 4.1.1.

4.2 Operational Problems and Solutions

Several problems were encountered during the initial running of the final build. Early in the build, problems with the electric heat sources (EHSA's) arose. The problems were associated with the wiring pigtail between the heater block and the connector on the EHSA housings. The problem resulted from overheating of the pigtail. The problem appears to be more

Table 4.1.1 Operational Hours Summary

Phase	Build	Period	Hours
I	Development Unit	Dec 1977 - Mar 1978	540
I	Mod 1	April 1978 - Aug 1978	1124
		Sub-Total	1664
II	Build A	Sept 1978 - April 1979	3182
II	Build B	May 1979 - May 1980	4298
II	Endurance	Aug 1980 - Dec 1980	2002
		Sub-Total	9482
		Total	11146

severe on the voltage tap leads in that the voltage tap leads appear to fail prior to the power leads. The overheating problem had been encountered in Phase I and Teledyne had relocated the pigtail to reduce the length of the wire run near the heater block. It is apparent that relocation of the pigtail did not solve the problem. The pigtail design had attempted to trade off heat loss conducted through the pigtail against thermal problems resulting, in part, from electrical losses in the wiring. During the run EHSA #1 and EHSA #3 were replaced and at the end of the run both EHSA #1 and EHSA #2 were being operated with failed voltage tap leads. The voltage tap inputs for the EHSA #1 and EHSA #2 watt transducers were taken from points in their power supply consoles and the readings corrected for losses in the feeder cables based on tests of EHSA #3.

The second problem encountered with the final build was liquid leakage from the non-condensable gas separator (NCGS). NCGS was received from Dynatherm the evaporator and condenser jackets were found to have many leaks. The jackets were removed from the NCGS, cleaned and vacuum baked, and leak checked to determine leak locations. The jackets were a two piece construction. Each piece was a welded aluminum assembly with aluminum tubes for inlet and outlet flow. The connection between each piece of the jackets was made with a Swagelok union. The inlet and outlet connections at the condenser jacket were made with Swagelok to CPV adapters. The inlet and outlet connections at the evaporator jacket were made with Swagelok to VCR adapters. Dynatherm had installed all Swagelok fittings with stainless ferrules.

Leaks were found at all Swagelok fittings and in the jacket welds. Since there was insufficient tubing to cut off the swaged segment of tubing and remake the joint, it was decided to seal the leaks with an epoxy. Epoxylite 6203 was selected because it is known to be compatible with Dowtherm. The leaks in the jacket welds were weld repaired. The jackets were leak checked after the weld repair to verify they were leak tight.

The jackets were then reassembled to the NCGS. The jackets were evacuated and the epoxy applied to the Swagelok fittings. After the epoxy had cured the assemblies were again leak checked. It

was discovered that some Swagelok joints still leaked and that leaks had reappeared at the jacket welds. Since the epoxy was being used to seal leaks at the Swageloks, it was decided to apply it to the jacket welds to seal those leaks. The jackets were then evacuated and epoxy applied to the leak sites. After curing the assembly was again leak checked and found to be leak tight. After the GDS was assembled, GDS leak checks again located leaks at the NCGS jackets. Epoxy was applied and the leaks were stopped. After the first run of the GDS, leaks were again located on the NCGS jackets. RTV was applied and the leaks were stopped. Leaks were again discovered the next time the GDS was checked. Since the leaks had affected neither vacuum system operation nor system operation, it was decided to continue operation without repairing the jackets. The remainder of the GDS operation was with leaks into the vacuum chamber at the NCGS jackets.

Another problem encountered in the early portion of the final build operation was a sequence of jet condenser floodouts followed by very slow drains. The jet condenser funnel was removed and two large pieces of Viton were found to be lodged in the throat. The Viton was removed and found to be from the grommet which had been used as a seal between the pressure sensing tube to the alternator cavity and the "cone" mounted on the transition housing. The cone provides the inside diameter of the vapor flow path in the transition housing. Since the tube passed through the grommet and the grommet was mounted in a slot in the cone, the grommet had to fail in three locations to enable the two pieces to migrate to the jet condenser throat. The two pieces made up substantially all the Viton which had been mounted on the outside of the cone. Since the remainder of the grommet was located on the tube inside the cone and was larger than the slot through the cone, it was believed to be trapped in the cone and to be unlikely to cause further operational problems. It was therefore decided to reassemble the GDS and continue operation without removing the remainder of the grommet.

Removal of the Viton allowed the jet condenser to be started reliably but another problem remained which also resulted in a jet condenser flood.

Data traces of the shutdowns made at normal paper speeds did not indicate a problem. Since no indication of trouble right up to the time of the shutdown could be found, the possibility that the shutdown could result from spurious safety system signals was investigated.

A time lag was added to the safety shutdown system between the time the shutdown condition was sensed and the time the shutdown sequence was begun. An indicator of safety system sensed shutdown condition was added to the magnetic tape. The GDS was then started and a shutdown recorded. The tape was played back through the data recorders at a high paper speed. The safety system was found to be operating properly.

Further examination of the high speed traces revealed a small fluctuation in the jet condenser diffuser outlet pressure during the time period prior to the shutdown. Based on jet condenser rig testing experience and KIPS development system starting experience, these fluctuations were taken to be indicative of liquid Dowtherm droplets in the vapor stream. Liquid in the vapor stream is known to be a cause of floodouts.

A possible source of liquid droplets is condensation on the lower coils of the regenerator. Recognition of the potential for problems resulting from condensation on the lower coils of the regenerator had led to the incorporation of a thermal shunt from regenerator liquid out to liquid in on the GDS.

As a result of the flood problem, an additional shunt and a 250 watt electric heater were installed on the regenerator inlet line. Power to the electric heater was controlled with a variable transformer. The power was adjusted to maintain the regenerator liquid inlet temperature above the saturation temperature at the measured regenerator vapor outlet pressure. After taking this corrective action, the GDS was able to operate for much longer periods of time. The requirement for a large shunt may have resulted from a lower turbine outlet temperature resulting from higher efficiency and lower heat losses.

With the GDS capable of longer periods of operation, a problem of non-condensable gas accumulation was encountered. Accumulation of non-condensable gases had been encountered in the previous GDS build. The symptoms of the problem were the gradual increase in pressures measured in the low pressure vapor portion of the cycle. The eventual consequence of the gas accumulation is a system shutdown caused by a jet condenser floodout. The non-condensable gas separator (NCGS) was intended to prevent gas accumulation and was shown to be operational during bench tests. Examination of temperatures along the NCGS body indicated that the thermal linkage between the condenser jacket and the NCGS body was not adequate. The NCGS installed on the GDS was the EX version. The EX separator utilized a combination of Torlon and teflon rings for heat conduction from the separator body to the jacket. Torlon rings were preferred with respect to teflon because of the propensity of the teflon to cold flow. There was insufficient Torlon, however, so the teflon rings were alternated with the Torlon.

Inspection of the NCGS revealed that the teflon rings had flowed and fitted very loosely in the gap between the condenser jacket and the NCGS body. In order to achieve a better thermal linkage, a light coating of vacuum grease was applied to the inside of the teflon rings and a heavier coating of vacuum grease applied to the outside of the rings. The condenser jacket was reinstalled and after the bolts were torqued down the excess grease that was squeezed from the assembly was removed.

The GDS was restarted and temperatured along the NCGS body were monitored. The NCGS temperatures indicated that the thermal linkage was now adequate and that the NCGS was now functioning. Pressures in the low pressure vapor portion of the cycle were monitored continually throughout the remainder of GDS operation and were very stable.

The NCGS thermal link problem is unique to the EX version of the separator. The planned production NCGS would have integral evaporator and condenser jackets. The EX version had the Torlon/teflon ring configuration to allow thermal conductance

to be varied during bench testing. After the resolution of the thermal conductance problem the NCGS operated as expected.

The NCGS problem was the final problem encountered during running of the final build of the GDS. The last three runs of the build were terminated by intentional shutdowns.

4.3 Measurement System Improvements

A significant Phase II effort was expanded in the area of improvement of the instrumentation system. Special thermocouple probes were designed and installed in the low pressure vapor portion of the DIPS. The design and installation of these probes is described in Appendix B. Thermocouples were made from specially aged and calibrated wire as described in Appendix B.

The thermocouple wiring and data acquisition system were also improved. The thermocouples installed on the DIPS were made from segments of thermocouple wire cut sufficiently long to allow all connections to the thermocouple feed through wires to be made in uniform temperature region (UTR) boxes. The UTR boxes minimized the temperature measurement errors resulting from temperature gradients which might otherwise have existed at locations where the slightly dissimilar thermocouple extension wires were connected to the thermocouples. The thermocouple feed throughs at the chamber wall for thermocouples required to have high accuracy were made without using connectors. The resulting continuous length of wire fed through the chamber wall eliminated other possible sources of error caused by dissimilar material joints.

Outside the chamber wall another set of connections was made in another set of UTR's. The cables from these UTR's extended to the data logger with no intervening connections. Shielded cable was used outside the chamber.

The primary difficulty encountered in installing the improved temperature measurement system was in making connections from the stainless steel sheathed thermocouples to the UTR's in the chamber.

After removing the thermocouple sheath a ceramic material was used to maintain separation between the individual wires making up the thermocouple. The ceramic material proved to be very susceptable to handling damage during connection to the UTR. The result of the handling damage was a thermocouple junction in the UTR. Repairs were made in the chamber after the thermocouples had been secured in the UTR strain reliefs. After these installation problems were resolved, the thermocouple measurement system was trouble free.

Another measurement system improvement was in the area of pressure measurements in the low pressure vapor portion of the cycle. The pressure measurement improvement is described in Appendix C.

An additional improvement to the measurement system was the addition of a magnetic tape recorder. The magnetic tape recorder was intended to facilitate definition of causes of GDS shutdowns. Fifteen data channels were continuously recorded and, in the event of a GDS shutdown, these channels were played back on the test stand data recorders. The data recorders were run at a low paper speed during normal GDS operation and at a high paper speed during tape playback. The combination of the data recorders at high paper speed and the magnetic tape recorder greatly facilitated analysis of GDS problems.

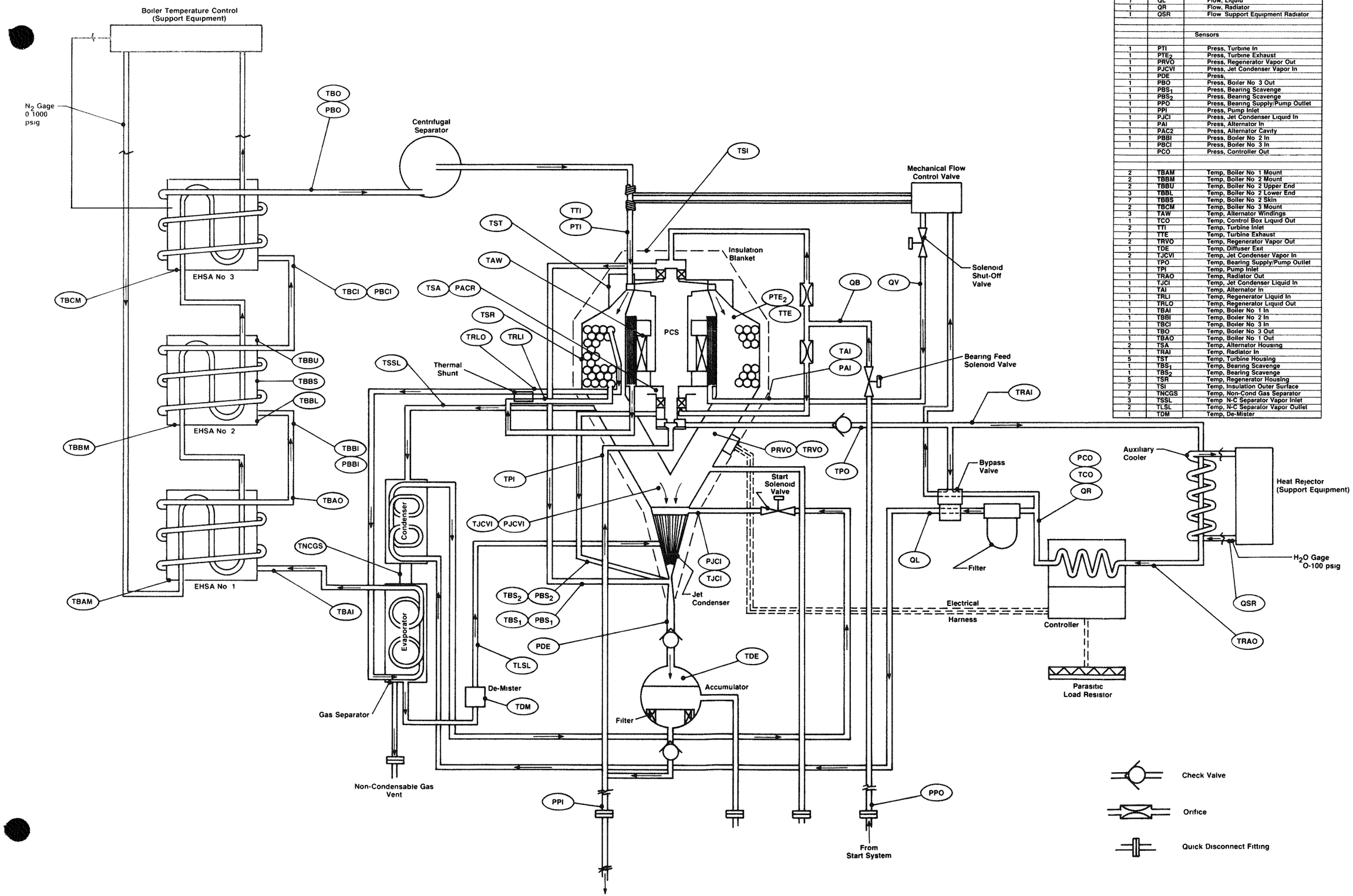

Quantity	Ident	Table Of Instrumentation Description
		Meters
1	QB	Flow, Bearing
1	QV	Flow, Vapor
1	QL	Flow, Liquid
1	QR	Flow, Radiator
1	QSR	Flow Support Equipment Radiator
		Sensors
1	PTI	Press, Turbine In
1	PTE_2	Press, Turbine Exhaust
1	PRVO	Press, Regenerator Vapor Out
1	PJCVI	Press, Jet Condenser Vapor In
1	PDE	Press,
1	PBO	Press, Boiler No 3 Out
1	PBS_1	Press, Bearing Scavenge
1	PBS_2	Press, Bearing Scavenge
1	PPO	Press, Bearing Supply/Pump Outlet
1	PPI	Press, Pump Inlet
1	PJCI	Press, Jet Condenser Liquid In
1	PAI	Press, Alternator In
1	PAC2	Press, Alternator Cavity
1	PBBI	Press, Boiler No 2 In
1	PBCI	Press, Boiler No 3 In
	PCO	Press, Controller Out
2	TBAM	Temp, Boiler No 1 Mount
2	TBBM	Temp, Boiler No 2 Mount
2	TBBU	Temp, Boiler No 2 Upper End
3	TBBL	Temp, Boiler No 2 Lower End
7	TBBS	Temp, Boiler No 2 Skin
2	TBCM	Temp, Boiler No 3 Mount
3	TAW	Temp, Alternator Windings
1	TCO	Temp, Control Box Liquid Out
2	TTI	Temp, Turbine Inlet
7	TTE	Temp, Turbine Exhaust
2	TRVO	Temp, Regenerator Vapor Out
1	TDE	Temp, Diffuser Exit
2	TJCVI	Temp, Jet Condenser Vapor In
1	TPO	Temp, Bearing Supply/Pump Outlet
1	TPI	Temp, Pump Inlet
1	TRAO	Temp, Radiator Out
1	TJCI	Temp, Jet Condenser Liquid In
1	TAI	Temp, Alternator In
1	TRLI	Temp, Regenerator Liquid In
1	TRLO	Temp, Regenerator Liquid Out
1	TBAI	Temp, Boiler No 1 In
1	TBBI	Temp, Boiler No 2 In
1	TBCI	Temp, Boiler No 3 In
1	TBO	Temp, Boiler No 3 Out
1	TBAO	Temp, Boiler No 1 Out
2	TSA	Temp, Alternator Housing
1	TRAI	Temp, Radiator In
5	TST	Temp, Turbine Housing
1	TBS_1	Temp, Bearing Scavenge
1	TBS_2	Temp, Bearing Scavenge
5	TSR	Temp, Regenerator Housing
7	TSI	Temp, Insulation Outer Surface
7	TNCGS	Temp, Non-Cond Gas Separator
3	TSSL	Temp N-C Separator Vapor Inlet
2	TLSL	Temp, N-C Separator Vapor Outlet
1	TDM	Temp, De-Mister

Fig. 3.0.3

Controller Schematic - Phase II

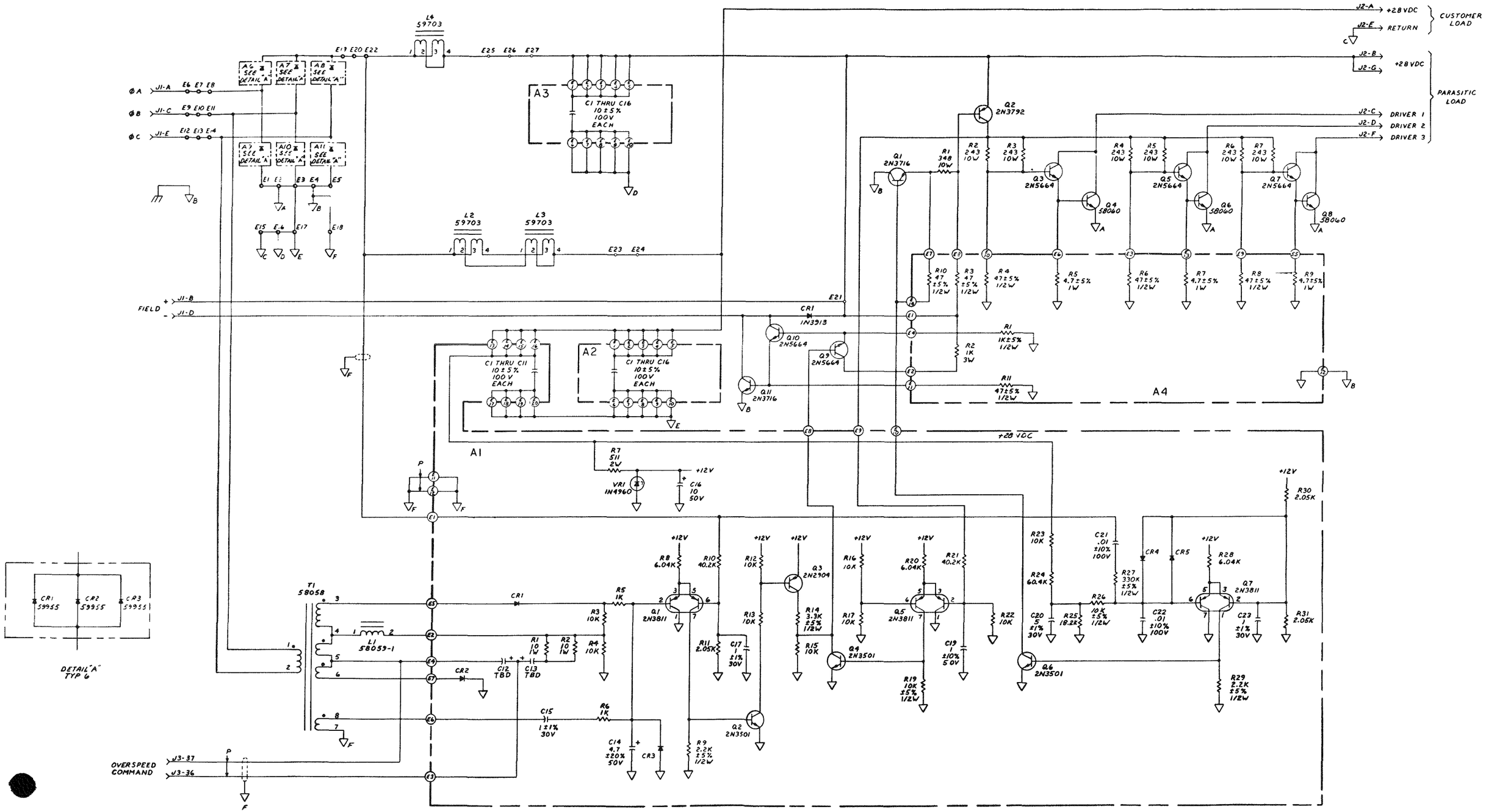

Figure 3.8.8